# Modern Structural Practice

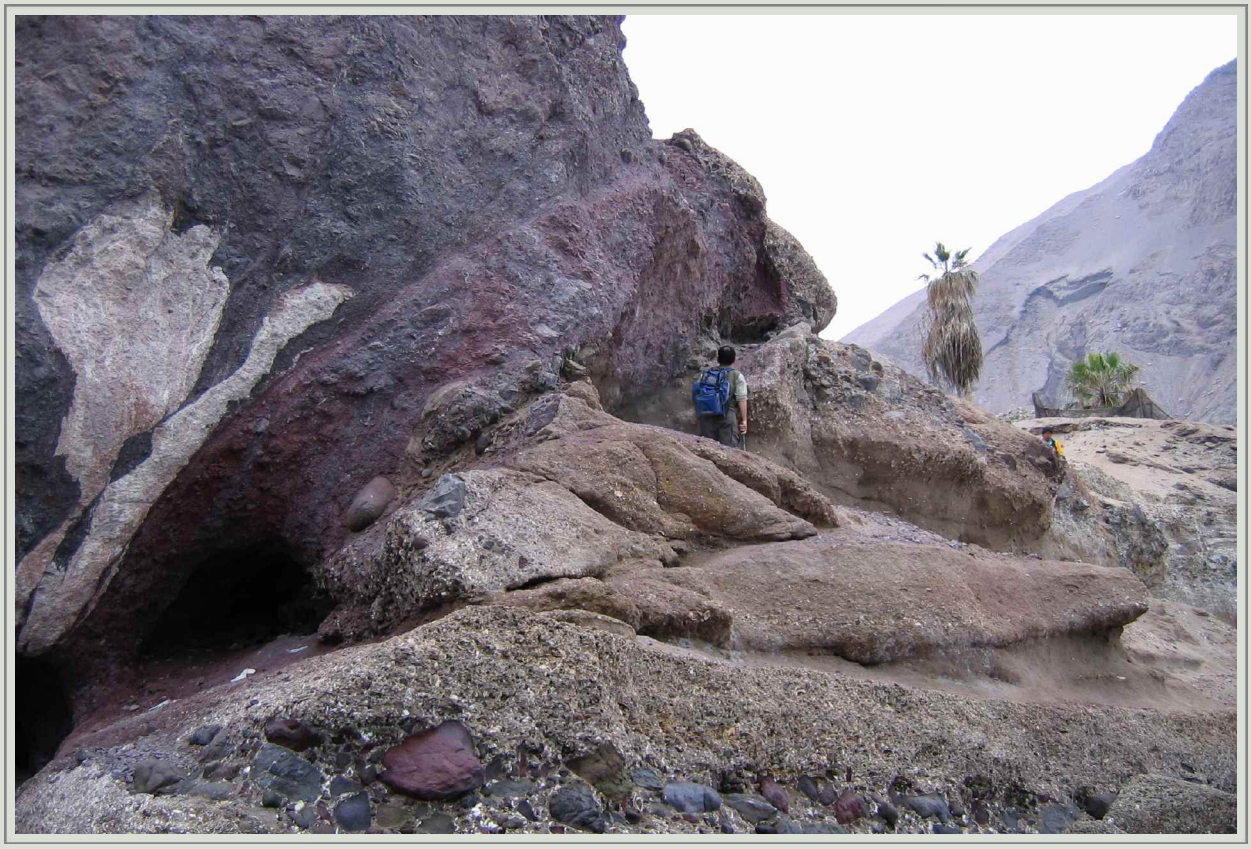

*A structural geology laboratory manual for the 21st Century*

Richard W. Allmendinger

v. 1.9.1, 

Download most recent version from:

https://www.rickallmendinger.net/download

 

 

 

 

# Preface

The subtitle, "A structural geology lab manual for the 21st Century", as well as the rationale for a new manual, needs a little explanation (and, perhaps, some justification). There are several decent structural geology lab manuals out there and the fact that a new one has not appeared in many years would suggest that the field is mature and not changing rapidly, so why write a new one? Because the field of structural geology, indeed all of geology, has changed enormously in the last decade or two. Consider the following:

- Large online digital databases for topography, satellite imagery, scanned geologic maps, GPS data, earthquake data, etc have become readily available
- Digital devices are seeing increasing use in the field. We collect data using tablets and, increasingly, smart phones will replace analog compasses
- Using programs, apps, and web apps to analyze data is now common place. Most structural geologists use such programs in preference to paper, whether drawing sections or plotting stereonets

The world has gone digital, but our teaching of structural geology has lagged far behind: many of the exercises that we ask students to do in structure lab have changed little over the last fifty years. We are not teaching our students how to take advantage of this new world, nor how the tools that they will use in their profession (e.g., stereonet programs, etc.) actually work internally. Digital means that, suddenly, lots of numbers are available to us. To analyze those numbers, requires some math and computing. Most of the math is just additions and multiplications done in a very systematic way as well as, of course, trigonometry. Students have much of the needed math background already (vectors, calculus) so why don't we encourage them to use those skills in their chosen major? Additional concepts — for example matrices — can be learned in the context of problems that are actually of interest to us.

Computing can take many forms but the lowest common denominator is the humble spreadsheet program, which is what *Modern Structural Practice* uses. Everyone

already knows the basics of using a spreadsheet and it is almost certain that everyone already has a spreadsheet on their computer. This enables us to implement algorithms without the overhead of learning a computer language. Students who already know how to program should be encouraged to use their skills rather than the spreadsheet. For the rest, once you see the power of algorithms, you can decide what flavor of computing to learn and use in your subsequent endeavors.

A more mathematical approach benefits all of us in another way: it helps lay the necessary groundwork for understanding difficult concepts from mechanics. This manual has several chapters devoted to stress and strain which, of course, constitute only a very small part of the field of solid mechanics. However, the background gained will help the motivated student to understand the entirety of mechanics in subsequent studies.

The other thing that is almost entirely lacking from current lab manuals is even a passing emphasis on uncertainty and error analysis. *Modern Structural Practice* does not delve into these topics in great detail but does, at least, mention them. Even something as seemingly well know as the elevation of a point on the surface of the earth can vary by 15 m or more depending on the dataset used. This is particularly important when a student first encounters a geologic map or makes a measurement with a compass. If you can make a lot of measurements, which digital tools now enable us to do, then you can begin to evaluate uncertainty.

Some might question whether this approach removes us from classical geology but quite the opposite is true: if you go digital, there is a huge amount of quantitative information that can be extracted from a geologic map or a digital data set. In the past, the manual methods of extracting that information were so tedious that it was too painful to explore the map. Some of the software tools that are used in *Modern Structural Practice* make it trivially easy to extract quantitative 3D information which can then be analyzed as the student and professor wish.

This manual is a work in progress: The current version has been used by my own students to whom I am deeply grateful for their feedback and their willingness to try something different. I also appreciate the time that Néstor Cardozo, Haakon Fossen, David Pollard, and Ray Fletcher have taken to read over parts of this material, though they are neither responsible for any errors nor do they necessarily en-

dorse the overall approach! I welcome comments and suggestions from faculty and students. I know that some of the material is hard — nothing ventured nothing gained — so the type of feedback that really helps me is to help identify sections that are unclear or missing entirely. Students, please note that, while I would like to help with the solution to the exercises at the end of each chapter, I really don't have time to do so.

My current plan is that *Modern Structural Practice* remain a free resource, updated periodically. It is more important to me that it is widely used (nothing like free to help make that happen) than that it is published. Besides, students already pay too much for textbooks. Think of it as crowd-sourcing the revisions. The downside of this "self-published" version is that the reader has to suffer with my minimal page layout skills and limited artistic ability with the figures. An advantage is that color can be used with abandon and it is still free!

This manual is for teaching and learning. Most of the concepts herein are delivered more rigorously and in more detail in:

Allmendinger, R. W., Cardozo, N. C., and Fisher, D., 2012, Structural Geology Algorithms: Vectors & Tensors: Cambridge, England, Cambridge University Press, 289 pp.

Please refer to that published resource if you use the concepts here in your own research.

Rick Allmendinger

Ithaca, New York, August 2015

 

 

# Chapter 1

## *Measurement: What and How*

### Introduction

The purpose of the laboratory portion of most structural geology courses is to learn how to define quantitatively the geometry of deformed rocks. Furthermore, we would like to develop the tools to allow us to convert, easily and precisely,

between the geometries of rock bodies at two different times in their history. These times may be the present, deformed, state and the initial, undeformed state or the two times may capture only a small part of the rock's history. Finally, the lab should lay the groundwork for at least a basic understanding of mechanics. All of these goals require that the structural geologist be very precise about geometry and the coordinate systems used to define the geometry, so that is where we will start.

### Primitive Geometric Objects

Rocks are composed of linear and planar elements: bedding and secondary foliations such as cleavage can be defined, at least locally, by ***planes*** whereas things

like fold axes, mineral lineations, and paleocurrent directions are ***lines***. It turns out that, because there is one line oriented perpendicular to any particular plane, all planes can also be represented by their corresponding perpendicular line which is known as the ***normal*** or the ***pole*** to a plane.

The previous paragraph is an oversimplification because, in the vast majority of cases, all of these lines have a direction in which they point. The paleocurrent, for example, flowed towards a particular direction. The pole to bedding can point in either the direction in which strata become younger or become older. The direction matters and thus our geological lines commonly have an arrowhead and tail; that is, they are a geometric and mathematical quantity known as a ***vector***. In some cases, we care about the length, or ***magnitude***, of our vector as in the case of the displacement of a fault or the thickness of a stratigraphic unit. But in many other cases, we only care about its ***orientation*** in space. We will use vectors extensively in subsequent chapters but before we can do that there are some more basic things to address: how do we measure lines and planes and what coordinate systems do we use, because it is impossible to talk about vectors without reference to a coordinate systems.

## Data Collection

### *Instruments Used in the Field*

Traditionally, a structural geologist used a geological compass/clinometer to measure the orientation of features of interest. These are precision analog instruments that enable the geologist to measure the orientation of a feature of interest to within a degree or less. The Brunton Pocket Transit (Fig. 1.1), most commonly used in North America, excels at taking ***bearings*** — horizontal angles measured with respect to North — and ***inclinations*** — angles in a vertical plane measured with respect to the horizontal — over long distances; thus the word "transit" in its formal name, though most people just refer to it as a "Brunton compass". In Europe and other parts of the world, a Freiberg compass is more common. This type of instrument is less suitable for sighting bearings over long distances but is very efficient at measuring planar and linear features by placing the top or edge of the compass flush against the rock.


**Figure 1.1 — Two ways of measuring the orientations of geological lines and planes. Smartphone app (*Stereonet Mobile*) on left and traditional Brunton Compass on right.**

Precision analog compasses have been around for centuries but it is likely that, within a few years, they will largely be replaced by digital devices, most commonly in the form of smart phone programs or apps (Appendix B). Most smart phones contain accelerometers, gyroscopes, and electronic magnetometers which enable apps to determine the exact orientation in space. Additionally, such devices also keep accurate track of the time and date and can determine their position very accurately using the Global Positioning System (GPS) as well as triangulation on cell phone towers and wireless networks. Thus, one can hypothetically capture a large number of measurements quickly using a compass app on a smart phone. Several such apps are already available for iOS and Android operating systems and, with proper calibration, can yield excellent results. To date, most smart phone compass apps for geological use have taken to mimicking analog compasses and thus use the same terminology and coordinate system. There is a great deal of room for innovation in this space and it is likely that future apps will provide substantially more information. As a simple example, it is not possible to measure directly the pole to a plane with a traditional analog compass; the geologist must do a simple calculation in the field or more likely back in the office to get this value. A smart phone app, like *Stereonet Mobile* (Appendix B), measures the pole to a plane directly rather than the strike and dip separately. Thus, the phone can be placed flush on the bedding surface in any orientation, yielding the correct result.

## *Measuring Lines and Planes*

Both types of compasses and most smart phone compass apps measure bearings or azimuths clockwise with respect to the rotation axis of the Earth, i.e., north, and the angle downward or upward from the horizontal. The previous sentence has several important assumptions built in that are seldom explicitly stated: what is our

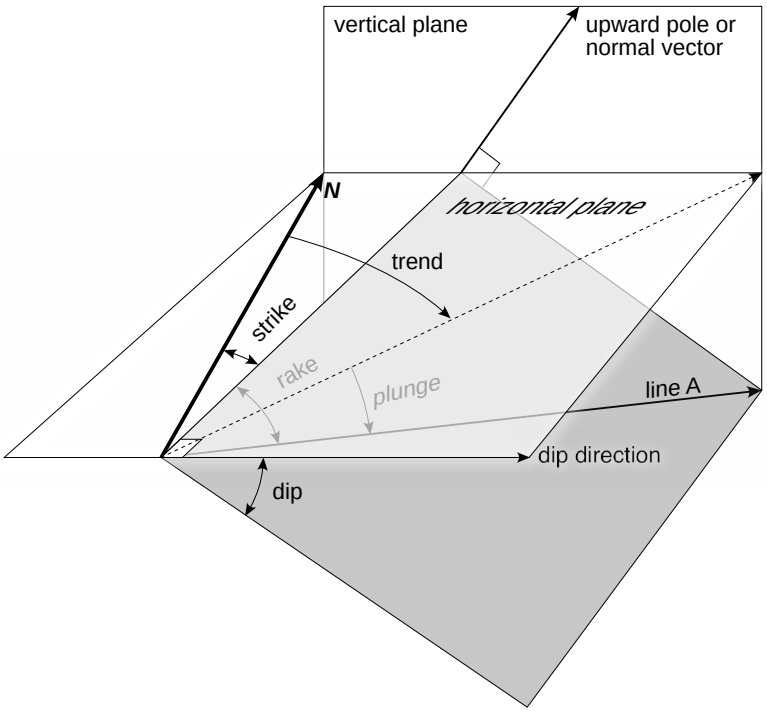


**Figure 1.2 — Orientations of lines and planes. Lines are defined by their azimuth or bearing — the angle with respect to North measured in a horizontal plane — and their plunge, and angle measured downwards from the horizontal in a vertical plane. Likewise, planes are represented by the orientation of a horizontal line within the plane (the strike) and a vertical angle (the dip). Alternatively, you can specify the orientation of a plane by its dip direction and dip, or the trend and plunge of its pole.**

coordinate system and what are the conventions used to indicate whether a number is positive or negative? Traditionally in structural geology, horizontal angles are positive measured clockwise from North and vertical angles are measured positive downwards. If you think about it for a minute, this is just the opposite of the convention that you use when you make a graph or plot data on a map. Graphs follow an engineering convention where angles are measured positive up from the x-axis (i.e., counterclockwise) and on maps, elevations are positive upward and depths are negative! The point is, it doesn't matter what convention you choose as long as you are clear and consistent. In a subsequent chapter, we will learn how to change from one convention and corresponding coordinate system to another, an operation that will help us solve lots of interesting problems.

A plane can be defined by the azimuth of a horizontal line contained within it, known as the ***strike*** and the maximum angle measured downward from the horizontal to the plane, a quantity knows as the ***dip*** (Fig. 1.2). The azimuth of the dip — that is, the projection of the dip onto the horizontal — is known as the ***dip direction*** or ***dip azimuth***. The true dip direction is always 90° from the strike. The most convenient way to think of the strike line is to imagine the plane half-

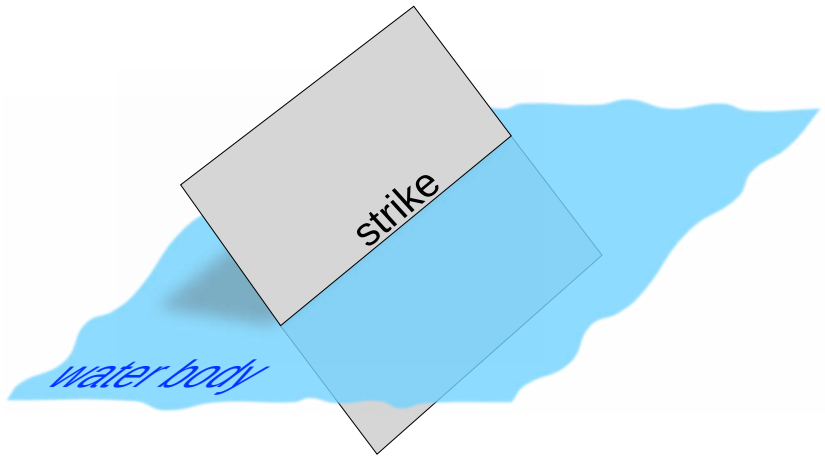


**Figure 1.3 — The strike visualized as the water line on an inclined plane partially submerged in water.**

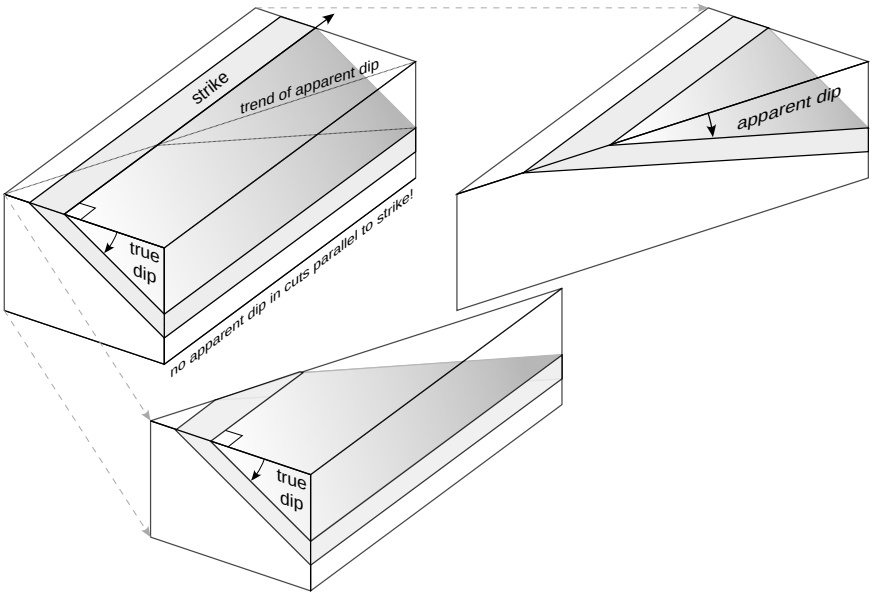


**Figure 1.4 — True dip and apparent dip. True dip is the largest angle between the horizontal and the plane of interest (left block). Apparent dip is the angle between the horizontal and the plane observed in a vertical cut parallel to the trend of the apparent dip (expanded right block). The apparent dip in cuts parallel to the strike is zero.**

submerged in a body of water. Because the surface of the water is necessarily horizontal, the waterline on the plane is a horizontal line in the plane (Fig. 1.3).

The dip deserves further consideration. Let's say that you are studying a vertical road cut in a region where the rocks have a uniform strike and dip. The orientation of the road cut will determine what you see: if the road cut is parallel to the strike, then the strata will *appear* to be flat because the strike is a horizontal line in the plane of bedding (Fig. 1.4, left block). If the road cut is perpendicular to strike, then you will see the ***true dip*** of bedding. At any other orientation of the road cut, you will see an ***apparent dip*** of bedding, which is always less than the true dip (Fig. 1.4, right block). Problems involving apparent dips are extremely common in

structural geology. In subsequent chapters, we will learn quantitative methods for calculation of true dip from two apparent dips or apparent dip given true dip and apparent dip direction but for now a little practice in visualization is in order.

The specification of a strike and dip for a plane is subject to a number of potential ambiguities that do not plague the dip direction and dip format. Which direction of the strike line do you use? How do you make sure that the plane dips in the correct direction? Because in the past structural geologists have tried to accommodate all possible combinations of strike direction and dip direction — that is they did not settle upon a standard and stick to it — a number of inefficient and potentially error-prone formats have sprung up (Fig. 1.5). The "quadrant" format is perhaps the worst offender: one must write down (correctly!) a combination of five numbers and letters such as "N 47 W, 22 S". The student is strongly encouraged not to use this format even though you will need to know how to read it. One can eliminate two letters simply by using the azimuth of the horizontal bearing: 313, 22 S. In this book, we will use either dip direction/dip or more commonly a format known as the ***right hand rule*** (RHR). Using the RHR, one gives the strike direction such that the dip is to the right when looking in the direction of the strike az-

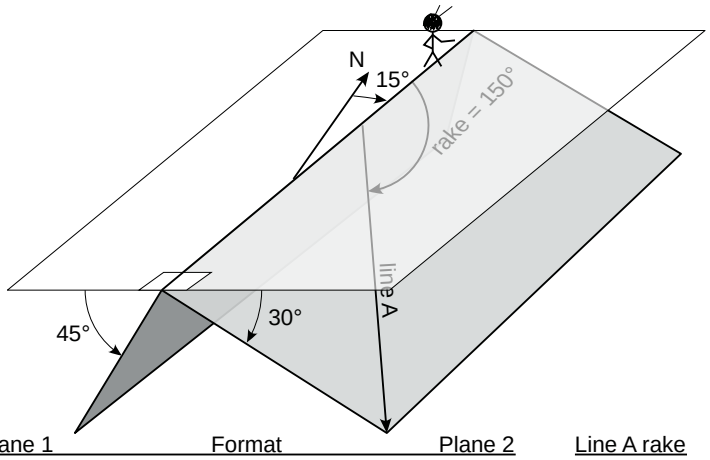


| Plane 1 | Format | Plane 2 | Line A rake |
|---|---|---|---|
| N 15 E, 45 W | Quadrant | N 15 E, 30 E | 30 SE |
| 015, 45 W | Azimuth | 015, 30 E | 150 |
| 195, 45 | Right-hand Rule | 015, 30 | 150 |
| 285, 45 | Dip direction & Dip | 105, 30 | |

**Figure 1.5 Conventions for how to specify the orientations of two planes that share the same strike line. Specifying the rake of a line is also given. Stick figure is looking away from the reader and holding out his/her right hand. Avoid using the quadrant format!**

imuth (Fig. 1.5)[1]. Thus, we can further reduce the plane orientation given previously to: 133, 22.

The orientation of a line is also specified by a horizontal azimuth, or ***trend***, defined by the projection of the line onto the horizontal plane and the ***plunge***, a vertical angle measured from the horizontal downwards to the line (Fig. 1.2). Note that for lines, or vectors, where the the arrowhead points upwards, their plunge has a negative value. There are many times in geology when we are interested in lines that are contained within planes: for example, a paleocurrent direction in sedimentary bedding or slickensides on a fault plane. In these cases, it is often most convenient to measure the angle between the strike of the plane and the line of interest, which is known as the ***rake*** or ***pitch*** (Figs. 1.2, 1.5). Although strikes and trends are measured in horizontal planes and dips and plunges in vertical planes, the rake is commonly measured in an inclined plane. Traditionally, the rake has been measured from either end of the strike line, yielding two possible values, with the correct value identified by giving the general quadrant direction. This is a recipe for confusion! The convention followed here is that the rake is always measured from the given strike azimuth and thus varies between 0 and 180°.

There are several ways to measure the orientations of lines and planes. The two most common have their origins in the unique capabilities of the two types of compasses mentioned earlier: Freiberg compasses, as well as certain modern versions of the Brunton compass, can measure dip and dip direction in a single operation. To measure a plane, the top cover of the compass is rotated so that it is flush against the rock layer. An air bubble is brought to the center of the bullseye level on the face of the compass, ensuring that the compass face defines a horizontal plane. The geologist can then read the dip azimuth of the plane from the number that the North needle points at on the face of the compass. The vertical angle that represents the dip is read directly off a scale on the side of the compass.

If one is using a traditional Brunton compass, a different approach is used: First, the side edge of the main part of the compass is placed on the rock and ad-

[1] Two other reasons for using the RHR will be seen in a later chapter: (a) the strike, true dip, and pole (SDP) define a right handed cartesian coordinate system that is convenient for solving problems related to bedding; and (b) double couple focal mechanisms of earthquakes are commonly giving using the Aki-Richards convention where the plane is specified using RHR and the sign of the rake gives the sense of slip (positive for thrust faulting and negative for normal faulting.

justed by rotating it until the bullseye level is level. One can then read the strike of the plane as the number to which the north arrow points. It takes a second operation to measure the dip angle: the side edge of the compass is placed flush on the rock so that the brass arm of the compass points either up or down dip. The lever on the back side of the compass is then rotated until the bar level is horizontal and the dip value (or apparent dip value) read off of the clinometer scale on the face of the compass.

### *Uncertainties*

Of course, rocks seldom define perfectly smooth planes or exactly straight lines. They have irregularities that can be quite significant. Several field methods have been developed for dealing with this fact. Students are commonly admonished to place a field book or other non-magnetic planar object on the surface of the plane to be measured to smooth out the irregularities. Using a more advanced field technique, the geologist positions themselves so that their eye is in the plane of bedding and they see the plane "edge-on". They then set the clinometer of a Brunton-style compass to horizontal and sight through the hole in the mirror to located a horizontal line in the plane. Finally, they take a bearing on the horizontal line in the plane to get the strike. This method does a better job of smoothing out the irregularities at the scale of the entire outcrop and can also be used to measure a plane's orientation where one cannot physically access the plane (e.g., across a roaring river or a busy six lane highway). It does, however, take considerable practice to master!

Without knowing why one is measuring the plane in the first place, it is impossible to know which is the best method to use. For a regional mapping job, one commonly wants the best orientation at the scale of the entire outcrop. On the other hand, the variations, themselves, maybe the subject of study as for example where one is trying to define asperities on a fault plane. However, the scale-invariant nature of irregularities in any natural surface or linear feature means that, whatever the scale of the problem being addressed, the measurement of its orientation will not be perfect.

In addition to natural irregularities, there are other reasons why it is impossible to define the "correct" strike and dip of the plane. Two different geologists may use slightly different methods for measuring a line or plane and even the same geologist who makes multiple measurements of the same plane at the same location will come up with a range of values because of seemingly trivial changes in measurement methodology. Thus, ideally one would make multiple measurements of a plane or a line and average them. That way, although we cannot state with certainty what the "correct" orientation is, we could at very least come up with the best estimate of the orientation and even use standard statistical techniques to calculate the uncertainty (standard deviation) in the orientation. We will do exactly that in a following chapter.

> In past times and even today, some structural geologists acknowledge(d) that their strike and dip measurements were "only good to about 5°" and thus they would round their dip values on their maps to the nearest five degree increments. It is relatively easy to tell on a published map when they did this even though it is seldom stated explicitly because all of the dips on the map end in either a 0 or a 5! Needless to say, this is a poor substitute for actually determining the natural variation in our measurements, and even stating that a dip is 33±5° is better than recording the dip as "35°". Maps with strike and dip value recorded to the nearest 5° leave something to be desired!

The uncertainties we have discussed so far are of the type known as ***random, uncorrelated errors*** (Fig. 1.6a, b). There is no way to predict whether the next measurement will be higher or lower than the previous one or, within some range, by how much. They result from ***stochastic variations*** in natural features and our own inability to measure them completely accurately. These errors are amenable to calculation of a mean and a standard deviation (which we will do in the next chapter). The smaller the uncertainty, for these types of errors, the more reliable the result. Non-random***, systematic or correlated errors*** are an entirely different beast (Fig. 1.6c, d). Take for example, the geologist who unwittingly measured a bunch of strikes and dips near a large magnetic body or with the declination set incorrectly on his or her compass. In the case of nonrandom errors, even though the statistics might be good (e.g., Fig. 1.6c), the results will be crummy.

This discussion brings up two important terms: accuracy and precision. ***Accurate*** means that our measurements are a reasonably good representation of the

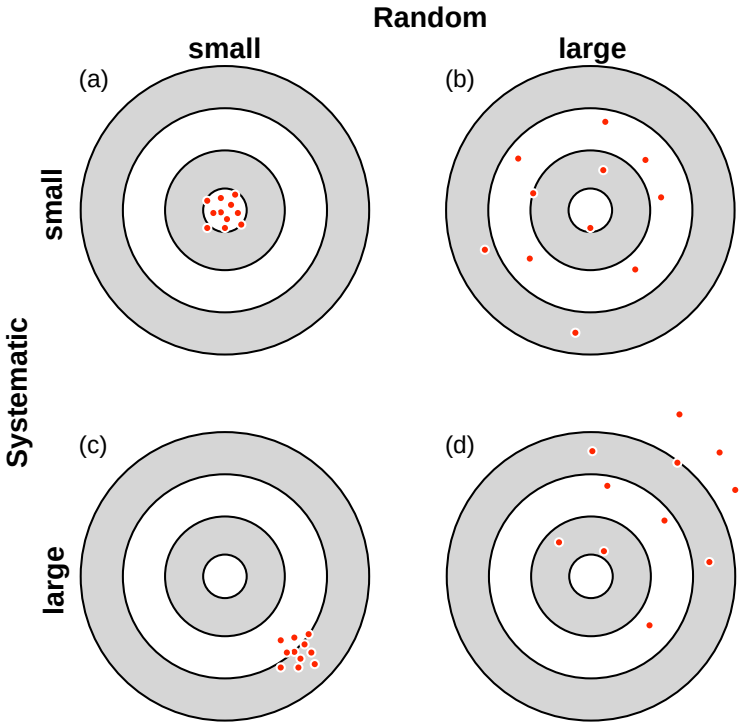


**Figure 1.6 — Illustration of the difference between random and systematic errors. Each diagram shows a target with a number of shots. Note that, in this case, we know what the "right" answer was (i.e., the center of the target) and therefore the systematic error is clear. In the natural features that we study, we don't know what the right answer is (i.e., there is no target) and thus we can evaluate whether the random errors are large or small but we cannot evaluate the systematic errors. Based on a concept by Taylor (1997).**

true value, even if we can never know exactly what the true value is. ***Precise***, on the other hand, means that a measurement has been made with instruments that record the observation to a large number of significant figures. Ideally, our measurements should be both accurate and precise (Fig. 1.6a). Even experienced scientists, however, often fall into the trap of thinking that because a measurement is precise, it must also be accurate; that is a fallacy. In the case of nonrandom errors, our measurement can be very precise but not very accurate (Fig. 1.6c). Earlier in this chapter, we mentioned the advent of data collection via digital devices such as smart phones. With any digital device, however, one must be careful to acknowledge that, although the answer produced is precise, its accuracy must not be assumed but proven. Digital sampling systems are highly subject to nonrandom errors!

## Graphical Representation of Orientation Data

There are two fundamental ways that structural geologists display their orientation data with quantitative rigor. In ***maps***, we are concerned about both orientation and the spatial relation of one feature to another. In the second type,

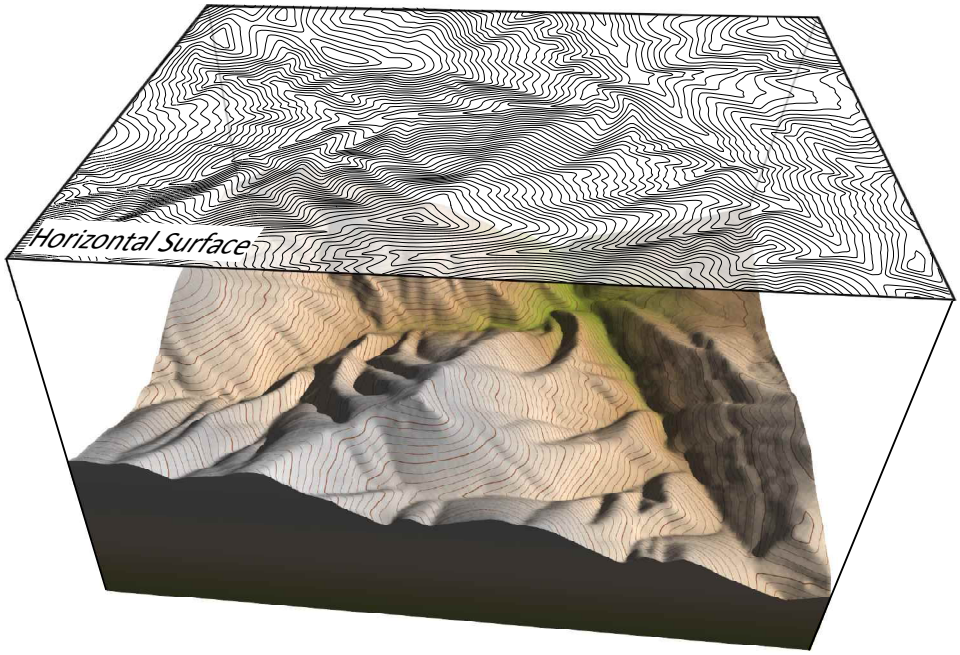


**Figure 1.7 — Map as a projection onto the horizontal surface. In this case, we show contour lines (lines of equal elevation) on an oblique view of the topography and projected onto a horizontal surface**

stereographic projections, commonly called ***stereonets***, we are just concerned with orientations, alone.

## *Maps*

Geological maps are one of the most fundamental, original data sources in our profession. They show the distribution, known and inferred, of rock units on the surface of the earth, the nature of contacts separating them (e.g., stratigraphic, unconformities, intrusive contacts, faults), and are the basic way that we evaluate the distribution and geometry of deformed rock layers. Maps commonly show strike and dip symbols in the layered units, and may show the orientations of secondary structures such as cleavage, lineations, and joints. A map is a formal scientific document and should be treated as such.

All maps are a ***projection*** of features that lie on the irregular, but approximately spherical, surface of the earth onto a horizontal plane (Fig. 1.7). This has an immediate practical implication: when you measure a distance on a map (i.e., a ***map distance***), it is a horizontal distance not the longer distance that you actually

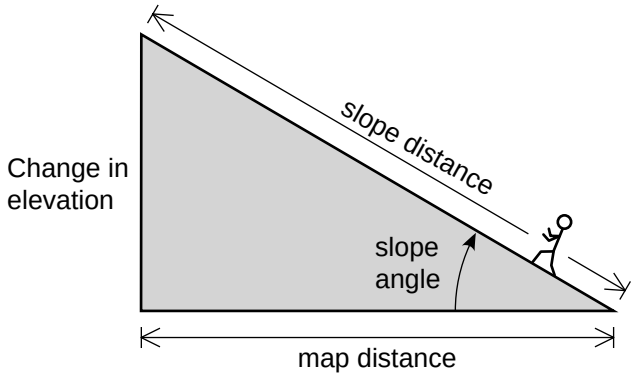


**Figure 1.8 — Map distance, slope distance, and slope angle. The slope distance is always larger than or equal to the map distance.**

travel along a slope (i.e., the ***slope distance***; Fig. 1.8). The ***slope angle*** is measured between the slope and the horizontal and is usually calculated by:

$$\text{slope angle} = \tan^{-1}\left(\frac{\Delta \text{ elevation}}{\text{map distance}}\right)$$

where $\Delta$ means "change in". A related measure of steepness of slope is the percent grade, which you are likely to have seen on highway signs in mountainous terrain:

$$\text{percent grade} = \left(\frac{\Delta \text{ elevation}}{\text{map distance}}\right) \times 100 \, .$$

Humans are notoriously poor at estimating slopes. On a road over a steep mountain pass, you are likely to see a sign reporting "8% Grade Ahead". If you take the arctangent of 0.08, that "steep" grade has a slope angle of just 4.6°!

Beyond this practical implication, there is a more profound aspect to the fact that maps represent projections: Although the Earth is approximately spherical, the piece of paper or computer screen that displays the map is flat. There is inevitably some distortion that occurs when we project a spherical surface onto a flat medium. There are a myriad of ***map projections*** that accomplish this task depending on the size of the map area and the purpose for which the map is needed (Snyder, 1987). For now, you mostly need to know that all maps represent tradeoffs of the following factors:

- ***Conformal*** — preserves the same scale in every direction, locally, thus maintaining the correct shape of the features

- ***Equal Area*** — preserves the area throughout, but distorts the shape
- ***Equidistant*** — depicts the correct distance between a point at the center of the projection and points in any direction away from the center
- ***Equal Angle*** — Shows true angles or bearings, locally

You cannot have all of the above in a single map! For example, a map that is both conformal and equal area is impossible, as is a map that is equidistant and equal angle. As we shall see below, stereonets have exactly the same limitations because they are fundamentally the same thing: a projection of spherical data onto a flat screen or paper.

Map coordinates are usually given in terms of ***longitude*** and ***latitude***. You are, of course, familiar with a globe with its lines of longitude running from pole to pole and lines of latitude running around the globe perpendicular to its rotation axis (Fig. 1.9). Lines of longitude are known as ***great circles***; if you slice the globe

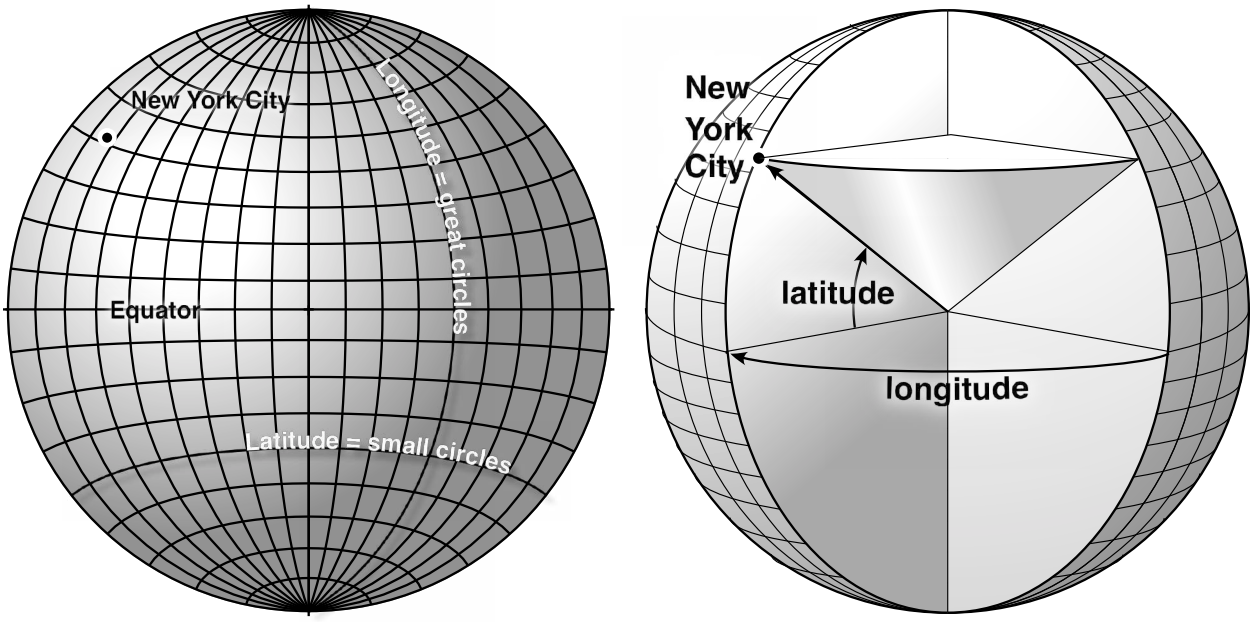


**Figure 1.9 — Left: the globe with lines of longitude and latitude. Right: a cut-away view of the earth showing how the position of New York City is defined by a vector from the center of the Earth that pierces the surface of the sphere in a point**

through the middle, the intersection on the surface is a great circle. A more concrete way of visualizing great circles is to think of a peeled orange or grapefruit: the lines made by the segments of the fruit are great circles because all of the segments meet in the middle. You have probably heard people speak of "great circle routes" as the shortest distance between two points. That is true because that line is an ***arc*** or segment of a great circle. The lines of latitude are ***small circles*** because they do not cut through the center of the globe. The complete coordinates of any point on a globe, say New York City, are given by its longitude — the angle between the great circle that goes through Greenwich, England and that which goes through New York — and the latitude — the angle between the equator and a line drawn from the center of the Earth to New York (Fig. 1.9 right). *Lines through the center of a sphere intersect the surface at a point* (e.g., New York City). Finally, you can see that if you were to rotate the vector from the center to New York City about the rotation axis of the Earth, it would sweep out a cone and the intersection of the cone with the sphere produces a small circle (Fig. 1.9), which is why they are sometimes called ***conic sections***.

Mapping has been revolutionized in the last decade or two by three trends: (1) the advent of geographic information systems (GIS) of varying complexity, (2) the availability of large digital data sets, especially digital topography and ubiquitous satellite imagery with resolutions of a few meters, and (3) small portable devices like tablets, smart phones, and ruggedized laptops equipped with GPS receivers for accurate positioning. Mapping has gone digital and with it, the need for geologists who know how to manipulate and extract information from large collections of numbers has increased dramatically.

Ironically, as the power of the tools and data sets we use has increased, the number of geologists creating new maps has plummeted. Many students in structural geology today will never get a chance to make a geologic map beyond whatever they experience in field camp. Even so, today's geologists need to know how to extract quantitative information from the reams of paper maps published by state and federal geological surveys for more than 100 years. A few years ago, this would have meant spreading the map out on a drafting table with scale, compass, and protractor in hand and carefully carrying out graphical constructions. Today, we have a variety of software tools available to do these tasks and many government

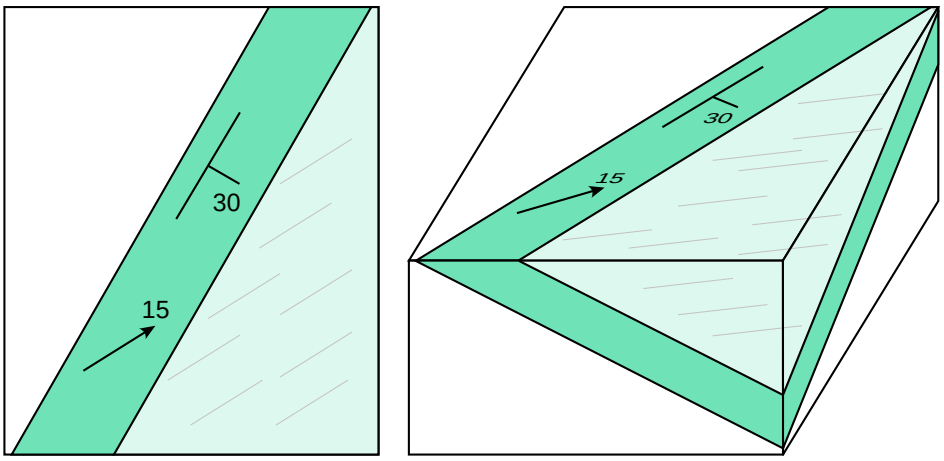


**Figure 1.10 — Strike and dip symbol for bedding dipping 30° to the east-southeast and a lineation symbol showing the trend and plunge of a linear feature in the plane of bedding in map view (left) and visualized as a block diagram (right).**

entities have made raster images of maps available online at little or no cost. We will work with these scanned maps extensively in this course.

The way we represent the orientation of a planar feature on a map is with a ***strike and dip symbol*** (Fig. 1.10). The exact nature of the symbol varies with the feature that it represents, but they all have the same basic design: a long line drawn parallel to the strike of the planar feature and a short tick mark indicating the dip direction. The magnitude of the dip is commonly shown whereas the strike value is not. Linear features, like paleocurrent directions, are shown with a ***lineation symbol*** which is an arrow with the value of the plunge shown at the arrowhead (Fig. 1.10).

In addition to strike and dip symbols on maps, there is another way to extract orientation data: because surface of the Earth is irregular — that is, it has topography — the way planar units cross the surface of earth reflects their orientation. We call this the ***rule of V's*** because, when seen in map view, contacts that represent planar surfaces make the form of the letter "V" when they cross topography. Where a bed crosses a valley, the tip of the "V" points downstream when the bed is inclined or dips downstream (Fig. 1.11) and it points upstream when the bed dips upstream, is horizontal, or dips downstream at an angle less than the stream

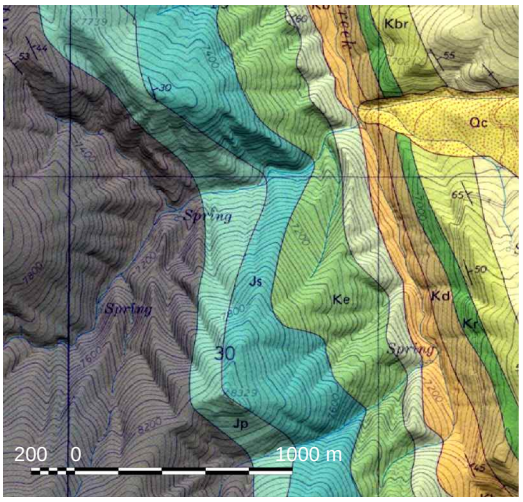


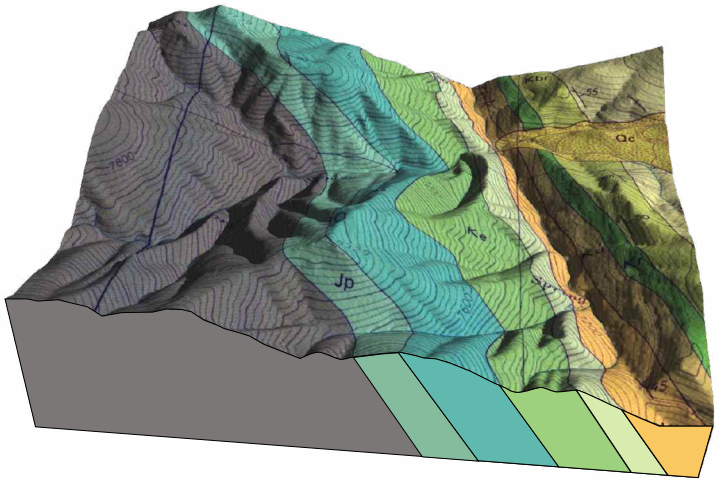


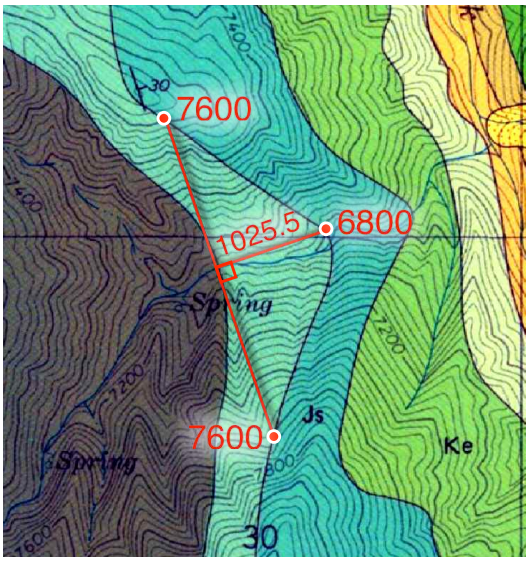


**Figure 1.11 — The Rule of V's depicted using the same geologic map visualized in different ways. Upper left: the map has been draped over a digital elevation model and shaded with an artificial sun in the northeast. Note how the geological units, especially "Js" cross the valley in the middle of the map, "V-ing" down stream. Upper right: oblique block diagram of the same map area, illustrating how the beds dip down stream to the East (right). Lower left: traditional three-point construction for calculating the dip. Two points along the lower surface of Js are at the same elevation (7600 ft.) and thus determine the strike direction. The third point is at a lower elevation. See Figure 1.12 for construction.**

gradient. Vertical surfaces cross topography in a straight line, V-ing neither up nor downstream.

Of course, to interpret correctly the orientation of beds using the rule of V's, one has to be able to determine hills, valleys, and which way the rivers flow. Most geologic maps published by geological surveys contain ***topographic contours***, lines of equal elevation. If you were to walk exactly along a contour line, you would go neither up nor down hill; walk perpendicular to the contours and you are going in the direction of maximum slope. Modern mapping increasingly uses shaded ***digital elevation models (DEMs)*** to portray topography but for quantitative analysis students still need to know how to use topographic contour maps.

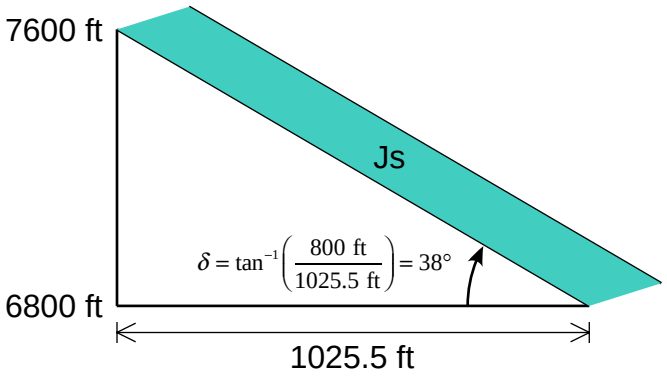


**Figure 1.12 — Classical three point construction to determine the dip of bed Js in Figure 1.11. The diagram is a vertical plane oriented in the true dip direction (parallel to the line labeled "1025.5" in Figure 1.11. Note that maps are a projection onto a horizontal plane.**

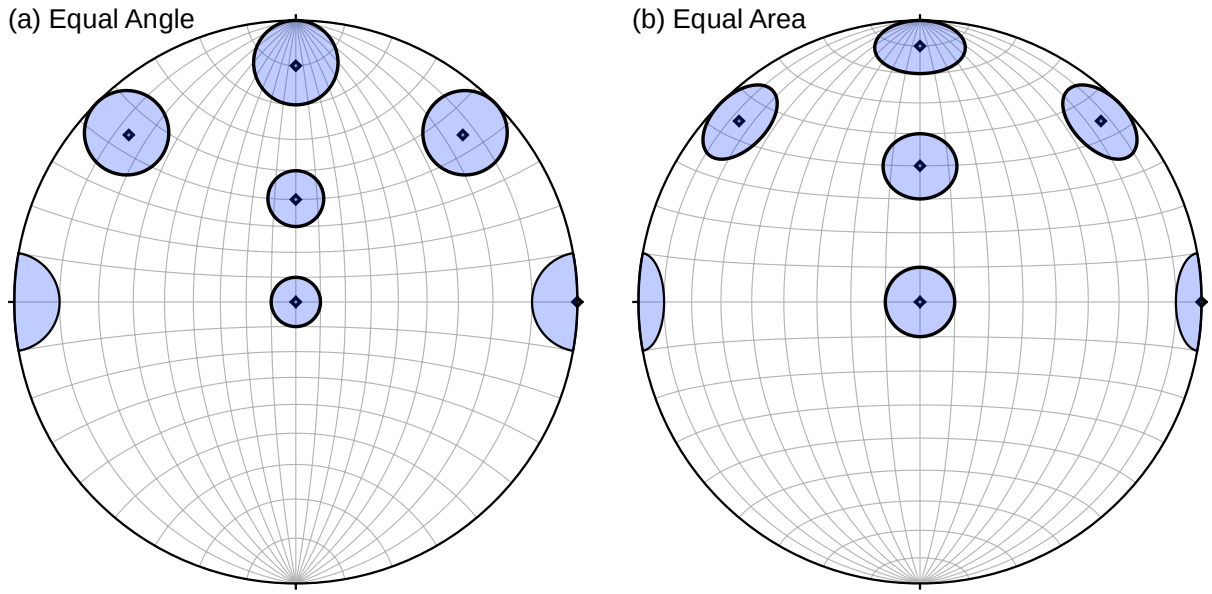


**Figure 1.13 — Two types of stereonets: (a) the equal angle, or Wulff, net; and (b) the equal area, or Schmidt, net. All of the blue shaded small circles are the same size and shape on the surface of the sphere (they all have a 10° radius). You can see that the equal angle net in (a) is conformal (shape is preserved, that is they are all circles) but is not equal area or equidistant (the 10° spacing gets bigger as you go from the center to the edge of the net). Conversely, in the equal area net (b) the circles are distorted except at the center but they all have the same area and the 10° spacing from the center outward is constant (equidistant).**

## *Stereonets*

Structural geologists use stereographic projections to display orientation data when the spatial relation of the individual observations with respect to each other is not important. A stereonet can also be used to do complex calculations such as rotations, calculating lines of intersection, etc. by placing a sheet of tracing paper over the grid of lines and rotating it about the center. That function has been large-

ly replaced by computer stereonet programs that are far more powerful, accurate, and precise in terms of computation and provide publication quality graphics automatically. Here, we use stereonets only to display orientation data.

One's first view of a stereonet is instantly familiar: it looks like a globe or a map of the entire Earth (Fig. 1.9 left). There are great circles, just like lines of longitude, running from pole to pole, and small circles, similar to lines of latitude, that run across the globe from east to west. Of course, our picture of a stereonet, just like the globe, on the screen is a ***projection*** of a sphere onto a flat surface and, as shown in Figure 1.9, left, can only display half of the sphere. As with any mapping, depicting a sphere on a flat surface inevitably involves distortion. Two types of stereonets are commonly in use: the equal area (Schmidt) net and the equal angle (Wulff) net (Fig. 1.13).

Stereonets used in mineralogy, structural geology, geophysics embody all of the same concepts as our globe. Planar features are plotted as great circles and linear features plot as points and there are different types of distortion depending on the type of projection used. In a similar fashion to our example of a globe, miner-

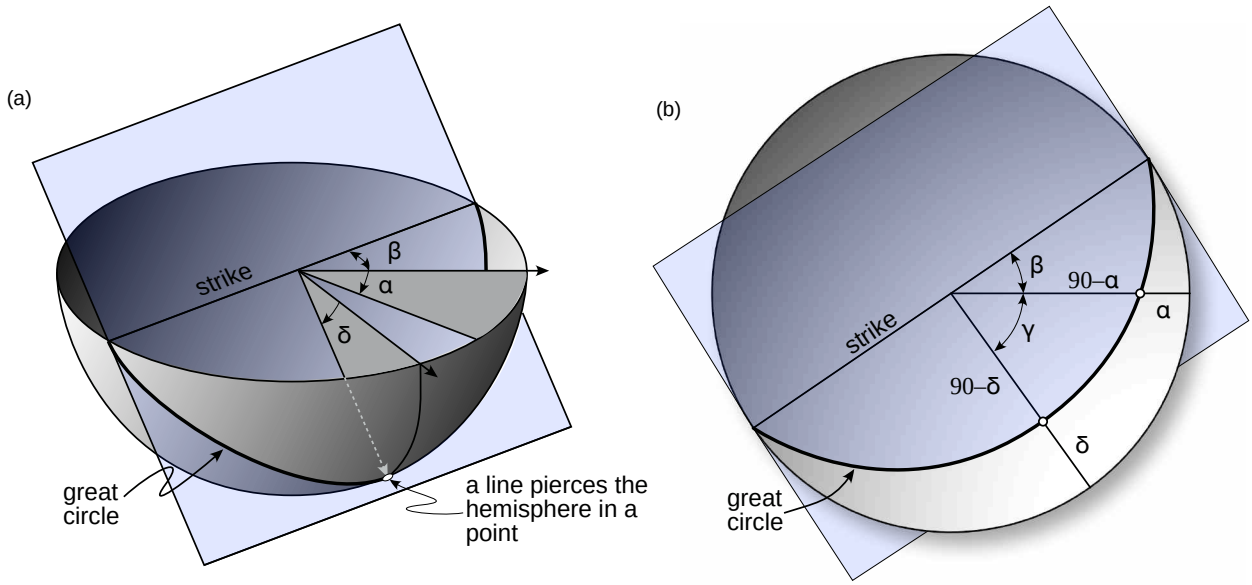


**Figure 1.14 — The lower hemisphere projection (a) oblique view, and (b) top view. Planes intersect the hemisphere as great circles and lines plot as points. δ is the true dip, α is the apparent dip, and β is the angle between the strike and the trend of the apparent dip. Note similarity of (b) with Figure 1.15b.**

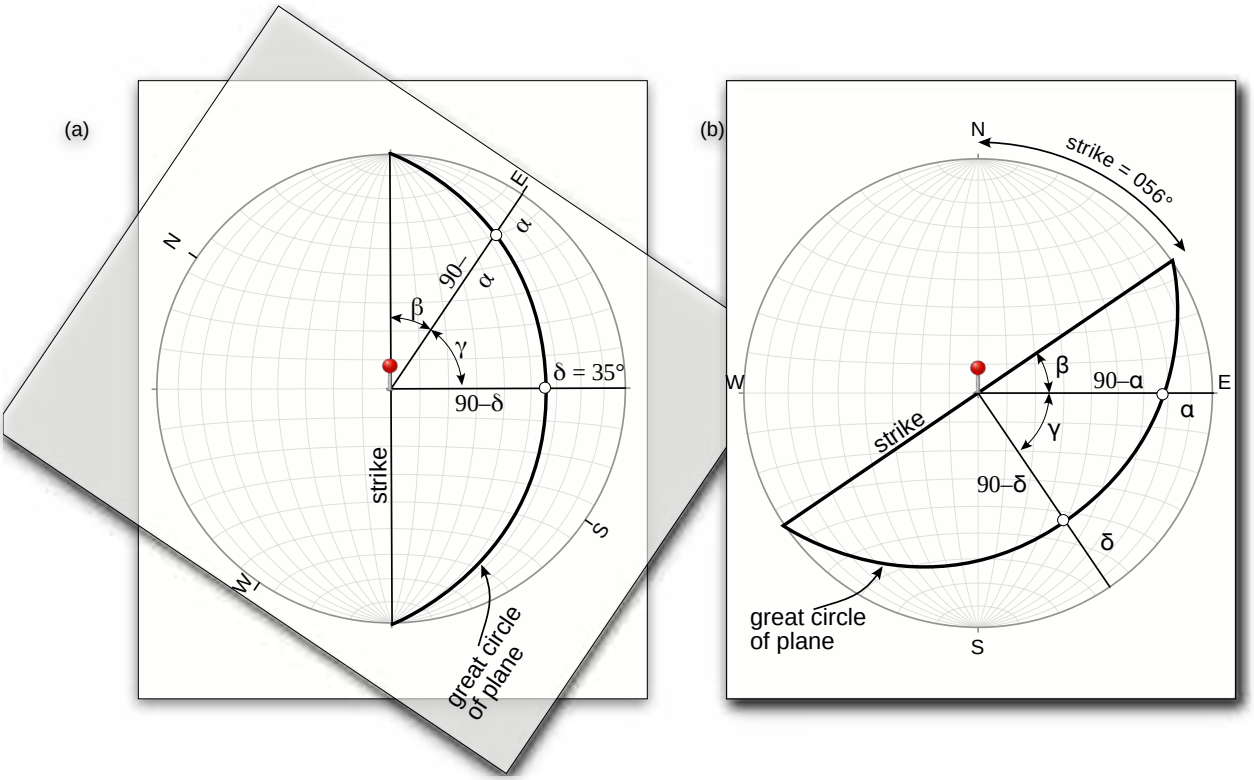


**Figure 1.15 — Plotting a plane and doing an apparent dip calculation by hand, by rotating a piece of tracing paper over the stationary grid of the stereonet. (a) shows the paper rotated so that one can plot the great circle that represents the plane, and (b) shows the tracing paper rotated back so that N on the paper and on the grid are aligned.**

alogists use an ***upper hemisphere*** projection whereas in structural geology and geophysics we use a ***lower hemisphere*** projection (Fig. 1.14). The latter projection means that we are looking down into a cereal bowl and seeing the inside of the bowl projected onto the horizontal plane through the center of the sphere (Fig. 1.14). Visualizing this geometry is fundamental to understanding how stereonets display data.

Plotting stereonets by hand is tedious and imprecise. The basic idea is shown in Figure 1.15. An equal angle, or more likely equal area, grid is mounted on a piece of cardboard or some other firm but thin surface. The geologist then places a sheet of tracing paper over the grid and puts a push pin or thumbtack through the tracing paper into a hole in the center of the firm backing to which the grid is mounted. The tracing paper can now rotate about the center of the grid. After marking North on the tracing paper, the geologist is ready to begin plotting. To plot

a plane, rotate the tracing paper by an amount equal and opposite to the strike of the plane. For example, in Figure 1.15, the plane has a strike of 056° so the geologist rotates the tracing paper by 56° *counterclockwise*. Once this rotation is accomplished, one counts in on the east axis of the grid an amount equal to the dip value and then traces by hand the corresponding great circle. Rotating the tracing paper back to alignment with the grid — so that north on the tracing paper is aligned with north on the grid puts the great circle that represents the plane in its correct position (Fig. 1.15b).

The great circles and small circles on the stereonet grid are read in degrees, just like longitude and latitude are marked off in degrees on the globe. In Figure 1.15, the grid is drawn in 10° increments, whereas most paper stereonets are in 2° increments (most computer programs allow you to adjust the grid increment). If you read in along the EW grid line (Fig. 1.15), you'll see that you can measure from 0° at the edge of the net (known as the primitive or horizontal) to 90° at the center; a vertical line will plot as a point exactly at the center of the net (a plunge of 90°). Angles measured in the plane (e.g., rakes) can be determined by counting off the number of degrees along the great circle. For example, in Figure 1.15a, you can see that the rake of the apparent dip line (that has a plunge of $\alpha$) is 40°; likewise, the angle in the plane between the apparent dip line and the true dip line is 50°.

If all that sounds complicated, it is but nonetheless the procedure is a skill that can be learned with a small amount of practice. The problems with this approach, however, are two-fold: first, several of the operations have nothing to do with learning how to interpret these displays

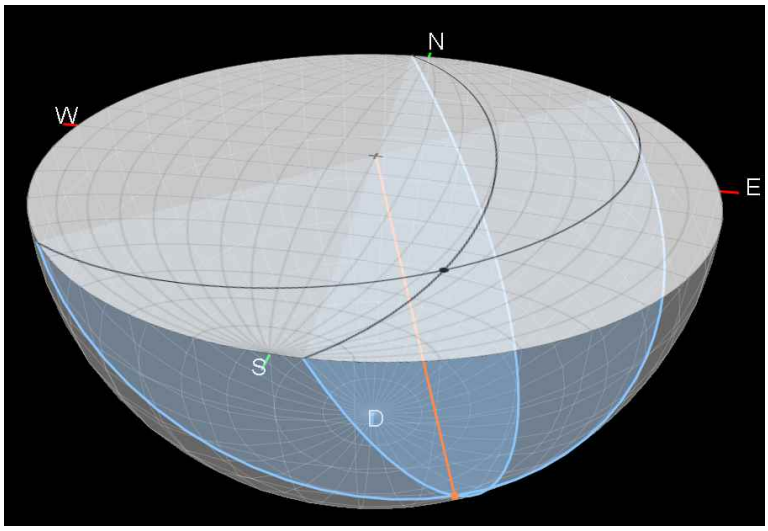


**Figure 1.16 — Two planes and the line of intersection between the visualized in three dimensions using the Macintosh program Stereonet3D (Cardozo and Allmendinger, 2013). Programs like this can help if you are having trouble relating a stereonet plot to the three dimensional objects it represents.**

but only with the limitations of drawing great circles by hand. How does rotating the tracing paper in a direction opposite to the rotation of the strike with respect to north make this process clearer? Hint: it doesn't! Second and more importantly, few structural geologists use paper stereonets now, anyway, as there are a number of good programs available for Mac, Windows, Android, and iOS. The computer certainly isn't virtually rotating a piece of paper with respect to a grid; it is using simple but powerful mathematical algorithms and displaying the results on a stereonet because that's what structural geologists are used to! Thus, in most of this book, we are going to learn how to do structural calculations the way the computer does and only use stereographic projects to visualize our results (Fig. 1.16).

## Computing

Structural geologists use a large number of computer programs to speed up their work. These programs may be written in a variety of languages: a few decades ago the language was likely to be Fortran, Pascal, or Basic; today it is more likely to written in some flavor of C, Python, Java, or Matlab. What is important, however, is not the language but the algorithm behind the language. In this book, we will use a very simple computing environment, the humble spreadsheet program, usually exemplified by Microsoft Excel®. There are several advantages to this approach:

1. You have probably used spreadsheets before so they are familiar. That means that you can just focus on the algorithm and not worry about language syntax, development environment, etc.
2. It is quite likely that you already have Microsoft Office® installed on your computer and thus you already have Excel®. No additional purchase necessary!
3. A spreadsheet is naturally in the form of a table, or matrix, and many of the things we would like to calculate in structural geology are best thought of as tables of numbers.

Computers have a couple of traits that you will probably find either exhilarating or frustrating: they are dumb and they are logical. Because computers are dumb machines, they are extremely literal: they will do exactly what you tell them to do, even

if it is not really what you wanted! Second, because they are logical, you have to understand the logic of your calculation before you can tell the computer what to do. Nonetheless, computing is a profoundly powerful skill for a scientist to possess, and it is in that spirit that this book emphasizes simple computing via spreadsheets to solve structural geology problems. Once you understand the power of the calculation, that is the algorithm, you will have greater motivation to learn a programming environment much more powerful than a spreadsheet program.

Those of you who already know a programming language should, by all means, do the exercises in this book using that language rather than in a spreadsheet. More advanced programing languages have many features that simplify the overall task of implementing an algorithm. For example, a simple do/for loop in a programing language is more cumbersomely implemented in a spreadsheet by manually copying and pasting rows containing formulae and nested loops are even more difficult.

A spreadsheet, like any program, has certain rules that one must follow. For those of you who have never used a spreadsheet for anything more than making a table, we offer the following abbreviated set of rules:

- To fill a cell with a computed value, the first character in the cell must be the equals sign, "=". Following the equals sign is the formula that you want to compute.
- In formulas, one refers to the input data, whether a number or another computed value, via its cell address. The cell address is composed of a letter that indicates the column of the cell followed by a number that indicates the row. For example, "C3" refers to the value in column C, row 3. When entering a formula, after the equals sign you can usually enter the cell address by just clicking on the cell that you want.
- When you copy a formula from one part of the spreadsheet to another, the cell addresses are adjusted automatically — that is, the cell addresses are relative. If you have a formula in C3 that uses the value in A1, when you copy the formula to D4 (one column over and one row down from the original), it will automatically adjust to

use the value in B2 (one over and one down from A1). Relative cell addresses are one of the reasons why spreadsheets are so powerful.

- Sometimes, however, you want to keep using the original value even though you have copied the formula. For this you need an absolute cell address which is indicated with a "$" in front of the column and/or row letter/number. If, in the above example, you wanted to keep using the value in A1 when the formula was copied to a different cell, you would type the address as "$A$1" in the formula.
- Finally, for now, all computer languages, including spreadsheets, do trigonometric calculations using radians rather than degrees. Useful formulae for converting from radians to degrees are:

$$1 \text{ radian} = \frac{180^\circ}{\pi} = 57.2958^\circ \tag{1.1}$$

$$90^\circ = \frac{\pi}{2}; \quad 180^\circ = \pi; \quad 270^\circ = \frac{3\pi}{2}; \quad 360^\circ = 2\pi$$

Say you want to calculate the sine of the angle in cell A3. In the cell where you want the answer to appear (e.g., A4) you would type:

```
=SIN(RADIANS(A3))
```

To convert the value in A4 back to degrees you would enter

```
=DEGREES(ASIN(A4))
```

 

# Exercises—Chapter 1

1. For the following block diagrams, fill in the bed geometry on each exposed side of the block. For each side, indicate whether one would see a true dip or an apparent dip of the bed if you observed that side of the block head on (looking perpendicular to that face of the block).

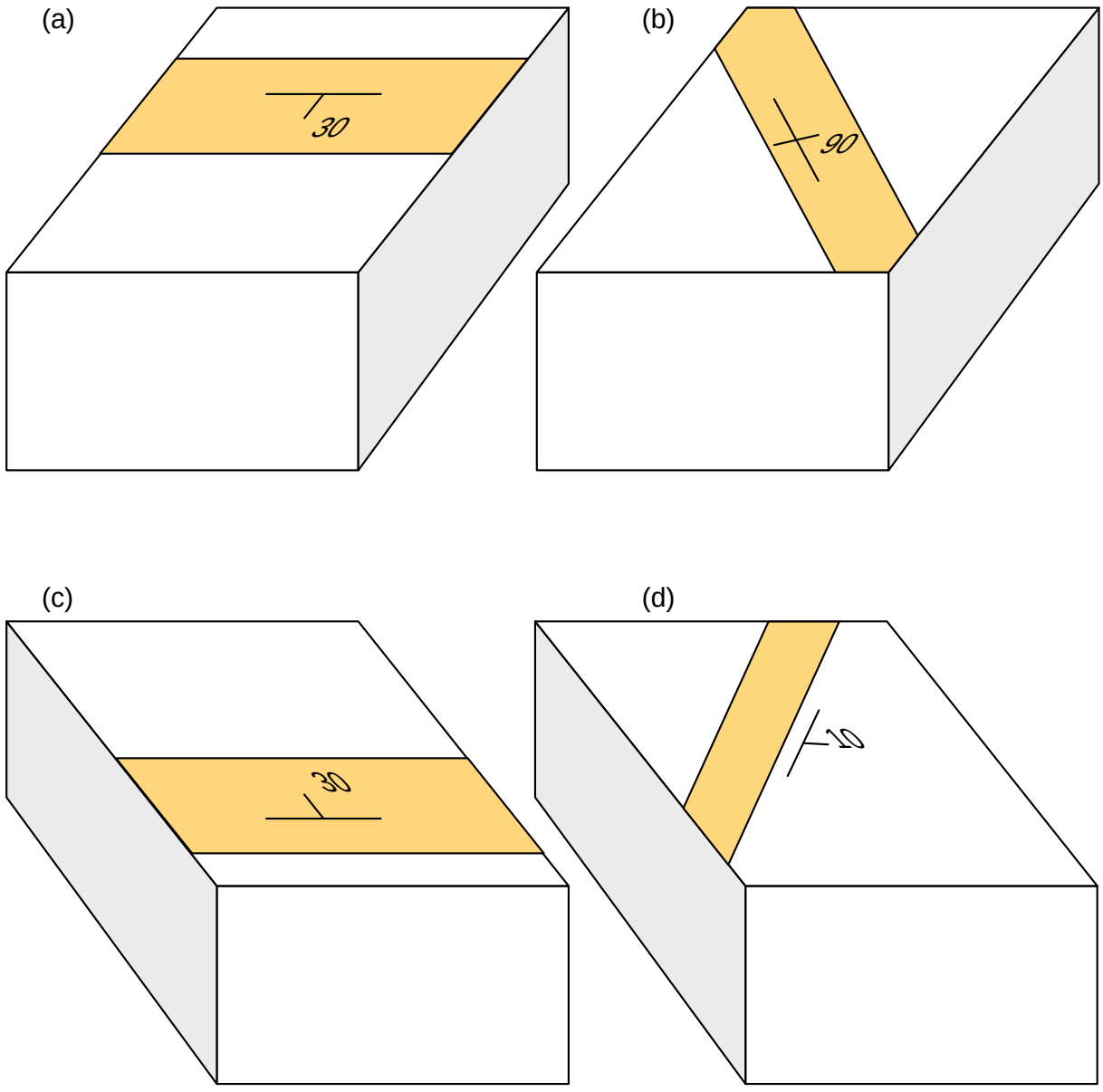

2. For each of the map snippets below, state qualitatively which way the bedding dips. Start by using the topographic contours to identify ridges and valleys and then determine which way the creeks in the valley flow (i.e., the up- and down-stream directions). Then, use the way that the stratigraphic contacts cross the valley to determine the dip direction. For each map, it is sufficient to state that "the bedding dips to the east" or "the bedding dips to the SW".

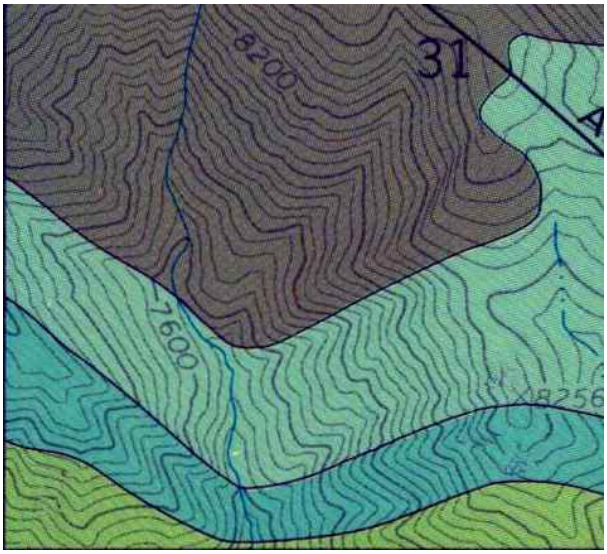


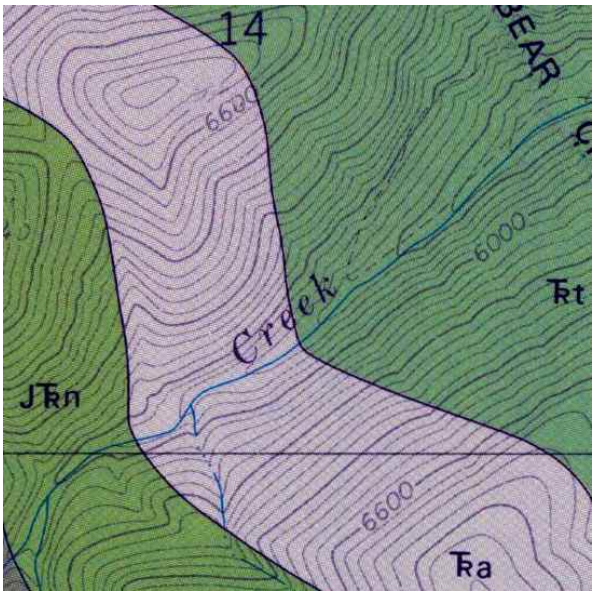


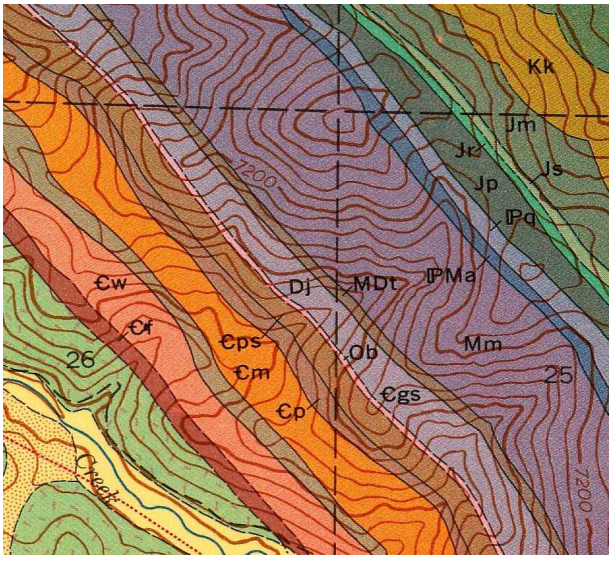


3. Below are five orientations of planes. Convert them into right-hand rule format:
   a. Convert from Quadrant to RHR format: (i) W 15 S, 61 S; (ii) N 56 E, 20 NW; (iii) S 30 E, 33 W;
   b. Convert from Dip direction and dip to RHR format: (i) 237, 74; (ii) 099, 48

4. The instructor will set up a tilted layer or rock in the lab or will take you out to a place where you can measure strikes and dips of a natural planar surface. Each person in the class, including the instructor or other experienced geologist, should measure the plane the same number of times, at least10 or 15 times would be good.
   a. Describe the variation in your answers: How much variation in strike is there? In dip? Does it appear easier to measure the strike or the dip more accurately? What factors might determine which is easier?
   b. Now compare your answers to those of your classmates and instructor. Can you tell which answers are more precise or whose are more accurate? How?

5. Plot your results from Question 4 in a stereonet program as (a) great circles, and (b) poles to the planes.

6. The following stereonet plots show planes and or lines. Describe the orientations in each and answer any additional questions written next under the plot.

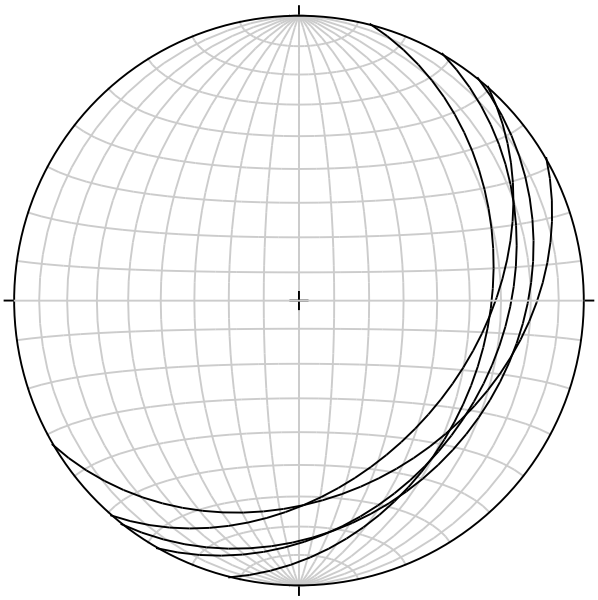

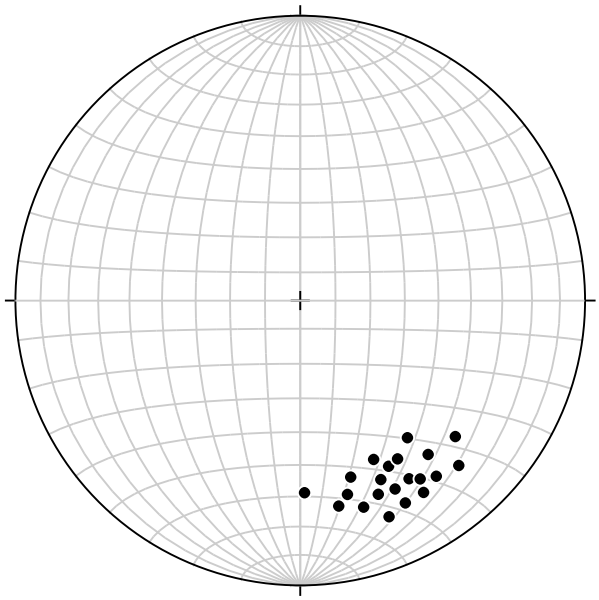

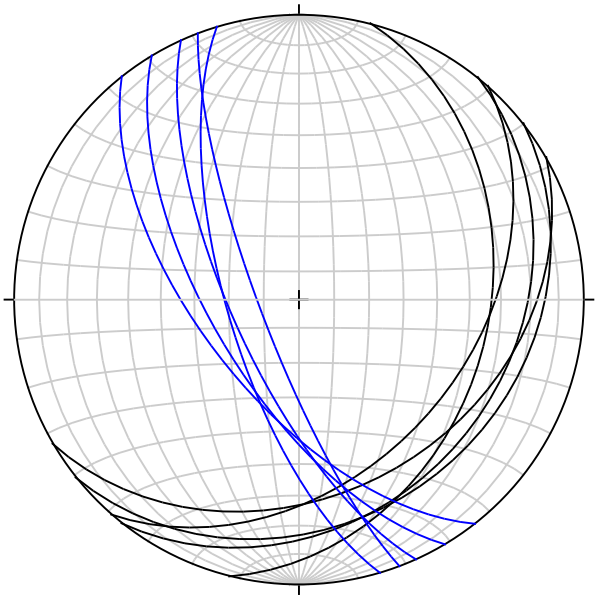

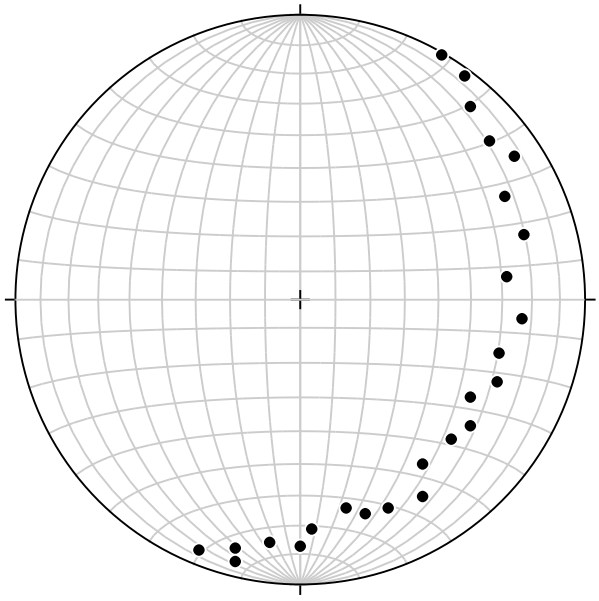

**what is the approximate orientation of the line of intersection of the black and blue planes?**

 

All of the questions below apply to the following table. Each row in the table is a single datum, i.e. a single plane with one or more lines in it. Planes are given in azimuth format and lines in trend, plunge format. Asterisks show missing values; *** is a missing azimuth or bearing, and ** is a missing plunge or dip. Some of the values are redundant: for example, once you know the true dip and dip direction, you also know the strike and dip.

| *Datum* | *Strike & Dip of Plane* | *True Dip (T&P)* | *Apparent Dip(s) (T&P)* |
|---|---|---|---|
| *1* | 050, **, * | ***, ** | 090, 25 |
| *2* | ***, **, * | ***, ** | 159, 34 and 270, 43 |
| *3* | ***, **, * | 010, 48 | 321, ** and 090, ** |

7. Solve for the missing values for each of the three datums using a stereonet to solve for each of the missing values in each row.
   (a) In the second datum, above, you are given two apparent dips. Use a stereonet to determine the angle between those to apparent dips, measured in the plane that contains them.
   (b) Assume that the plane in datum three is a bedding plane. Restore the plane to horizontal. What were the original bearings of the two apparent dip directions prior to the tilt of the bedding?

Rotate the plane in row 1 by returning the plane in row 2 back to its original horizontal position. What is the orientation of the plane in row one after you have performed this rotation?

# Chapter 2

## *Coordinate Systems and Vectors*

### Coordinate Systems

When we use a compass to measure features of interest to the structural geologist, we are implicitly using a spherical coordinate system defined by the rotation axis and surface of the Earth. Another spherical coordinate system based on the

Earth is given by latitude and longitude. Geologists have successfully used these coordinate system for a couple hundred years; they are accurate and work well because the Earth is a nearly spherical body. As we saw in the last chapter, any rectangular coordinate system applied to the Earth must necessarily have some distortion. The most obvious examples of this are maps where, via various algorithms, the sphere of the earth is projected onto a flat piece of paper (or computer screen). A map can display areas or angles correctly but not both, something that also applies to Stereonets.

Even so, just as it is more convenient to carry around a flat map that can be folded, rolled up, or displayed on a computer screen rather than a physical globe, it

is commonly more convenient to do structural calculations in ***rectangular Cartesian coordinates***. Those are the main focus of this section. Before we get to Cartesian coordinates commonly used in geology, a few formalities are in order.

The three axes of a Cartesian coordinate system are commonly referred to as **X**, **Y**, and **Z**. We start out the same way here because that is most familiar, but when we start talking about coordinate systems more formally, we will switch to using $\mathbf{X_1}$, $\mathbf{X_2}$, and $\mathbf{X_3}$, which are more convenient for numerical calculations in a computer.

The axes of any graph have positive and negative directions, of course, and most of us are used to seeing two dimensional graphs where the horizontal axis, commonly referred to as the "X" axis or abscissa, is positive to the right and the vertical "Y" axis (the ordinate) is positive upwards. This means that angles are measured positive in a counterclockwise direction from the horizontal axis, just the opposite of how angles are measured on a compass rose (clockwise from the top). But, what happens if we add a third axis? How do we determine the positive direction for that axis?

Convention suggests that we should follow a ***right-handed naming convention***: If you hold you hand so that your thumb points in the positive direction of the first axis, your fingers should curl from the positive direction of the second axis toward the positive direction of the third (Fig. 2.1). To follow this convention in the case of our graph above where X is horizontal and points to the right, we have two options: the new third, or "Z", axis can be horizontal and point off the page

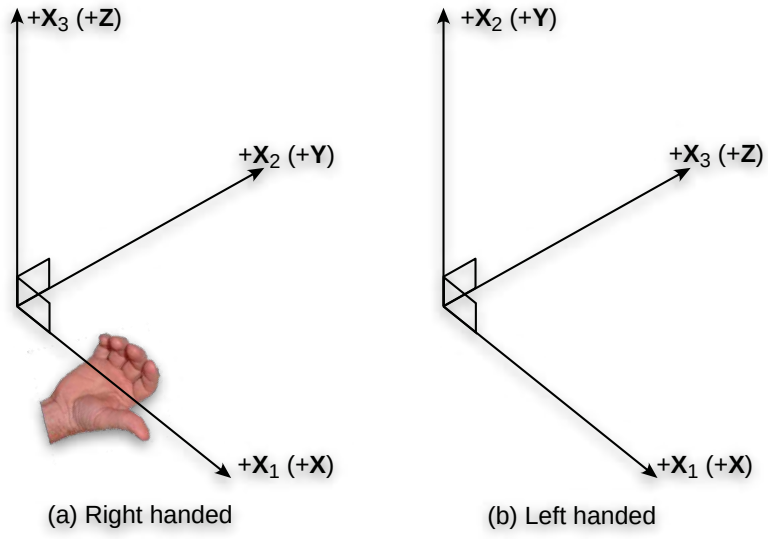


**Figure 2.1 — (a) Right-handed and (b) left-handed coordinate systems. As the disembodied hand shows, for a right-handed system, if the thumb of the right hand points in the direction of positive $X_1$, then the fingers curl from positive $X_2$ towards positive $X_3$.**

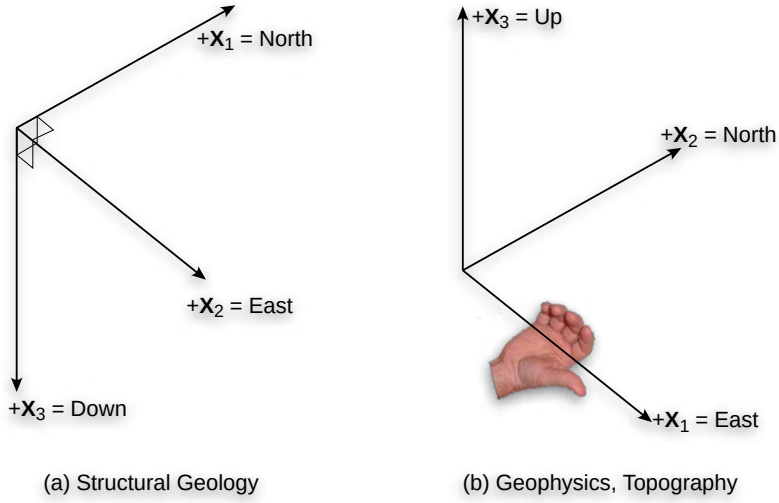


**Figure 2.2 — Right-handed coordinate systems commonly used in structural geology, geophysics, and mapping.**

towards the viewer, or we can rename the vertical axis the Z-axis and add a new horizontal Y-axis pointing into the page away from the viewer. Though neither are wrong, the second option is the more common of the two and is, in fact, the coordinate system used in maps: the east direction is the first axis, the north direction the second, and elevation (positive upwards) is the third. This means that a car traveling southward is going in the negative direction. The point is, the labeling of axes is not arbitrary but follows well-established conventions. This "map" convention of axes is used extensively in geophysics as well as mapping and is sometimes referred to as an ***East-North-Up (ENU)*** system (Fig. 2.2).

Structural geologists, because of our reliance on magnetic compasses and out predilection for treating angles measured downwards from the horizontal as positive, use a different convention: We treat the North direction as the first axis, the East direction as the second axis and the Down axis as the third axis, an ***NED coordinate system*** (Fig. 2.2). This system is consistent with angles like strikes and trends measured clockwise from North, and because down is positive, angles measured downwards from the horizontal (e.g., dips, plunges) are positive. Of course it is easy to change between the two coordinate systems: A point that has coordinates (100, 200, 350) in an ENU system would have coordinates (200, 100, and −350) in a NED system.

# Vectors: A Review

Most structural geology students have learned the basics of vectors in their math courses. We'll first review those basic concepts and then put that knowledge to work because, as mentioned in the last chapter, most linear features that we might wish to measure in structural geology are vectors.

## *Vector components, magnitude, and unit vectors*

Because structural geometry is three dimensional, all of our vectors will have three components. Each of the three numbers that define a vector refer to a specific coordinate axis: for example, $v_2$ (or $v_y$) is the value of our vector, $\mathbf{v}$, projected onto the second axis of the coordinate system, $\mathbf{X}_2$ or $\mathbf{Y}$. In a NED coordinate system, $v_2$ is the projection of $\mathbf{v}$ onto the East axis, but in an ENU coordinate system, $v_2$ is $\mathbf{v}$ projected onto the North axis. Therefore, the numbers that define a vector depend on the specific coordinate system. We write out vector as:

$$\mathbf{v} = [v_1 \quad v_2 \quad v_3] = \begin{bmatrix} v_x & v_y & v_z \end{bmatrix} \tag{2.1}$$

One of the most fundamental characteristics of a vector is its length or ***magnitude***. Magnitude is a scalar quantity because it has no directional significance and furthermore, it is the same in all coordinate systems. The magnitude is given by:

$$|\mathbf{v}| = \sqrt{v_1^2 + v_2^2 + v_3^2} \tag{2.2}$$

In two dimensions, you can see that the magnitude is calculated from the Pythagorean theorem which gives the length of a hypotenuse as the square root of the sum of the squares of the two sides (Fig. 2.3). The extension to three dimensions is straightforward.

But, what if we don't care about the magnitude? What if we are only interested in the orientation of our vector? In this case, we simply assume that the vector has a length of one and call it a ***unit vector***. A special symbol is reserved for a unit vector, a triangular hat or circumflex accent over the vector symbol: $\hat{\mathbf{v}}$. Unit vectors have a special property that makes them especially useful for orientations. The projection of a unit vector onto a coordinate axis is just equal to the cosine of

 

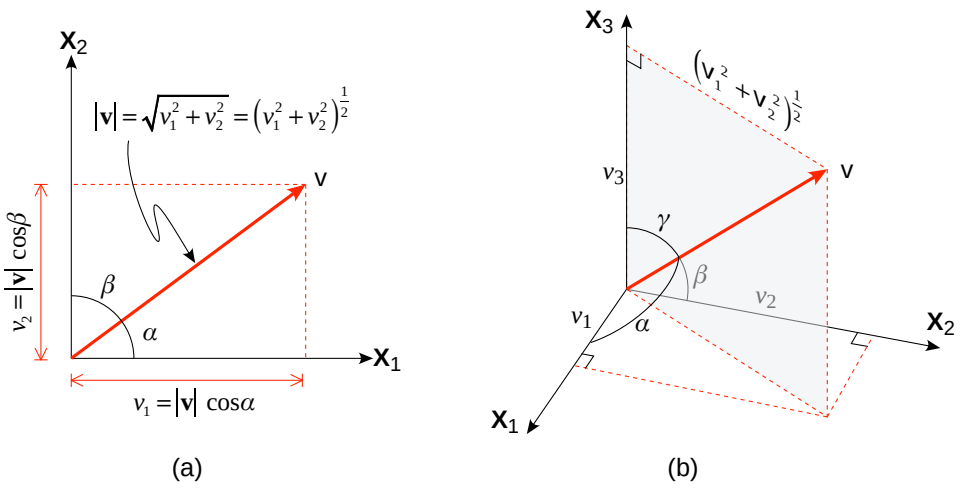


**Figure 2.3 — The length or magnitude of a vector, v (in red) is calculated using the Pythagorean Theorem in both two (a) and three (b) dimensions.**

the angle that the vector makes with that axis (Fig. 2.3a). Thus, the components of a unit vector are:

$$\hat{\mathbf{v}} = \begin{bmatrix} \cos\alpha & \cos\beta & \cos\gamma \end{bmatrix} \tag{2.3}$$

where $\alpha$ is the angle with respect to the $\mathbf{X}_1$ axis, $\beta$ with $\mathbf{X}_2$, and $\gamma$ with $\mathbf{X}_3$. cos$\alpha$, cos$\beta$, and cos$\gamma$ are known as ***direction cosines*** and, as with the magnitude, the proof is straightforward in two dimension and easily extended into three dimensions.

## *Vector Addition, Subtraction, and Scalar Multiplication*

***Vector addition*** or ***subtraction*** from another is no more complicated than adding, or subtracting, the individual components (Fig. 2.4):

$$\mathbf{v} + \mathbf{u} = \begin{bmatrix} v_1 & v_2 & v_3 \end{bmatrix} + \begin{bmatrix} u_1 & u_2 & u_3 \end{bmatrix} = \begin{bmatrix} (v_1 + u_1) & (v_2 + u_2) & (v_3 + u_3) \end{bmatrix} \tag{2.4a}$$

And likewise

$$\mathbf{v} - \mathbf{u} = \begin{bmatrix} v_1 & v_2 & v_3 \end{bmatrix} - \begin{bmatrix} u_1 & u_2 & u_3 \end{bmatrix} = \begin{bmatrix} (v_1 - u_1) & (v_2 - u_2) & (v_3 - u_3) \end{bmatrix} \tag{2.4b}$$

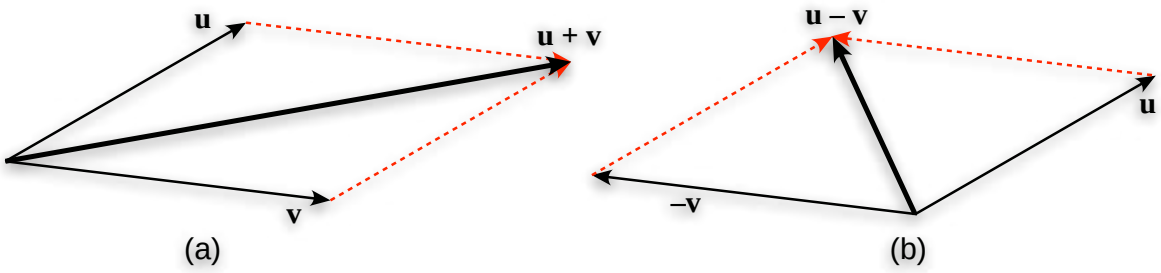


**Figure 2.4 — Vector addition (a) and subtraction (b) via the parallelogram rule.**

In ***scalar multiplication***, each component of the vector is multiplied by the same scalar quantity:

$$a\mathbf{v} = a\,[v_1 \quad v_2 \quad v_3] + = [av_1 \quad av_2 \quad av_3] \tag{2.5}$$

The concept of a unit vector and vector addition allows us to define vectors in a more explicit and elegant way: ***base*** or ***reference vectors*** are unit vectors parallel to the three axes of the coordinate system. Any vector can thus be written as the sum of the three base vectors multiplied by the scalar components of the vector:

$$\mathbf{v} = v_1\hat{\mathbf{i}} + v_2\hat{\mathbf{j}} + v_3\hat{\mathbf{k}}$$

### *Dot Product and Cross Product*

There are two operations that are unique to vectors and uniquely useful to structural geology: the ***dot product*** (also known as the ***scalar product***) and the ***cross product*** (or ***vector product***). The dot product of two vectors yields a single, scalar number:

$$\mathbf{u} \cdot \mathbf{v} = \mathbf{v} \cdot \mathbf{u} = |\mathbf{u}|\ |\mathbf{v}| \cos\theta = v_1u_1 + v_2u_2 + v_3u_3 \tag{2.6}$$

If $\mathbf{u}$ and $\mathbf{v}$ are both unit vectors, then the term $|\hat{\mathbf{u}}||\hat{\mathbf{v}}| = 1$. We can then rearrange equation 2.6 to give us an extremely convenient equation for the angle between two lines, which we will be using a lot:

$$\theta = \cos^{-1}\left(v_1u_1 + v_2u_2 + v_3u_3\right) \tag{2.7}$$

The cross product is similarly useful because it yields a third vector which is perpendicular to the first two vectors (Fig. 2.5). There will be many times in structural geology when we will want to calculate a vector which is perpendicular to two other vectors. Notice that the direction that the third vector points depends on the order in which you cross the first two. The formula for the cross product is:

$$\mathbf{v} \times \mathbf{u} = -\mathbf{u} \times \mathbf{v} = |\mathbf{v}|\,|\mathbf{u}| \sin\theta = \left[(v_2u_3 - v_3u_2) \quad (v_3u_1 - v_1u_3) \quad (v_1u_2 - v_2u_1)\right] \qquad (2.8)$$

If **v** and **u** are unit vectors, then the length or magnitude of the new vector is equal to the sine of the angle between the two vectors. This brings up an important point: the cross product of two unit vectors produces a third vector, perpendicular to the first two, whose length varies between zero and one. The only time that the cross product produces a unit vector is when the first two vectors are at 90° to each other. It turns out that this is a surprisingly common occurrence in some, but not all, of the problems we will face in structure.

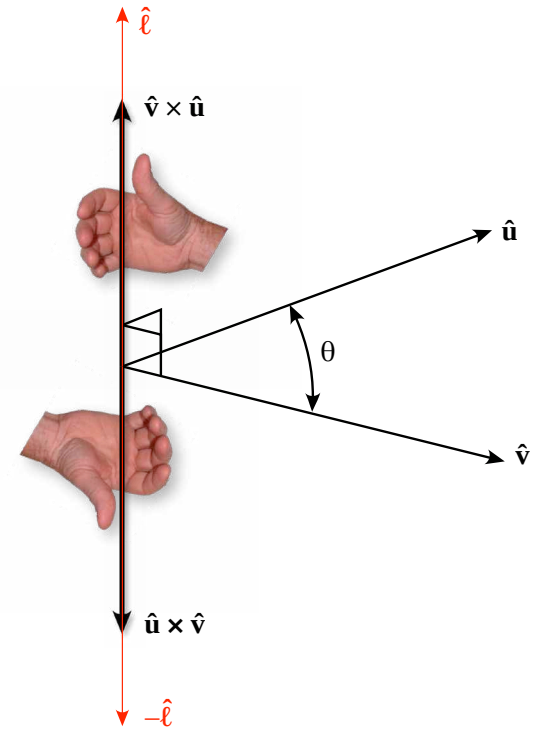


**Figure 2.5 — The cross product produces a third vector that is perpendicular to the first two vectors. If u and v are unit vectors, then the magnitude of the cross product is equal to the sine of the angle between u and v. The cross product follows a right-hand rule convention.**

# Geological Features in Cartesian Coordinates

## *Direction Cosines from Trend and Plunge*

As mentioned before, all lines in geology are vectors so it makes sense that, in Cartesian coordinates, the orientation of a line should be represented by direction cosines. We will also represent planes by their pole or their normal vector. So, the question becomes, how to convert from the familiar trend and plunge, or strike and dip, to direction cosines? As shown in Figure 2.3, we will by convention represent the angle that our vector makes with the first axis (North) by the Greek letter $\alpha$, the angle with the second axis (East) with $\beta$ and the angle with the third axis (Down) as $\gamma$. We can get some idea of the orientation of a vector simply by looking at the signs of the direction cosines (Fig. 2.6). The cosine function is positive (or zero) between $-90°$ (or 270°) and 90 and negative (or zero) between 90 and 270°. Thus, a line that has a trend and plunge in the northeast quadrant will have all positive direction cosines because the angle that it makes with each of the three axes is between zero and 90° (red point in Fig. 2.6). A point in the southwest quadrant will be more than 90° from East and more than 90° from North and thus cos$\alpha$ and cos$\beta$ will both be less than zero.

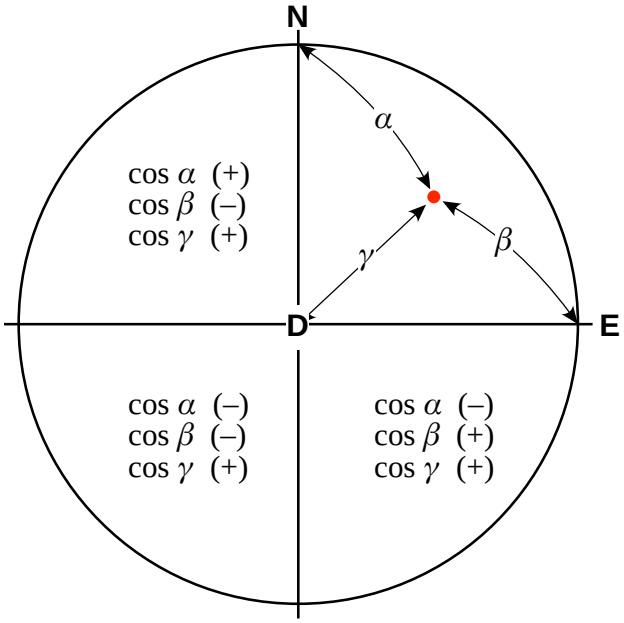


**Figure 2.6 — Lower hemisphere projection showing how the sign of each direction cosine varies with quadrant. Note that $\alpha$ and $\beta$ are angles from N and E respectively measure in inclined (i.e., non-vertical) planes, whereas $\gamma$ is measured in a vertical plane. In the northeast quadrant where the red point is, all three direction cosines are positive.**

However, what we would really like are formulae for converting from spherical coordinates (trend and plunge or strike and dip) to direction cosines and back again. To calculate these exact values, we're going to have to do a bit of trigonometry be-

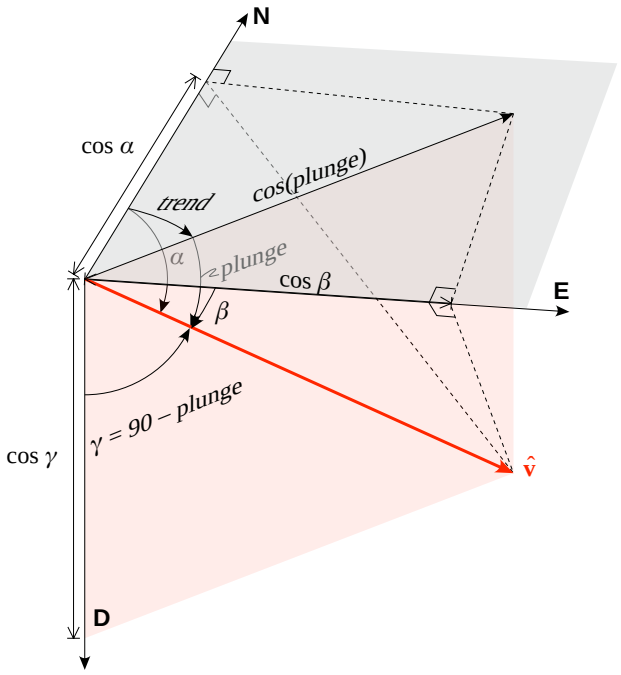


**Figure 2.7 — Perspective view of the geometry needed to derive the direction cosines of a unit vector, v, given its trend and plunge. The pink plane is the vertical plane that contains the vector.**

cause $\alpha$ and $\beta$ are not measured in vertical planes (Fig 2.6). The basic geometry and the angles involved are shown in Figure 2.7. The easiest direction cosine to calculate is cos$\gamma$ because it is just equal to the sine of the plunge. From the relationships on the horizontal plane of Figure 2.7, you can see that:

$$\cos\alpha = \cos\left(trend\right)\cos\left(plunge\right) \qquad (2.9)$$
$$\cos\beta = \sin\left(trend\right)\cos\left(plunge\right)$$

With a similar set of derivations, one can also calculate the directions cosines for the pole to a plane from the plane's strike and dip. Table 2.1 gives the complete set of equations for determining the direction cosines from the spherical coordinates.

**Table 2.1**

| Axis | Direction Cosine | Lines | Poles to Planes (strike & dip using RHR) |
|---|---|---|---|
| **North** | cos$\alpha$ | cos(*trend*)cos(*plunge*) | sin(*strike*)sin(*dip*) |
| **East** | cos$\beta$ | sin(*trend*)cos(*plunge*) | −cos(*strike*)sin(*dip*) |
| **Down** | cos$\gamma$ | sin(*plunge*) | cos(*dip*) |

### *Trend and Plunge from Direction Cosines*

Doing the reverse calculation — trend and plunge given the direction cosines — is a little less straightforward. The plunge is a piece of cake:

$$plunge = \sin^{-1}\left(\cos\gamma\right)$$

If the trend varied only from zero to 180° there would be no problem, but the trend in fact varies from 0 to 360°. For any inverse trigonometric function — arc-sine, arccosine, or arctangent — there are two possible angles between 0 and 360°. How do you choose the correct one? The answer is to use the signs of the direction cosines to determine which quadrant the trend lies within.

There are several possible ways to solve for the trend. The simplest, though with a caveat, is to observe from Equation 2.9 that:

$$\frac{\cos\beta}{\cos\alpha} = \frac{\sin\left(trend\right)\cos\left(plunge\right)}{\cos\left(trend\right)\cos\left(plunge\right)} = \tan\left(trend\right) \;\;\therefore\;\; trend = \tan^{-1}\left(\frac{\cos\beta}{\cos\alpha}\right) \quad (2.10)$$

From the graph in Figure 2.8 and by inspection of Figure 2.6, you can see that:

$$trend = \tan^{-1}\left(\frac{\cos\beta}{\cos\alpha}\right) \text{ if } \cos\alpha > 0 \quad (2.11a)$$

$$trend = 180^\circ + \tan^{-1}\left(\frac{\cos\beta}{\cos\alpha}\right) \text{ if } \cos\alpha < 0 \quad (2.11b)$$

The caveat, of course, is that you have to test for the special case of $\cos\alpha = 0$:

$$trend = 90^\circ \text{ if } (\cos\alpha = 0 \text{ and } \cos\beta \geq 0) \quad (2.11c)$$

$$trend = 270^\circ \text{ if } (\cos\alpha = 0 \text{ and } \cos\beta < 0) \quad (2.11c)$$

There are several other ways of solving for the trend, but all involve testing the sign of either cos$\alpha$ or cos$\beta$. Despite the extra test required for $\cos\alpha = 0$, the tangent is convenient because it involves a simple addition of 180° ($\pi$ radians) when $\cos\alpha < 0$.

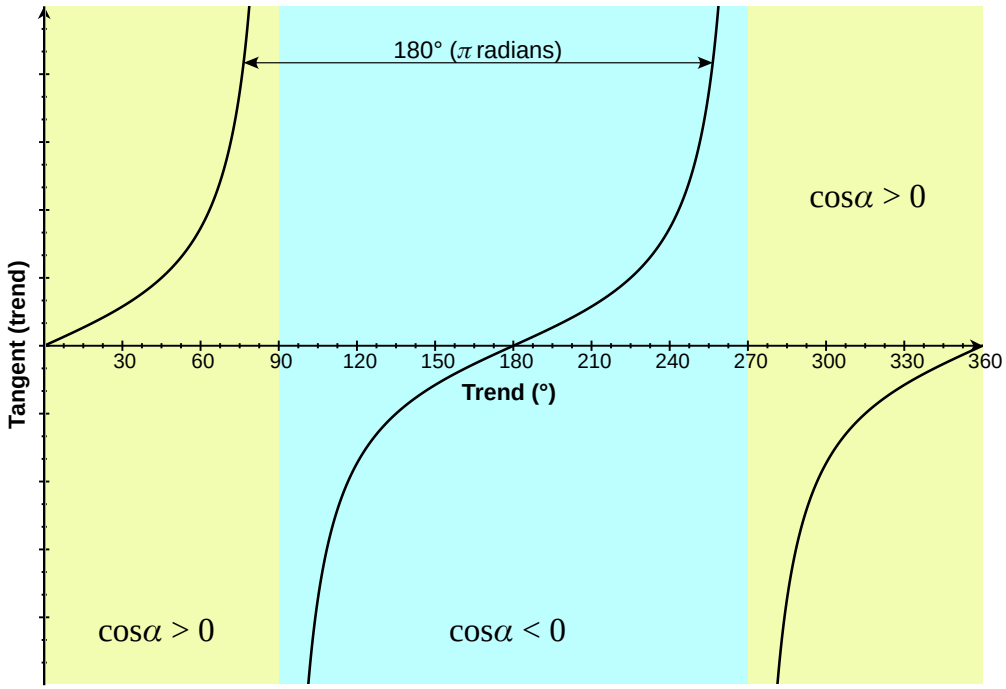


**Figure 2.8 — Plot of the trend versus the tangent of the trend.**

## Some Practical Applications Using Vectors

Okay, it is time to dust off your spreadsheet skills because even the basic vector operations we have looked at so far enable us to do some very powerful calculations. At the start, here, we will see how to set up the spreadsheet and what formula to type into each cell. After this section, it will be assumed that you can do so on your own and we will just concentrate on the equations, themselves.

### *Mean Vector*

Suppose we have group of vectors, how do we calculate the average or mean vector that represents the entire population of vectors? Our vectors may represent paleocurrent directions, paleomagnetism vectors, slip vectors on a fault surface, or any other geological feature that can be represented as a vector. This first example involves nothing more than vector addition, with some scalar division at the end. Even so, this example is impossible to do via a paper Stereonet or by any other approach. For the very final step, we will see how to calculate the uncertainty about the mean vector.

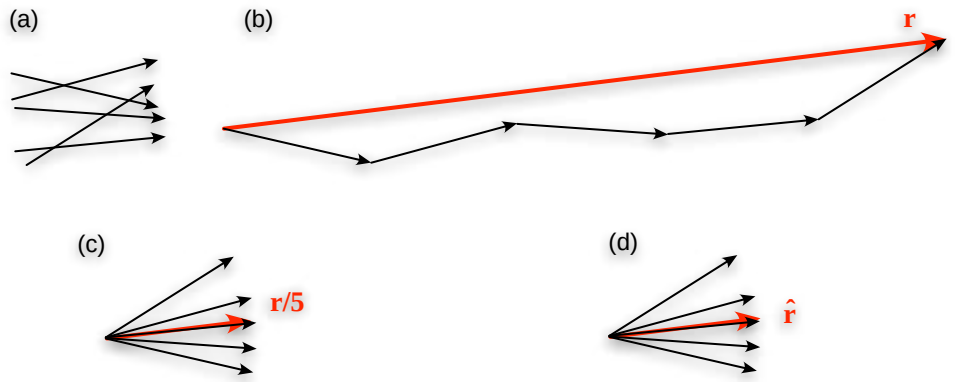


**Figure 2.9 — The steps in a mean vector calculation, depicted graphically. (a) a group of five unit vectors. (b) Adding the five vectors together and drawing the resultant vector (red). (c) Normalizing the resultant vector. Note that the red vector is somewhat shorter than the five unit vectors. (d) the mean vector (unit vector parallel to the resultant vector) calculated by dividing r by its own magnitude.**

To determine the mean of any scalar measurement, say temperature, we simply add together all of the measurements and divide by the number of measurements. The procedure is exactly the same with unit vectors, except now you sum each of the three scalar components of the vector with the corresponding components of every other vector. The ***resultant vector***, **r**, is what you get when you add several vectors together. Graphically, vector addition is just like placing the tail of one vector at the head of a previous vector; the resultant vector is drawn from the tail of the first vector to the head of the last vector (Fig. 2.9b). The length of the resultant vector is, itself, a measure of the ***preferred orientation*** of the group of unit vectors. If all of the unit vectors had exactly the same orientation, then the magnitude of resultant vector, $|\mathbf{r}|$, would be equal to the number of vectors (if there were five vectors, $|\mathbf{r}| = 5$). When comparing different groups of unit vectors with different numbers, it is convenient to normalize **r** by dividing each of its components by the number so that **r** will always vary between zero and one (Fig. 2.9c). Eventually, though, we will have to convert **r** into its

Spreadsheets and full-fledged computer programs are not very useful if they are not well organized and clearly labeled (i.e., commented). People who use or modify the program after you, not to mention your Professor and Teaching Assistant, will thank you!

| | A | B | C | D | E | F | G |
|---|---|---|---|---|---|---|---|
| 1 | | Trend | Plunge | cos(alpha) | cos(beta) | cos(gamma) | magnitude |
| 2 | 1 | 45 | 62 | 0.3320 | 0.3320 | 0.8829 | 1 |
| 3 | 2 | 37 | 22 | 0.7405 | 0.5580 | 0.3746 | 1 |
| 4 | 3 | 95 | 14 | -0.0846 | 0.9666 | 0.2419 | 1 |
| 5 | 4 | 51 | 55 | 0.3610 | 0.4458 | 0.8192 | 1 |
| 6 | 5 | 65 | 30 | 0.3660 | 0.7849 | 0.5000 | 1 |
| 7 | | | | v(N) | v(E) | v(D) | |
| 8 | resultant vector = | | | 1.7148 | 3.0872 | 2.8186 | 4.5184 |
| 9 | normalized r = | | | 0.3430 | 0.6174 | 0.5637 | 0.9037 |
| 10 | | | | cos(alpha) | cos(beta) | cos(gamma) | |
| 11 | mean vector = | 60.95 | 38.59 | 0.3795 | 0.6832 | 0.6238 | 1 |
| 12 | | | | | | | |
| 13 | Two sigma uncertainty calculation | | | | | | |
| 14 | | N = | 5 | | | | |
| 15 | | R = | 4.5184 | two sigma uncertainty = | | 0.8812 | |
| 16 | | p = | 0.95 | | | 28.21 | |

**Figure 2.10 — Simple spreadsheet to calculate the mean vector for five vectors whose orientation in spherical coordinates is shown in columns A and B, rows 2-6. Areas with calculated values shown in blue shading and the answer in yellow. The formulae for those cells are given in Table 2.2. See text for discussion.**

equivalent unit vector, $\hat{\mathbf{r}}$ (Fig. 2.9d), so that we can extract the ***mean vector*** orientation. Now, let's do the same thing numerically.

The completed spreadsheet to calculate the mean vector for five lines is shown in Figure 2.10. The original data are outlined in the box beneath the trend and plunge and all data calculated by formulae are in blue. Note that calculating the magnitude of the unit vector from the original direction cosines is redundant: we know that they have a magnitude of one already. Nonetheless it is a useful check on your calculations to make sure that you didn't enter any equations incorrectly. For this particular data set, you can see that the normalized resultant vector magnitude is 90% of a unit vector indicating a fairly strong preferred orientation.

The equations in each of the cells in row 2-11 is given in Table 2.2 (the equals sign, "=", has been omitted from in front of each equation). Note that, for rows 2-6, you would use the appropriate row number in each of the equations; all you have to do is fill in the equations for row 2 and then copy them to rows 3-6 and the spreadsheet program will automatically adjust the row numbers. Line 8 does the vector addition simply by summing the columns of individual direction cosines. Finally, note that we have used an absolute cell reference, "$G$9", in row 11 be-

cause all three formulae in columns D, E, and F reference the same cell in column G. If we had not used an absolute reference, then when the formula in D11 was copied to E11, the spreadsheet would have adjusted it automatically to read E9/H9 … not what we want at all.

**Table 2.2**

| row(s) | D (cos(alpha)) | E (cos(beta)) | F (cos(gamma)) | G (Magnitude) |
|---|---|---|---|---|
| 2-6 | COS(RADIANS(B2)) *COS(RADIANS(C2)) | SIN(RADIANS(B2)) *COS(RADIANS(C2)) | SIN(RADIANS(C2)) | SQRT(D2^2 + E2^2 + F2^2) |
| 8 | SUM(D2:D6) | SUM(E2:E6) | SUM(F2:F6) | SQRT(D8^2 + E8^2 + F8^2) |
| 9 | D8/5 | E8/5 | F8/5 | SQRT(D9^2 + E9^2 + F9^2) |
| 11 | D9/$G$9 | E9/$G$9 | F9/$G$9 | SQRT(D11^2 + E11^2 + F11^2) |

To get the trend of the mean vector in row 11, column B, we need to use a conditional statement (i.e., if… then… else…) because we have to check the sign of cos$\alpha$ as described above. The formula for the trend is:

```
=IF(D11>=0, DEGREES(ATAN(E11/D11)), DEGREES(ATAN(E11/D11))+180)
```

Between the parentheses following the IF are three statements separated by commas (this is how spreadsheets do these things…): the first is the logical test (i.e., if the value in D11 is greater than or equal to zero), the second statement is what to do if the logical test is true, and the third is the calculation if the logical test is false. This formula takes a shortcut because it does not check for whether or not cos$\alpha$ is equal to zero, which you would clearly want to do in any general purpose program. The formula for the plunge in C13 is:

```
=DEGREES(ASIN(F11))
```

In both formulae, DEGREES converts from radians to degrees because the inverse trigonometric functions always return the angle in radians.

Like any calculation that involved determining a mean, we can also determine the statistical ***standard deviation***. For three dimensional mean vector data, the standard deviation is given by:

$$\cos \delta\alpha_p = 1 - \left(\frac{N-R}{R}\right)\left[\left(\frac{1}{1-p}\right)^{\frac{1}{N-1}} - 1\right] \tag{2.12}$$

where $p$ is the probability, $N$ is the number of vectors, $R$ is the magnitude of the resultant vector. $\delta\alpha_p$ is the apical angle of the cone of uncertainty at probability, $p$. For example, if you wanted to calculate the probability at two standard deviations, or 95%, you would set $p = 0.95$. You can see that, for the perfect case of all vectors having the same orientation, $\cos\delta\alpha_p = 1$ and $\delta\alpha_p = 0$ because $N$=$R$. Though not terribly useful with so few measurements, the 2σ (or $\delta\alpha_{95}$) cone of uncertainty around our mean vector in the data set shown if Figure 2.10 is 28.2°: we are 95% certain that the correct answer lies within 28.2° of the mean vector that we calculated.

What we have just seen is undeniably powerful: it is exactly the calculation that geologists who study paleomagnetism make when they determine a paleomagnetic pole. However, be careful: the mean vector calculations is very literal. That raises a common pitfall: the case where the direction of the vector doesn't matter and we are plotting exclusively in the lower hemisphere. We commonly think of lines that plot on the opposite sides of a stereonet — say, 090, 05 and 270, 05 — as having very nearly the same orientation, that is they are very nearly parallel. However, the mean vector calculation treats them as vectors pointing in opposite directions as shown in Figure 2.11. When we add the two together, the resultant vector is vertical and very short. This is the right thing to do if we are summing anything where the direction matters but it is not what we want if, say, intersection lineations are being analyzed. For these lines that have no directional significance, there are

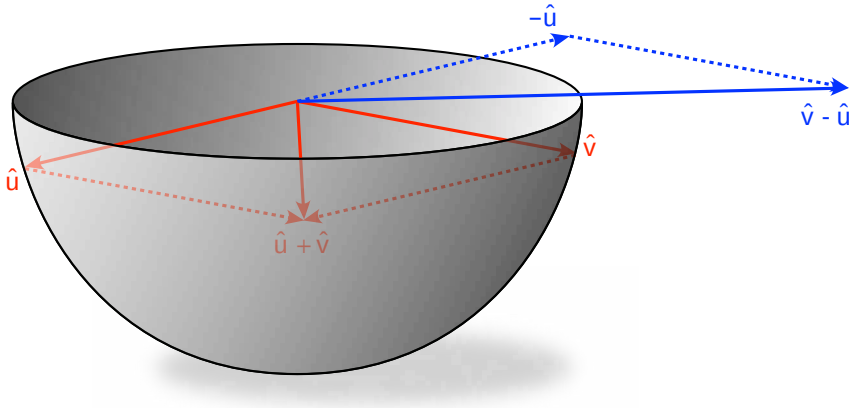


**Figure 2.11 — Oblique view of a lower hemisphere projection showing the result of adding to vectors with shallow plunges on opposite sides of the net (red vectors). When the vectors have no directional significance, we usually want the blue vector.**

other methods but we'll need to develop some additional concepts before we get there.

## *Rake of a Line in a Plane*

Recall that the rake of a line is just the angle between the line and the strike of a plane that contains the line. Here, we are going to follow the format that the rake is always given with respect to the right-hand rule strike. The dot product (Eqn. 2.7) will serve us nicely for this calculation. One line is given by its trend and plunge; the second line is the strike line which has a trend equal to the strike and a plunge of zero.

The spreadsheet for this calculation is shown in Figure 2.12. The formulae for the direction cosines of the line in row 2 are straightforward and the same as used in the previous example. The plane in row 3 requires a bit more explanation: we are treating the strike as a horizontal line in the plane so we don't actually use the dip value at all! Instead, the direction cosines are calculated for a line with a trend equal to the strike and a plunge of zero (because the strike is a horizontal line… you get the idea). That is why the third direction cosine for the strike in F3 is equal to zero. If a line has zero plunge, the angle that it makes with the down axis, gamma, is 90° and cosine of 90° is equal to zero.

The formula for the rake in cell B5 is just:

| | A | B | C | D | E | F | G |
|---|---|---|---|---|---|---|---|
| 1 | | Trend or strike | Plunge or Dip | cos(alpha) | cos(beta) | cos(gamma) | magnitude |
| 2 | Line: | 182.1 | 30.3 | -0.8628 | -0.0316 | 0.5045 | 1 |
| 3 | Plane: | 53 | 37 | 0.6018 | 0.7986 | 0.0000 | 1 |
| 4 | | | | | | | |
| 5 | rake = | 123.0 | | | | | |

**Figure 2.12 — Spreadsheet for calculating the rake of a line in a plane. Note that the direction cosines in row 3 are for a line with a trend of 053 and a plunge of 00.**

```
=DEGREES(ACOS(D2*D3 + E2*E3 + F2*F3))
```

As before, we don't really need and don't even use the magnitude column but it is a useful check to make sure that our formulae are entered correctly.

## *True Dip from Two Apparent Dips*

There are many times when we observe in nature two cuts or slices through a plane, but neither cut is in the true dip direction (i.e., perpendicular to strike). This can happen in quarry walls, road cuts, mine tunnels, etc. In these cases, we may have to calculate the orientation of the plane — that is, the strike and true dip — from the available observations of apparent dip. In terms of the concepts developed in this Chapter, we know two vectors that lie in the same plane and want to calculate the orientation of the plane, itself. You may recall that one way to specify a plane is by the normal to the plane or the pole (Fig. 2.13). The pole is, by definition, perpendicular to every line in the plane, including the two apparent dip lines, so our solution to this problem will use the cross product (Eqn. 2.8, Fig. 2.5).

As before, the procedure that we will follow is similar to what we've done in other examples in this chapter:

1. Calculate the direction cosines of the two apparent dip lines from their trends and plunges
2. Calculate the cross product using Equation 2.8
3. If the cross product gives us an upper hemisphere pole, which you can determine from the sign of the third direction cosine, then convert it to a lower hemisphere pole by multiplying all three direction cosines by −1.
4. Convert the vector product to a unit vector by dividing by the magnitude of the vector (which, remember, is equal to the sine of the angle between the two vectors).

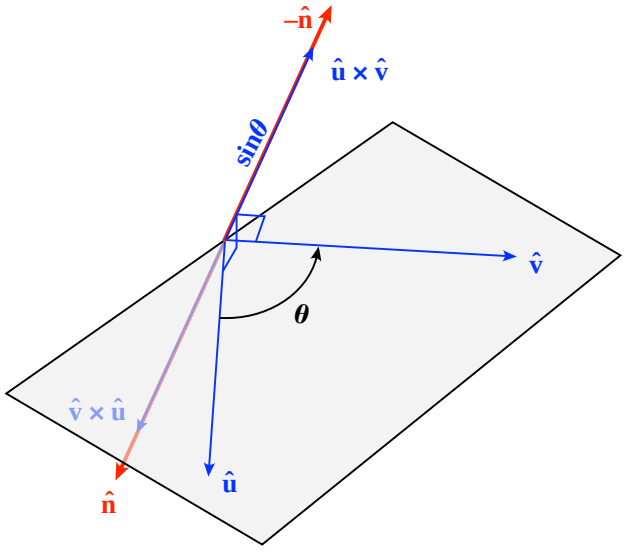


**Figure 2.13 — Any two vectors in a plane can be used to find the pole to the plane using the cross product. As shown, the order in which you cross the vectors determines whether the pole is upward or downward pointing. The cross product of any two unit vectors has a length equal to the sine of the angle between the two vectors. You must calculate the unit pole vector, n̂, parallel to the cross product before converting it back to trend and plunge.**

5. Determine the trend and plunge of the pole from the direction cosines of the unit vector calculated in step 4.
6. The right hand rule strike of the plane will just be equal to the pole plus 90° and the dip will be 90°–plunge of the pole.

The spreadsheet that carries out these steps is shown in Figure 2.14. The two lines in rows 2 and 3 are processed just the way they were in the previous examples. The cross product in row 5 is an upward pointing vector as shown by the fact that the third component is negative. To reverse the direction of the vector so that it points into the lower hemisphere, each component is multiplied by −1 in row 6. The direction cosines for the unit vector parallel to the cross product are calculated in row 8 by dividing the components in row 6 by the magnitude of the vector. The trend of the pole to the plane is calculated from these direction cosines by using the same formula that we used in the mean vector example:

```
=IF(D8>=0, DEGREES(ATAN(E8/D8)), DEGREES(ATAN(E8/D8))+180)
```

As before, we haven't checked for the special case of $\cos\alpha = 0$. The resulting trend of the pole is a negative number, which translates to an azimuth of 308.35°; we don't bother to change it because we need to add 90° to it, anyway, to get the right-hand rule strike, which is done in row 10.

| | A | B | C | D | E | F | G |
|---|---|---|---|---|---|---|---|
| 1 | | Trend | Plunge | cos(alpha) | cos(beta) | cos(gamma) | magnitude |
| 2 | Line 1 | 209 | 22 | -0.8109 | -0.4495 | 0.3746 | 1 |
| 3 | Line 2 | 56 | 37 | 0.4466 | 0.6621 | 0.6018 | 1 |
| 4 | | | | v(N) | v(E) | v(D) | |
| 5 | cross product = | | | -0.5185 | 0.6553 | -0.3362 | 0.9008 |
| 6 | lower hemisphere cross product = | | | 0.5185 | -0.6553 | 0.3362 | 0.9008 |
| 7 | | | | cos(alpha) | cos(beta) | cos(gamma) | |
| 8 | pole to plane | -51.65 | 21.91 | 0.5757 | -0.7275 | 0.3732 | 1 |
| 9 | | | | | | | |
| 10 | strike & dip | 38.35 | 68.09 | | | | |

**Figure 2.14 — Spreadsheet for calculating the orientation of a plane from two apparent dips, labeled line 1 and line 2. The strike of the plane is given using right-hand rule format.**

# Exercises—Chapter 2

1. Practice thinking about coordinate system labeling.
   (a) Devise three different right-handed coordinate systems that start with West as the positive $\mathbf{X}_1$ axis.
   (b) Likewise, determine three different left-handed coordinate systems that start with South as the positive $\mathbf{X}_1$ axis.

2. If you multiply a vector times 3, does the resulting vector have a magnitude three times greater than the original vector? Prove your answer.

3. From the poles to bedding that you calculated for your measurements in exercise 1.4 in Chapter 1, calculate the mean pole vector and its uncertainty (Eqn 2.12).

You should recognize the table below; they are the same problems as in Week 1 of the course. The table below lists a series of orientations. Planes are given in azimuth format and lines in trend, plunge format. Asterisks show missing values; *** is a missing azimuth or bearing, and ** is a missing plunge or dip. Some of the values are redundant: for example, once you know the true dip and dip direction, you also know the strike and dip.

| *Datum* | *Strike & Dip of Plane* | *True Dip (T&P)* | *Apparent Dip(s) (T&P)* |
|---|---|---|---|
| *1* | 050, **, * | ***, ** | 090, 25 |
| *2* | ***, **, * | ***, ** | 159, 34 and 270, 43 |
| *3* | ***, **, * | 010, 48 | 321, ** and 090, ** |

4. Solve each of these problems with a spreadsheet program or Matlab using the cross product or dot product as necessary. You will need to convert all of the values to direction cosines, do the calculations, then convert the values back to trend and plunge or strike and dip. Remember that the cross product does not normally give you a unit vector so you must convert your answer to a unit vector before you can get its orientation in trend and plunge.

# Chapter 3

## *Extracting Information from Geological Maps & Folds*

### Geologic Maps

Geologic maps are one of the most fundamental types of geologic documents and yet they are a strange mixture of data and interpretation; it is often not easy to tell one from the other. Published maps are all solid colors and bold, confident lines; they look like they are representing data. In this Chapter, we will build on the visualization that we began in Chapter 1 and the vector methods from

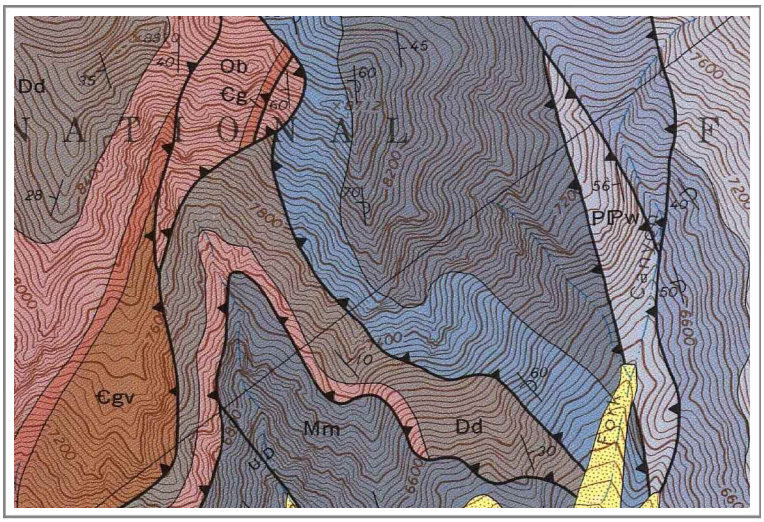


Chapter 2 to introduce you to some of the types of information that you can extract from a geologic map.

Most of the features that we deal with at a map scale are approximately planar features — stratigraphic contacts, faults, dikes, etc. — and, more often than not, they are not horizontal. At a regional scale, the surface of the earth where we make most of our observations is pretty planar but, at more detailed scales, topography is very irregular. Mapping the outcrop patterns of these planar features is basically an exercise in locating the line of intersection between the planar feature and the irregular 3D surface of the Earth.

## Three Point Problems

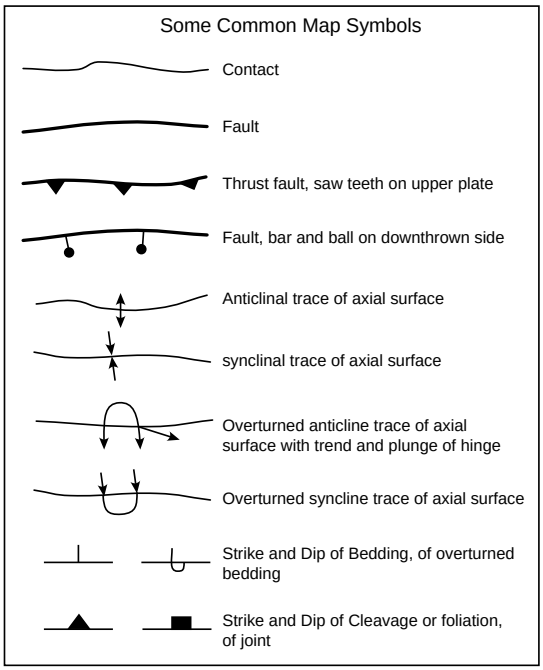


A geologist cannot always go the the field and put a compass on the rock to determine a strike and dip. Even when s/he can do so, we frequently want to know the orientation of a planar rock unit at a scale larger than the outcrop scale. That is, we want to know the average orientation at a map scale. Fortunately, our geologic maps provide sufficient information to enable the structural geologist to determine orientation independent of outcrop and compass.

The orientation of a plane can be determined if we know the positions of three non-collinear points within the plane. Because the surface of the earth has variable topography, we can commonly find three points on a plane at different topographic elevations. Geologic maps com-

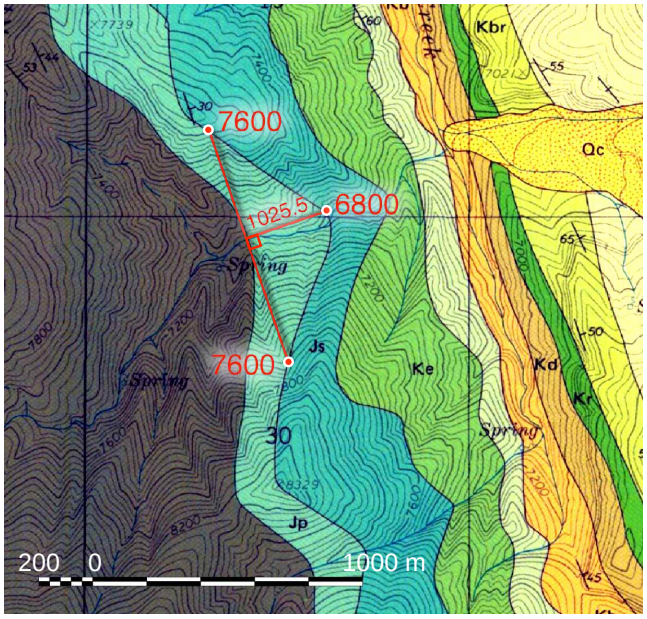


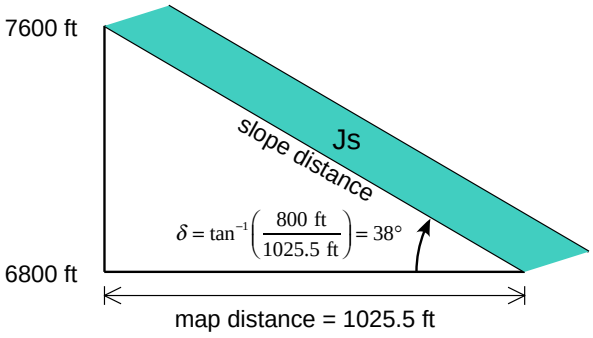


**Figure 3.1 — The classical three-point problem where a line is draw between two points of equal elevation on a planar surface, yielding the strike (left). On the right is the construction in a vertical plane parallel to the line labeled "1025.5" (feet) on the map for calculating the dip using the elevation values (in feet) and map distance.**

monly depict topography with contour lines and, even if they don't, modern digital elevation models are available for most of the earth's surface and the elevation of any point can be determined via the Internet.

Figure 3.1 shows the classical way of determining strike and dip from a geologic map with topographic contours. This simple method takes advantage of the fact that a line connecting two points of equal elevation along a mapped contact of a planar feature define the strike of a plane. The dip can then be calculated from a third point at different elevation from a simple geometric construction. Both the map distance, and the elevation difference to the third point, perpendicular to the strike, can be read directly off the geologic map.

A more general method takes advantage of the vector methods we've just learned in the previous chapter. It is more flexible because all three points can be at different elevations and can be used wherever we have spot elevations but no topographic contours (e.g., in Google Earth). We use the cross product of two vectors in a plane — just like we did in the previous chapter to determine the true dip from two apparent dips — but this time we are not using unit vectors describing orientations of two lines in the plane, but are using ***position vectors*** whose magnitudes are much greater than one (Fig. 3.2).

A position vector is a line connecting a point in space to the origin of the coordinate system (P1, P2, and P3 in Fig. 3.2). The coordinates of the position vector are just the scalar components of the vector projected onto the coordinate system axes. In the case of our geologic map, we could use the UTM coordinates (eastings

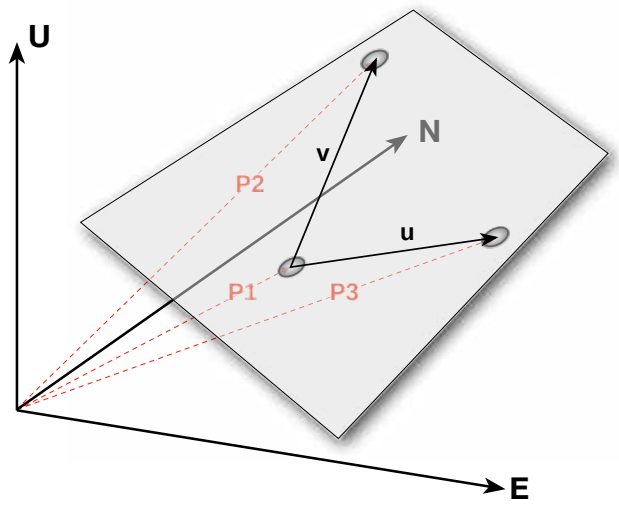


**Figure 3.2 — Three points in a plane can be used to calculate the orientation of a plane. The coordinates of the three points are the coordinates of the three position vectors, P1, P2, and P3. To get the vectors that lie within the plane, v and u, we use vector subtraction as described in the text. The pole to the plane is calculated from v × u.**

and northings) plus elevation to define the position vector in an East-North-Up coordinate system. Or, we could use any other local Cartesian coordinate system.

To calculate the pole to the plane, we will use the cross product of two vectors in the plane, **v** and **u**. These two vectors can be calculated from the position vectors using vector subtraction. The complete sequence of steps is given, below:

The first step is to subtract the position vectors to get **v** and **u**. Note that at this point, we are working in an ENU coordinate system so the subscripts in the following equation correspond to the axes of our coordinate system: 1=E, 2=N, and 3=U.

$$\mathbf{v} = \begin{bmatrix}(P2_1 - P1_1) & (P2_2 - P1_2) & (P2_3 - P1_3)\end{bmatrix} \tag{3.1}$$

$$\mathbf{u} = \begin{bmatrix}\left(P3_1 - P1_1\right) & \left(P3_2 - P1_2\right) & \left(P3_3 - P1_3\right)\end{bmatrix}$$

To convert these to a lower hemisphere NED centric coordinate system — which we will need in order to calculate our orientations — we switch the order of the first two components of the vector and multiply the third by −1:

$$\mathbf{v} = \begin{bmatrix}(P2_2 - P1_2) & (P2_1 - P1_1) & -(P2_3 - P1_3)\end{bmatrix} \tag{3.2}$$

$$\mathbf{u} = \begin{bmatrix}\left(P3_2 - P1_2\right) & \left(P3_1 - P1_1\right) & -\left(P3_3 - P1_3\right)\end{bmatrix}$$

The cross product is defined as:

$$\mathbf{v}' \times \mathbf{u}' = \begin{bmatrix}\left(v_2u_3 - v_3u_2\right) & \left(v_3u_1 - v_1u_3\right) & \left(v_1u_2 - v_2u_1\right)\end{bmatrix} = [s_1 \quad s_2 \quad s_3] \tag{3.3}$$

The cross product gives us the pole to the plane but we need to convert it to a unit vector before it can be transformed back into geographic orientations like trend and plunge or strike and dip. We start by calculating the magnitude of cross product, $s_{magn}$:

$$s_{magn} = \sqrt{s_1^2 + s_2^2 + s_3^2} \tag{3.4}$$

And now we calculate the unit pole vector, $\hat{\mathbf{p}}$, by dividing each component of **s** by its magnitude, $s_{magn}$.

| | A | B | C | D | E |
|---|---|---|---|---|---|
| 1 | | East | North | Up | Magnitude |
| 2 | A | 4116.29 | 46791.16 | 8591.69 | 47751.1637 |
| 3 | B | 4515.93 | 46171.72 | 8886.56 | 47235.4983 |
| 4 | C | 3963.095 | 45006.11 | 8193.42 | 45917.1884 |
| 5 | | | | | |
| 6 | AB | 399.64 | -619.44 | 294.87 | 793.956145 |
| 7 | AC | -153.195 | -1785.05 | -398.27 | 1835.34498 |
| 8 | | | | | |
| 9 | AB x AC | 773062.062 | 113992.013 | -808272.49 | 1124243.55 |
| 10 | unit vector | 0.68762864 | 0.10139441 | -0.7189479 | 1 |
| 11 | NED | 0.10139441 | 0.68762864 | 0.71894786 | 1 |
| 12 | pole trend: | 81.61 | plunge = | 45.967682 | |
| 13 | | | | | |
| 14 | Strike = | 171.61 | dip = | 44.03 | |

**Figure 3.4 — The spreadsheet to do the same calculation as shown in Figure 3.3. Note that the switch from an ENU to a NED coordinate system occurs in row 11.**

$$\hat{\mathbf{p}} = [p_1 \quad p_2 \quad p_3] = \left[\frac{s_1}{s_{magn}} \quad \frac{s_2}{s_{magn}} \quad \frac{s_3}{s_{magn}}\right] \tag{3.5}$$

If the third component is negative, i.e., $p_3 < 0$, then the unit pole vector we have calculated points into the upper hemisphere. To covert to the lower hemisphere in this case, multiply each component by −1.

We're now ready to convert our unit pole vector back to trend and plunge. The plunge is straightforward because it is just the arcsine of the $p_3$ component of the pole to the plane:

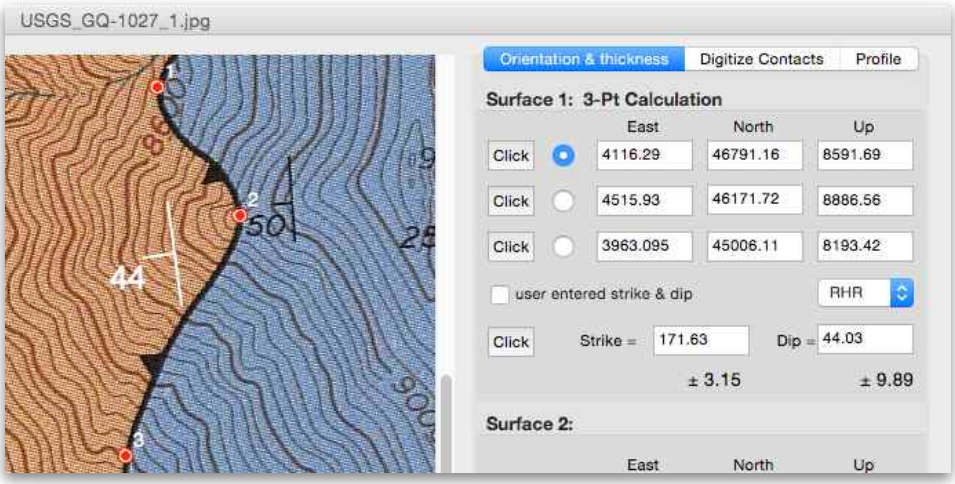


**Figure 3.3 — A three point calculation in GMDE. This program can also calculate the uncertainties; those shown here are given a horizontal and vertical uncertainty of 40 ft.**

$$plunge = \sin^{-1}(p_3) \tag{3.6}$$

As we saw in Chapter 2, the trend is a function of $p_2$ and $p_1$ and the sign of $p_1$. If $p_1 \geq 0$ then you use the equation on the left, below; otherwise use the equation on the right:

$$trend = \tan^{-1}\left(\frac{p_2}{p_1}\right) \quad \text{or} \quad trend = 180^\circ + \tan^{-1}\left(\frac{p_2}{p_1}\right) \tag{3.7}$$

To get the right-hand rule strike, just add 90° to the trend; the dip is 90°–plunge.

The program GeolMapDataExtractor (GMDE) can do this calculation for you automatically (Fig. 3.3), and the equations we have just seen are exactly how the program does it. As a scientist, you are, of course, not content to trust your precious data to a canned program, and thus will want to calculate these values yourself. Figure 3.4 shows you how to set up your spreadsheet using the same values as in Figure 3.3.

## Stratigraphic Thickness from Maps

Stratigraphic thickness is defined as the thickness of a unit measured perpendicular to the upper and lower surfaces of the unit. For people truly interested in stratigraphic sequences, there is still no substitute for going out in the field and measuring a stratigraphic section with tape, compass, Jacob staff, or whatever. Measuring section that way is certainly the most accurate way to determine the thickness of a unit but the process is time-consuming. For the rest of us, especially when drawing cross sections, we are more likely to calculate the thickness of a stratigraphic unit from a geologic map, commonly called a ***map thickness***. In this section, we will see how to determine the map thickness in the way that geologists have for many decades. In the next chapter, we'll learn how to do the calculation in a much more flexible way after learning a new concept.

To calculate a map thickness, $t$, using traditional methods (Fig. 3.5), you must determine the map distance, $h$, between the top and bottom of the unit measured in the true dip direction (i.e., perpendicular to strike); the vertical distance, $v$, between base and top along the same transect; and the true dip, $\delta$. There are three equations and the correct one to use depends on the relationship between the dip

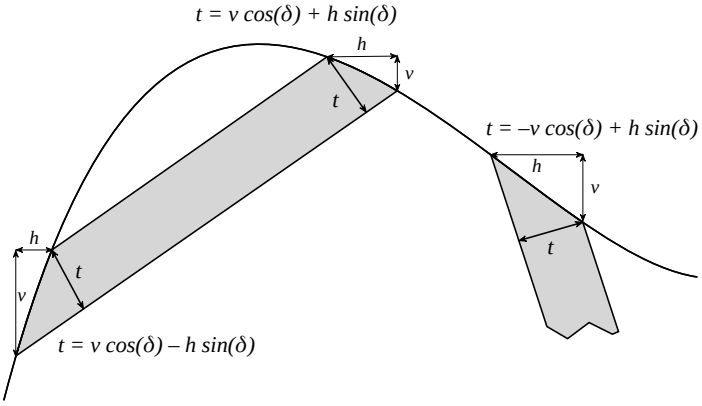


**Figure 3.5 — Cross section illustrating the traditional way of calculating map thickness. In all three cases, the cross section is perpendicular to the strike of the unit so that the true dip, δ, is used. There are three cases (from left to right): the unit dips in the same direction but less steeply than the slope; the unit dips in the opposite direction from the slope; and, the unit dips in the same direction as the slope but more steeply.**

direction and the slope direction (Fig. 3.5). For cases where the stratigraphic unit dips more steeply and in the same direction as the slope, one uses:

$$t = -v\cos\delta + h\sin\delta \tag{3.8a}$$

When the slope and dip direction are the same, but the slope is steeper, the correct formula to use is:

$$t = v\cos\delta - h\sin\delta \tag{3.8b}$$

And finally, where the dip and the slope are in opposite directions, the equation is:

$$t = v\cos\delta + h\sin\delta \tag{3.8c}$$

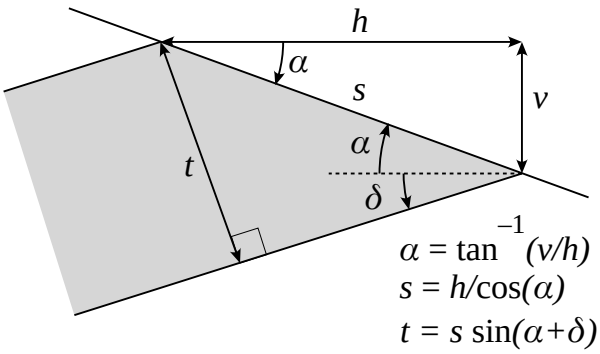


**Figure 3.6 — The two right triangles necessary to solve for the thickness on your own. The equations shown in the graphic will eventually simplify to Equation 3.8c, though it is not necessary to take it that far.**

I highly recommend that, rather than memorizing these equations, you simple derive the equation from the geometry when you need it. Trying to recall which special case to use can lead to errors and it is usually faster to derive the correct equation than to look up and use an equation out of a book, cookbook style. To work out the equations yourself, note that there are two right triangles as shown in Figure 3.6. You first calculate the slope angle, $\alpha$, and slope distance, $s$, and then you use those quantities along with the dip to derive the thickness. Similar graphics can be devised for the other two special cases.

The necessity to construct these diagrams in the true dip direction and remember the three special cases (Fig. 3.5) is limiting when it come to writing a single general equation to accomplish the task of determining map thickness. In the next chapter, we will learn a powerful set of methods known as coordinate transformations that will enable, not only a general solution to this problem but to a whole set of interesting problems typically encountered in structural geology.

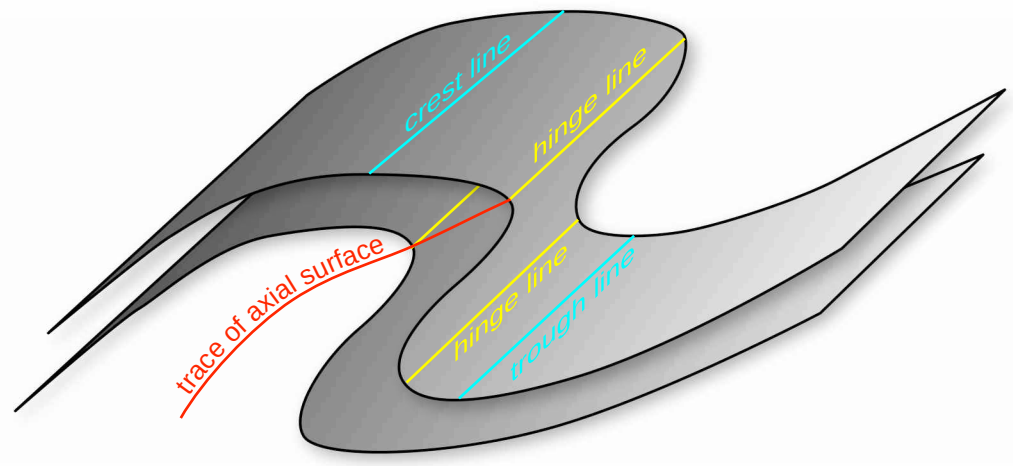


**Figure 3.7 — Basic fold terminology illustrated with two folded surfaces. The hinge line connects points of maximum curvature on a surface whereas the crest and trough lines connect the topographically highest and lowest points, respectively, on the surface. The axial surface is the surface that contains all of the hinge lines on all of the folded surfaces.**

# Analysis of Folded Rocks

Folded rocks (Fig. 3.7) are some of the most aesthetically pleasing of all geological structures and are quite important economically as hydrocarbon traps. When folded rocks intersect the irregular surface of the Earth, the resulting outcrop patterns can be quite complex. On a map, the fold is usually represented by the trace of the axial surface (the intersection between the surface of the earth and the axial surface) or sometimes the crest line. For folds with shallowly dipping axial surfaces (i.e., recumbent folds) the trace can be quite complex.

## *Cylindrical Folds*

The simplest fold model is that of a ***cylindrical fold*** (Fig. 3.8) in which there is a line of zero curvature, known as the ***fold axis***, and non-zero curvature at any point along the fold in a direction perpendicular to the fold axis. the resulting structure is completely two dimensional such that a measurement of bedding orientation in one part of the fold should be identical to bedding measured in any other part of the fold parallel to the fold axis. If you were to measure bedding throughout a cylindrical fold and plot the poles. They would lie within a single plane known as the ***profile plane*** (Fig. 3.8). The profile plane is perpendicular to the fold axis and provides the "truest" view of the fold. Any profile plane constructed anywhere along the fold will show the same view as long as it is perpendicular to the fold axis.

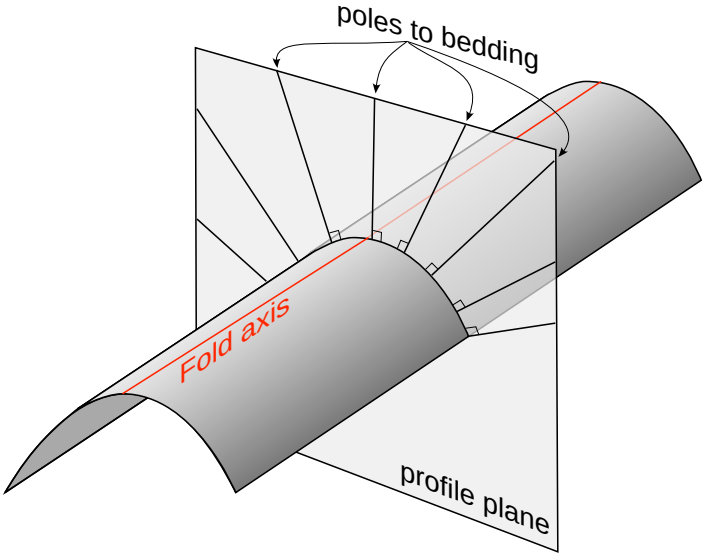


**Figure 3.8 — A perfect cylindrical fold illustrating the concept of a fold axis (line of zero curvature shown in red) and profile plane. All of the poles to bedding should be oriented parallel to the profile plane. In the real case, bedding is *not* measured along a single arc, but can be measured anywhere on the surface and the projected parallel to the fold axis to a common plane.**

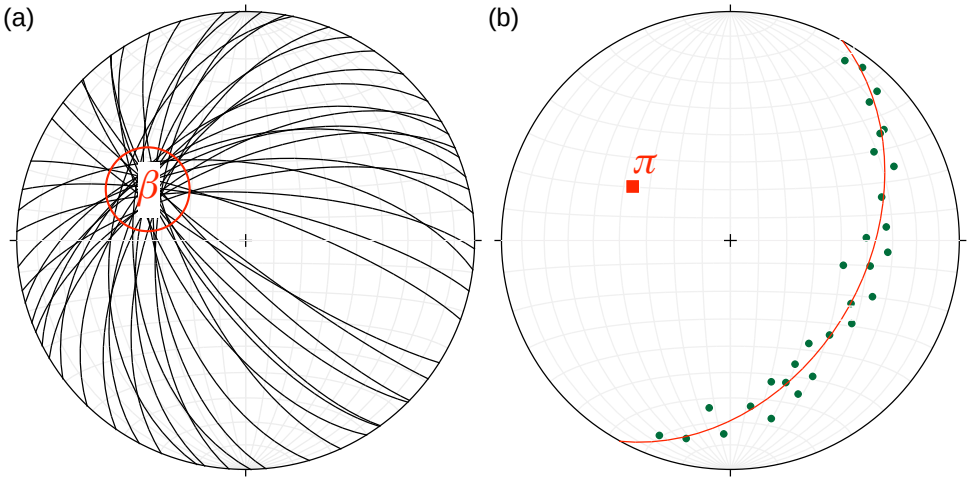


**Figure 3.9 — Finding a cylindrical fold axis by plotting bedding orientations on a stereonet. (a) *β*-diagram of great circles representing the strikes and dips of bedding and the region of intersection defines the fold axis. (b) π-diagram of poles to bedding. The pole to the best fit great circle through the bedding poles defines the fold axis.**

The cylindrical fold model is highly oversimplified and very few natural folds are perfectly cylindrical. Nonetheless, the model provides a quick way of determining a fold axis and it allows us to project a plunging fold geometry to depth.

Determining the fold axis is simple: as implied in the previous paragraph, we measure a number of bedding orientations around a fold and plot them on a stereonet. Two different approaches can be used: in a ***β-diagram***, we plot the great circles of bedding and locate the fold axis where the maximum number of intersections occur (Fig. 3.9a). In the ***π-diagram***, the poles to the bedding planes are calculated and a great circle fit to the bedding poles. The pole to the best fit great circle defines the fold axis (Fig. 3.9b). As you can imagine looking at Figure 3.9a, the β-diagram can get messy very quickly with a lot of bedding measurements. For that reason, and because the numerical solution to this problem uses the poles anyway as we shall see in a later chapter, most structural geologists prefer the π-diagram. Either type of diagram is easy to use in a stereonet program (look for the "Cylindrical best fit" menu option).

Most folds are not as nicely curved as the idealized folds depicted in Figures 3.8 and 3.9. Instead, they tend to have mostly planar limbs and a narrow hinge zone where the dip changes occur over a narrow area. In this case, the geologist

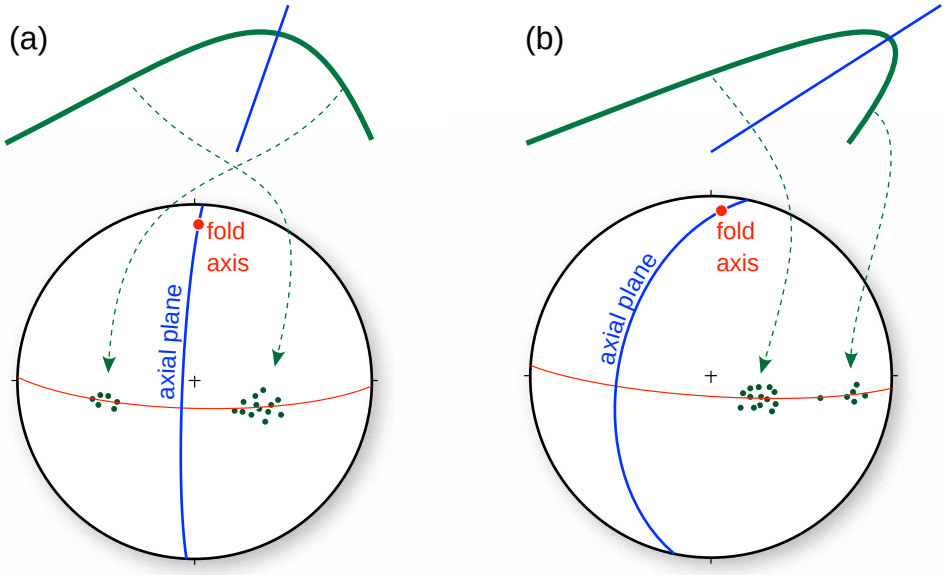


**Figure 3.10 — Determining the fold axis and axial plane on a stereonet. At the top of each diagram is a profile view of a bed (in green) with the axial plane in blue. In the stereonet views, below, the poles to bedding are shown with green dots, the cylindrical best fit and fold axis in red and the axial plane in blue. Dashed lines with arrows show where each limb plots on the stereonet. (a) and upright asymmetric fold. The downward pointing poles for both limbs are plotted. (b) an overturned asymmetric fold. The poles of the overturned limb are plotted as upward pointing poles.**

who conscientiously measures bedding orientations at regular intervals is more likely to see two point clusters, corresponding to the two limbs, with a relatively small number of measurements in-between (Fig. 3.10). Furthermore, if the fold is asymmetric, then there will be fewer measurements from the shorter limb. In these cases, the resulting π-diagram can be used to locate not only the fold axis but also the fold ***axial plane***. Where bedding thickness is preserved across the fold, the axial plane bisects the angle between the limbs of the fold and contains the fold axis. This calculation is straightforward for upright folds (Fig. 3.10a); you can see on the stereonet that the axial plane plots between the two point clusters. However, overturned folds are more problematical because, whereas for the upright limb we plot the downward pointing poles, for the overturned limb we are plotting the upward pointing poles so they will appear in the lower hemisphere (Fig. 3.10b). In this case the axial plane will bisect the large obtuse angle between the two point clusters.

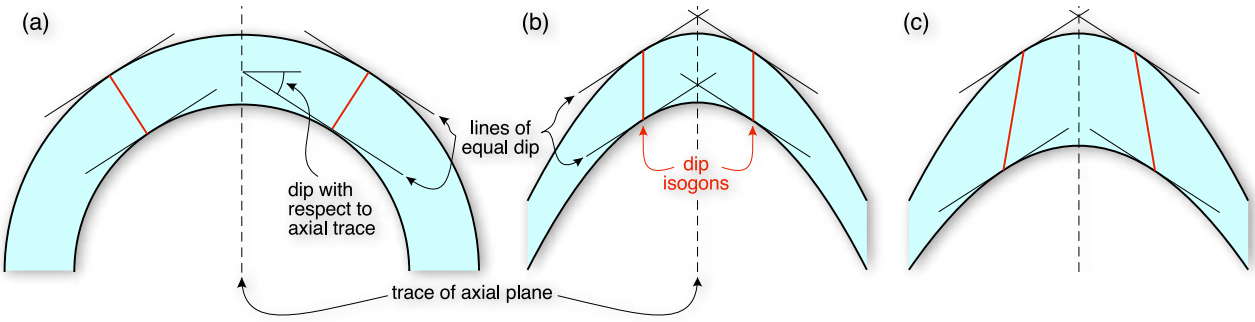


**Figure 3.11 — The construction of dip isogons and the three general classes of folds: (a) Class 1 dip isogons where the radius of curvature of the lower bedding surface is smaller than the upper surface. (b) Class 2 dip isogons where both bedding surfaces have the same curvature; and (c) class 3 dip isogons where the lower surface has a larger radius of curvature than the upper surface.**

## *Dip Isogons*

Cylindrical folds come in several flavors. A common way to classify them is with ***dip isogons***, which are used to describe the geometric relationship of one bedding surface to the next. A dip isogon connects two points on adjacent bedding surfaces which both have the same dip relative to the axial plane of the fold. As shown in Figure 3.11, there are three general classes of folds based on dip isogons. Where bedding thicknesses are preserved, Class 1 dip isogons are also known as ***parallel folds*** (Fig. 3.11a). Class 2 dip isogons result from ***similar folds*** (Fig. 3.11b). Finally, Class 3 dip isogons indicate a fold where the inner surface is less curved than the outer surface. We will return to fold geometry and kinematics in Chapter 10 because cross section construction relies heavily on choosing an appropriate fold model.

## *Folds in Map View*

A cylindrical fold is just about the simplest fold form you can imagine and yet, when you convolve the form with the topography of the earth, the resulting map pattern can be highly complicated. Even in the absence of topography, correct interpretation of the fold axis and axial trace can be counterintuitive. Because the axial plane is, well, a plane, the trace that the axial plane makes across the land surface is plotted on the map, i.e., the intersection between the plane and the topogra-

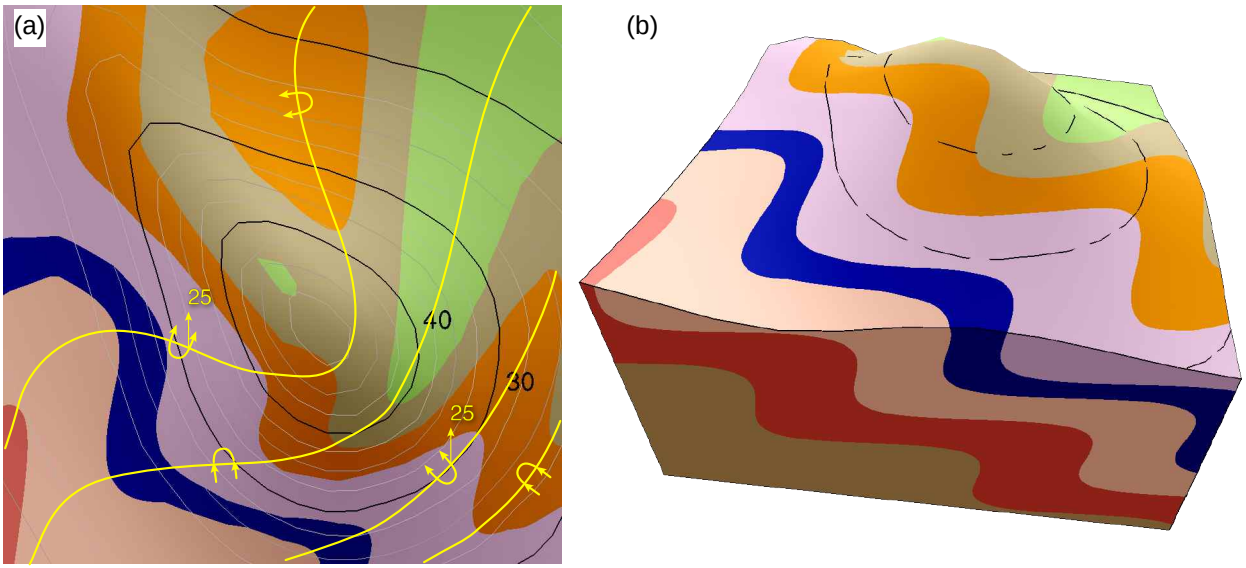


**Figure 3.12 — Folds and topography in (a) map view, and (b) down-plunge view. In the map view (a), the heavy black lines are index topographic contours and the light gray lines are other topo contours; a hill with NW-trending ridge is depicted. The yellow lines are traces of fold axial planes with standard symbols for over-turned anticlines and synclines. the block diagram in (b) shows the down-plunge view of the structure — tilted so the viewer is looking parallel to the trend and plunge of the folds — where the true fold geometry is revealed. In this view, axial traces are approximately straight lines. In (b) only the index contours are shown as discontinuous black lines. Diagrams created with Visible Geology (thanks, Rowan!).**

phy (Fig. 3.12a). The fold axis is a line that, in general, intersects the surface in a point (really a point for each geological surface). Thus, we show the trend and plunge of the fold axis as a small arrow pointing in the direction of the trend of the axis with a number next to it for the plunge (Fig. 3.12a). The ***down-plunge view*** of a cylindrical fold, which can be approximately achieved by tilting the map so that you are looking in the direction of plunge, provides the most accurate perspective on the fold geometry and can help make sense of a seemingly complicated map pattern (Fig. 3.12b). In the next chapter, we will see how to calculate down-plunge views of folds.

There is a spectacular web-based resource, ***Visible Geology***, where you can create your own 3D models, look at those created by other people or visualize a stereonet in 3D:

http://app.visiblegeology.com

Working out the geometry of fold axis and

axial plane is not always straight forward, even in the absence of significant topography. A couple of tricks will help you to interpret folds more quickly. Most importantly, as shown in Figure 3.10, the fold axis is a line contained within the axial plane, but it can have any rake within that plane. Thus, for some types of folds known as reclined folds, the trend of the fold axis can actually be as much as 90° to the strike of the axial plane. If we know the strike of the axial plane and the trend and plunge of the fold axis, we can determine the dip of the axial plane. Alternatively, by using the trace of the axial plane in down-plunge view and the trend and plunge of the axis from a π-diagram, we can calculate the orientation of the axial plane using the cross product or on a stereonet.

The other "trick" is equally useful, enabling rapid determination of the trend and plunge of the fold axis: ***the strike of any vertical bedding must be parallel to the fold axis trend and the dip of any bedding that strikes perpendicular to the fold axis must be equal to the plunge of the fold axis***. Thus, if you find bedding dipping 90° in one part of an area that has experienced one episode of cylindrical folding, you know that the trend of the folds is parallel to the strike of that bed!

## Structural Contour Maps

Just about any value can be contoured to show its spatial variation and structure data are no exception. In a structural contour map, one contours lines of equal elevation on a surface of interest. Surfaces can be smoothly varying or they can be disrupted by faults. Automatic contouring algorithms can do a good job where the elevations are smoothly varying but tend to have trouble where contours terminate abruptly against a fault. Furthermore, the geologist has a better idea of what deformed geological surfaces actually look like so is in a better position to draw realistic contours, though one must always be aware of unintended bias.

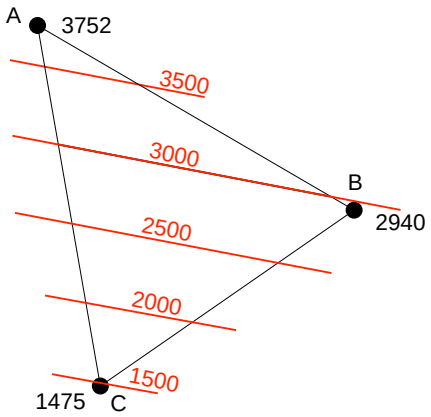


**Figure 3.12 — Contouring via linear interpolation along the sides of a triangle with apices of know elevation.**

A geologist doing a first pass at contouring a surface would operate very much as a computer program does: s/he would construct a mesh of triangles — such a mesh is frequently accomplished using ***Delaunay triangulation*** — with apices at the points of known elevation and would then linearly interpolate between the points (Fig. 3.12). This sort of contouring is tedious to do by hand but easy to implement in a computer program.

A significant difference between contours of the topographic surface and a geologic surface of interest is that the surface of the Earth is continuous whereas the geologic surface can have gaps and overlaps across faults. A normal fault will produce a gap (Fig. 3.13a) and a thrust fault will produce an overlap (Fig. 3.13b). Folded surfaces that are also faulted yield the most complex patterns (Fig. 3.13c). Clearly, a good structure contour map, except in the simplest case of an inclined planar surface with constant strike and dip, requires extensive subsurface data to construct. Such data may be available where there has been extensive hydrocarbon industry exploration.

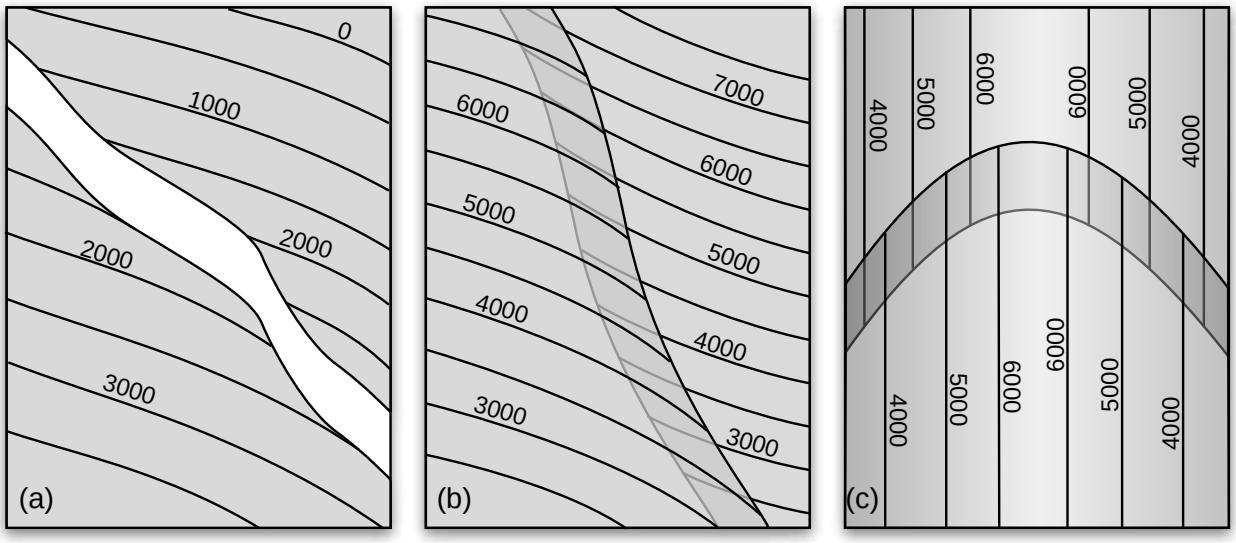


**Figure 3.13 — Examples of structure contour maps. (a) A normal fault produces a gap, (b) thrust or reverse fault an overlap, and (c) a cylindrically folded surface cut by a thrust fault striking perpendicular to the fold axis.**

# Exercises—Chapter 3

These exercises and those of the next Chapter will rely heavily on the program GeolMapDataExtractor (GMDE) and a digital copy of the Poker Peak geologic map from the US Geological Survey (Albee and Cullens, 1975). GMDE, in either Macintosh or Windows version can be downloaded from:

http://www.geo.cornell.edu/geology/faculty/RWA/programs/strikedipthickness.html

and the Poker Peak Quadrangle map can be downloaded from the class Web site. GMDE will allow you to make quick accurate measurements on the map. Note that you will need an Internet connection for the program to get elevations automatically. For Exercises 1 and 2, you will also need a copy of Google Earth, which you can download for free from:

http://www.google.com/earth/download/ge/agree.html

1. Open the Poker Peak Quad in GMDE and make sure it is georeferenced (it should automatically be unless you have separated the .jpg file of the map from the .txt file of the same name (the .txt file contains the georeferencing information.) Locate the part of the map shown to the right. Notice that a fault is shown offsetting the stratigraphic units.

   (a) *Across the entire segment of the map shown*, digitize the following contacts: base of Kp, top of Kp, top of Kb, top of Kd.

   (b) Save your contacts as a .kml file (File>Export KML>contacts), and then open the .kml file in Google Earth.

   (c) Kp and Kd are two very light gray to nearly white limestone units. Trace these white units on the Google Earth image from the northern end of your digitizing to the south.

   (d) Evaluate the mapping job and

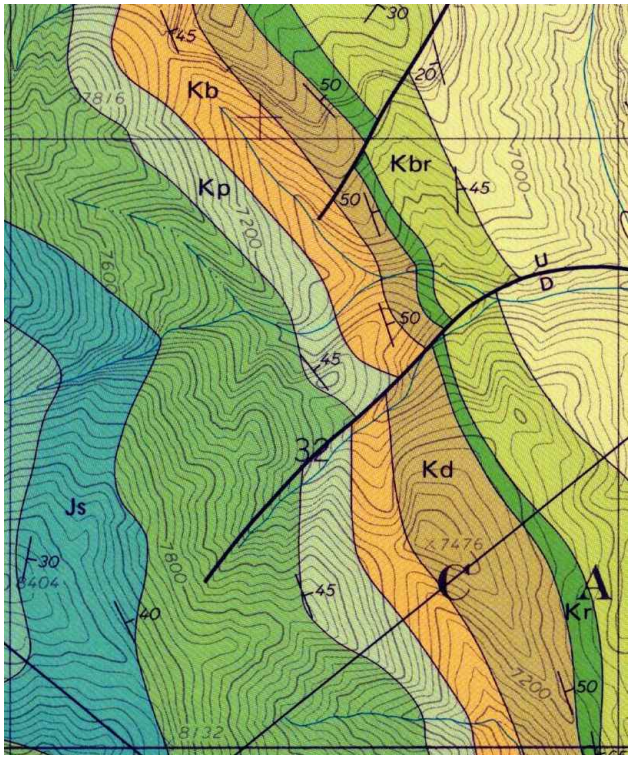

the evidence for a fault, based on the agreement or lack of agreement of your digitized contacts with the units that you see in Google Earth. It will probably help to tilt and pan the Google Earth view to evaluate different perspectives. Turn in a paragraph with your assessment of the mapping.

2. With the Poker Peak Quad loaded into GMDE, digitize about 60 strikes and dips around the Big Elk Anticline, the area outlined in the red polygon to the right.

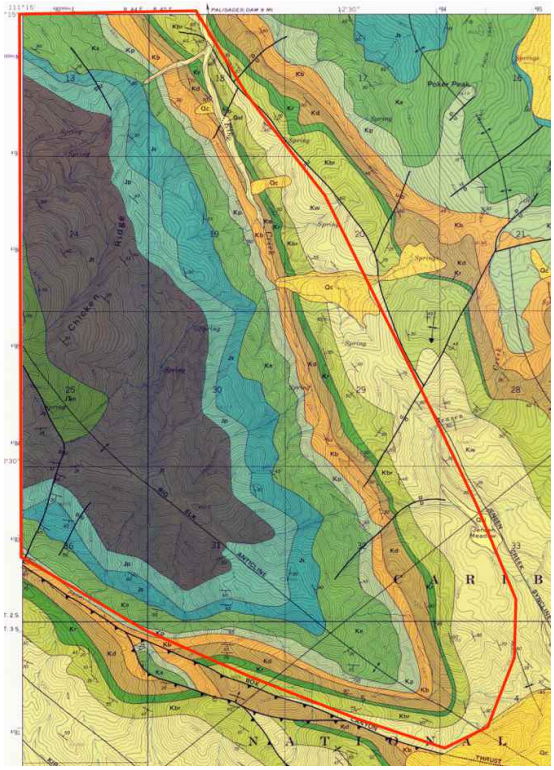

   (a) In GMDE, select Settings>Mode>Strike & Dip Only. Each time you want to measure a strike and dip, select Operations>Drag Strike Line or select ⌘D from the keyboard (easier). To drag a strike line, click at the intersection of the strike line and dip tick mark and then drag the mouse in the direction of the right-hand rule strike (you can correct it if you drag in the wrong direction with the pop-up menu). You will have to type the dip value in by hand. Once you are happy with the strike and dip, press the "Record Strike & Dip" Button. The program should draw a new strike and dip symbol over the one that you just measured.

   (b) When you have measured and recorded all of the strikes and dips in the outlined area, save your data. You should save it in three ways:

      (i) first, select File>Save Data>Thickness/Orientation Data. This will allow you to read your data back in to GMDE easily which will be useful in next week's lab.

      (ii) Next select File>Export Strikes & Dips. This file can be easily read into Stereonet.

      (iii) Finally, select File>Export KML>Strikes & Dips to make a file for visualization in Google Earth. In the dialog box that appears, just click Okay which will use the default values.

(c) Open the KML file in Google Earth. The strikes and dip symbols are rendered in three dimensions so you can clearly see the relationship between strike and dip and the actual stratification. Be sure that you have topography turned on in Google Earth and tilt and pan to get a good feeling for the 3D nature of the geology. **In Google Earth, save an image of the screen (File>Save image) which you think shows especially well the relationship between the measured strike and dip and the geology and turn it in with a sentence about why you liked it.**

(d) Open the second file in Stereonet. Calculate the poles to the plane, make a π-diagram, and determine the fold axis of the Big Elk Anticline. **Turn in your plot with the fold axis clearly annotated**.

3. In GMDE with the Poker Peak Quad loaded, find the area in the northeast corner of the map shown to the right.

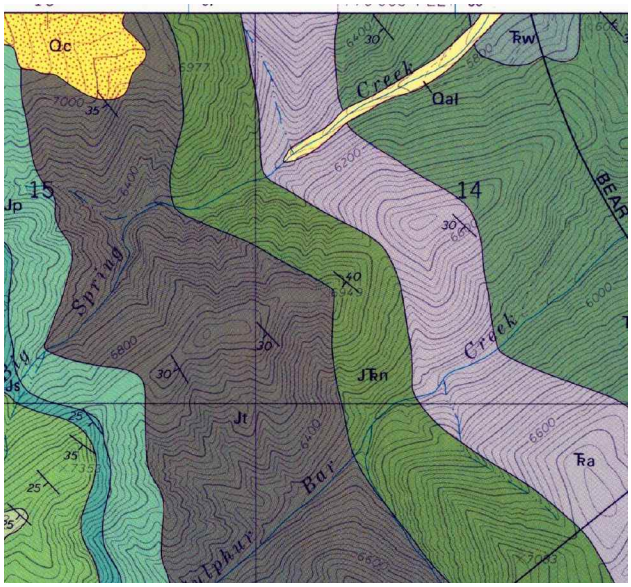


(a) Select Settings>Mode>Strike & Dip Only and uncheck the check box that says "user entered strike and dip". Use GMDE to find the East, North, and Up coordinates of three points on the base of the purple Tra where it crosses the ridge with the number "14" on it. To do so click the "click" button next to one row, then click on the map exactly where you want to place the point. Repeat for the other two points. If you have an Internet connection enabled, the program will get the elevation for you automatically; otherwise, you will have to type in the elevation coordinate by hand.

(b) Copy the ENU coordinates of the three points you have defined into a spreadsheet and calculate the strike and dip of the unit in the spreadsheet using vector subtraction and the cross product. You can compare your answer to the correct answer that GMDE calculates automatically.

(c) Compare your calculated value to the strike and dip symbol that the geologist measured on the ridge for the base of Tra and discuss the uncertainties and reasons for the difference in two values, if any. Once you record your

strike and dip, you can see it's location in a satellite image by choosing Datum Details from the Window menu. This may help you in your discussion. **Turn in both the spreadsheet with the calculation of the strike and dip and the your comparison with the mapped value and your discussion.**

4. GMDE allows you to make accurate distance measurements: just click and drag the mouse from the top (or base) of the unit in the direction of the true dip to the base (or top) of the unit. The distance and azimuth of the line you drag is shown in the box at the lower left corner of the map view. Be sure to read the distance before releasing the mouse! You can read the elevations off of the topo contours on the map or, if you have an Internet connection, hold down the option key while you click the mouse at the point for which you want the elevation.

   (a) On the same ridge that you used for problem 3, calculate the thickness of Tra using the appropriate Equation 3.8. Do the calculation for both the geologist measured orientation and the orientation that you determined from the three-point problem in Exercise 3.

   (b) Make a drawing and derive a set of equations for the two right triangles that you would use to get a the answer in part (a). You don't have to derive Equation 3.8 but the equations that you do get have to give you the same answer as Eqn. 3.8!

5. On the next page is a map showing a number of borings that were made to determine the elevation of the Jurassic Twin Creek Limestone in the subsurface around the nose of the Big Elk anticline. Contour these elevations by hand using a contour interval of 500 ft and describe the resulting surface. You do not need to do a formal linear interpolation between adjacent points.

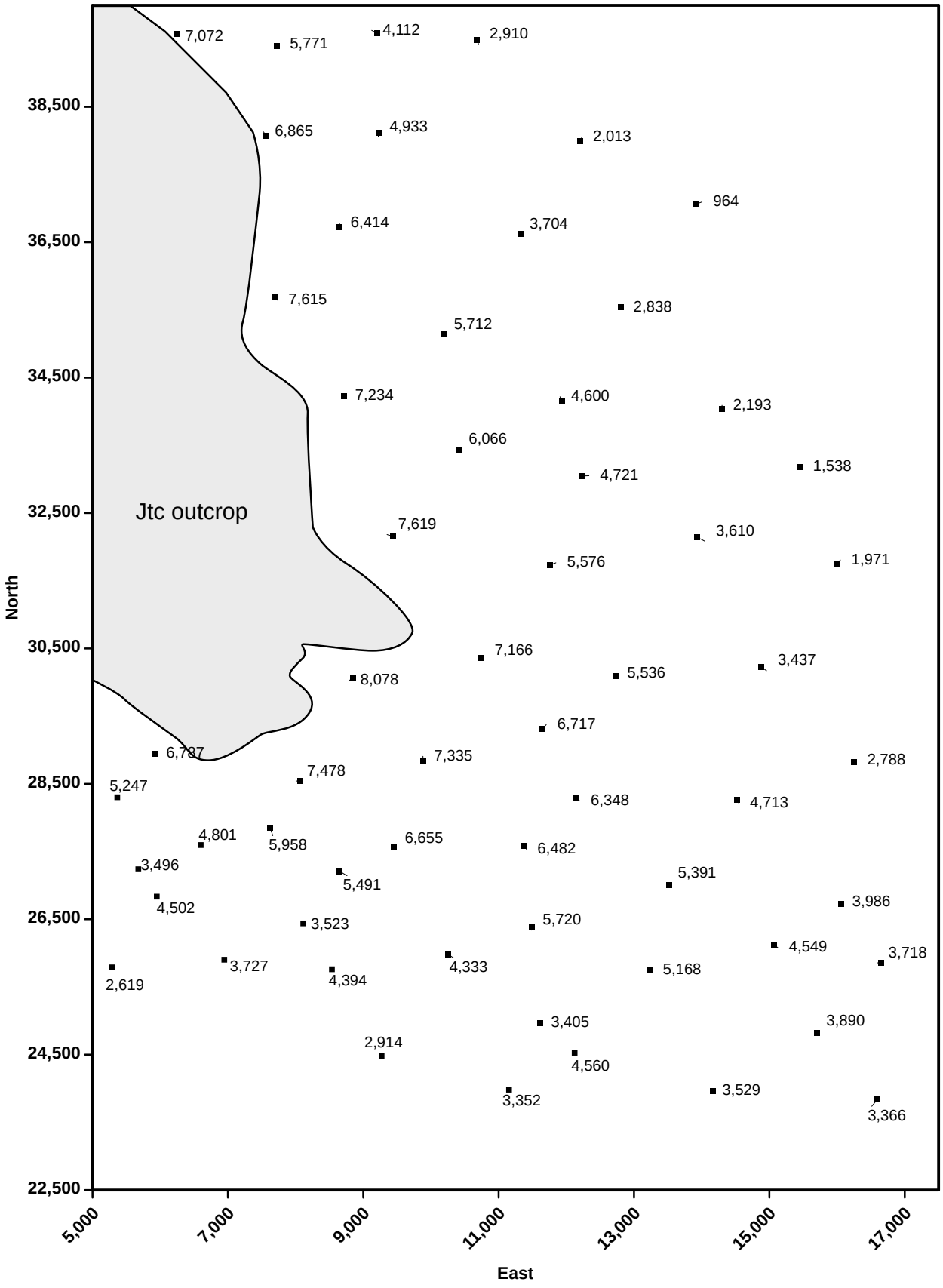
Jtc outcrop
North
East
38,500
36,500
34,500
32,500
30,500
28,500
26,500
24,500
22,500
5,000
7,000
9,000
11,000
13,000
15,000
17,000
7,072
5,771
4,112
2,910
6,865
4,933
2,013
964
6,414
3,704
7,615
2,838
5,712
7,234
4,600
2,193
6,066
1,538
4,721
7,619
3,610
5,576
1,971
7,166
3,437
8,078
5,536
6,717
6,787
7,335
2,788
7,478
5,247
6,348
4,713
4,801
5,958
6,655
6,482
3,496
5,491
5,391
4,502
3,986
3,523
5,720
4,549
3,718
3,727
4,333
5,168
2,619
4,394
3,405
3,890
2,914
4,560
3,529
3,352
3,366

# Chapter 4

## *Transformations*

### Introduction

Many times in geology, as in other disciplines, the problem we are interested in solving is simpler when viewed from a different perspective. Anyone who plays computer games or flight simulators knows this to be true. So far, we have been dealing with geographic-centric coordinate systems — either NED or ENU – because we measure our world with respect to geographic coordinates. But there is a

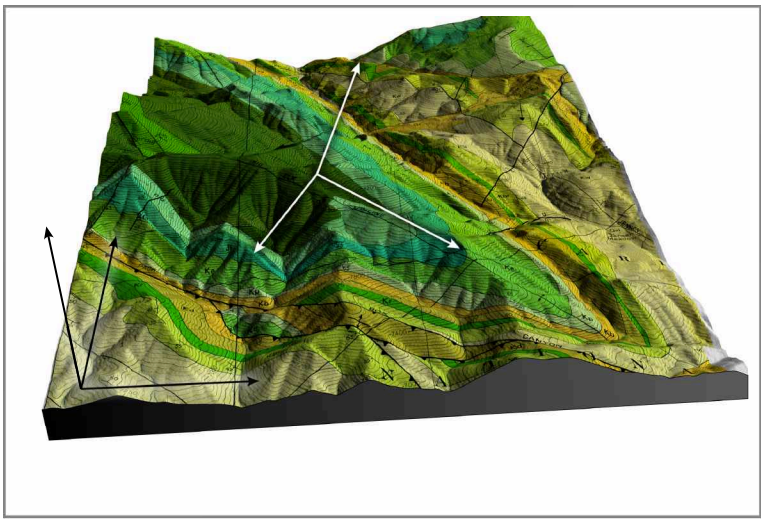

whole class of problems that benefit from a change in coordinate system or ***transformation***. In the last chapter, we noted that the profile view of a plunging fold is the most accurate representation of the structure. The profile view is defined by a different coordinate system — the fold coordinate system — rather than the geographic view. In this Chapter, we will learn how to switch back and forth between these two views and in the process begin to lay the foundation for understanding entities more complicated than geometry such as stress and strain. Before getting to interesting geological problems, however, we'll need to develop the simple mathematical foundation of transformations.

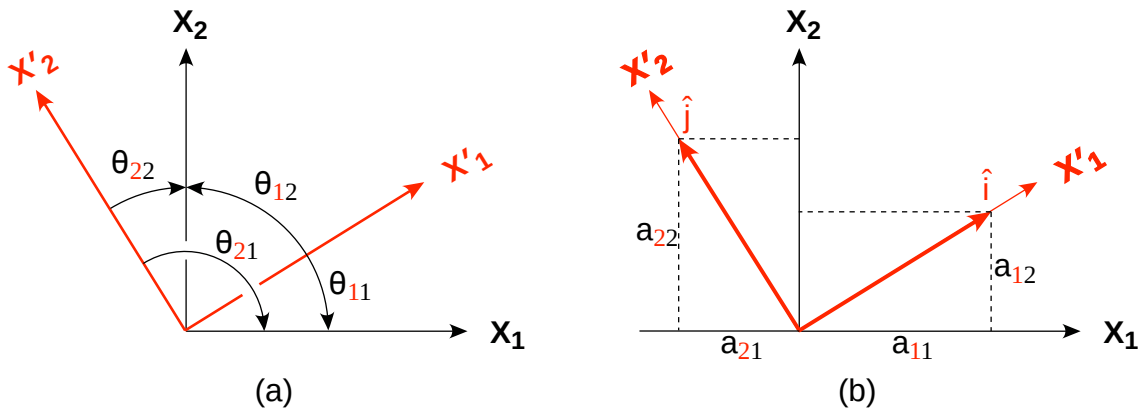


**Figure 4.1 — A two-dimensional rotation of a coordinate system between an old, unprimed coordinate system in black and a new primed coordinate system in red. (a) The rotation defined by four angles, and (b) defined by four direction cosines which are the projections of the base vectors of the new coordinate system on the axes of the old system. In both cases, the first subscript (in red) identifies the new axis and the second subscript (in black) the old axis**

# Transformations of Coordinates and Vectors

## *Coordinate Transformations*

At the simplest level, a transformation involves a change in orientation of the coordinate system. Like many things, we will visualize this first in two dimensions (Fig. 4.1) and then in three dimensions (Fig. 4.2). In the text that follows, we will always refer to the new coordinate axes as the primed coordinate system, X′, and the old coordinate system as the unprimed system, X. To define the rotation of a coordinate system in two dimensions, there are four angles between the two new coordinate axes and the two old axes. *One needs to be very careful systematic about naming these angles*: The first subscript refers to the new coordinate axis and the second subscript to the old coordinate axis. For example, $\theta_{21}$ is the angle between the $X_2'$ axis and the $X_1$ axis (Fig. 4.1a). After the last few chapters, it should come as no surprise that we will typically be using the direction cosines rather than the angles themselves (Fig. 4.1b). The subscript convention is exactly the same and the relations between the angles and their direction cosines are:

$$a_{11} = \cos\theta_{11}; \quad a_{12} = \cos\theta_{12}; \quad a_{21} = \cos\theta_{21}; \quad a_{22} = \cos\theta_{22} \tag{4.1}$$

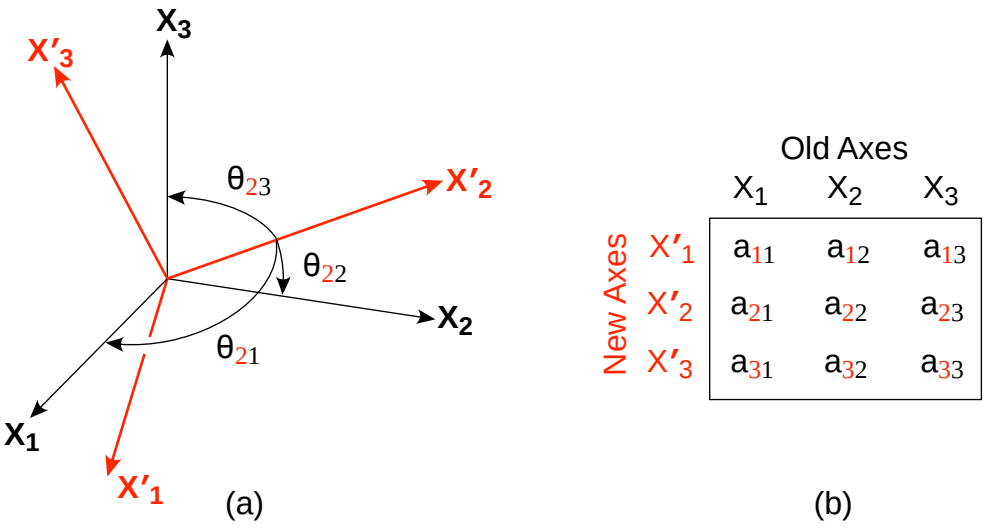


**Figure 4.2 — Coordinate transformation in three dimensions: (a) the new axes (primed) in red and the old in black. As before the first subscript refers to the new axis and the second to the old axis. (b) The array of directions cosines: each row refers to a new axis and each column to an old axis.**

The extension to three dimensions is quite straightforward (Fig. 4.2). Because we now have three coordinate axes in the new system and three in the old system, there will be nine angles and nine direction cosines. This 3×3 table, or array, of direction cosines is known as the ***transformation matrix***:

$$a_{ij} = \begin{pmatrix} a_{11} & a_{12} & a_{13} \\ a_{21} & a_{22} & a_{23} \\ a_{31} & a_{32} & a_{33} \end{pmatrix} = \begin{pmatrix} \cos\theta_{11} & \cos\theta_{12} & \cos\theta_{13} \\ \cos\theta_{21} & \cos\theta_{22} & \cos\theta_{23} \\ \cos\theta_{31} & \cos\theta_{32} & \cos\theta_{33} \end{pmatrix} \tag{4.2}$$

We will be using the shorthand $a_{ij}$ a lot in the following sections because it is much more compact than writing out those matrices all the time. Just recall that $i$ and $j$ can each have values ranging between 1 and 3.

As you no doubt notice in the case of the 2D transformation, not all of the angles, or direction cosines, are independent. In that case, only one angle is independent and the rest can be calculated from it. In the 3D case, only three angles are independent and the rest can be calculated from those three. Matrix **a** is technically known as an ***orthogonal matrix*** and the equations that relate the direction cosines are known as the ***orthogonality relations***:

$$\begin{aligned} a_{11}^2 + a_{12}^2 + a_{13}^2 &= 1 \\ a_{21}^2 + a_{22}^2 + a_{23}^2 &= 1 \\ a_{31}^2 + a_{32}^2 + a_{33}^2 &= 1 \end{aligned} \quad \text{and} \quad \begin{aligned} a_{21}a_{31} + a_{22}a_{32} + a_{23}a_{33} &= 0 \\ a_{31}a_{11} + a_{32}a_{12} + a_{33}a_{13} &= 0 \\ a_{11}a_{21} + a_{12}a_{22} + a_{13}a_{23} &= 0 \end{aligned} \tag{4.3}$$

While we won't bother to do so in detail here, both of these sets of equations are easy to prove: the left equations come from the fact that the base vectors of the new coordinate system have magnitudes of 1, and the right hand equations are due to the fact that, because the base vectors are perpendicular to each other, the dot product of each of the base vectors with the other is zero.

## *Transformation of Vectors*

The transformation matrix by itself is not very useful. Its power comes from the fact that, once we know the transformation matrix and the components of a vector in one coordinate system, we can immediately calculate the components of the vector in the other coordinate system. Figure 4.3 shows how this works in two dimensions to calculate the $v_1'$ component of the vector in the new coordinate system as a function of the old components $v_1$ and $v_2$. In terms of direction cosines we could write the equation as:

$$v_1' = a_{11}v_1 + a_{12}v_2$$

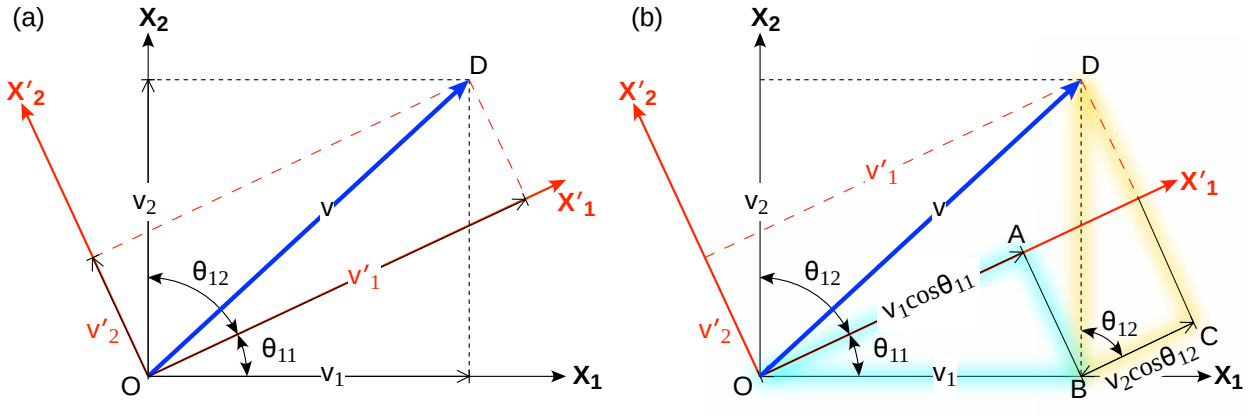


**Figure 4.3 — the transformation of a vector. (a) shows the components of vector v in the old (black, unprimed) and new (red, primed) coordinate systems. (b) the graphical construction to calculate the value of v′1 in terms of the old coordinates. The blue and yellow highlighted triangles are used to trigonometrically calculate v′1 in terms of $v_1$ and $v_2$.**

Perhaps the most important thing to notice is that, although the coordinate systems have changed, and therefore the values of the components of the vector in the two coordinate systems are different, the fundamental nature of the vector itself has not changed at all. This seems trivially obvious but it is exactly this property that determines whether or not something is a ***tensor*** property! Yes, a vector is sometimes referred to as a ***first order tensor***. More on that in later chapters.

In three dimensions, there are three equations that describe the components of the vector in the new system as a function of the old components:

$$\begin{aligned} v'_1 &= a_{11}v_1 + a_{12}v_2 + a_{13}v_3 \\ v'_2 &= a_{21}v_1 + a_{22}v_2 + a_{23}v_3 \\ v'_3 &= a_{31}v_1 + a_{32}v_2 + a_{33}v_3 \end{aligned} \tag{4.4}$$

And, there are another three equations that give the components of the vector in the old coordinate system as a function of the new coordinates:

$$\begin{aligned} v_1 &= a_{11}v'_1 + a_{21}v'_2 + a_{31}v'_3 \\ v_2 &= a_{12}v'_1 + a_{22}v'_2 + a_{32}v'_3 \\ v_3 &= a_{13}v'_1 + a_{23}v'_2 + a_{33}v'_3 \end{aligned} \tag{4.5}$$

These equations consist of nothing more than multiplications and additions done in an extremely systematic way. If you look at Equations (4.4), you can see that the order in which the **a** terms occur is that same as in the matrix in Equation (4.2). In each equation, you can see that the subscript of the **v** terms varies from 1 to 2 to 3; In fact, the subscript of the **v** term in each equation matches the second subscript of the **a** term that multiplies it. In Equation (4.5), you'll notice that the subscripts of **a** appear "flipped" relative to the **a** subscripts in (4.4). In technical terms, the matrix **a** has been ***transposed***. The reason for the systematic variation in subscripts is because Equations (4.4) and (4.5) represent matrix multiplications.

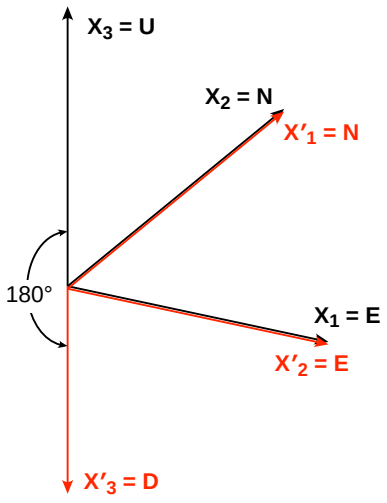


**Figure 4.4 — The transformation from ENU (a map coordinate system) to NED (structural geology coordinate system).**

### *A Simple Coordinate Transformation*

There is a coordinate transformation that we already know how to do but, nonetheless it is illustrative to see that it works as expected: the transformation from an ENU to a NED coordinate system. It is simple because all the angles involved are 0, 90, or 180° but important because it is a transformation that we do frequently. The geometry is shown in Figure 4.4. You can see that, for example $\theta_{11} = 90°$, $\theta_{12} = 0°$, and $\theta_{13} = 90°$. Writing it out in the form of the matrix, we have:

$$a_{ij} = \begin{pmatrix} \cos 90 & \cos 0 & \cos 90 \\ \cos 0 & \cos 90 & \cos 90 \\ \cos 90 & \cos 90 & \cos 180 \end{pmatrix}$$

This simplifies to:

$$a_{ij} = \begin{pmatrix} 0 & 1 & 0 \\ 1 & 0 & 0 \\ 0 & 0 & -1 \end{pmatrix} \tag{4.6}$$

When we use this transformation matrix in Equation 4.4, we get:

$$v'_1 = v_2; \quad v'_2 = v_1; \quad v'_3 = -v_3 \tag{4.7}$$

## Structural Geology Applications of Transformations

The equations (4.4) and (4.5) give us some real power to solve interesting problems in structural geology. In all of these problems, the key is determining what the transformation matrix, **a**, looks like and that is where we will spend most of our time, below. As a general rule, ***the components of the transformation matrix are just equal to the direction cosines of the new axes in the old coordinate system***. Thus, we will be seeing combinations of the equations in Table 2.1 a lot. Most importantly, though, recall that the math required is nothing more than multiplications and additions done in a very systematic way.

### *Stratigraphic Map Thicknesses*

We start with a problem first introduced in the previous chapter: determination of the thickness of a geological unit from map data. The general method in-

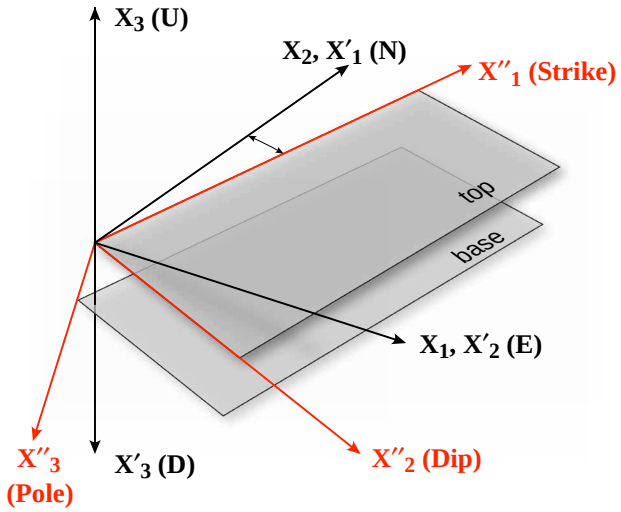


**Figure 4.5 — Diagram showing the coordinate transformation from an ENU to Strike-Dip-Pole (SDP) coordinate system. The thickness can be calculated from any point on the top and any point on the base of the bed by subtracting there $X'_3$ coordinates.**

troduced here (Allmendinger and Judge, 2013), like all methods to determine thickness assumes that the top and bottom surfaces of the bed are planar and parallel. Our basic approach will be a transformation into the bedding coordinate system where the strike is the first axis, the dip the second axis and the pole the third axis, an SDP system (Fig. 4.5). In this coordinate system, the thickness is just the difference between the $X''_3$ coordinate of a point on the top of the bed and $X''_3$ coordinate of any point on the base (not necessarily in the dip direction).

A slight wrinkle of this method is that the position vector of the points on the top and base of the bed are given in an ENU coordinate system but the direction cosines of the strike, the dip direction and the pole will be in a NED coordinate system (Fig. 4.5). Let's assume that the point (i.e., position vector) on the top has coordinates $[t_E, t_N, t_U]$ and the point on the base has coordinates $[b_E, b_N, b_U]$ in the ENU system. Our first step will be to transform that into the coordinates in a NED system as we have seen before. In the NED system the two vectors are:

$$\mathbf{t}' = [t_N \quad t_E \quad -t_U] \quad \text{and} \quad \mathbf{b}' = [b_N \quad b_E \quad -b_U]$$

Now we can use the direction cosines of the strike, dip and pole to construct the transformation matrix. The strike is our $X''_1$ axis so the first row of the transformation matrix will be its direction cosines in the NED system:

$$(\cos(strike)\cos(0) \quad \sin(strike)\cos(0) \quad \sin(0))$$

Recall that the strike is a horizontal line with a plunge of 0°. The second row of the transformation matrix are just the direction cosines of the dip and dip direction ($X''_2$) in an NED system (assuming strike in right hand rule format):

$$\begin{pmatrix}\cos(strike+90)\cos(dip) & \sin(strike+90)\cos(dip) & \sin(dip)\end{pmatrix}$$

Finally, the pole is the third axis of our new coordinate system, $X''_3$ and its direction cosines in the NED system are:

$$\begin{pmatrix}\cos(strike-90)\cos(90-dip) & \sin(strike-90)\cos(90-dip) & \sin(90-dip)\end{pmatrix}$$

Assembling all three rows of transformation matrix and making the necessary trigonometric simplifications, we get:

$$a_{ij}=\begin{pmatrix}\cos(strike) & \sin(strike) & 0\\ -\sin(strike)\cos(dip) & \cos(strike)\cos(dip) & \sin(dip)\\ \sin(strike)\sin(dip) & -\cos(strike)\sin(dip) & \cos(dip)\end{pmatrix} \tag{4.8}$$

Now we can transform the top position vector, $\mathbf{t'}$, in the NED coordinate system into the new bedding system (the bottom vector will look identical):

$$\begin{aligned}
t''_1 &= a_{11}t'_1 + a_{12}t'_2 + a_{13}t'_3\\
&= \cos(strike)t_N + \sin(strike)t_E + 0(-t_u)\\
t''_2 &= a_{21}t'_1 + a_{22}t'_2 + a_{23}t'_3\\
&= \left[-\sin(strike)\cos(dip)\right]t_N + \left[\cos(strike)\cos(dip)\right]t_E + \left[\sin(dip)\right](-t_u)\\
t''_3 &= a_{31}t'_1 + a_{32}t'_2 + a_{33}t'_3\\
&= \left[\sin(strike)\sin(dip)\right]t_N + \left[-\cos(strike)\sin(dip)\right]t_E + \left[\cos(dip)\right](-t_u)
\end{aligned} \tag{4.9}$$

The thickness is $t''_3 - b''_3$ so only the third line above matters and we can write the thickness as:

$$\begin{aligned}
t''_3 - b''_3 = &\left[\sin(strike)\sin(dip)\right](t_N - b_N) - \left[\cos(strike)\sin(dip)\right](t_E - b_E) +\\
&\left[\cos(dip)\right](b_U - t_U)
\end{aligned} \tag{4.10}$$

The order of $t$ and $b$ in the third term are reversed because it is really: $[-t_u - (-b_u)]$. To reemphasize, strike and dip must be in right hand rule format for this equation to work.

The spreadsheet solution to this problem is shown in Figure 4.6. The 3×3 block of numbers labeled "Transformation Matrix" are calculated using Equation 4.8. The actual transformation from NED to SDP coordinate system occurs in rows 14 and 15; you can see the formula for cell D15 expanded and color coded to show which values are being used. In those formulae, we use absolute cell references (i.e., the "$" signs) to the transformation matrix so their cell positions will not change when we copied the formulae from row 14 to row 15. Finally, note that because NED is positive downwards, we actually subtract the top from the base!

| | A | B | C | D | E | F |
|---|---|---|---|---|---|---|
| 1 | Surface | East | North | Up | Strike | Dip |
| 2 | Base | 28468.72 | 46068.41 | 6747.38 | 134 | 30 |
| 3 | Top | 27435.8 | 45581.94 | 6613.31 | | |
| 4 | | | | | | |
| 5 | | North | East | Down | | |
| 6 | Base (NED) | 46068.41 | 28468.72 | -6747.38 | | |
| 7 | Top (NED) | 45581.94 | 27435.8 | -6613.31 | | |
| 8 | | | | | | |
| 9 | Transformation | -0.6947 | 0.7193 | 0.0000 | | |
| 10 | Matrix | -0.6230 | -0.6016 | 0.5000 | | |
| 11 | | 0.3597 | 0.3473 | 0.8660 | | |
| 12 | | | | | | |
| 13 | SDP coord sys | X1 (strike) | X2 (dip) | X3 (pole) | | |
| 14 | Base(SDP) | -11523.12 | -49199.32 | 20614.04 | | |
| 15 | Top(SDP) | -11928.21 | -48207.83 | =$B$11*B7+$C$11*C7+$D$11*D7 | | |
| 16 | | | | | | |
| 17 | Thickness = | | | 417.62 | | |

**Figure 4.6 — The spreadsheet for calculating stratigraphic thickness using the Equations 4.6 and 4.7.**

## *Down-Plunge Projection*

As we saw in the previous Chapter, cylindrical folds have a profile plane that is perpendicular to the fold axis (Fig. 3.8). The profile plane contains the least distorted view of a cylindrically folded surface, known as a ***down-plunge projection***. Constructing down plunge projections by hand usually involves orthographic projection and can be particularly tedious, so much so that most structural geology lab manuals omit the 3D version entirely and instead only teach students how to do a two dimensional construction that assumes that the surface of the earth is flat!

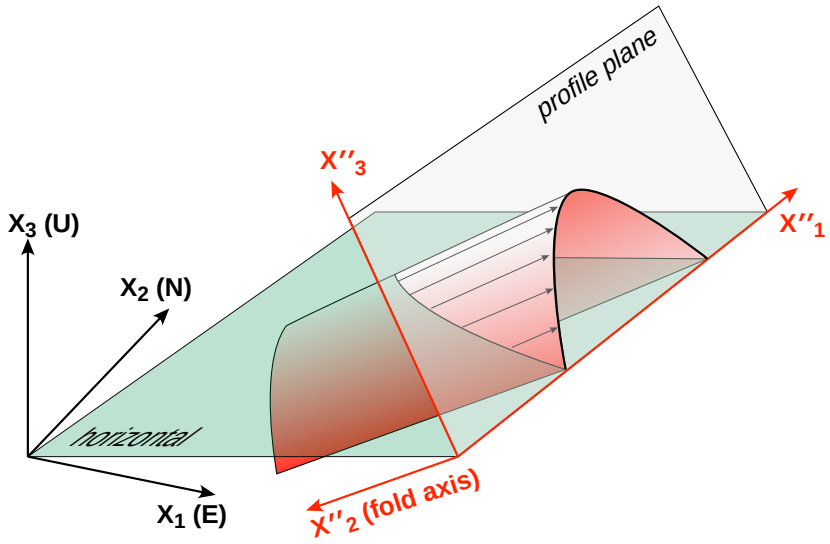


**Figure 4.7 — The two coordinate systems in the down plunge projection. See text for discussion.**

However, a full three dimensional down-plunge projection can be calculated using the transformation methods in this chapter.

The two coordinate systems are shown in Figure 4.7: the first is our usual geographic coordinate system East-North-Up. It makes sense to use a map coordinate system because the contacts that describe the bedding surfaces to be projected will be digitized from a geologic map. The second coordinate system is defined by the fold axis[2]. As before, if we want to use the trick that the direction cosines of the transformation matrix are just the direction cosines of the axes in NED given by Table 2.1, we first have to transform the position vectors of the digitized bed from ENU to NED, like we did in the previous example. Let's assume that a digitized point along a bedding surface has coordinates $x_1$, $x_2$, $x_3$ in an ENU coordinate system. Our first transformation using Equation (4.7) gives us:

$$x'_1 = x_2; \quad x'_2 = x_1; \quad x'_3 = -x_3 \tag{4.11}$$

The second transformation matrix will be based on the trend and plunge of the fold axis (X″$_2$), TFA and PFA, respectively. As you can work out from Figure 4.7, the trend and plunge of X″$_1$ will be (TFA+90), 0 and the trend and plunge of X″$_3$ will be TFA, PFA-90. The plunge of X″$_3$ will be negative because the arrow points

[2] The derivation that we do here is different from that in Allmendinger et al. (2012), including the numbering of the axes. In Allmendinger et al., they derive a single transformation from ENU directly to the fold coordinate system. Here we use an easier to follow two step transformation in which the fold axis is the X″$_2$ axis, not the X′$_3$ axis.

upwards in a NED coordinate system. Now, we can use the equations in Table 2.1 to construct the second transformation matrix from NED to the fold coordinate system. Without bothering with the intermediate steps, it is:

$$b_{ij} = \begin{pmatrix} \cos(TFA+90)\cos(0) & \sin(TFA+90)\cos(0) & \sin(0) \\ \cos(TFA)\cos(PFA) & \sin(TFA)\cos(PFA) & \sin(PFA) \\ \cos(TFA)\cos(PFA-90) & \sin(TFA)\cos(PFA-90) & \sin(PFA-90) \end{pmatrix}$$

$$b_{ij} = \begin{pmatrix} -\sin(TFA) & \cos(TFA) & 0 \\ \cos(TFA)\cos(PFA) & \sin(TFA)\cos(PFA) & \sin(PFA) \\ \cos(TFA)\sin(PFA) & \sin(TFA)\sin(PFA) & -\cos(PFA) \end{pmatrix} \tag{4.12}$$

The second transformation is then

$$x_i'' = b_{ij}x_j' \tag{4.13a}$$

$$\begin{aligned} x_1'' &= b_{11}x_1' + b_{12}x_2' + b_{13}x_3' \\ x_2'' &= b_{21}x_1' + b_{22}x_2' + b_{23}x_3' \\ x_3'' &= b_{31}x_1' + b_{32}x_2' + b_{33}x_3' \end{aligned} \tag{4.13b}$$

Where $x_i''$ is the coordinate of a point on a digitized bed in fold coordinates, $x_j'$ is the coordinate of the same point in NED coordinate system which was transformed from its original ENU coordinates via Equation. 4.11.

To implement these equations, you will first need to digitize some contacts, specifying an East coordinate, a North coordinate, and an elevation for each vertex of the polygon drawn along the contact. A program like GMDE makes the process relatively painless and will also show you what your calculated projection should look like. Then, you will import the coordinates of your digitized polygon along the bedding contact into a spreadsheet program (Fig. 4.8). The fold axis — presumably determined by constructing a π-diagram (Fig. 3.9b) — must also be entered. The first transformation (Fig. 4.8) follows Equation 4.11; the transformation matrix comes from Equation 4.12 and the actual transformation from Equation 4.13. Notice in the spreadsheet in Figure 4.8 that the equations implementing the second transformation should have absolute cell references to the transformation matrix.

| | A | B | C | D | E | F | G | H | I | J | K | L | M |
|---|---|---|---|---|---|---|---|---|---|---|---|---|---|
| 1 | Original Contact | | | First Transformation | | | Second Transformation | | | | Fold Axis Trend = | | 125 |
| 2 | East | North | Up | North | East | Down | X''(1) | X''(2) FA | X''(3) | | Fold Axis Plunge = | | 27 |
| 3 | 1232.845 | 46361.63 | 7092.539 | 46361.63 | 1232.845 | -7092.539 | -38684.355 | -26013.72 | -5294.5096 | | | | |
| 4 | 1399.445 | 46261.67 | 7062.455 | 46261.67 | 1399.445 | -7062.455 | -38698.03 | -25827.38 | -5233.3288 | | Transformation Matrix | | |
| 5 | 1606.03 | 46128.39 | 6962.905 | 46128.39 | 1606.03 | -6962.905 | -38707.346 | -25563.291 | -5210.4963 | | -0.819152 | -0.5735764 | 0 |
| 6 | 1765.967 | 46001.77 | 6898.733 | 46001.77 | 1765.967 | -6898.733 | -38695.361 | -25352.714 | -5175.2238 | | -0.5110603 | 0.72986982 | 0.4539905 |
| 7 | 1985.88 | 45895.15 | 6964.376 | 45895.15 | 1985.88 | -6964.376 | -38734.16 | -25167.518 | -5007.189 | | -0.2603983 | 0.37188725 | -0.8910065 |
| 8 | 2199.129 | 45755.2 | 6938.845 | 45755.2 | 2199.129 | -6938.845 | -38741.834 | -24928.76 | -4914.19 | | | | |
| 9 | 2359.065 | 45655.24 | 6931.239 | 45655.24 | 2359.065 | -6931.239 | -38751.687 | -24757.489 | -4835.4594 | | | | |
| 10 | 2565.65 | 45528.62 | 6883.64 | 45528.62 | 2565.65 | -6883.64 | -38766.459 | -24520.389 | -4768.0724 | | | | |
| 11 | 2792.227 | 45408.67 | 6793.16 | 45408.67 | 2792.227 | -6793.16 | -38798.16 | -24252.639 | -4733.1948 | | | | |
| 12 | 2992.148 | 45302.05 | 6720.477 | 45302.05 | 2992.148 | -6720.477 | -38825.492 | -24019.236 | -4695.8441 | | | | |
| 13 | 3205.396 | 45188.76 | 6651.309 | 45188.76 | 3205.396 | -6651.309 | -38855.005 | -23774.293 | -4648.6686 | | | | |
| 14 | 3365.333 | 45128.78 | 6605.448 | 45128.78 | 3365.333 | -6605.448 | -38897.608 | -23606.086 | =$K$7*D14+$L$7*E14+$M$7*F14 | | | | |
| 15 | 3598.574 | 45075.47 | 6545.818 | 45075.47 | 3598.574 | -6545.818 | -38987.721 | -23381.534 | -4566.9433 | | | | |
| 16 | 3851.807 | 45042.15 | 6515.746 | 45042.15 | 3851.807 | -6515.746 | -39105.675 | -23166.026 | -4490.8871 | | | | |
| 17 | 4018.408 | 44988.84 | 6458.07 | 44988.84 | 4018.408 | -6458.07 | -39157.564 | -22991 | -4466.4382 | | | | |
| 18 | 4145.024 | 44902.21 | 6411.583 | 44902.21 | 4145.024 | -6411.583 | -39159.225 | -22833.209 | -4438.2132 | | | | |
| 19 | 4191.672 | 44788.92 | 6405.115 | 44788.92 | 4191.672 | -6405.115 | -39093.18 | -22738.327 | -4397.1279 | | | | |

**Figure 4.8 — Part of the spreadsheet for doing a down-plunge projection. The first transformation switches from ENU to NED, and the second changes from NED to the fold coordinate system defined by the fold axis.**

To see your down-plunge projection in the spreadsheet, select the columns G and I, representing coordinates along the $X''_1$ and $X''_3$ axes respectively, and choose scatter plot (you can do non-contiguous selections in most programs using the command key rather than the shift key). The plot will probably be distorted because spreadsheet programs to do not try to scale the two axes equally. Thus you will have to, either by hand or using the chart dialog box, adjust the scales so that they are equal.

## *Rotations*

Rotations are a way of life in structural geology because we frequently want to restore some feature to its initial, pre-deformation orientation: What direction did the current flow prior to tilting of bedding? How can well tell whether magnetic vectors were imprinted on the rock before folding or after? What orientation was the dike when it was intruded? These questions have been answered for decades by using a stereonet with paper and pencil. Rotations done in this manner are straightforward when the rotation is about a horizontal axis (e.g., returning dipping bedding to horizontal) but rotations about inclined axes require breaking the rotation up into two or more separate rotations. Computer stereonets, of course, do rotations completely differently and thus do not suffer any of the limitations of paper stereonets. Let's see how computers accomplish this task.

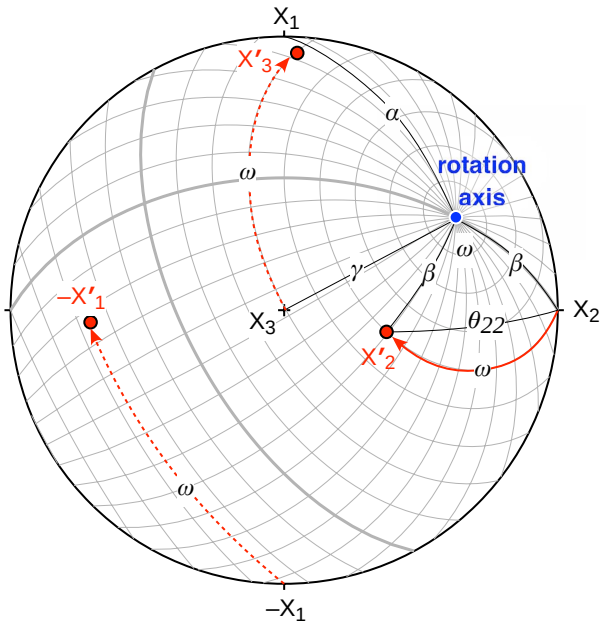


**Figure 4.9 — Rotation as a coordinate transformation. The old axes are NED and the new coordinate axes are shown in red. The rotation axis orientation is defined by the angles that it makes with the NED axes; the magnitude of rotation is $\omega$. Note that the rotation angles are defined along small circles centered on the rotation axis whereas the angles between axes such as $\theta_{22}$ are measured along great circles.**

Given its appearance in this Chapter, it should come as no surprise that most computer programs use coordinate transformations for rotations. The type of transformation, though, is a bit more complicated to derive than in previous examples because the rotation axis does not coincide with either the new or the old coordinate system. The old coordinates, of course, are our NED coordinate system, but we do not know a priori what the orientations of the new axes will be; we have to calculate them.

Figure 4.9 shows the angular relations involved. The stereonet grid has been repositioned to be centered on the rotation axis. All points will move parallel to the small circles in this projection. The givens are the orientation of the rotation axis, specified in terms of the angles $\alpha$, $\beta$, and $\gamma$ that it makes with North, East, and Down, respectively, and the magnitude of the rotation, $\omega$. As shown (Fig. 4.9), the amount of rotation and the angle between new and old axes are different things. From those values, the direction cosines of the transformation matrix must be calculated. Here, we'll just give you the matrix; the derivations are not particularly difficult but are tedious to follow. You can find the derivation in terms of spherical trigonometry in Allmendinger et al. (2012) and in terms of matrix multiplications in any linear algebra textbook.

The following equations (4.14) comprise the transformation matrix for a general rotations:

$$
\begin{aligned}
a_{11} &= \cos\omega + \cos^2\alpha\,(1-\cos\omega)\\
a_{12} &= -\cos\gamma\,\sin\omega + \cos\alpha\,\cos\beta\,(1-\cos\omega)\\
a_{13} &= \cos\beta\,\sin\omega + \cos\alpha\,\cos\gamma\,(1-\cos\omega)\\
a_{21} &= \cos\gamma\,\sin\omega + \cos\beta\,\cos\alpha\,(1-\cos\omega)\\
a_{22} &= \cos\omega + \cos^2\beta\,(1-\cos\omega)\\
a_{23} &= -\cos\alpha\,\sin\omega + \cos\beta\,\cos\gamma\,(1-\cos\omega)\\
a_{31} &= -\cos\beta\,\sin\omega + \cos\gamma\,\cos\alpha\,(1-\cos\omega)\\
a_{32} &= \cos\alpha\,\sin\omega + \cos\gamma\,\cos\beta\,(1-\cos\omega)\\
a_{33} &= \cos\omega + \cos^2\gamma\,(1-\cos\omega)
\end{aligned}
\tag{4.14}
$$

These equations are put into practice in the spreadsheet in Figure 4.10: (a) enter the trend and plunge of the lines to be rotated as well as the rotation axis and the magnitude of the rotation (columns A and B). (b) Calculate the direction cosines of those lines and the rotation axis (columns C, D, E). (c) Calculate the transformation matrix (F14-H16) using the Equations (4.14), above. Don't forget that you have already calculated the cos$\alpha$, cos$\beta$, cos$\gamma$ for the rotation axis so you do not need to do that again! Although it is not necessary, a quick check on your equations is to calculate the magnitude of the vector in each row of the transformation matrix; as

| | A | B | C | D | E | F | G | H | I | J |
|---|---|---|---|---|---|---|---|---|---|---|
| 1 | Original Orientation | | direction cosines | | | direction cosines (rotated) | | | rotated orientation | |
| 2 | Trend | Plunge | cos(alpha) | cos(beta) | cos(gamma) | cos(alpha) | cos(beta) | cos(gamma) | Trend | Plunge |
| 3 | 56 | 22 | 0.5185 | 0.7687 | 0.3746 | 0.2363 | 0.9706 | 0.0453 | 76.3 | 2.6 |
| 4 | 14 | 67 | 0.3791 | 0.0945 | 0.9205 | 0.6285 | 0.4500 | 0.6344 | 35.6 | 39.4 |
| 5 | 21 | 31 | 0.8002 | 0.3072 | 0.5150 | 0.7195 | 0.6912 | 0.0682 | 43.8 | 3.9 |
| 6 | 40 | 56 | 0.4284 | 0.3594 | 0.8290 | 0.5183 | 0.6833 | 0.5144 | 52.8 | 31.0 |
| 7 | 72 | 61 | 0.1498 | 0.4611 | 0.8746 | 0.2661 | 0.6864 | 0.6768 | 68.8 | 42.6 |
| 8 | 36 | 41 | 0.6106 | 0.4436 | 0.6561 | 0.5620 | 0.7812 | 0.2720 | 54.3 | 15.8 |
| 9 | 47 | 23 | 0.6278 | 0.6732 | 0.3907 | 0.3726 | 0.9279 | 0.0151 | 68.1 | 0.9 |
| 10 | 63 | 52 | 0.2795 | 0.5486 | 0.7880 | 0.2996 | =$F$15*C10+$G$15*D10+$H$15*E10 | | | 32.3 |
| 11 | | | | | | | | | | |
| 12 | Rotation Axis | | | | | | | | | |
| 13 | Trend | Plunge | | | | Transformation Matrix | | | Magnitude | |
| 14 | 110 | 41 | -0.2581 | 0.7092 | 0.6561 | 0.8121 | -0.4317 | 0.3927 | 1 | |
| 15 | Magnitude = | 37 | | | | 0.3580 | 0.8999 | 0.2490 | 1 | |
| 16 | | | | | | -0.4609 | -0.0617 | 0.8853 | 1 | |

**Figure 4.10 — Spreadsheet to rotate the eight lines in rows 3-10. See Text for discussion**

shown in I14-I16, they should all be equal to 1. (d) Transform the direction cosines in columns C-E to the rotated direction cosines in columns F-H using the transformation matrix. As you can see from the exposed formula, be sure to use absolute cell references. (e) Finally, convert your rotated direction cosines back to trend and plunge (columns I, J) using Equations (2.11).

## Summary

This chapter covers a hugely important technique — transformations — and the illustrations here only scratch the surface of what you can do with this approach. The theory is easy to grasp in two dimensions and the extension to three dimensions is straightforward. One only needs to be very systematic in making sure that the subscripts are in the correct order and apply to the axes we think they apply to. Most importantly, the subscripts always apply to a specific coordinate axis. Understanding this will help us a lot when we get to stress and strain. Finally, although the approach is very systematic and logical, the math is very simple: just multiplication and additions, something that you have know how to do since middle school!

# Exercises—Chapter 4

Once again, these exercises rely heavily on the program GeolMapDataExtractor (GMDE) and a digital copy of the Poker Peak geologic map from the US Geological Survey (Albee and Cullens, 1975). GMDE, in either Macintosh or Windows version can be downloaded from:

http://www.geo.cornell.edu/geology/faculty/RWA/programs/strikedipthickness.html

And the Poker Peak Quadrangle map can be downloaded from the web site. GMDE will allow you to make quick accurate measurements on the map. Note that you will need an Internet connection for the program to get elevations automatically. For Exercises 1 and 2,you will also need a copy of Google Earth, which you can download for free from:

http://www.google.com/earth/download/ge/agree.html

1. Open the Poker Peak Quad in GMDE and make sure it is georeferenced (it should automatically be unless you have separated the .jpg file of the map from the .txt file of the same name (the .txt file contains the georeferencing information.) Locate the part of the map shown to the right. Notice that a fault is shown offsetting the stratigraphic units.

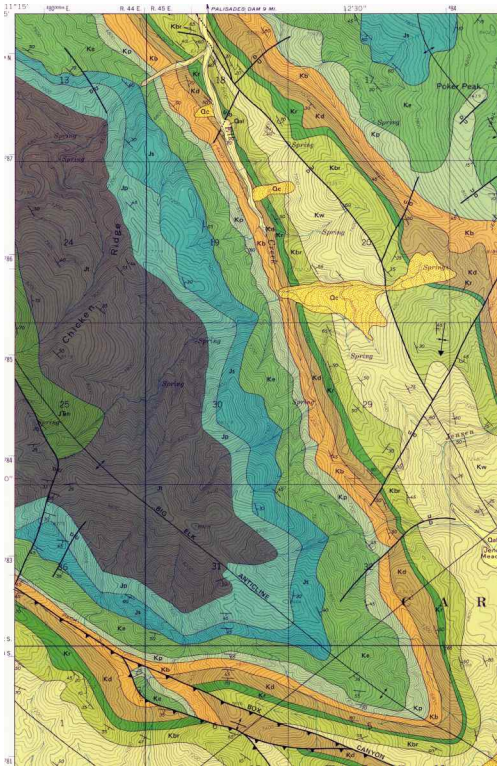


   (a) Digitize the tops of the following contacts all the way around the fold: Jn, Jp, Js, Ke, Kp, Kb, Kd.

   (b) Save the contacts as a text file (File>Save Data>Digitized Contacts), and then Save the contacts as .kml file (File>Export KML>Contacts).

   (c) Open the file you just saved in a spreadsheet program. Use the coordinate and vector transformation that we derived in class, and the fold axis that you determined last week, to produce a down-plunge projection of the Big Elk an-

ticline. Beside to adjust the scales of the two axes so they are approximately the same.

(d) Open the KML file in Google Earth and rotate the image around so that you see the same down plunge projection that you produced in your spreadsheet. Capture a screen shot in Google Earth and turn in with your spreadsheet.

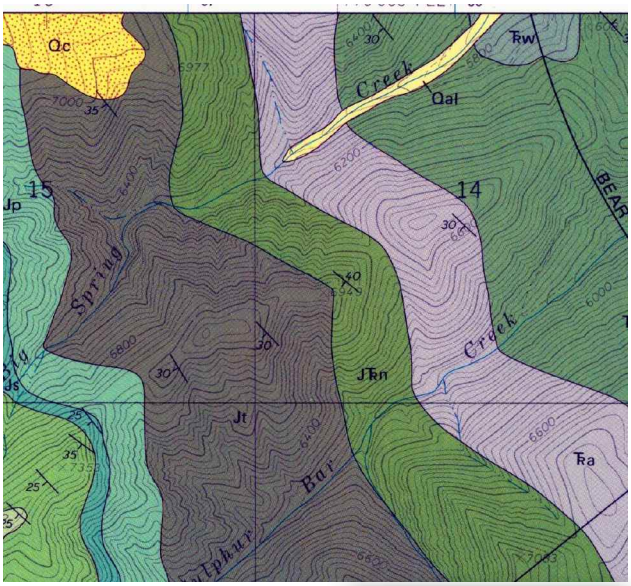


2. Back to the NE corner of the Poker Peak Quad: find, again the ridge shown to the right in GMDE. In this question, we will determine the thickness of the following units using a coordinate transformation: Tra, JTRn, and Jt.

(a) In GMDE, select Settings>Mode>Strike Dip Thickness. GMDE can and will calculate the thickness for you (which you can use as a check on your calculations), but for this problem, we are mostly interested in using the program to get accurate coordinates for two points, one on the top surface and one on the bottom surface. We will just use the strike and dip information measured by the field geologist for this problem.

(b) Once your have determined the coordinates of the points at the top and bottom of each surface, in a spreadsheet program, calculate the thickness of each unit using a coordinate transformation from geographic coordinates to bedding plane coordinates.

3. Using the transformation matrix for rotations about an arbitrary axis (equations 4.14) rotate the data to the right by a magnitude of 56° about an axis that has a trend and plunge of 113, 29. You should do the rotation in a spreadsheet. You may check your answer in a Stereonet Program.

| Trend | Plunge |
|---|---|
| 113 | 73 |
| 76 | 78 |
| 175 | 71 |
| 229 | 62 |
| 75 | 62 |
| 111 | 77 |
| 78 | 85 |
| 316 | 53 |
| 25 | 78 |
| 21 | 57 |
| 81 | 77 |
| 80 | 58 |
| 58 | 62 |
| 40 | 57 |
| 42 | 71 |
| 229 | 23 |
| 110 | 72 |
| 278 | 61 |
| 264 | 78 |

 

# Chapter 5

## *The Orientation and Stress Tensors*

### Introduction

The topic of tensors typically produces significant anxiety for students of structural geology. That is due, at least in part, to the fact that the term is studiously avoided until it is sprung on the student when introducing the topic of stress, thus conflating two difficult to grasp concepts. In our case, the previous chapters have already introduced the concept of vectors as a type of ***first order tensor*** so the

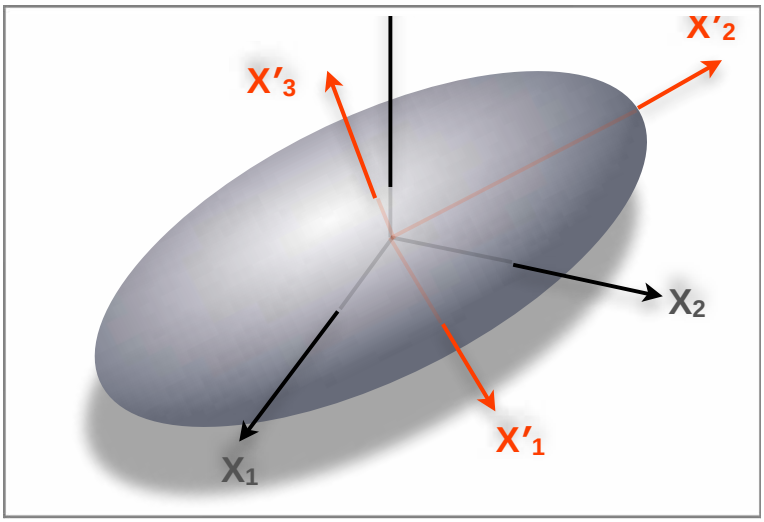


fundamental definition — an entity that can be transformed from one coordinate system to another, changing its components in predictable ways such that its fundamental nature doesn't change — is already understood on an intuitive level. In the case of our vector, it has the same magnitude and orientation on the page regardless of the orientation of the coordinate axes (Fig. 4.3). We are now fully prepared to tackle ***second order tensors***, which will allow us to quantify the relations between different families of vectors. These second order tensors will take us to the very core of structural geology. We will still be doing just multiplication and additions (mostly), but first, we'll need to introduce some concepts about matrices.

# Matrices and Indicial Notation

In the last chapter, we saw that the transformation of a vector could be described with three simple equations (4.4), repeated here:

$$\begin{aligned} v'_1 &= a_{11}v_1 + a_{12}v_2 + a_{13}v_3 \\ v'_2 &= a_{21}v_1 + a_{22}v_2 + a_{23}v_3 \\ v'_3 &= a_{31}v_1 + a_{32}v_2 + a_{33}v_3 \end{aligned} \tag{5.1}$$

As was pointed out at the time, the subscripts in these equations, all of which refer to specific coordinate axes, vary in an extremely systematic and precise way. That is because these equations are an alternative way of writing down a ***matrix multiplication***:

$$\mathbf{v}' = \mathbf{a}\mathbf{v} = \begin{bmatrix} v'_1 \\ v'_2 \\ v'_3 \end{bmatrix} = \begin{pmatrix} a_{11} & a_{12} & a_{13} \\ a_{21} & a_{22} & a_{23} \\ a_{31} & a_{32} & a_{33} \end{pmatrix} \begin{bmatrix} v_1 \\ v_2 \\ v_3 \end{bmatrix} \tag{5.2}$$

Note that the subscripts of the matrix a vary in exactly the same way as the subscripts, or indices, of $a_{ij}$ in (5.1). Equation (5.2) works because there are the same number of columns of **a** as there are rows of **v**. For this reason, you **cannot** write the left side of the equation as ~~$\mathbf{v}' = \mathbf{v}\mathbf{a}$~~ because **v** has only one column but **a** has three rows. That is, matrix multiplication is ***non-commutative***: the order of the multiplication matters. This will be an extremely important insight when we come to finite strain in a few more chapters; strain is mathematically represented as a matrix multiplication so the order in which strain is superimposed determines the final outcome.

Matrix multiplication gives us another way to write the dot product of two vectors, where we use the ***transpose*** of one of the vectors (i.e., one of the vectors is "flipped"):

$$\mathbf{u} \cdot \mathbf{v} = \mathbf{u}\mathbf{v}^{\mathbf{T}} = \begin{bmatrix} u_1 & u_2 & u_3 \end{bmatrix} \begin{bmatrix} v_1 \\ v_2 \\ v_3 \end{bmatrix} = u_1v_1 + u_2v_2 + u_3v_3 \tag{5.3}$$

You can imagine that it gets pretty tedious to keep writing out the equations in (5.1) or the right side of (5.2) and the bold text on the left side of (5.2), known as matrix notation, is one type of shorthand. There is a second type of shorthand, known as the ***summation convention***, that is more convenient, especially when it comes to implementing these equations in a programing language. Using the summation convention, we would write Equations (5.1) and (5.2) as:

$$v_i' = a_{ij} v_j \tag{5.4}$$

Let's break this down and see how it works. As we have already seen $i$ and $j$ can vary from 1 to 3 in value because there are three axes to our Cartesian coordinate system. There is one $i$ one each side of the equation and it is referred to as the ***free suffix***; that means there will be three equations and, in each, $i$ will have a constant value. The index $j$ is known as the ***dummy suffix*** and appears twice on the right hand side, only, of Equation (5.4). Thus, the summation occurs with respect to $j$ in each of the three equations as shown in the following equation:

$$v_i' = \sum_{j=1}^{3} a_{ij} v_j = a_{i1} v_1 + a_{i2} v_2 + a_{i3} v_3 \tag{5.5}$$

The "recipe" for the summation convention takes a little practice but it turns out to be quite powerful and so is worth learning.

We will encounter various properties of matrices in the subsequent chapters but for right now, we'll wrap up with three important terms: a matrix is ***symmetric*** if there are six independent values and the three off-diagonal components above the principal diagonal are the same as the three below the principal diagonal (Fig. 5.1). That is, $T_{12} = T_{21}$, $T_{13} = T_{31}$, and $T_{23} = T_{32}$. If a matrix is ***asymmetric*** then there are nine independent components and $T_{12} \neq T_{21}$, $T_{13} \neq T_{31}$, and $T_{23} \neq T_{32}$. Finally, a matrix can be ***antisymmetric*** with three independent components where the values along the principal diagonal are all zeros and $T_{12} = -T_{21}$, $T_{13} = -T_{31}$, and $T_{23} = -T_{32}$.

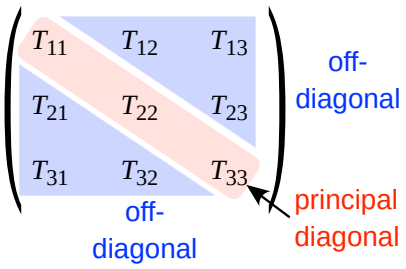


**Figure 5.1 — Anatomy of a 3 × 3 matrix.**

# Tensors

In this Chapter, when we use the term "tensors", we are specifically referring to second order or second rank tensors. All tensors can be expressed as matrices (a 3 × 3 matrix in the case of second order tensors) but ***not all matrices are tensors***. In order to be a tensor, the matrix must represent an entity or quantity that transforms like a tensor; that is, the components must change in a logical and systematic way during a coordinate transformation. Note that the transformation matrix, **a**, is itself not a tensor! A common convention is that tensors are written with brackets, [ ], whereas matrices that are not tensors are written with parentheses, ( ). We used this convention, for example, in Equation (5.2). Because all tensors can be written as matrices, they can be symmetric, asymmetric, etc., and any operation that can be performed on a matrix can likewise be performed on a tensor.

## *Tensors as Linear Vector Operators*

The best way to think of a second order tensor is that it relates two families of vectors. In the case of stress, discussed later in this chapter, the stress tensor relates the stress vector (or traction) on a plane to the orientation of the plane. In the case of strain, as we shall see in a subsequent chapter, the displacement gradient tensor (one of many tensors related to strain!) relates the position vector of a point to the displacement of the point during a deformation. If we know the stress tensor, we can calculate the stress vector on a plane of any orientation within a body. You can imagine that this is hugely important in any study of earthquakes, induced seismicity, faulting, etc. Likewise, with the displacement gradient tensor, we can calculate how all points within a body are displaced as a function of position during a deformation.

The basic way that this relationship is written is as follows:

$$u_i = T_{ij} v_j \tag{5.6a}$$

Where **u** and **v** are generic vectors and **T** a generic tensor that relates the two vectors. This equation expands following the rules of summation or tensor notation:

$$\begin{bmatrix} u_1 \\ u_2 \\ u_3 \end{bmatrix} = \begin{bmatrix} T_{11} & T_{12} & T_{13} \\ T_{21} & T_{22} & T_{23} \\ T_{31} & T_{32} & T_{33} \end{bmatrix} \begin{bmatrix} v_1 \\ v_2 \\ v_3 \end{bmatrix} \tag{5.6b}$$

$$\begin{aligned} u_1 &= T_{11}v_1 + T_{12}v_2 + T_{13}v_3 \\ u_2 &= T_{21}v_1 + T_{22}v_2 + T_{23}v_3 \\ u_3 &= T_{31}v_1 + T_{32}v_2 + T_{33}v_3 \end{aligned} \tag{5.6c}$$

You already know how to do this expansion because it looks a lot like Equations (5.1-5.3). All of these equations represent the multiplication of a 3 × 3 and a 3 × 1 matrix. Beyond this mathematical similarity, they are entirely different. First, in Equation (5.1) it is the same vector, **v**, on both sides of the equation whereas **u** and **v** are two entirely different vectors in Equation (5.6). Secondly, **T** is a tensor as shown by the brackets in (5.6b), whereas **a** in Equation (5.2) is not.

There is a second way to make a second order tensor out of two vectors by taking the ***dyad (tensor) product*** of those two vectors. In indicial notation, we can write:

$$\mathbf{T} = \mathbf{u} \otimes \mathbf{v} = \mathbf{u}^{\mathbf{T}}\mathbf{v} \quad \text{or} \quad T_{ij} = u_i v_j \tag{5.7a}$$

The right hand side of (5.7) does not involve any summation because there is no dummy (i.e., repeated) suffix. So **T** simply works out to:

$$T_{ij} = \begin{bmatrix} u_1v_1 & u_1v_2 & u_1v_3 \\ u_2v_1 & u_2v_2 & u_2v_3 \\ u_3v_1 & u_3v_2 & u_3v_3 \end{bmatrix} \tag{5.7b}$$

The dyad product has important applications in earthquake and faulting studies and also in constructing the orientation tensor as we shall see below. This is just one example of the magic of matrix multiplication: $\mathbf{uv^T}$ (eqn. 5.3) give you a scalar whereas $\mathbf{u^Tv}$ (eqn. 5.7) yields a second order tensor!

## *Principal Axes of a Tensor*

Because our second order tensor is, well, a tensor, we can rotate the axes of the coordinate system and the values of the tensor will change. It turns out that, for

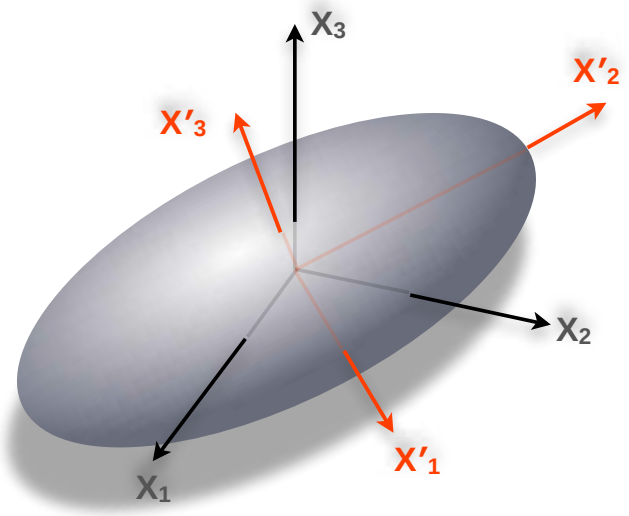


**Figure 5.2 — The magnitude ellipsoid of a tensor and two different coordinate axes through the ellipsoid. The red, primed coordinate system coincides with the principal axes of the ellipsoid. In that coordinate system, we can define the principal axes of the tensor.**

symmetric tensors, there is one set of axes where all the off-diagonal components will be zero and there will only be values along the principal diagonal. Because symmetric tensors can be represented by ellipsoids, this special set of axes occurs when the coordinate system is aligned with the principal axes of the ellipsoid (Fig. 5.2). Not surprisingly, these are called the ***principal axes of the tensor*** and, ***when referring to magnitude and not orientation***, are labeled from largest to smallest $T_1$, $T_2$, and $T_3$. For the magnitude ellipsoid shown in Figure 5.2 we would write:

$$T_{ij}' = \begin{bmatrix} T_{11}' & 0 & 0 \\ 0 & T_{22}' & 0 \\ 0 & 0 & T_{33}' \end{bmatrix} = \begin{bmatrix} T_2 & 0 & 0 \\ 0 & T_1 & 0 \\ 0 & 0 & T_3 \end{bmatrix} \tag{5.8}$$

The magnitude does not have to coincide with the number of the same axis! In figure 5.2, the long axis of the magnitude ellipsoid is parallel to the $X'_2$ axis. Double subscripts and the position in the matrix always refer to the coordinate system axes and not to the magnitude. Thus, in this example, $T'_{22} = T_1$.

The transformation from a random coordinate system to one where the axes are parallel to the principal axes is usually determined numerically by solving the ***eigenvalue*** problem. The derivation and solution to the eigenvalue problem is be-

yond the scope of this manual; see Allmendinger et al. (2012) or any book on Linear Algebra. The mathematical procedure gives us a cubic polynomial:

$$\lambda^3 - I\lambda^2 - II\lambda - III = 0 \tag{5.9}$$

The three roots of $\lambda$ are the three eigenvalues, which correspond to the magnitudes of the three principal axes. Once one has the eigenvalues you can calculate the ***eigenvectors***, which give the orientations of the three principal axes. The three coefficients, I, II, and III are known as the ***invariants*** of the tensor and they turn out to have important physical significance in many cases. Their values are:

$$\begin{aligned} I &= T_{11} + T_{22} + T_{33} + = T_1 + T_2 + T_3 \\ II &= \frac{\left(T_{ij}T_{ij} - I^2\right)}{2} = -\left(T_1T_2 + T_2T_3 + T_3T_3\right) \\ III &= \det T = \left|T_{ij}\right| = T_1T_2T_3 \end{aligned} \tag{5.10}$$

Where $\det T = \left|T_{ij}\right|$ is the ***determinant*** of tensor **T**. The significance of the invariants is that they have the same values in *any* coordinate system. When we say that the fundamental nature of a second rank tensor doesn't change upon transformation, we are referring to the invariants.

### *Tensor Transformations and the Mohr's Circle*

Given that we just mentioned tensor transformations, how does one go about transforming a tensor? In principle, it is similar to a vector transformation: if we have a transformation matrix and a tensor in the old coordinate system, we can calculate the same tensor in the new system. However, it is more involved because a second order tensor is a more complicated entity than a first order tensor (i.e., a vector). The derivation of the tensor transformation equation is relatively straightforward; you can find it in Nye (1959), Allmendinger et al. (2102), or a variety of other sources. Here it is using the summation convention, yielding the new tensor in terms of the old:

$$T_{ij}' = a_{ik}a_{jl}T_{kl} \tag{5.11}$$

This equation looks complicated and it does represent nine equations with nine terms each! The expansion is not so much complex as it is tedious. Here, for example is the expansion of one of the nine terms:

$$T_{13}' = \begin{array}{ccc} (l=1) & (l=2) & (l=3) \\ a_{11}a_{31}T_{11} + a_{11}a_{32}T_{12} + a_{11}a_{33}T_{13} & & (k=1) \\ +a_{12}a_{31}T_{21} + a_{12}a_{32}T_{22} + a_{12}a_{33}T_{23} & & (k=2) \\ +a_{13}a_{31}T_{31} + a_{13}a_{32}T_{32} + a_{13}a_{33}T_{33} & & (k=3) \end{array} \tag{5.12}$$

Don't worry! You're not going to be asked to expand these equations. This type of systematic equation is what computers live for and nobody solves these by hand anymore. If you ever want to impress your friends (uh… sure), the parenthetical statements in Equation (5.12) show you how $k$ and $l$ vary systematically. With the single equation arranged the way it is, you can see that $k$ increments by one in each row whereas $l$ increments by 1 in each column.

Long before there were computers to do these calculations for us, in the late 1800s a German engineer by the name of Otto Mohr introduced a clever graphical solution to a common, but special case of tensor transformation which has become known as ***Mohr's Circle***. In the Mohr construction, the old coordinate system is parallel to the principal axes of the tensor. The coordinate system is then transformed by rotating by θ° about one of the principal axes, commonly $T_2$ (Fig. 5.3). Thus the initial form of the tensor in the old coordinate system is:

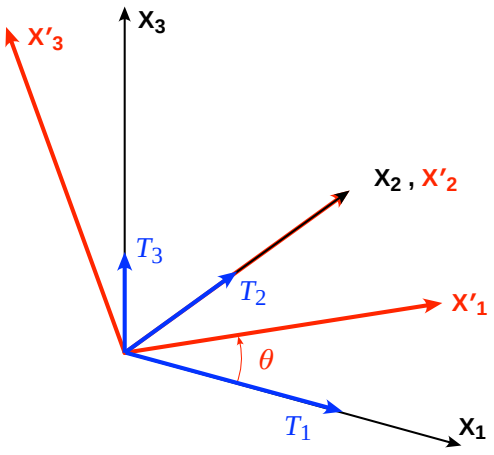


**Figure 5.3 — The coordinate transformation involved in constructing Mohr's circle for a generic tensor, T, by rotating the coordinate system around the intermediate principal axis of the tensor**

$$T_{ij} = \begin{bmatrix} T_1 & 0 & 0 \\ 0 & T_2 & 0 \\ 0 & 0 & T_3 \end{bmatrix} \tag{5.13}$$

And the transformation matrix is:

$$\mathbf{a} = \begin{pmatrix} \cos\theta & \cos 90 & \cos(90-\theta) \\ \cos 90 & \cos 0 & \cos 90 \\ \cos(90+\theta) & \cos 90 & \cos 0 \end{pmatrix} = \begin{pmatrix} \cos\theta & 0 & \sin\theta \\ 0 & 1 & 0 \\ -\sin\theta & 0 & \cos\theta \end{pmatrix} \tag{5.14}$$

For example, expanding Equation (5.12) we get:

$$\begin{aligned} T_{ij}' &= \cos\theta\left(-\sin\theta\right)T_1 + \cos\theta\,(0)\,(0) + \cos\theta\cos\theta\,(0) \\ &\quad +(0)\left(-\sin\theta\right)(0) + (0)\,(0)\,T_{22} + (0)\cos\theta\,(0) \\ &\quad +\sin\theta\left(-\sin\theta\right)(0) + \sin\theta\,(0)\,(0) + \sin\theta\cos\theta T_3 \\ &= -\cos\theta\sin\theta T_1 + \sin\theta\cos\theta T_3 \\ &= \left(T_3 - T_1\right)\cos\theta\sin\theta \end{aligned}$$

The entire tensor, **T**, in the new coordinate system is:

$$T_{ij}' = \begin{bmatrix} \left(T_1\cos^2\theta + T_3\sin^2\theta\right) & 0 & \left(T_3 - T_1\right)\sin\theta\cos\theta \\ 0 & 1 & 0 \\ \left(T_3 - T_1\right)\sin\theta\cos\theta & 0 & \left(T_1\sin^2\theta + T_3\cos^2\theta\right) \end{bmatrix} \tag{5.15}$$

These equations can be put into a more useful form by substituting some common double angle formulae:

$$\sin 2\theta = 2\sin\theta\cos\theta; \quad \sin^2\theta = \frac{1-\cos 2\theta}{2}; \quad \cos^2\theta = \frac{1+\cos 2\theta}{2} \tag{5.16}$$

The coordinates of the tensor in the new coordinate system are:

$$
\begin{aligned}
T_{11}' &= \left(\frac{T_1 + T_3}{2}\right) + \left(\frac{T_1 - T_3}{2}\right)\cos 2\theta \\
T_{33}' &= \left(\frac{T_1 + T_3}{2}\right) - \left(\frac{T_1 - T_3}{2}\right)\cos 2\theta \\
T_{13}' &= T_{31}' = -\left(\frac{T_1 - T_3}{2}\right)\sin 2\theta
\end{aligned}
\tag{5.17}
$$

These equations are in the parametric form of a circle with

$$\text{center at: } \left(\frac{T_1 + T_3}{2}, 0\right) \text{ and a radius, } r = \left(\frac{T_1 - T_3}{2}\right)$$

We'll see just how this works in the section on stress, below. However, you should realize that just about any second order tensor can be represented by a Mohr Circle construction. Time for some geological applications.

## The Orientation Tensor

The first application harkens back to Chapter 2 and the limitations of the mean vector calculation (Fig. 2.11) and Chapter 3 and the π-diagram (Fig. 3.9). The solution is to calculate the least squares best fit to a distribution of lines (poles, really). The result, however, will allow us to characterize any line distribution and it will not suffer from the lower hemisphere artifacts that plague the mean vector calculation.

### *Least Squares Best Fit Fold Axis*

In Chapter 3, we simply "eye-balled" in a great circle which fit the bedding poles in the π-diagram (or perhaps you used a cylindrical best fit plotting option without knowing how it worked). Here, we will actually calculate the best fitting great circle and fold axis by minimizing the sum of the squares (Charlesworth et al., 1976). If a unit bedding pole $\hat{\mathbf{p}}_{[i]}$ is perfectly oriented, then the angle between it and the unit vector parallel to the fold axis, $\hat{\mathbf{f}}$, is 90° (Fig. 5.4); it is the deviation from this perfect case that we will minimize. Fortunately, there is a simple function that we can use: the dot product of $\hat{\mathbf{f}}$ and $\hat{\mathbf{p}}_{[i]}$, written as in Equation (5.3) is:

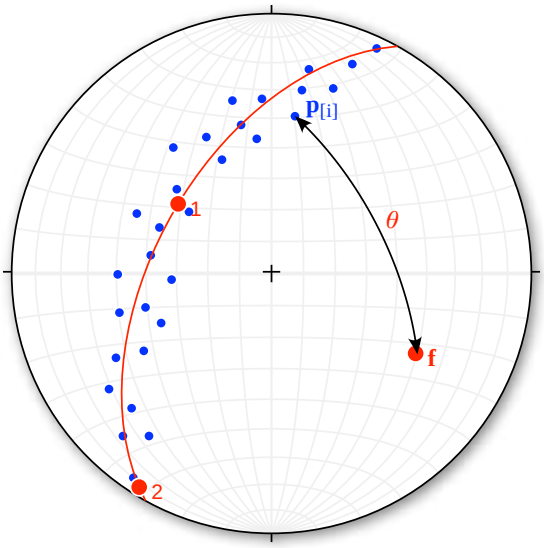


**Figure 5.4 — Finding the best fit fold axis given a number number of bedding poles. The dot product of a single bedding pole unit vector $\mathbf{p}_{[i]}$ and and the fold axis unit vector, f, is the cosine of the angle between them, $\theta$. A perfectly oriented pole should be 90° from the fold axis and so the cosine should equal zero. The deviation from zero is the deviation we are trying to minimize.**

$$\cos\theta_i = \hat{\mathbf{p}}_{[i]}\hat{\mathbf{f}}^{\mathbf{T}} \tag{5.18}$$

where $\hat{\mathbf{p}}_{[i]}$ is the i'th bedding pole in the data set. The sum of the squares of the deviations of all of the poles, S, is:

$$S = \sum_{i=1}^{n} \cos^2\theta_{[i]} = \sum_{i=1}^{n} \left(\hat{\mathbf{p}}_{[i]}\hat{\mathbf{f}}^{\mathbf{T}}\right)^2 \tag{5.19}$$

Because the dot product is commutative, it can be written as:

$$\hat{\mathbf{p}}_{[i]}\hat{\mathbf{f}}^{\mathbf{T}} = \hat{\mathbf{f}}\hat{\mathbf{p}}^{\mathbf{T}}_{[i]} \tag{5.20}$$

And we can rewrite Equation (5.19) as:

$$S = \sum_{i=1}^{n} \hat{\mathbf{f}}\hat{\mathbf{p}}^{\mathbf{T}}_{[i]}\hat{\mathbf{p}}_{[i]}\hat{\mathbf{f}}^{\mathbf{T}} = \hat{\mathbf{f}}\mathbf{T}\hat{\mathbf{f}}^{\mathbf{T}} \text{ where } \mathbf{T} = \sum_{i=1}^{n} \hat{\mathbf{p}}^{\mathbf{T}}_{[i]}\hat{\mathbf{p}}_{[i]} = \sum_{i=1}^{n} \left(p_i p_j\right)_{[i]} \tag{5.21}$$

**T** is known as the ***orientation tensor*** and it is composed of the sum of the dyad products of each unit pole vector with itself (Eqn. 5.7a). Expanding for one vector:

$$\hat{\mathbf{p}}^{\mathbf{T}}_{[i]}\hat{\mathbf{p}}_{[i]} = \begin{bmatrix} \cos\alpha_{[i]} \\ \cos\beta_{[i]} \\ \cos\gamma_{[i]} \end{bmatrix} \begin{bmatrix} \cos\alpha_{[i]} & \cos\beta_{[i]} & \cos\gamma_{[i]} \end{bmatrix} = \begin{bmatrix} \cos^2\alpha_{[i]} & \left(\cos\alpha_{[i]}\cos\beta_{[i]}\right) & \left(\cos\alpha_{[i]}\cos\gamma_{[i]}\right) \\ \left(\cos\beta_{[i]}\cos\alpha_{[i]}\right) & \cos^2\beta_{[i]} & \left(\cos\beta_{[i]}\cos\gamma_{[i]}\right) \\ \left(\cos\gamma_{[i]}\cos\alpha_{[i]}\right) & \left(\cos\gamma_{[i]}\cos\beta_{[i]}\right) & \cos^2\gamma_{[i]} \end{bmatrix}$$

So the entire orientation tensor, **T**, will be:

$$\mathbf{T} = \begin{bmatrix} \sum \cos^2 \alpha_{[i]} & \sum \left(\cos \alpha_{[i]} \cos \beta_{[i]}\right) & \sum \left(\cos \alpha_{[i]} \cos \gamma_{[i]}\right) \\ \sum \left(\cos \beta_{[i]} \cos \alpha_{[i]}\right) & \sum \cos^2 \beta_{[i]} & \sum \left(\cos \beta_{[i]} \cos \gamma_{[i]}\right) \\ \sum \left(\cos \gamma_{[i]} \cos \alpha_{[i]}\right) & \sum \left(\cos \gamma_{[i]} \cos \beta_{[i]}\right) & \sum \cos^2 \gamma_{[i]} \end{bmatrix} \tag{5.22}$$

The smallest eigenvalue of this symmetric matrix is the minimization of the sum of the deviations; thus the corresponding eigenvector should be the fold axis.

## *Types of Line Distributions*

The orientation tensor was derived for fitting a fold axis to the distribution of lines in a plane (i.e., the profile plane). It turns out that it is a much more generally useful calculation. Figure 5.5 depicts three very different end member types of line distributions and the resulting eigenvalues and eigenvectors of the orientation tensor. The bipolar distribution (Fig. 5.5a) is the one that fails miserably in a mean vector calculation because the vectors plunging in opposite directions cancel each other out. However, the orientation tensor captures the preferred orientation quite nicely with the eigenvector of the largest eigenvalue coinciding with the NW-SE orientation of the point cluster. The relative values of the three eigenvalues clearly identify a single cluster because there is one large eigenvalue (near 1) and two small,

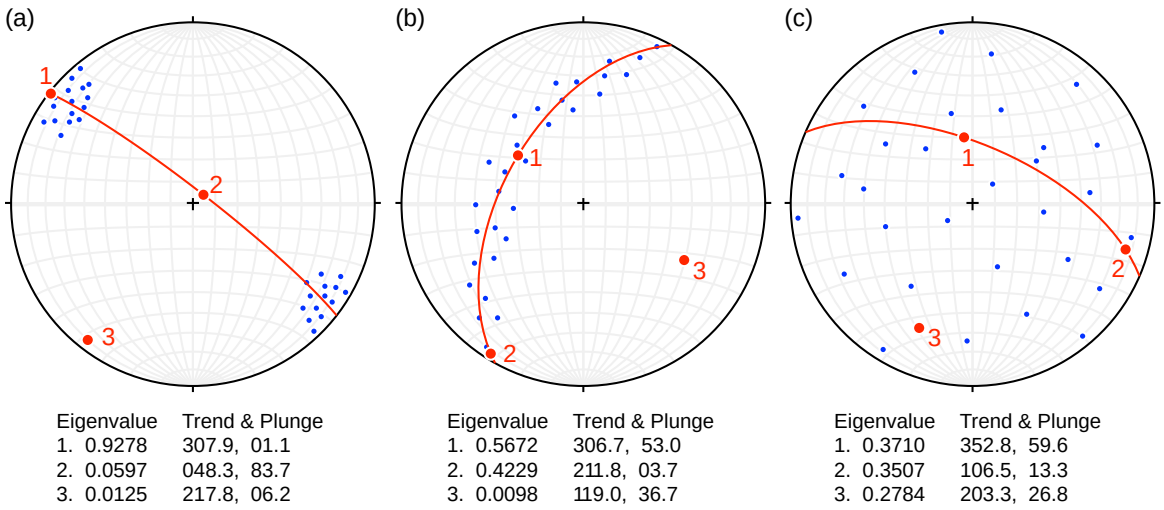


**Figure 5.5 — Different types of lines distributions: (a) bipolar; (b) girdle; and (c) random. Each diagram has 30 lines.**

near zero eigenvalues. In the ***girdle distribution*** (Fig. 5.5b), there is one small, near zero eigenvalue that corresponds to the fold axis and two large, relatively equal eigenvalues (near 0.5) whose eigenvectors lie within the profile plane through the points. Finally, the random distribution (Fig. 5.5c) has three relatively equal eigenvalues. Note that it would be quite possible to have a non-random distribution produce three equal eigenvalues if you had three clusters of points representing an equal number of lines with each cluster 90° from the others. In general, though, the eigenvalues give you a first order way of characterizing point distributions.

A spreadsheet to calculate the orientation tensor is shown in Figure 5.6. Note that eigenvalues suggest something between a girdle and a point distribution.

| | A | B | C | D | E | F | G | H | I | J | K | L |
|---|---|---|---|---|---|---|---|---|---|---|---|---|
| 1 | | Trend | Plunge | cos(α) | cos(β) | cos(γ) | cos^2(α) | cos(α)*cos(β) | cos(α)*cos(γ) | cos^2(β) | cos(β)*cos(γ) | cos^2(γ) |
| 2 | 1 | 9.4 | 29.2 | 0.8612 | 0.1426 | 0.4879 | 0.7417 | 0.1228 | 0.4201 | 0.0203 | 0.0696 | 0.2380 |
| 3 | 2 | 353.7 | 46.7 | 0.6817 | -0.0753 | 0.7278 | 0.4647 | -0.0513 | 0.4961 | 0.0057 | -0.0548 | 0.5297 |
| 4 | 3 | 334.5 | 41.4 | 0.6770 | -0.3229 | 0.6613 | 0.4584 | -0.2186 | 0.4477 | 0.1043 | -0.2136 | 0.4373 |
| 5 | 4 | 311.7 | 49.6 | 0.4311 | -0.4839 | 0.7615 | 0.1859 | -0.2086 | 0.3283 | 0.2342 | -0.3685 | 0.5799 |
| 6 | 5 | 292.3 | 51.5 | 0.2362 | -0.5760 | 0.7826 | 0.0558 | -0.1361 | 0.1849 | 0.3317 | -0.4507 | 0.6125 |
| 7 | 6 | 269.7 | 40.5 | -0.0040 | -0.7604 | 0.6494 | 0.0000 | 0.0030 | -0.0026 | 0.5782 | -0.4938 | 0.4218 |
| 8 | 7 | 266.5 | 58.4 | -0.0320 | -0.5230 | 0.8517 | 0.0010 | 0.0167 | -0.0272 | 0.2735 | -0.4455 | 0.7254 |
| 9 | 8 | 254.9 | 48.4 | -0.1730 | -0.6410 | 0.7478 | 0.0299 | 0.1109 | -0.1293 | 0.4109 | -0.4793 | 0.5592 |
| 10 | 9 | 238.8 | 42 | -0.3850 | -0.6357 | 0.6691 | 0.1482 | 0.2447 | -0.2576 | 0.4041 | -0.4253 | 0.4477 |
| 11 | 10 | 226.1 | 26.2 | -0.6222 | -0.6465 | 0.4415 | 0.3871 | 0.4022 | =D11*F11 | 0.4180 | -0.2854 | 0.1949 |
| 12 | | | | | | | | | | | | |
| 13 | | | | | | Summed columns: | 2.4727 | 0.2857 | 1.1857 | 2.7808 | -3.1475 | 4.7465 |
| 14 | | | | | | | | | | | | |
| 15 | | | | | | Orientation tensor: | 2.4727 | 0.2857 | 1.1857 | paste this orientation | | |
| 16 | | | | | | | 0.2857 | 2.7808 | -3.1475 | tensor into EigenCalc | | |
| 17 | | | | | | | 1.1857 | -3.1475 | 4.7465 | | | |
| 18 | | | | | | | | | | | | |
| 19 | | | | From EigenCalc | | | | | | | | |
| 20 | | Trend | Plunge | cos(α) | cos(β) | cos(γ) | Eigenvalue | Eigenvalue/n | | | | |
| 21 | 1 | 286.62 | 53.87 | 0.16861 | -0.56495 | 0.80771 | 7.195519 | 0.7195519 | | | | |
| 22 | 2 | 23.8 | 5.21 | 0.91119 | 0.40185 | 0.09086 | 2.716934 | 0.2716934 | | | | |
| 23 | 3 | 117.55 | 35.63 | -0.37591 | 0.72066 | 0.58253 | 0.0875471 | 0.00875471 | | | | |

**Figure 5.6 — Spreadsheet for calculating the orientation tensor from trends and plunges of ten poles to planes. Note that you only need to calculate six components because the tensor is symmetric.**

# The Stress Tensor

## *Cauchy's Law*

Whereas the orientation tensor is created by the dyad product of a pole vector with itself, the stress tensor is a more normal type of linear vector operator. In this section, I'll assume that you've already learned about stress — the mechanics type, that is — in the lecture part of your structural geology class. When most people say that "stress is equal to force [a vector] divided by area [a scalar]" what they

are really referring to is the ***stress vector*** or ***traction*** on a particular plane of interest. The ***stress tensor*** is different: it relates the stress on planes of all possible orientations through a point in a body to the tractions on those planes.

$$p_i = \sigma_{ij}\ell_j \tag{5.23a}$$

Where $p_i$ is the traction on a particular plane, $\ell_j$ is the direction cosines of the pole to the plane and and $\sigma_{ij}$ is the stress tensor. Equation (5.23a) is very important and is known as ***Cauchy's Law***. It expands as follows:

$$\begin{aligned} p_1 &= \sigma_{11}\ell_1 + \sigma_{12}\ell_2 + \sigma_{13}\ell_3 \\ p_2 &= \sigma_{21}\ell_1 + \sigma_{22}\ell_2 + \sigma_{23}\ell_3 \\ p_3 &= \sigma_{31}\ell_1 + \sigma_{32}\ell_2 + \sigma_{33}\ell_3 \end{aligned} \tag{5.23b}$$

We can get insight into the meaning of the components of the stress tensor by looking at some special cases. Let's assume first that the plane we're interested in is perpendicular to the $X_1$ axis. In this case, the pole direction cosines will be [1, 0, 0]. Substituting these values into Equation (5.23) we see that the tractions on the plane, **p**, are $p_i = [\sigma_{11} \quad \sigma_{21} \quad \sigma_{31}]$. Likewise, a plane perpendicular to the $X_2$ axis will have direction cosines of [0, 1, 0] and the tractions on that plane are $[\sigma_{12} \quad \sigma_{22} \quad \sigma_{32}]$ and the plane perpendicular to $X_3$ will have tractions of $[\sigma_{13} \quad \sigma_{23} \quad \sigma_{33}]$. In other words, ***the components of the stress tensor are simply the tractions on the planes that are perpendicular to the three coordinate axes***.

Written as they are in the preceding paragraph, derived from Cauchy's Law, the subscripts of the stress tensor have the following meaning: the first subscript indicates which axis the traction vector is parallel to and the second subscript indicates that axis that the plane is perpendicular to. This is opposite to the convention that one sees more commonly in structural geology textbooks. That's okay, though, because it turns out that the stress tensor is symmetric (thanks to conservation of angular momentum and Cauchy's 2nd Law of Motion). That is,

$$\sigma_{12} = \sigma_{21}, \quad \sigma_{13} = \sigma_{31}, \quad \sigma_{23} = \sigma_{32} \tag{5.24}$$

Thus, it is also true that the first subscript indicates the axis perpendicular to the plane and the second subscript the axis to which the traction vector is parallel

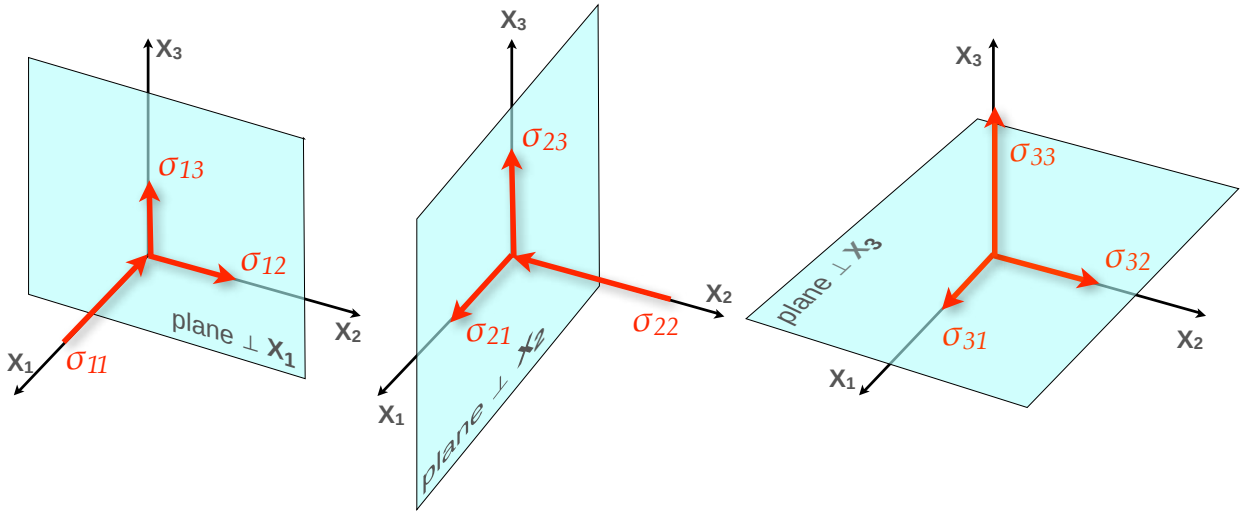


**Figure 5.7 — The meaning of the components of the stress tensor. They are the normal and shear stresses on planes perpendicular to the axes of the coordinate system. Normal stresses have equal subscripts whereas shear stresses have unequal subscripts**

(Fig.5.7). Thus each of the three planes normal to the coordinate system has one stress vector perpendicular to the plane and two stresses vectors parallel to the plane. The perpendicular stress, or ***normal stress vector***, has two equal subscripts and occur along the principal diagonal of the stress tensor. Those parallel to the plane, or ***shear stress vectors***, have unequal subscripts and are in the off-diagonal position in the tensor. We will use $\sigma_n$ to indicate the normal traction (or stress vector) on a plane and either $\tau$ (tau) or $\sigma_s$ for shear stress vectors on a plane The symmetry of the stress tensor and the equivalence of the shear stresses (Eqn. 5.24) is sometimes called the theorem of conjugate shear stresses.

Note that when we calculate the traction on a plane using Cauchy's Law (Eqn. 5.23), the vector is, in the most general case, neither normal nor parallel to the plane. The components of **p** are always parallel to the axes of the coordinate system (Fig. 5.8). As we will see later on, one way to calculate the normal and shear stress on the plane is to transform the vector into a coordinate system where the $X'_1$ axis is perpendicular to the plane. The normal and shear stress vectors on a plane are key pieces of information to determine whether or not faulting, or earthquakes, will occur.

## *Mohr's Circle for Stress*

Like any symmetric second order tensor, stress can be represented on a Mohr Circle construction. This graphic is a very common way of displaying stress on planes, even if behind the scenes the values are calculated using tensor transformations. In Mohr's Circle for stress, one plots normal stress the horizontal axis and shear stress on the vertical axis. Before making a plot, though, we need to discuss sign conventions for both of these quantities. Although the engineering sign convention is that tension is positive and compression negative, within the Earth, almost all normal stresses are compressions except close to the surface. Thus, ***in geology, compression is treated as positive and tension negative***. The sense of shear also has a sign and this, too, depends on your perspective. If one derives the Mohr's Circle in the traditional way as a force balance, counterclockwise (i.e., left-lateral) shear is positive and clockwise (i.e., right-lateral) shear is negative. However, if it is derived as a tensor transformation, then the opposite convention applies. We will use the geological sign convention.

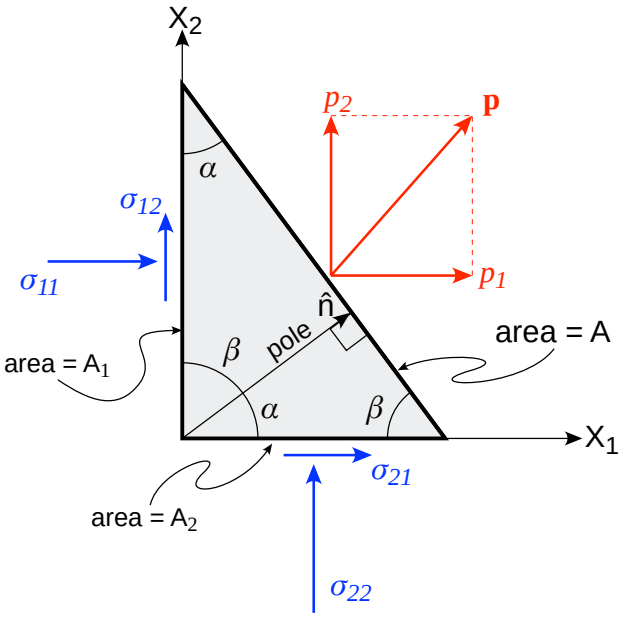


**Figure 5.8 — The traction vector, p, on a plane whose pole that makes an angle of α with respect to $X_1$ and β with respect to $X_2$. The plane is viewed edge on so it appears as a diagonal line. The traction vector is scaled correctly given the components of the stress tensor and angles shown.**

The equations for the Mohr's Circle for stress for planes that are parallel to $\sigma_2$ are:

$$\sigma_n = \left(\frac{\sigma_1 + \sigma_3}{2}\right) + \left(\frac{\sigma_1 - \sigma_3}{2}\right)\cos 2\theta \qquad (5.25a)$$

$$\tau = \sigma_s = \left(\frac{\sigma_1 - \sigma_3}{2}\right)\sin 2\theta \qquad (5.25b)$$

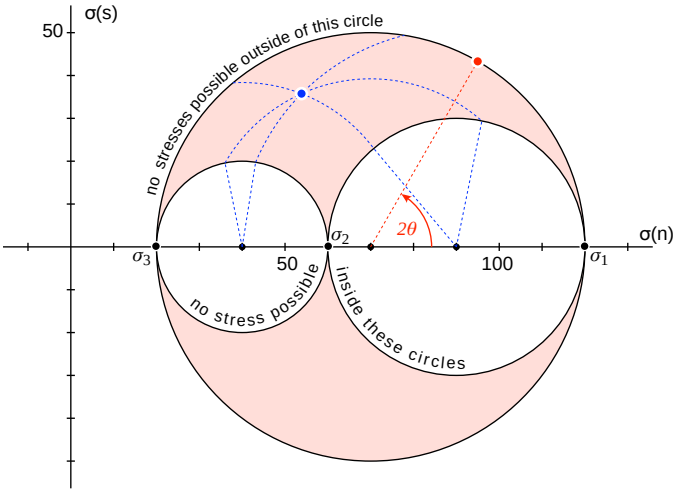


**Figure 5.9 — Basic Mohr's Circle construction for stress where $\sigma_1$ = 120 MPa, $\sigma_2$ = 60 MPa, and $\sigma_3$ = 20 MPa. The only possible normal and shear stress combinations are along the edges of the circles or in the pink shaded region. Two planes are shown: that in red is parallel to $\sigma_2$ and its pole is 30° (2θ = 60°) from $\sigma_1$. The blue plane is not parallel to any principal stress; its pole is 65° from $\sigma_1$, 50.74° from $\sigma_2$, and 49.55° from $\sigma_3$. Dashed lines are construction lines.**

$\theta$ is the angle between the pole to the plane of interest and $\sigma_1$. Similar equations can be derived for the two inner circles. There are many ways of deriving the Mohr Circle equations: as a force balance, using Cauchy's law and a vector transformation, or using a tensor transformation (Eqns. 5.11 - 5.17).

In the most general case of Mohr's Circle for stress, there will be three nested circles defined by the three principal stresses (Fig. 5.9). The simplest case for plotting normal and shear stresses is when the plane of interest is parallel to one of the three principal axes (e.g., the red dot in Fig. 5.9). In that case, one simply determines the angle between the pole to the plane and the largest principal stress, $\theta$, and then measures $2\theta$ counterclockwise from the side of the circle with largest principal stress as shown in Figure 5.9. When the plane is not parallel to any of the principal stresses, the manual plotting procedure is more cumbersome and consists of drawing arcs of concentric circles defined by the three angles, $\alpha$, $\beta$, and $\gamma$, that the pole makes with the three principal stresses (see Allmendinger et al., 2012, if you want to know how to do this). A program like MohrPlotter can do this calculation and plot directly. But, of course, it is more satisfying to calculate the stresses

| | A | B | C | D | E | F | G | H |
|---|---|---|---|---|---|---|---|---|
| 1 | | Angles wrt Principal Axes | | | Direction Cosines | | | |
| 2 | | Alpha | Beta | Gamma | cos(alpha) | cos(beta) | cos(gamma) | Magnitude |
| 3 | Plane: | 65 | 50.74 | 49.55 | 0.4226 | 0.6328 | 0.6488 | 1.0000 |
| 4 | | | | | | | | |
| 5 | | | | Stress tensor: | 120 | 0 | 0 | |
| 6 | | | | | 0 | 60 | 0 | |
| 7 | | | | | 0 | 0 | 20 | |
| 8 | | | | | | | | |
| 9 | p(1) = | 50.7141914 | | | | | | |
| 10 | p(2) = | 37.9704286 | | | | | | |
| 11 | p(3) = | =E7*E3+F7*F3+G7*G3 | | | | | | |

**Figure 5.10 — spreadsheet for calculating the tractions on a plane whose pole makes angles of alpha, beta, and gamma with respect to the three principal stresses.**

directly! We can use Equation (5.23) to calculate the tractions on the plane directly and this is done in the spreadsheet in Figure 5.10 for the same angle values as blue plane in Figure 5.9. In the next chapter, we'll actually calculate the normal and shear stresses.

A couple of things bear emphasizing in the example in Figure 5.10. First, this calculation takes place in the principal stress coordinate system, which is why the stress tensor has such a simple appearance. Without knowing the orientation of the plane or of the principal stresses, we have no idea the values of the tractions in a geographic coordinate system. The same is true of the Mohr's Circle construction: it represents a principal stress coordinate system; without knowing the orientations of the stresses, a plane represented could be a normal, thrust, or strike-slip fault plane. Second, the angles $\alpha$, $\beta$, and $\gamma$ are not independent of each other; only two out of the three can be independently specified. Their direction cosines must yield a unit vector (thus the magnitude test in column H).

## *Mean Stress & Deviatoric Stress*

Earlier in the Chapter, we saw that symmetric tensors have invariants, and the first invariant of the stress tensor is the sum of the stresses along the principal diagonal. This allows us to define the mean stress, $\sigma_m$, which is the same in all coordinate systems:

$$\sigma_m = \frac{I_\sigma}{3} = \frac{\sigma_{11} + \sigma_{22} + \sigma_{33}}{3} = \frac{\sigma_1 + \sigma_2 + \sigma_3}{3} \tag{5.26}$$

The total stress can then be defined as the mean stress plus the ***deviatoric stress***:

$$\sigma_{ij} = \begin{bmatrix} \sigma_m & 0 & 0 \\ 0 & \sigma_m & 0 \\ 0 & 0 & \sigma_m \end{bmatrix} + \begin{bmatrix} \sigma_{11} - \sigma_m & \sigma_{12} & \sigma_{13} \\ \sigma_{21} & \sigma_{22} - \sigma_m & \sigma_{23} \\ \sigma_{31} & \sigma_{32} & \sigma_{33} - \sigma_m \end{bmatrix} \tag{5.27}$$

# Exercises—Chapter 5

All of the following exercises should be done either in a spreadsheet or Matlab. If you use a spreadsheet, you will need to download the simple utility program EigenCalc in either Macintosh or Windows version:

http://www.geo.cornell.edu/geology/faculty/RWA/programs/utility-programs/eigencalc.html

This program will take the matrix that you calculate in the spreadsheet and calculate the eigenvalues and eigenvectors for you, which is much less cumbersome than trying to figure out how to get the spreadsheet to do it!

You might also find useful a program to plot Mohr Circles for stress, MohrPlotter, which can be downloaded from:

http://www.geo.cornell.edu/geology/faculty/RWA/programs/mohrplotter.html

Even though MohrPlotter can do some of the calculations for you, you must still do the calculations in a spreadsheet or Matlab. For all problems, assume a North-East-Down coordinate system unless otherwise noted.

1. In a spreadsheet or in Matlab, calculate the orientation tensor for the strikes and dips that you used to construct a pi-diagram of the Big Elk anticline in Chapter 3. Note that you do not have to find the eigenvalues or eigenvectors of the resulting matrix, just construct the orientation tensor in a North-East-Down coordinate system. If you choose to use Matlab, please write your own code rather than just cutting and pasting the code from Allmendinger et al.

2. A state of stress with the following principal stress magnitudes $\sigma_1$ = 40 MPa, $\sigma_2$ = 20 MPa, $\sigma_3$ = 10 MPa, has $\sigma_1$ axis oriented vertically, $\sigma_2$ aligned in a horizontal E-W direction, and $\sigma_3$ in a horizontal N-S direction. Using Cauchy's law, calculate the magnitude and orientation of the tractions acting on a plane striking 060° and dipping 55° SE.

3. For the same state of stress described in question 2, but a different plane that has a strike in right hand rule of 270, 60,
   (a) Use Cauchy's law to calculate the tractions on the plane

(b) Use Mohr's Circle for stress to calculate the normal and shear stress on the plane

(c) Reconcile your answers in parts (a) and (b) by showing that they are actually the same answer.

(d) If the plane with strike of 270, 60 were a fault plane, what type of fault would it be?

4. The following matrix gives the stress tensor in a NED coordinate system (units are MPa):

$$\sigma_{ij} = \begin{bmatrix} 20 & 6 & 15 \\ 6 & 45 & 20 \\ 15 & 20 & 30 \end{bmatrix}$$

(a) Use Cauchy's Law to determine the tractions on a plane with a strike and dip (right hand rule) of 045, 22.

(b) The principal stresses for this stress tensor, given by calculating the eigenvalues and eigenvectors, are $\sigma_1$ = 63.23 MPa with a trend and plunge of 068, 36; $\sigma_2$ = 24.4 MPa, 317, 26; and $\sigma_3$ = 7.39 MPa, 200, 43. Plot the normal and shear stress on the 3D Mohr circle for stress as shown on page 110 of ACF (2012).

5. Two planes are both parallel to $\sigma_2$. The first has a normal stress, $\sigma_n$ = 55 and shear stress, $\tau$ = 17 MPa. For the second, $\sigma_n$ = 27 and shear stress, $\tau$ = 13 MPa.

(a) Use a Mohr Circle construction to calculate the magnitude of the principal stresses, $\sigma_1$ and $\sigma_3$. [Hint: the perpendicular bisector of a chord in a circle goes through the center of the circle].

(b) If plane 1 has a strike and dip (RHR) of 084.7, 40.3 and plane 2, 046.3, 70.7, use a stereonet to determine the trends and plunges of the three principal stresses.

# Chapter 6

## *Faulting and Stress*

### Introduction

We now have the tools necessary to begin to understand faulting. Faulting is probably the most important type of deformation in the upper crust of the earth and, as we'll see in later chapters, is often accompanied by folding. An ***earthquake*** is just a single, rapid (i.e., geologically instantaneous) movement on a fault and ***induced seismicity*** are earthquakes cause by humans, often due to subsurface pumping of fluids and the interaction of those fluids with pre-existing faults.

Needless to say, these are phenomena of great, and increasing, societal interest!

As you know from the lecture part of your course, a fault is a break or fracture in the rock across which there has been movement parallel to the fault surface. We know that movement parallel to a surface is called ***shear*** and so it won't come as a surprise that the shear stress on a fault plane is an important parameter to quantify. However, as we shall see, the normal stress on a fault plane is equally important. We now have the ability to analyze these parameters and will do so after a brief review of fault geometry and the introduction of two additional key concepts: friction and pore pressure.

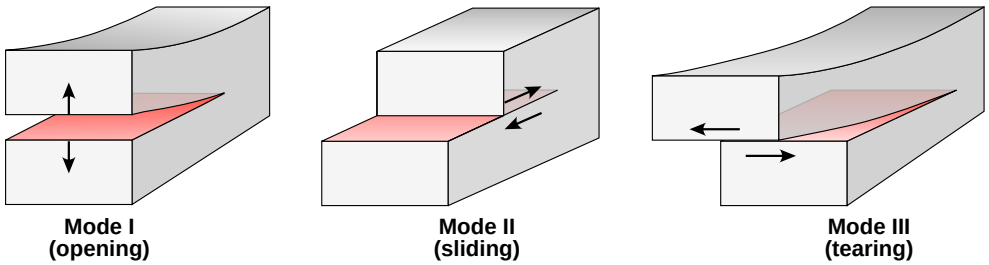


**Figure 6.1 — The three modes of cracking, with the crack surface colored red. Mode I cracks correspond to joints or veins because they have opening but no shear. Modes II and III are faults.**

# Fault Geometry Review

## *Terminology*

Cracks or fractures in a rock can occur in one, or a combination, of three fundamental modes (Fig. 6.1). In mode I, there is opening perpendicular to the crack but no shear and we call the resulting geological structure a ***joint*** or, if it is filled with mineral precipitate, a ***vein***. Most faults in the subsurface are approximately elliptical surfaces that terminate in a ***tip line*** (really a loop) which separates faulted from unfolded (i.e., intact) rock. Depending on the position along the fault surface, the fault may resemble either a mode II (shearing perpendicular to the tip line) or a mode III (shearing parallel to the tip line) crack. For example, near where a dip slip fault dies out along strike, you are likely to see mode III style behavior whereas in the middle of the fault trace, mode II would be more common.

Faults are classified in a variety of ways (Fig. 6.2). For faults in which the movement is parallel to the dip direction, they are further subdivided in terms of whether the hanging wall block moved down (***normal faults***, Fig. 6.2a) or up (***reverse faults***, Fig. 6.2b). Faults that moved parallel to the strike likewise are subdivided into whether the opposing block (i.e., the one opposite the block the observer is on) appears to move to the right (Fig. 6.2c) or left (Fig. 6.2c). Of course, few faults fit these end members exactly and most have combinations of movement parallel to strike and to dip; these are known as ***oblique-slip faults***.

Faults can also produce a component of rotation of one block relative to the other. If the two blocks are to remain in contact (a constraint known as strain com-

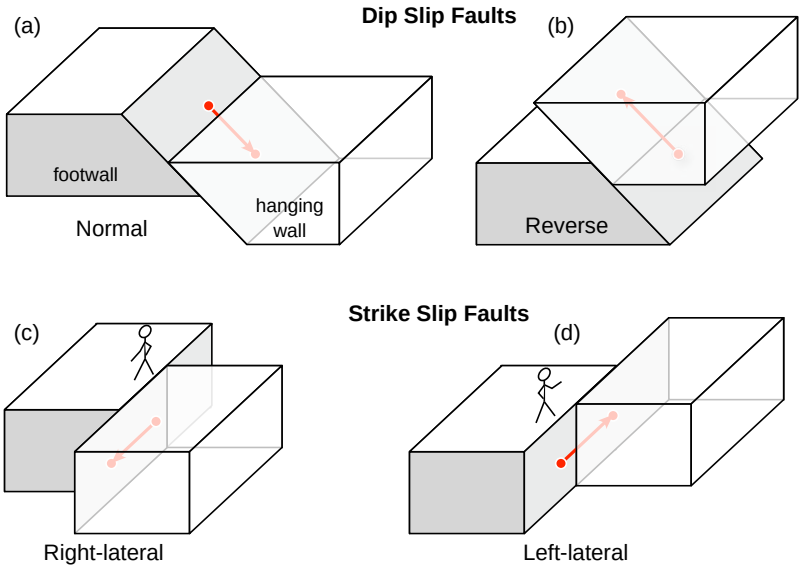


**Figure 6.2 — Basic end-member fault types. In each case, the red arrow is a slip vector which shows the offset of two originally adjacent points. The slip is in the dip direction in (a) and (b), and in the strike direction in (c) and (d). The stick figure is holding out their right arm in (c) and their left arm in (d).**

patibility, which we will see later on), then only two different orientations of the rotation axis are possible: (a) perpendicular to the fault plane, or (b) parallel to the fault plane. The latter case is only possible if the fault plane is a curved surface. Curved fault surfaces where the dip diminishes with depth are known as ***listric faults***. A rotation axis perpendicular to the plane will produce a ***scissors fault*** (Fig. 6.3).

Planar features like stratification are common in geology and it is tempting to think that the apparent offset that one sees of such features, either on the surface or in cross section, represents the actual movement of the fault. We call such apparent offset of a planar feature ***separation*** (Fig. 6.4) The actual vector displacement of

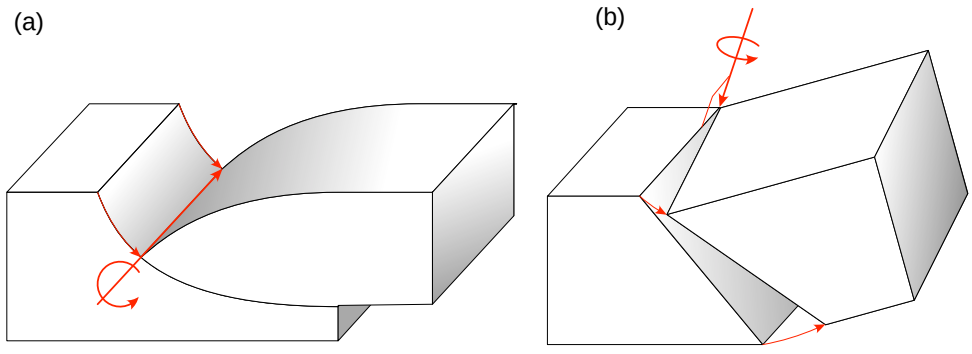


**Figure 6.3 — Rotational faults: (a) listric normal fault where the rotation axis (in red) is parallel to the curved fault surface. (b) Scissors fault where the rotation axis is perpendicular to the planar fault plane.**

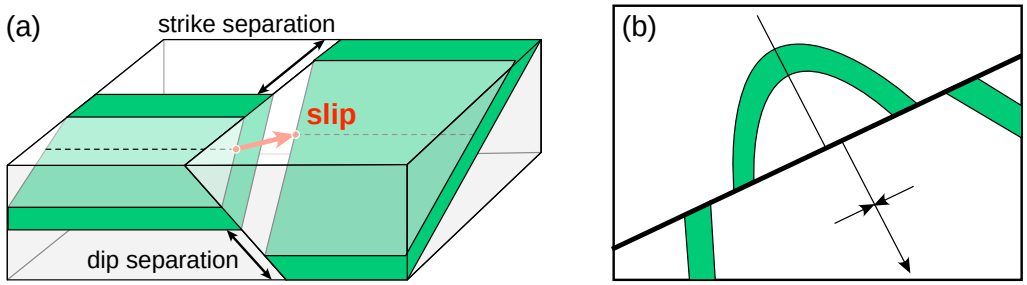


**Figure 6.4 — Slip versus separation.** (a) **Block diagram illustrating an offset planar layer that contains a linear feature shown as a dashed line. The linear feature intersects the fault plane in two red points known as piercing points and the slip vector (heavy red arrow) connects the piecing points. Note that the strike and dip separation shown are neither parallel to, nor the same magnitude as the slip vector.** (b) **schematic map view of a plunging syncline offset by a fault. Note that the strike separation is in the opposite direction on the two limbs of the fold!**

two originally adjacent points across a fault surface is called ***slip***. It is critically important to distinguish clearly between these two concepts. Separation is not very useful (e.g., Fig. 6.4b) except when accompanied by independent evidence such as observation of striations or slickensides on the fault surface. It is seldom possible to find two originally adjacent points that have been offset across a fault so, instead, we use offset linear features. A line intersects a plane in a point, and therefore our offset lines intersect the fault plane in what are known as ***piercing points***. The slip can be determined if piecing points on the fault surface can be calculated.

## *Determining Slip from Piercing Points*

As we have just seen, separation, although easy to determine, is not very useful. Slip, on the other hand, is incredibly useful for a whole range of problems in structural geology. Slip is most effectively determined from offset piercing points of linear features so the question becomes: how does one determine a piercing point, especially given that, in general the piercing point will either be in the subsurface or in the air and thus not directly observable? The vector methods we learned in earlier chapters come to the rescue for the

As you begin to derive your own functions related to geometry, you may find the web site by Paul Bourke (http://paulbourke.net) very useful. The derivation in this section is modified from an algorithm on his site.

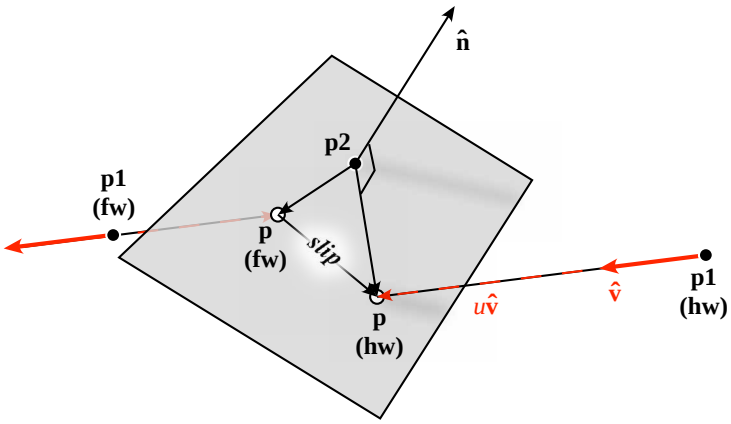


**Figure 6.5 — Calculation of piercing points, p, in the hanging wall (hw) and the footwall (fw) of a fault plane shown as a gray-shaded surface. n is the normal or the pole to the fault plane and v is the unit vector defined by the trend and plunge of the line that produces the piercing points. Only p1, p2, n and v are needed to calculate the piercing points, p.**

solution to this problem (Fig. 6.5). To solve this problem, we need to know one point, **p1**, on the line with a known trend and plunge that pierces the plane, and one point, **p2**, on the plane as well as the strike and dip of the plane. Points **p1** and **p2** will usually be points on the surface of the earth or well determined (e.g., drilled) points in the subsurface. The line, of course could be any geological feature that can be identified — fold axis on a particular stratigraphic horizon, the intersection of a dike and bedding, the intersection of a stratigraphic horizon beneath an angular unconformity — as long as we can determine its trend and plunge and at least one point on each side of the fault plane.

For simplicity's sake, our derivation only treats one of the two piercing points. As you can see in Figure 6.5, the dot product of the normal vector, **n**, and the vector between the position vectors **p2** and **p** (the point in which we are interested) is zero because **n** is perpendicular to all vectors in the plane:

$$\hat{\mathbf{n}} \cdot \left[\mathbf{p} - \mathbf{p2}\right] = 0 \tag{6.1}$$

Point **p** also occurs along the line that pierces the plane. The vector distance between **p1** and **p** is $u\hat{\mathbf{v}}$ where $\hat{\mathbf{v}}$ is the unit vector calculated from the trend and plunge of the linear feature. We can write that:

$$\mathbf{p} = \mathbf{p1} + u\hat{\mathbf{v}} \tag{6.2}$$

Substituting Equation (6.2) into (6.1) and rearranging, we get:

$$\hat{\mathbf{n}} \cdot \left[\mathbf{p1} + u\hat{\mathbf{v}}\right] = \hat{\mathbf{n}} \cdot \mathbf{p2} \tag{6.3}$$

And solving for $u$ we have:

$$u = \frac{\hat{\mathbf{n}} \cdot [\mathbf{p2} - \mathbf{p1}]}{\hat{\mathbf{n}} \cdot \hat{\mathbf{v}}} = \frac{n_1\left(p2_1 - p1_1\right) + n_2\left(p2_2 - p1_2\right) + n_3\left(p2_3 - p1_3\right)}{n_1 v_1 + n_2 v_2 + n_3 v_3} \tag{6.4}$$

There is one special case that will result in an error: if the pole to the plane is perpendicular to the line then the denominator of (6.4) will be zero. This means that the line is parallel to the plane and either does not intersect it at all or lies within the plane and there are an infinite number of intersections! Once we know the scalar $u$, we can substitute it into Equation (6.2) and solve for the piercing point, **p**:

$$p_1 = p1_1 + u v_1; \quad p_2 = p1_2 + u v_2; \quad p_3 = p1_3 + u v_3 \tag{6.5}$$

We can repeat this process for the piercing point on the other block of the fault. Note that the trends and plunges of the lines on the two sides of the fault do not have to be equal to each other, thus accounting for faults across which there has been rotation. The final slip magnitude on the fault is just the magnitude of the vector connecting the two piercing points:

$$slip = \sqrt{\left(p\left(hw\right)_1 - p\left(fw\right)_1\right)^2 + \left(p\left(hw\right)_2 - p\left(fw\right)_2\right)^2 + \left(p\left(hw\right)_3 - p\left(fw\right)_3\right)^2} \tag{6.6}$$

Where *p(hw)* is the piercing point in the hanging wall and *p(fw)* is the offset piercing point in the footwall (Fig. 6.5). A sample calculation is shown in the spreadsheet in Figure 6.6. The expanded equation in the spreadsheet is the realization of Equation (6.4). The only special note is that one must remember to calculate the direction cosines of the trend and plunge of the line and the pole to the plane in East-North-Up coordinates rather than North-East-Down. The formula for Equation (6.6) is in cell B12 of the spreadsheet.

Note that the calculation we have just done can be used for a variety of other useful tasks in geology. For example, you could use this same approach to determine the distance that you would need to drill along a particular trend and plunge, starting at some point on the surface, to intersect a fault plane, knowing nothing more than the strike and dip of the plane and a single well determined point on the plane. The scalar distance, $u$, is given by Equation (6.4).

| | A | B | C | D | E | F | G | H | I |
|---|---|---|---|---|---|---|---|---|---|
| 1 | | East | North | Up | trend/strike | plunge/dip | cos(alpha) | cos(beta) | cos(gamma) |
| 2 | p1-hw (line) | 27096 | 42996 | 6094 | 232 | 35 | -0.6455 | -0.5043 | -0.5736 |
| 3 | p2 (fault plane) | 22464 | 39804 | 6841 | 350 | 58 | -0.8352 | -0.1473 | -0.5299 |
| 4 | p1-fw (line) | 20492 | 39511 | 7401 | 232 | 35 | -0.6455 | -0.5043 | -0.5736 |
| 5 | | | | | | | | | |
| 6 | u-hw = | 4298.1 | | | | | | | |
| 7 | u-fw = | =(G3*(B3-B4)+H3*(C3-C4)+I3*(D3-D4))/(G3*G4+H3*H4+I3*I4) | | | | | | | |
| 8 | | | | | | | | | |
| 9 | p (hw) | 24321.6 | 40828.4 | 3628.7 | | | | | |
| 10 | p (fw) | 21472.6 | 40277.2 | 8271.9 | | | | | |
| 11 | | | | | | | | | |
| 12 | slip = | 5475.4 | | | | | | | |

Note: These direction cosines are in an ENU coordinate system, not a NED system!

**Figure 6.6 — spreadsheet to calculate the slip on a fault, given the strike and dip of the fault plane and a position vector of a point in the fault plane (p2), and the trend and plunge of a line in the hanging wall and footwall, position vectors somewhere along those lines, and the trends and plunges of the lines. In this example, we have assumed that the trend and plunge of the line on either side of the fault is the same but that is not necessary. The calculation of the scalar quantity, *u*, has been expanded for view.**

## Stress and Faulting

Faulting occurs when the yield stress of a material is exceeded and the material fails locally. Ductile failure is an extremely important process in geology but we are going to leave it for a later chapter. In this chapter, we are only concerned with brittle failure, friction, reactivation, and the influence of fluid pressure in the pores of the material. Thus, the material here corresponds to the upper 10±5 km of the Earth's crust, an area of particular interest for humans because of earthquakes, as well as exploitation of the subsurface for resources (hydrocarbons, water) and storage of waste (e.g., water water, carbon sequestration, etc.). There are two separate questions: (a) what are the macroscopic conditions under which a rock will break? and (b) under what conditions will preexisting fractures be reactivated? Pore fluid pressure will be important in both cases, but we will first examine the case without pore pressure.

### *Failure in the Brittle Realm*

You have, no doubt, in the lecture part of your structural geology course been introduced to the concept of a ***failure envelope***. This envelope is most often depicted on a plot of shear stress versus normal stress as a line, symmetric about the normal stress axis, with several distinct parts (Fig. 6.7). A combination of normal and shear stress that lies outside of the envelope is one that will cause the ma-

terial to fail whereas those inside the envelope are stable. The important points on the failure envelop are: $T_o$ — ***tensile strength***; 1. ***transitional-tensile behavior***; $S_o$ — ***cohesive strength***; 2. ***Coulomb failure***; and 3. ***von Mises failure***. The last of these is equivalent to ductile failure and will not be discussed further in this chapter. The field of Coulomb behavior is the most important for upper crustal faulting whereas tensile strength and transitional-tensile behavior are most important for near surface jointing or for cases of small ***differential stress*** — $\Delta\sigma = \sigma_1 - \sigma_3$ — and large pore fluid pressures, $P_f$. We will start with Coulomb failure, the linear part of the envelope.

For Coulomb failure, only the $\sigma_1$-$\sigma_3$ part of the Mohr's circle matters because, in plane strain, planes parallel to $\sigma_2$ will always fault before planes in other orientations (except for the cases where $\sigma_2$=$\sigma_3$ or $\sigma_2$=$\sigma_1$). At failure, the Mohr's circle touches the failure envelope in two places (Fig. 6.8). Somewhat paradoxically at first glance, the plane that actually breaks is **not** the plane at 45° to $\sigma_1$ which has the maximum shear stress, $\tau_{max}$, on it! Instead, there are two potential ***conjugate fault planes*** with their poles at angles of $\theta = \pm(45+\phi/2)$ to $\sigma_1$. $\phi$, the ***angle of internal friction***, is the slope of the Coulomb part of the failure envelope and $\tan(\phi) = \mu = \Delta\tau/\Delta\sigma_n$ is the ***coefficient of internal friction***. The complete equation for the Coulomb part of the failure envelope is:

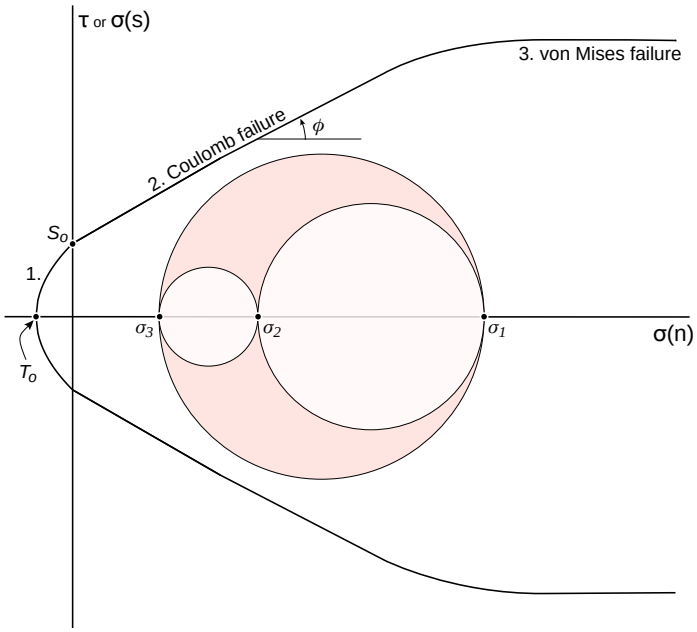


**Figure 6.7 — The anatomy of the failure envelope, plotted on axes of shear stress (vertical axis) and normal stress (horizontal axis). The Mohr's circle for stress is also shown.**

$$\tau = \sigma_s = S_o + \sigma_n \mu \tag{6.7}$$

Where $S_o$ is the ***cohesion***, essentially the shear strength of a material under zero normal stress load. The reason why the plane with $\tau_{max}$ does not fault is that it has much higher normal stress on it than the plane that does fault. We call this balance between shear stress and normal stress ***friction***.

Equation (6.7) is written in terms of the normal and shear stress at failure but there are times when we want to know the Coulomb failure criterion in terms of the principal stresses. There are several ways to achieve this result. For example, you could substitute Equations (5.25) into (6.7) or you can do a simple graphic construction based on the Mohr's Circle and Coulomb failure envelopes. The failure criterion in terms of the principal stresses is (Eqn. 6.8):

$$\sigma_1 = C_o + K\sigma_3 \quad \text{where} \quad K = \frac{1 + \sin\phi}{1 - \sin\phi} \quad \text{and} \quad C_o = 2S_o\sqrt{K} \tag{6.8}$$

## *Reactivation of Pre-existing Planes of Weakness*

The upper crust of the earth is anything but homogeneous and isotropic: even a casual glance at any outcrop will reveal numerous pre-existing planes of weakness. The rocks are beset with fractures — both joints and faults — in a variety of orientations and stratification itself can commonly represent a significant an-

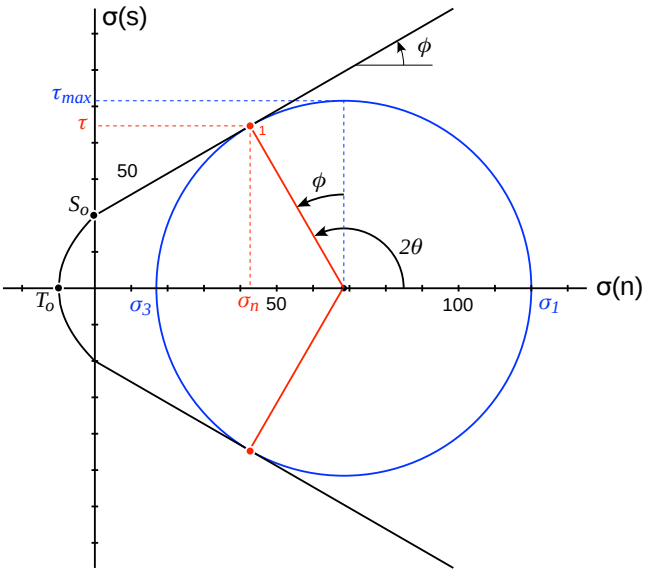


**Figure 6.8 — Coulomb failure. The Mohr circle intersects the failure envelope in two places (two red dots) so two different conjugate planes are equally likely to fracture in shear. $\phi$ is the angle of internal friction and $\theta$ is the angle between the pole to the fault plane and $\sigma_1$.**

isotropy. These pre-existing planes of weakness commonly have little or no cohesion and, because the fracture is already there, the ***coefficient of static friction*** on the plane, $\mu_s$, is different than the coefficient of internal friction. Thus, the failure envelope is different for pre-existing fractures than for Coulomb failure. The formula for the failure envelope for slip on preexisting planes is:

$$\tau = \mu_s \sigma_n \tag{6.9}$$

As you can see in Figure 6.9, the Mohr's Circle crosses the envelope for failure along pre-existing planes with zero cohesion but does not touch the Coulomb part of the failure envelope for intact rock. Just because it crosses the pre-existing failure envelope, however, does not mean that failure will actually occur; the preexisting weak planes must lie within a range of orientations defined by the intersections. In the case of Figure 6.9, the poles to the preexisting planes must be oriented between 48.75 and 79.25° to $\sigma_1$ (of course, the doubles of those angles are what's

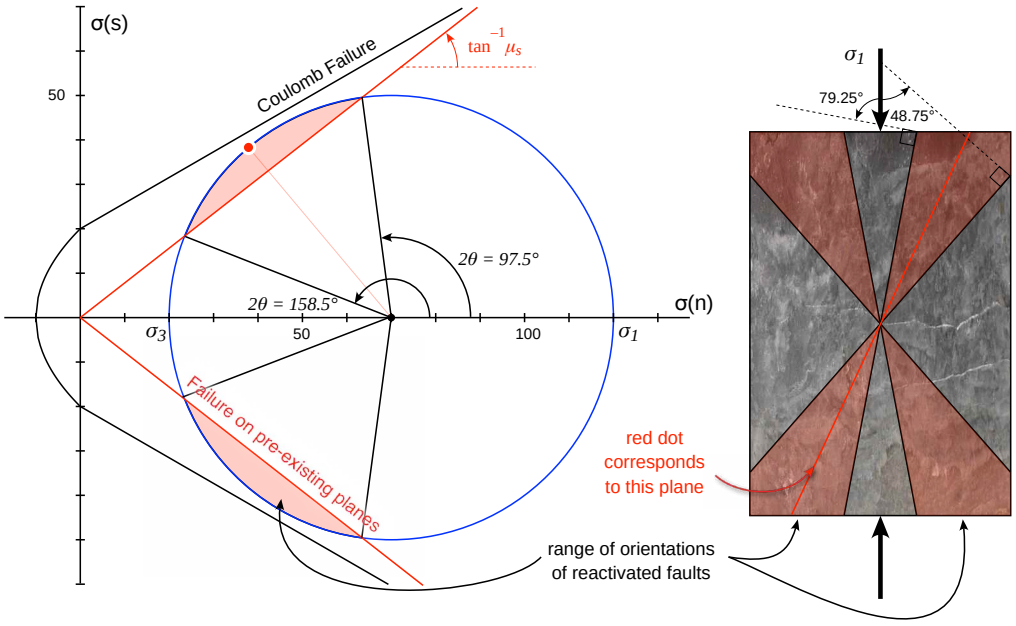


**Figure 6.9 — Left: Mohr's circle for stress and failure envelopes for preexisting fractures (in red) and for Coulomb failure. The circle intersects the preexisting fractures envelope but not the Coulomb failure envelope. Planes with normal and shear stress that plot in the pink region will be reactivated. Right: the physical orientation of $\sigma_1$ and the range of orientation of potential planes (in cross-section view so they appear as lines) that will be reactivated under these stress conditions in the shaded pink region. The red plane on the right corresponds to the red dot in the Mohr diagram on the left.**

plotted on the Mohr's Circle). In the rectangular rock sample on the right hand side of Figure 6.9, the regions where reactivation will occur are shown in pink color. If there are no weak planes with those orientations, then failure will not occur. If there are (e.g., the plane represented by the red dot), and loading occurs slowly enough, the failure on existing planes will relieve the stresses and prevent them from getting large enough to cause new faults to form.

A geologist at the U.S. Geological Survey, James Byerlee (1978), summarized a large amount of experimental data on rock friction and demonstrated that, to a first order, $\mu_s$, is independent of rock type (Fig. 6.10). For a wide variety of rock types, the data show that:

$$\tau = 0.85\sigma_n \text{ for } \sigma_n \leq 200 \text{ MPa} \quad \text{and} \quad \tau = 0.5 + 0.6\sigma_n \text{ for } \sigma_n > 200 \text{ MPa} \qquad (6.10)$$

The only significant deviations in Byerlee's data are rocks composed of the clay minerals, illite, vermiculite, and montmorillonite. However, these clay minerals are

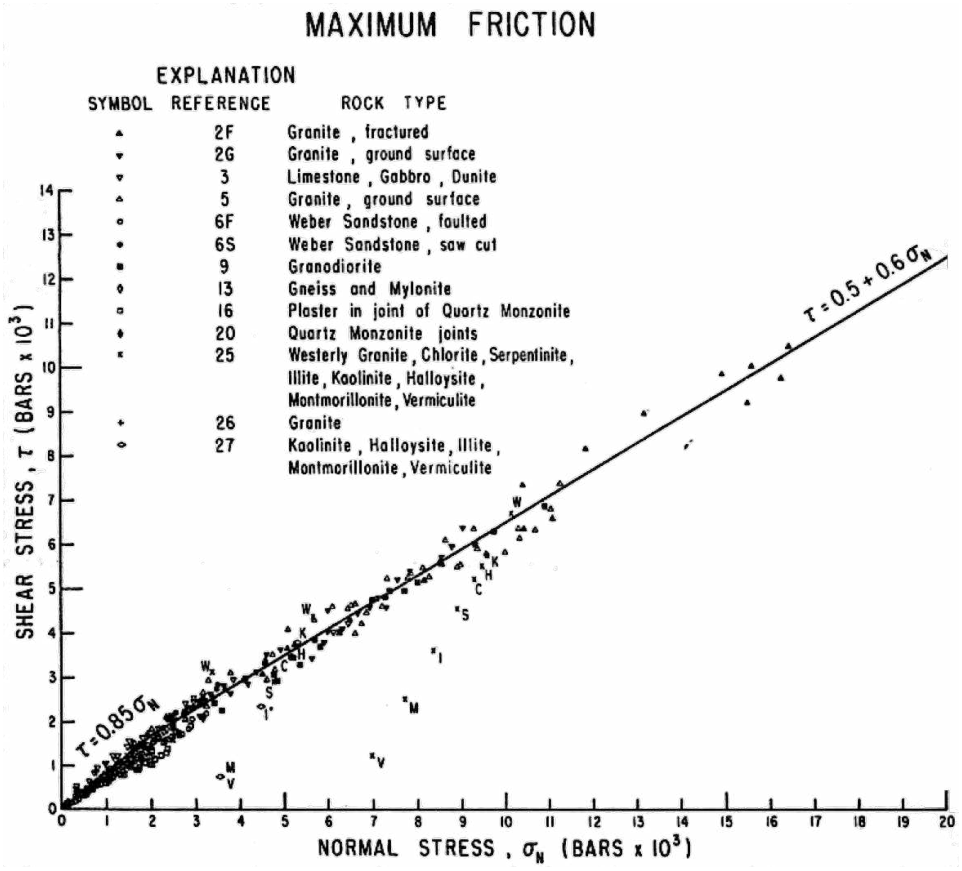


**Figure 6.10 — Experimental data summarized by Byerlee (1978) showing that $\mu_s$ is commonly relatively independent of rock type.**

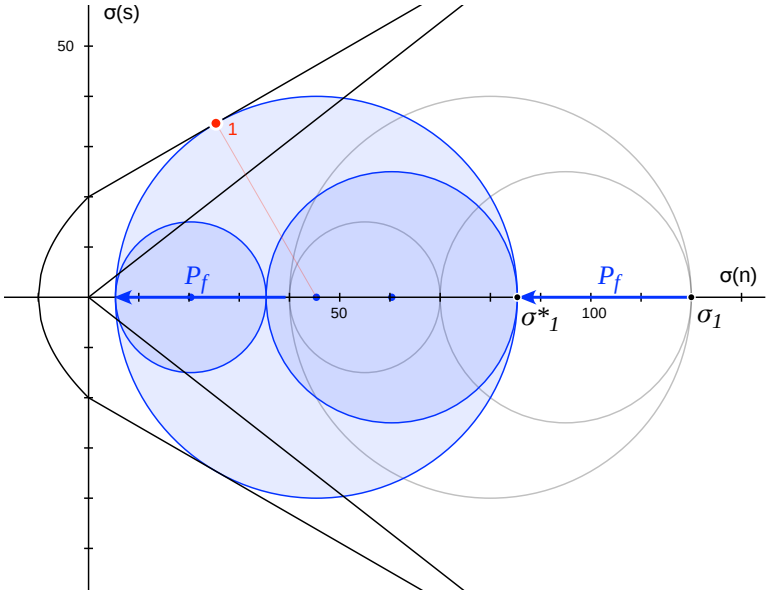


**Figure 6.11 — Mohr's Circle and failure envelopes in the presence of pore fluid pressure, $P_f$ (blue circles and arrows). The initial stress state in the absence of pore pressure is shown as light gray circles which do not intersect either failure envelope.**

commonly found in fault gouge. This relationship has become known as Byerlee's "Law" even though it is just an empirical relationship.

### *The Effect of Pore Fluid Pressure*

One of the most important controls on the strength of rocks in the upper crust is the pressure of fluid in the pores of the rocks. A fundamental property of fluids is that they cannot support any shear stress in any direction. Thus, every plane in a fluid is free of shear stress and thus every direction in a fluid is a principal stress direction. This is known as a ***spherical state of stress*** because the stress, or ***pressure***, is the same in every direction. Because pressure in the pores of the rock pushes outward in every direction, it affects the normal stress but not the shear stress. Thus, we can write the ***effective stress tensor*** as:

$$\sigma^*_{ij} = \begin{bmatrix} \left(\sigma_{11} - P_f\right) & \sigma_{12} & \sigma_{13} \\ \sigma_{21} & \left(\sigma_{22} - P_f\right) & \sigma_{23} \\ \sigma_{31} & \sigma_{32} & \left(\sigma_{33} - P_f\right) \end{bmatrix} \tag{6.11}$$

where $P_f$ is the pore fluid pressure. This has a profound effect on the deformation, most easily illustrated with the Mohr's Circle (Fig. 6.11). The differential stress, $\sigma_1$–

$\sigma_3$ or the diameter of the circle, is unaffected by pore pressure but the entire circle is shifted to the left because the normal stresses are reduced. Thus a rock which exists in a stable stress state without pore pressure can be made to fracture, or slip on pre-existing weak planes, simply by raising the pore fluid pressure. All of our failure criteria in Equations 6.7, 6.8, and 6.9 really ought to be written in terms of effective normal stresses. For example, Coulomb failure should be written:

$$\tau = \sigma_s = S_o + \left(\sigma_n - P_f\right)\mu = S_o + \sigma_n^*\mu \tag{6.12}$$

This process is known as ***hydraulic fracturing***, sometimes referred to by the increasingly pejorative term "fracking", the new f-word in environmental politics. Many natural processes can produce elevated pore pressure which can lead to natural hydraulic fracturing. Many human enterprises — water well improvement, oil and gas development, enhanced geothermal, carbon sequestration — also either rely on hydraulic fracturing (commonly referred to as ***stimulation***), or inadvertently weaken the rock while storing fluids in the subsurface (waste water storage, carbon sequestration). Weakening of pre-existing buried fault zones has been implicated in human ***induced seismicity*** as you will see in the exercises.

An important parameter for many studies is the ***pore fluid pressure ratio***, λ, a term first introduced by Hubbert and Rubey (1959). This ratio is defined as:

$$\lambda = \frac{P_f}{P_{lithostatic}} \quad \text{where} \quad P_{lithostatic} = \bar{\rho}_{rock} g z \tag{6.13}$$

where $\bar{\rho}_{rock}$ is the average density of the rocks. λ varies between 0 and 1; when it equals 1, the pore fluid pressure is high enough to support the weight of the overlying column of rock. In natural settings such as the Gulf Coast or the Barbados accretionary prism, values of λ approaching 1.0 have been measured. ***Hydrostatic pressure*** is the weight of a column of fluid in the interconnected pores in a rock. In that case, λ = 0.4, assuming an upper crustal rock density of 2500 kg×m$^{-3}$.

### *Calculating the Normal and Shear Stress Vectors on any Plane*

Clearly, from all of the preceding discussion, the normal and shear stress vectors on a plane is a fundamental parameter to determine. In Chapter 5, we saw

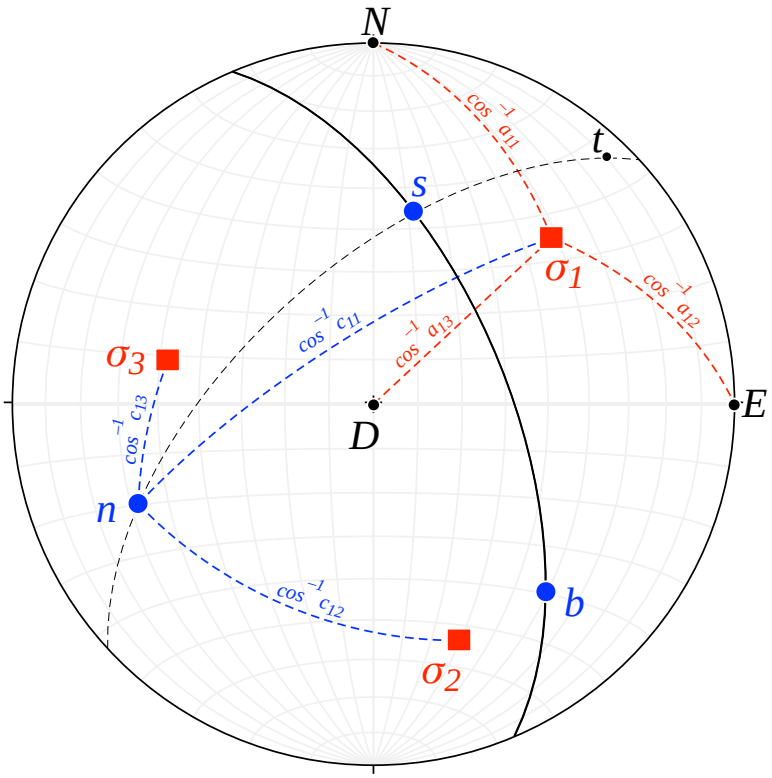


**Figure 6.12 — the coordinate systems used to calculate normal and shear stress on a plane (black great circle). The first is the North-East-Down (NED) system, the second is defined by the principal stresses (in red), and the third is the fault plane system (nbs) in blue.The direction cosines of the new coordinate system in the old coordinate system define the transformation between the two. "t" is the traction vector on the plane, which is coplanar with the pole (n) and the slip vector (s) on the plane.**

how to calculate stress on a plane for a special case where the principal stresses were parallel to the axes of our coordinate system. Here, we tackle the more general case where the principal stresses, and the plane, can have any orientation. This general case is depicted in Figure 6.12.

There are three coordinate systems and thus two transformations. We start in our usual NED coordinate system because the orientations of the principal stresses and planes are specified by their trend and plunge or strike and dip. The second coordinate system is defined by the principal stresses. The first transformation matrix, **a**, is composed of the direction cosines of the principal stresses in the NED coordinate system (Fig. 6.12). The third coordinate system is defined by the pole to the plane, **n** (X″1), the slip direction on the fault plane, **s** (X″2), and null or **b** axis (X″3), on the fault plane. The second transformation matrix, **c**, is given by the direction cosines of **nbs** in the principal stress coordinate system. Here are the steps to calculate the normal and shear stress orientations and magnitudes on the plane of interest:

1. Calculate the direction cosines of the principal stresses, and the pole to the plane, in the NED coordinate system (i.e., $X_1X_2X_3$). We assume that the trends and plunges of the three principal stresses are already known, so we can just use the equations in Table 2.1 of Chapter 2. Let's assume the those trends and plunges are labeled $trd_{\sigma i}$ and $plg_{\sigma i}$ where "$i$" is the number of the principal stress (e.g., $trd_{\sigma 1}$ is the trend of $\sigma_1$, etc.):

$$a_{ij} = \begin{pmatrix} \cos\left(trd_{\sigma 1}\right)\cos\left(plg_{\sigma 1}\right) & \sin\left(trd_{\sigma 1}\right)\cos\left(plg_{\sigma 1}\right) & \sin\left(plg_{\sigma 1}\right) \\ \cos\left(trd_{\sigma 2}\right)\cos\left(plg_{\sigma 2}\right) & \sin\left(trd_{\sigma 2}\right)\cos\left(plg_{\sigma 2}\right) & \sin\left(plg_{\sigma 2}\right) \\ \cos\left(trd_{\sigma 3}\right)\cos\left(plg_{\sigma 3}\right) & \sin\left(trd_{\sigma 3}\right)\cos\left(plg_{\sigma 3}\right) & \sin\left(plg_{\sigma 3}\right) \end{pmatrix} \tag{6.14}$$

2. Transform the pole, **n**, into the principal stress coordinate system ($X'_1X'_2X'_3$). We use our standard vector transformation to accomplish this:

$$n_i' = a_{ij}n_j \tag{6.15}$$

where $n_j$ are the direction cosines of the plane in the NED coordinate system and $a_{ij}$ is the transformation matrix composed of the direction cosines of the principal stresses calculated in Equation (6.14).

3. Calculate the traction vector, **t**, in the principal stress coordinate system using Cauchy's Law (Eqn. 5.23). Because we are in the principal stress coordinate system, the stress tensor has the form:

$$\sigma_{ij}' = \begin{bmatrix} \sigma_1 & 0 & 0 \\ 0 & \sigma_2 & 0 \\ 0 & 0 & \sigma_3 \end{bmatrix} \tag{6.16}$$

$$t_i' = \sigma_{ij}'n_j' \tag{6.17}$$

Where $n_j'$ is the pole direction cosines calculated in Equation (6.15).

4. Calculate **b'** and **s'** in stress coordinates from the following cross products (from Eqn. 2.8):

 

$$\begin{aligned}\mathbf{b}' &= \mathbf{n}' \times \mathbf{t}' = \left[\left(n_2't_3' - n_3't_2'\right)\left(n_3't_1' - n_1't_3'\right)\left(n_1't_2' - n_2't_1'\right)\right] \\ \mathbf{s}' &= \mathbf{n}' \times \mathbf{b}' = \left[\left(n_2'b_3' - n_3'b_2'\right)\left(n_3'b_1' - n_1'b_3'\right)\left(n_1'b_2' - n_2'b_1'\right)\right]\end{aligned} \tag{6.18}$$

Because $\mathbf{t}'$ is not a unit vector, $\mathbf{b}'$ and $\mathbf{s}'$ are also not unit vectors. We need to convert these to unit vectors by dividing by their magnitude in order to use them as the second transformation matrix, $\mathbf{c}$.

$$c_{ij} = \begin{pmatrix} n_1' & n_2' & n_3' \\ \dfrac{b_1'}{|\mathbf{b}|} & \dfrac{b_2'}{|\mathbf{b}|} & \dfrac{b_3'}{|\mathbf{b}|} \\ \dfrac{s_1'}{|\mathbf{s}|} & \dfrac{s_3'}{|\mathbf{s}|} & \dfrac{s_3'}{|\mathbf{s}|} \end{pmatrix} \tag{6.19}$$

Note that, unlike $\mathbf{b}'$ and $\mathbf{s}'$, we don't need to divide $\mathbf{n}$ by it's magnitude because $\mathbf{n}$ is already a unit vector.

5. Transform $\mathbf{t}'$ into the fault coordinate system using the transformation matrix, $\mathbf{c}$.

$$t_i'' = c_{ij}t_j' \tag{6.20}$$

In this coordinate system, $t''_1$ is the normal stress magnitude on the plane and $t''_3$ is the shear stress magnitude. We could do this step using a tensor transformation, but we have already calculated the traction vector so we do this simpler calculation that is easy to implement in a spreadsheet.

6. Of course, we want to know the orientations of the shear stress vector (we already know the orientation of the normal stress because it is parallel to the pole to the plane). We already know $\mathbf{s}'$ in the principal stress system so we can use a reverse transformation from that system to the NED system using the transpose of the transformation matrix, $\mathbf{a^T}$. Assuming that we have calculated $\hat{\mathbf{s}}'$ in Equation (6.19), the formula for getting the orientation of the shear stress on the fault plane is:

$$s_i = a_{ji} s_j' \tag{6.21}$$

Note that the indices of **a** have been switched in Equation (6.21) because it is a reverse transformation (old coordinates in terms of new).

7. The final step is to convert the direction cosines of **s** from Equation (6.21) back into trend and plunge format. At this point, you have had lots of practice with that but if you have forgotten, check out Equations (2.11).

The spreadsheet that accomplishes all of these steps is shown in Figure 6.13. It has been set up for the same plane and principal stress orientations as shown in Figure 6.12. When you enter principal stress orientations in a spreadsheet, make sure that the three axes are perpendicular to each other! This can be accomplished with a stereonet program. Programs such as MohrPlotter ensure that the axes are orthogonal by only allowing you to enter the truly independent parameters. This may seem to be a particularly tedious calculation, but as you will see in the Exercises, it is very powerful with a lot of practical importance for serious issues of our times.

| | A | B | C | D | E | F | G | H | I | J | K | L |
|---|---|---|---|---|---|---|---|---|---|---|---|---|
| 1 | **Principal stress** | **Trend** | **Plunge** | **Magnitude** | | **Cos alpha** | **Cos beta** | **Cos gamma** | | | | |
| 2 | Sigma 1 | 47 | 33 | 120 | | 0.5720 | 0.6134 | 0.5446 | | | | |
| 3 | Sigma 2 | 160.04 | 31.07 | 60 | | -0.8051 | 0.2924 | 0.5161 | This is the transformation matrix a(i,j) | | | |
| 4 | Sigma 3 | 282.1 | 41.38 | 20 | | 0.1573 | -0.7337 | 0.6610 | | | | |
| 5 | | | | | | | | | | | | |
| 6 | | strke/trend | Dip/Plunge | | | | | | | | | |
| 7 | Plane | 337 | 60 | | | | | | | | | |
| 8 | Pole | 247 | 30 | | | -0.3384 | -0.7972 | 0.5000 | | | | |
| 9 | | | | | | | | | | | | |
| 10 | 1. Transform the pole, **n**, into the Principal stress coordinate system: | | | | | | | | | | | |
| 11 | | | | | | | | | | | | |
| 12 | | | n(i)'=a(i,j)*n(j) | | | -0.4102 | 0.2974 | 0.8622 | 1.0000 | | | |
| 13 | | | | | | | | | | | | |
| 14 | 2. Calculate the traction vector, **p**, in the principal stress coordinate system: | | | | | | | | | | | |
| 15 | | | | | | | | | | | | |
| 16 | | | p(i)' = sigma(i,j)*n(j)' | | | -49.2226 | 17.8429 | 17.2434 | | | | |
| 17 | | | | | | | | | | | | |
| 18 | 3. Calculate **b'** and **s'** in stress coordinates from cross products: | | | | | | | | | | | |
| 19 | | | | | | | | | | Unit vectors: | | |
| 20 | | | b' = n' x p' | | | -10.2557 | -35.3653 | 7.3190 | | -0.2732 | -0.9420 | 0.1950 |
| 21 | | | | | | | | | | | | |
| 22 | | | s' = n' x b' | | | 32.6674 | -5.8401 | 17.5563 | | 0.8701 | -0.1556 | 0.4676 |
| 23 | | | | | | | | | | | | |
| 24 | 4. Transformation matrix from streee coordinate system into fault coordinate system: | | | | | | | | | | | |
| 25 | | | | | | | | | | | | |
| 26 | | | | | | -0.4102 | 0.2974 | 0.8622 | This transformation matrix c(i,j), is composed of the direction cosines of **n**, **b**, and **s** in the stress coordinate system | | | |
| 27 | | | | c(i,j) = | | -0.2732 | -0.9420 | 0.1950 | | | | |
| 28 | | | | | | 0.8701 | -0.1556 | 0.4676 | | | | |
| 29 | | | | | | | | | | | | |
| 30 | 5. Transform the traction vector into the fault coordinate system: | | | | | | | | | | | |
| 31 | | | | | | normal stress | | Shear stress | | | | |
| 32 | | p(i)'' = c(i,j)*p(j)' | | | | 40.3635 | 0 | -37.5421 | | | | |
| 33 | | | | | | | | | | | | |
| 34 | 6. Transform the shear stress vector back into geographic coordinates: | | | | | | | | | | | |
| 35 | | | | | | | | | | | | |
| 36 | | s(i) = a(j,i)*s(j)' | | | | 26.1480 | 5.4489 | 26.3836 | | 0.6965 | 0.1451 | 0.7028 |
| 37 | | | | | | | | | | | | |
| 38 | 7. Convert to trend and plunge of the slip vector | | | | | | | | | | | |
| 39 | | Trend | Plunge | | | | | | | | | |
| 40 | s= | 11.77127 | 44.6481114 | | | | | | | | | |

note switch of indices because it is the reverse transformation!

**Figure 6.13 — The spreadsheet to calculate the normal and shear stress on a plane of any orientation, given a randomly orientated set of principal axes.**

## *The Principal Stress Ratio*

There is one final issue that is important for understanding the relationship between stress and faulting: the importance of $\sigma_2$ relative to $\sigma_1$ and $\sigma_3$. This relationship is called the principal stress ratio and it takes the form of:

$$R = \frac{\sigma_2 - \sigma_1}{\sigma_3 - \sigma_1} = \left| \frac{c_{13}c_{23}}{c_{12}c_{22}} \right| \tag{6.22}$$

Remarkably enough, this ratio depends on nothing more that the direction cosines of the second transformation matrix, **c**, as you can demonstrate to yourself by calculating $R$ from **c** in Figure 6.14. $R$ varies between 0 and 1; when $R = 0$, $\sigma_2 = \sigma_1$ and when $R = 1$, $\sigma_2 = \sigma_3$. For planes that are not parallel to a principal stress, $R$ can have a very significant effect on whether or not the plane is likely to be reactivated — because the magnitude (but not the orientation) of the normal stress on the plane varies with $R$ — as well as the orientation of shear stress on the plane. Because $R$ is a function of the direction cosines of **c**, it is the one additional parameter that can be determined when fault planes or earthquake focal mechanisms are inverted for principal stress orientations.

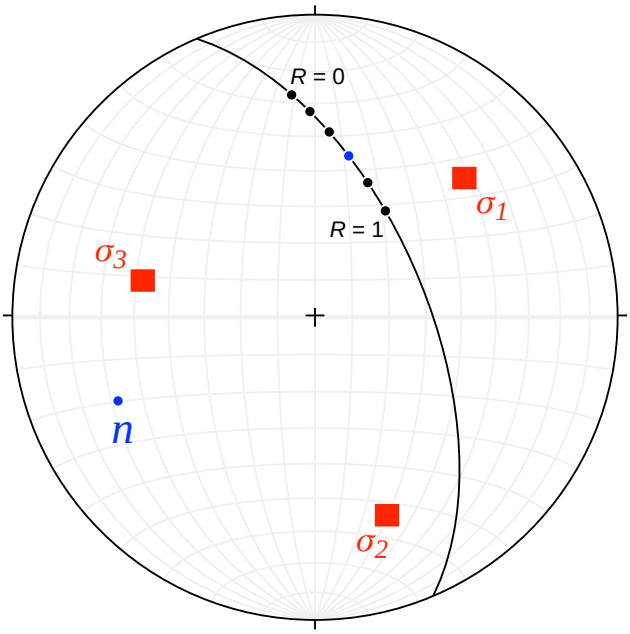


**Figure 6.14 — The variation in orientation of shear stress resolved on a plane with change in the parameter, *R*. The magnitudes of $\sigma_1$ and $\sigma_3$ are held fixed and the only thing that varies is the magnitude of $\sigma_2$. The fault plane and orientation and magnitudes of the stresses are the same as in Figures 6.12 and 6.13. The blue dot at $R = 0.6$ is the actual value calculated in Figure 6.13. In this case, the variation in shear stress on the plane is about 40°; with other geometries the variation can approach 90°.**

Although we will not do a full inversion for stress in this course, it is a common calculation amongst structural geologists and geophysicists. Some authors use a different formulation of the principal stress ratio:

$$\Phi = \frac{\sigma_2 - \sigma_3}{\sigma_1 - \sigma_3} \tag{6.23}$$

Thus, $\mathbf{\Phi} = 1-R$. As we're talking about inverting fault planes and earthquakes for stress, we should wrap up this section with a note of caution. All methods to do this calculation have two assumptions in common: (a) that faults slip in the direction of maximum resolved shear stress on the plane, and (b) that the stress orientation and magnitude does not vary during the faulting. Both of these assumptions require careful evaluation as there are many instances where they could be questioned. In a subsequent chapter, we will see a simpler approach to analyzing faults using infinitesimal strain.

 

# Exercises—Chapter 6

All of the following exercises should be done either in a spreadsheet or Matlab. You will need the MohrPlotter program that you downloaded last week for some of the exercises.

1. The map, below, is a modified version of the Mystic Lake Quadrangle. The objective is to calculate the slip on the unnamed fault that crosses the image and has a strike and dip of 299, 38 (RHR). Coordinates of three points are given, one on the fault plane and the others on the fold axis at the contact between Kmt and Kk in the hanging wall and the footwall. Southwest of the fault, the fold axis has a trend and plunge of 056, 25 and to the northeast it is 042, 12. Construct a spreadsheet (or use Matlab) to calculate the slip on the fault as in Figure 6.5, using Equations 6.4 and 6.5.

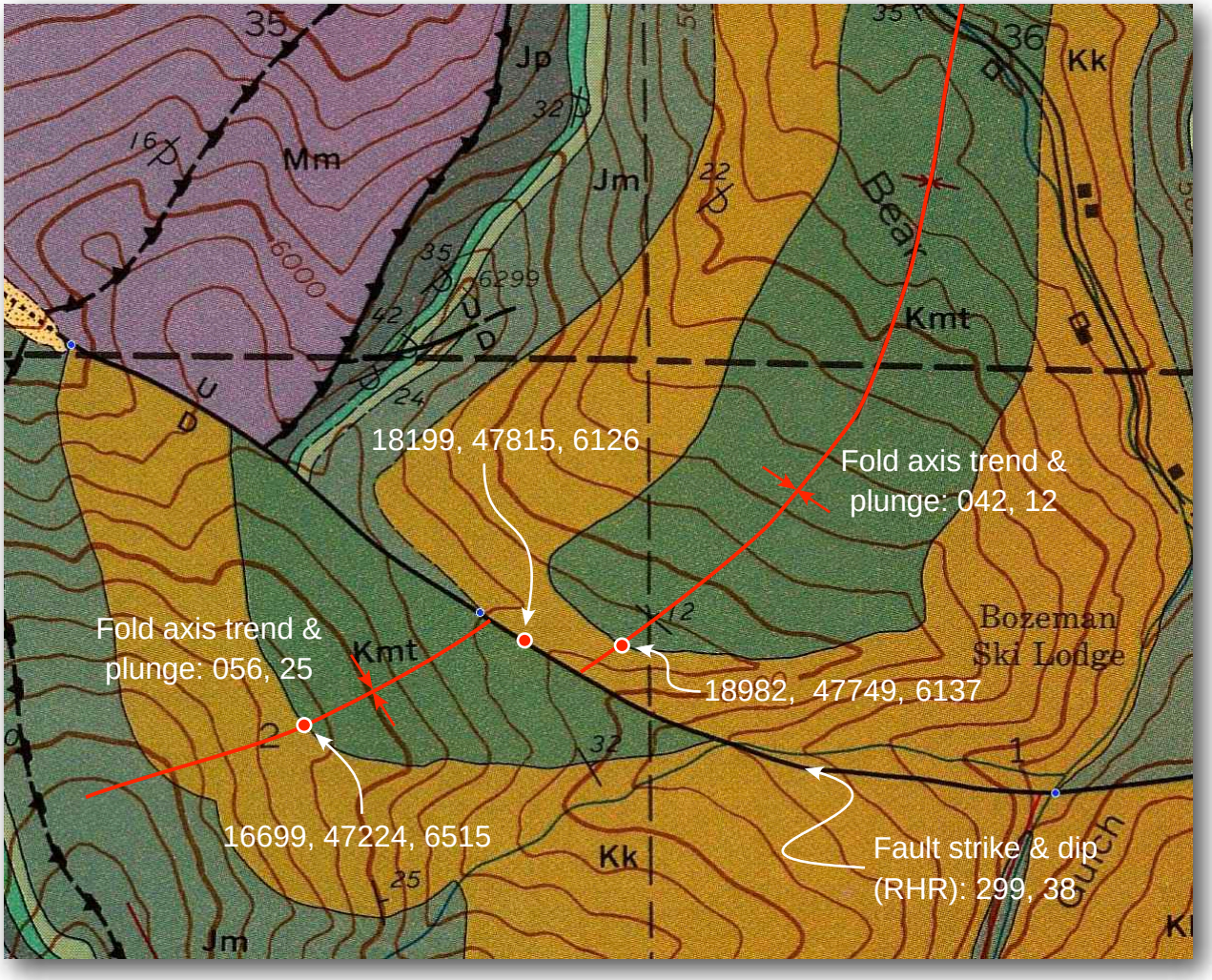

2. Principal stresses are shown below in a North-East-Down coordinate system. They have the following values and their orientations are known in the stereonet, below. You can check your answer in MohrPlotter but must do the problem in a spreadsheet or Matlab:

| Stress | Trend | Plunge | Magnitude |
|---|---|---|---|
| $\sigma_1$ | 20 | 30 | 50 |
| $\sigma_2$ | 255.8 | 44.2 | 30 |
| $\sigma_3$ | 130 | 31 | 10 |

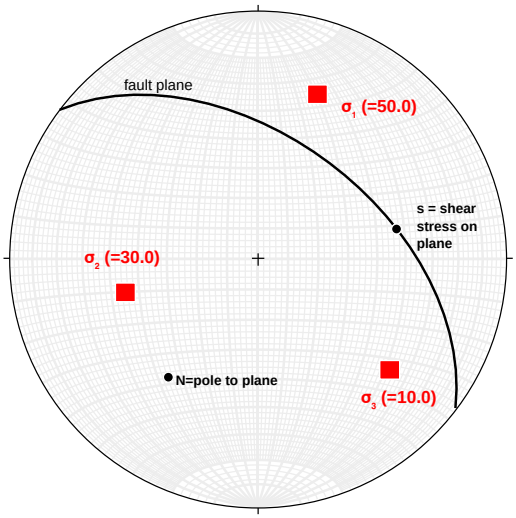


a. Calculate the orientation and magnitude of the shear stress on the plane which is oriented 307, 50 as outlined in this chapter or following the steps in section 6.5 of Allmendinger et al. (2012). You do not have to do the tensor transformation described in section 6.5.5; instead, transform the traction vector, **t**, into the fault plane coordinate system. Note: stresses, above, define a left-handed coordinate system but you want a right handed system!

b. Part (a) uses a principal stress ratio of 0.5; try the problem again using values of 0.1 and 0.9 to see how that affects the orientation of the shear stress on the plane.

3. A geologist measures 8 conjugate faults in a region; the strikes and dips are listed, below. All have normal displacement.

| | | | | | |
|---|---|---|---|---|---|
| 090.0 | 68.6 | S | 083.1 | 66.0 | S |
| 088.4 | 52.6 | S | 097.1 | 64.3 | S |
| 304.4 | 68.3 | N | 311.6 | 58.0 | N |
| 298.7 | 57.6 | N | 296.5 | 69.6 | N |

a. Determine the orientation of $\sigma_1$, $\sigma_2$, and $\sigma_3$ from these data. Be as accurate as possible

b. What are the angle and the coefficient of friction for this data set?

4. The state of Oklahoma has seen a very substantial increase in induced seismicity since 2005 as large volumes of waste water related to conventional oil production have been reinjected into the subsurface. The map to the right shows known faults in red, injection wells in black target circles scaled by injection volume and earthquakes in blue. The red star labeled OKC is Oklahoma City. Earthquake and in situ stress measurements suggest that, at 3 km depth (most of the seismicity occurs between 2 and 4 km depth) $\sigma_1$ is horizontal and trends 070, $\sigma_3$ is also horizontal and trends 340, and $\sigma_2$ is vertical and equal to the lithostatic load, for which you can assume a density of 2500 kg m$^{-3}$. The faults are high angle reverse faults; their detailed dips are poorly know but for this problem we will assume that they dip 70°. A downloadable data file with orientations of about 40 faults can be found on the course web site. This problem will also require your use of MohrPlotter.

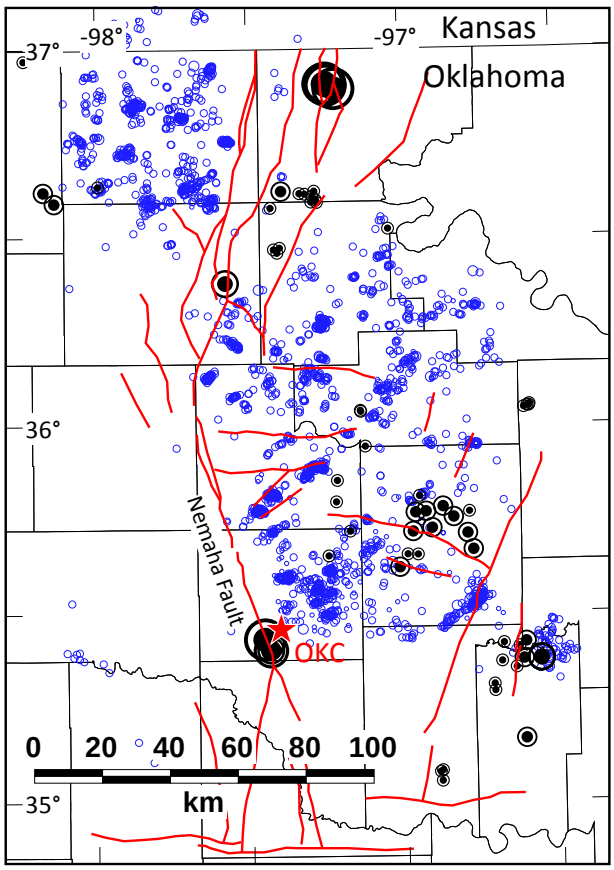


(a) The magnitudes of the principal stresses, especially $\sigma_1$ and $\sigma_3$, are not well known. You should calculate $\sigma_2$ assuming that it is equal to the lithostatic load. Assume that $\sigma_1$ = 100 MPa and $\sigma_3$ = 40 MPa.

(b) Open MohrPlotter and enter the stresses and their orientations as described above in the stress tensor window (Calculate>Enter as Tensor). To complete the entry, press the Calculate button. In the MohrPlotter Window, enter the coefficient of static friction of 0.85 which corresponds with Byerlee's law for these depths. Choose File>Import Planes to read in the data file on fault plane orientations that you downloaded from the course Web site. You will probably want to turn off plotting of construction lines (Plot>Show Construction Lines is unchecked). In the Inspector Palette (Window>Inspector), select the Envelopes & Points tab and make sure that the slip tendency checkbox is checked. Slip tendency will color the fault planes both in the stereonet view and the Mohr's Circle view according to how likely the fault is to slip under these conditions: the warmer (i.e., more red) the color, the

more likely slip is to occur. Once you have done all that, does any plane appear that it will slip (and produce an earthquake) under these circumstances?

(c) Now use the up-arrow next to the "P(fluid) =" text box to increase the pore fluid pressure gradually. Watch both the Mohr Circle plot and the stereonet view to see how the color of the planes changes as the pore fluid pressure increases. When the pressure reaches hydrostatic (which you will need to calculate), stop increasing the pore fluid pressure. Save your plot to print and turn in. The program saves plots as .svg files that can be read by most modern vector graphics programs. SVG files can also be displayed and printed at high resolution by opening them in any web browser.

(d) Which faults are highly susceptible to reactivation? What are their orientation(s) and how do they compare to the streaks of seismicity visible in the map that accompanies the beginning of this question?

(e) The Nemaha fault which runs right next to Oklahoma City has some of the largest injection wells located right along it's trace. Given the length of the fault, it would be capable of generating a large, destructive earthquake. What is the likelihood that it will be reactivated and why?

(f) A group of large injection wells are located along faults immediately south of the Kansas-Oklahoma border, and yet they do not appear to be associated with significant seismicity. Why is that the case and does that mean that companies can continue to inject waste water there with impunity?

 

# Chapter 7

## *Deformation and Infinitesimal Strain*

### Introduction

In this chapter, we turn our focus to ***deformation*** — the quantification of changes in shape and/or volume of a rock, plus any associated translations and rotations — that is the bread and butter of most structural geologists. It will be a significant departure from the topics of the last two chapters in several fundamental ways: stress is an instantaneous property that exists only in the instance that the

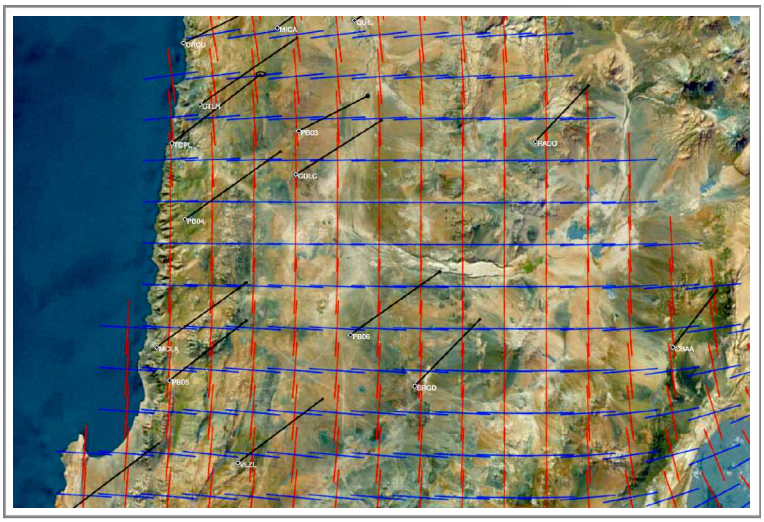

force is applied. Deformation, on the other hand, still exists in rocks hundreds of millions, or even billions, of years after the associated stresses have dissipated. Deformation is also cumulative: one can superpose many episodes of deformation produced by completely unrelated geologic events. Finally, because deformation represents a change in shape or size, it is a comparison between two different states, an initial and a final state of the material. Eventually, we will have to come to grips with the fact that these represent two possible reference states. Whenever we consider the change in some property, we are really talking about mathematical derivatives: local slopes along a curve of a continuous function. In our case, we will be looking at the change in position, or the change in displacement, with respect to position.

# Strain

## *One Dimensional Measures of Strain*

A structural geologist can make three different types of measurements in order to quantify strain: changes in line length, angles, or volumes. In the discussion that follows, we'll use a capital "$X$" to indicate the coordinate of a point in the initial state (the ***material coordinate system***) and a small "$x$" for the final state (the ***spatial coordinates***, implicitly at time, $t$). We'll start with the change in length of a line. As you can see in Figure 7.1, the initial and final lengths of the line are:

$$\ell_i = X_b - X_a = \Delta X \quad \text{and} \quad \ell_f = x_b - x_a = \Delta x \tag{7.1}$$

Thus, the ***stretch***, S can be defined as:

$$S = \frac{\ell_f}{\ell_i} = \frac{\Delta x}{\Delta X} \tag{7.2a}$$

$$s = \frac{\ell_i}{\ell_f} = \frac{\Delta X}{\Delta x} \tag{7.2b}$$

The initial length, $\ell_i$, in the denominator of Equation (7.2a) means that the initial state is the reference state. In (7.2b), $\ell_f$ occurs in the denominator so the final state is the frame of reference. Another way to describe this deformation is by looking at the displacement, $u$, of the end points of the lines:

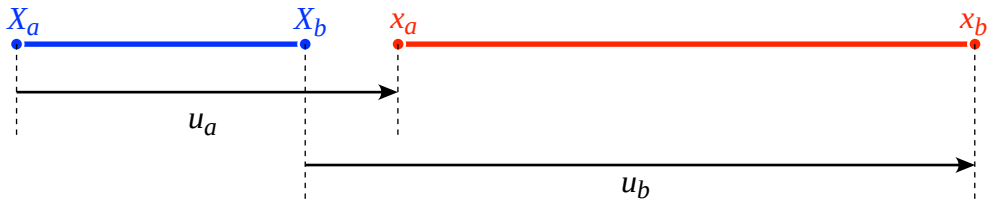


**Figure 7.1 — The change in length of a line. The initial state is shown in blue with capital "X"s and the final state in red with small "x"s. $u_a$ and $u_b$ are the displacements of the end points of the line.**

$$u_a = x_a - X_a \quad \text{and} \quad u_b = x_b - X_b \tag{7.3}$$

And the change in displacement, $\Delta u$, is:

$$\Delta u = u_b - u_a = (x_b - X_b) - (x_a - X_a) = (x_b - x_a) - (X_b - X_a) = \ell_f - \ell_i = \Delta\ell \tag{7.4}$$

Thus, the ***extension***, $E$ or $e$, can be defined as the change in length over the initial length (an initial state frame of reference) or the final length (a final state frame of reference):

$$E = \frac{\ell_f - \ell_i}{\ell_i} = \frac{\Delta\ell}{\ell_i} = \frac{\Delta u}{\Delta X} \tag{7.5a}$$

$$e = \frac{\ell_f - \ell_i}{\ell_f} = \frac{\Delta\ell}{\ell_f} = \frac{\Delta u}{\Delta x} \tag{7.5b}$$

Now let's turn our attention to changes in angles and to do so we need to bring a second dimension which we will (temporarily) call $Y$ and $y$. Consider a line initially perpendicular to the X direction that is displaced in the X direction by an amount that varies with the distance, or length, $\Delta Y$ (Fig. 7.2). We can write:

$$u_a = x_a - X_a \quad \text{and} \quad u_b = x_b - X_b$$
$$\Delta u = u_b - u_a = (x_b - X_b) - (x_a - X_a) = (x_b - x_a) - (X_b - X_a) \tag{7.6}$$

But, $(X_b - X_a) = 0$, so $\Delta u = (x_b - x_a)$

We define the ***shear strain***, $\gamma$, and the ***angular shear***, $\psi$, as:

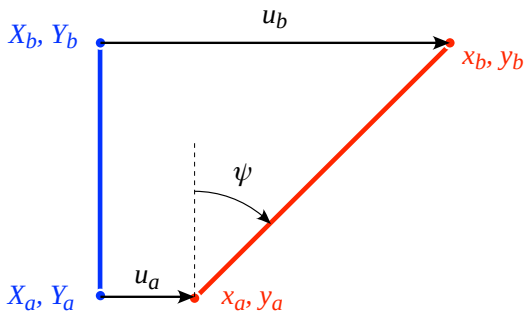


**Figure 7.2 — the change in angle of a line that is originally perpendicular to the X-axis and the displacement, *u*.**

$$\gamma = \frac{\Delta u}{\Delta Y} \quad \text{and} \quad \psi = \tan^{-1}\left(\frac{\Delta u}{\Delta Y}\right) \tag{7.7}$$

As we will see a bit later, $\gamma$ as defined in Equation 7.7 is actually known as the ***engineering shear strain*** to distinguish it from a similar but distinct quantity known as the ***tensor shear strain***.

## *Three Dimensional Deformation*

Now it is time to extend these concepts to three dimensions. The ratios in Equations (7.2) and (7.5) are gradients of change in position with respect to the new or old position and gradients of displacement with respect to position. In an arbitrarily deformed body, these should vary in the three directions of our Cartesian coordinate systems. That is:

$$\frac{\Delta x}{\Delta X} = \lim \frac{\partial x_i}{\partial X_j} = D_{ij} \quad \text{and} \quad \frac{\Delta u}{\Delta X} = \lim \frac{\partial u_i}{\partial X_j} = E_{ij} \tag{7.8}$$

where $D_{ij}$ is the ***deformation gradient tensor*** and $E_{ij}$ is the ***displacement gradient tensor***. The equations in (7.8) are referenced to the initial state and, as you might expect, there are equivalent forms referenced to the final state. We need to use partial derivatives because the displacement is a function of gradients along the three axes of the coordinate system.

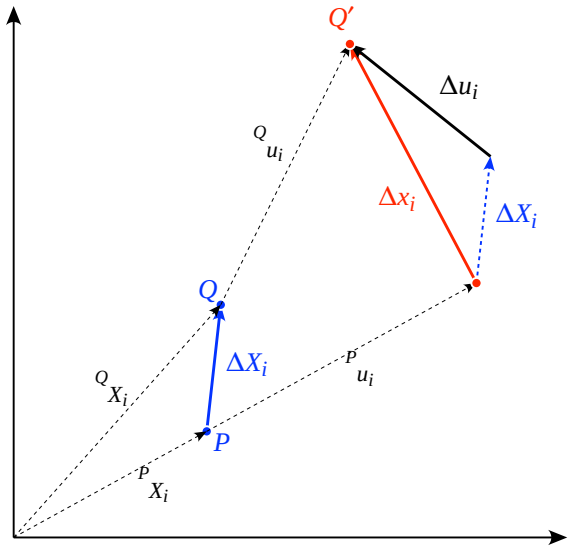


**Figure 7.3 — The deformation of line PQ in undeformed state (in blue) to P′Q′ in the final state (in red).**

Figure 7.3 shows a more general case. The difference in displacement vectors is:

$$\Delta u_i = {}^{Q}u_i - {}^{P}u_i = \frac{\partial u_i}{\partial X_j}{}^{Q}X_j - \frac{\partial u_i}{\partial X_j}{}^{P}X_j = \frac{\partial u_i}{\partial X_j}\left({}^{Q}X_j - {}^{P}X_j\right) = \frac{\partial u_i}{\partial X_j}\Delta X_j \tag{7.9}$$

Thus, we can write:

$$\Delta u_i = \frac{\partial u_i}{\partial X_j}\Delta X_j = E_{ij}\Delta X_j \quad \text{or} \quad du_i = \frac{\partial u_i}{\partial X_j}dX_j = E_{ij}dX_j \tag{7.10}$$

We can integrate the right side of equation (7.10) to yield a general expression for the displacement at any position:

$$\int du_i = \int E_{ij}dX_j \quad \Rightarrow \quad u_i = t_i + E_{ij}X_j \tag{7.11}$$

where **u** is the displacement vector at position **X**, and **t** is a constant of integration that represents the displacement of a point at the origin of the coordinate system. This equation holds as long as the strain is ***homogeneous***; that is, $E_{ij}$ is the same throughout the deformed body. Because Equation (7.11) represents three linear equations, it follows that *a line that is straight before deformation will also be straight after the deformation*; likewise *parallel lines in the initial state will remain parallel in the final state*.

Just as we did for the displacement gradient tensor, the relationships depicted in Figure 7.3 can also be used to derive an expression for mapping points in the initial state into the final state:

$$\Delta x_i = {}^{Q}x_i - {}^{P}x_i = \frac{\partial x_i}{\partial X_j}{}^{Q}X_j - \frac{\partial x_i}{\partial X_j}{}^{P}X_j = \frac{\partial x_i}{\partial X_j}\left({}^{Q}X_j - {}^{P}X_j\right) = \frac{\partial x_i}{\partial X_j}\Delta X_j = D_{ij}\Delta X_j \tag{7.12}$$

Once again, assuming homogeneous strain, we can integrate both sides of the equation to get:

$$\int dx_i = \int D_{ij}dX_j \quad \Rightarrow \quad x_i = c_i + D_{ij}X_j \tag{7.13}$$

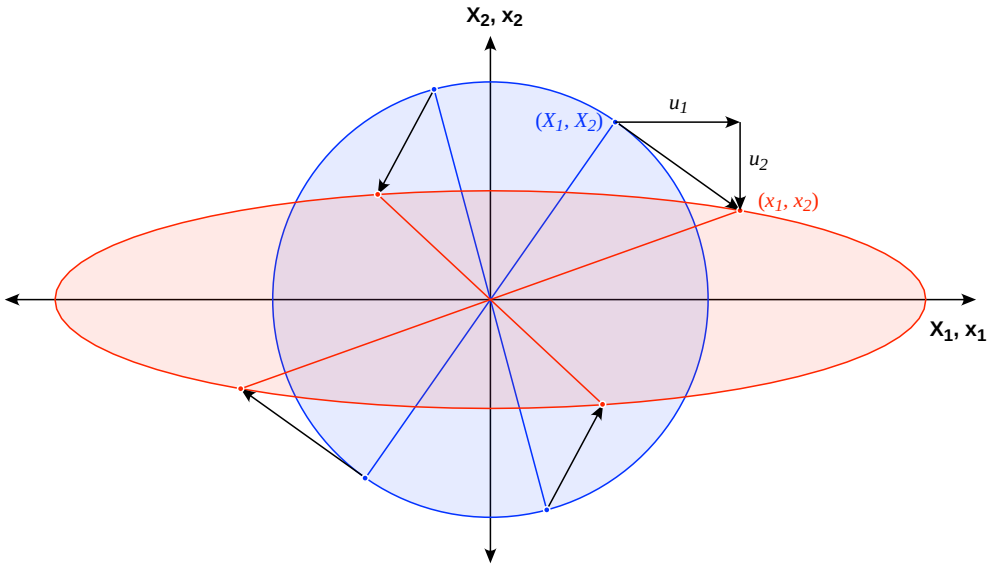


**Figure 7.4 — The displacement of points in an initial circle depend on their initial positions. Overall, the circle deforms to an ellipse. Note that the arrows represent finite displacement and not the path that the point follows.**

Where **x** is the new position, **X** is the old position, and **c** is a constant of integration that represents the coordinates of a point initially at the origin of the coordinate system.

Recall that a second order tensor is a linear vector operator. The displacement gradient tensor relates the displacement of a point to its position, whereas the deformation gradient tensor relates the position in the initial state to the position of the same point in the final state (Fig. 7.4). If we know the tensor, then the displacement of the point and it's new position can be calculated from Equations (7.11) and (7.13). ***All of the equations that we have developed so far hold for any magnitude of deformation***. To understand the nature of these tensors, and explore some common applications, some simplifying assumptions are in order.

## *Infinitesimal Strain*

If we assume that the distortions are small, a number of simplifications can be made. At the most basic level, a small or ***infinitesimal strain*** assumption permits us to consider that the initial and final states are identical, thus cutting in half the number of tensors to worry about. Additional benefits will become appar-

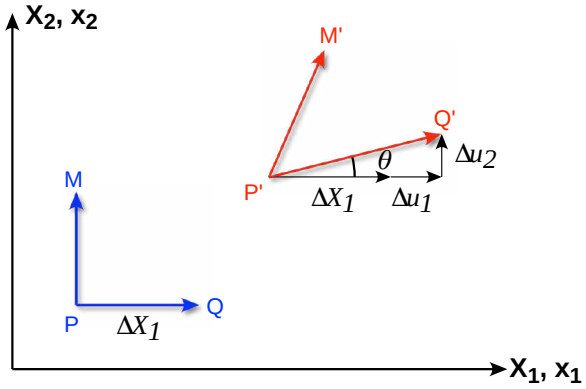


**Figure 7.5 — The deformation of two lines originally perpendicular to the axes of the coordinate system.**

ent, below, but first let's take a closer look at the components of the displacement gradient tensor, $E_{ij}$.

It will probably come as no surprise the values along the principal diagonal, $E_{11}$, $E_{22}$, and $E_{33}$ represent the extensions of lines that are parallel to the corresponding axes. The off-diagonal components are more interesting, which will be illustrated by examining a special case in two dimensions (Fig. 7.5). From the geometry, you can see that:

$$\tan\theta = \frac{\Delta u_2}{\Delta X_1 + \Delta u_1} \tag{7.14}$$

and by making our infinitesimal strain assumption, you can see that $\Delta X_1 \gg \Delta u_1$. Thus, we can write that:

$$\tan\theta \approx \frac{\Delta u_2}{\Delta X_1} \tag{7.15}$$

For very small angles, the tangent of an angle is equal to the angle itself measured in radians, so we can further write:

$$\theta \approx \frac{\Delta u_2}{\Delta X_1} = \frac{\partial u_2}{\partial X_1} = E_{21} \tag{7.16}$$

Thus $E_{21}$ is the counterclockwise rotation of a line parallel to the $X_1$ axis towards the $X_2$ axis. Likewise, $E_{12}$ would be the clockwise rotation of a line parallel to the $X_2$ axis towards the $X_1$ axis. The first subscript indicates the axis that the rotation is towards and the second subscript indicates the axis to which the line is, initially,

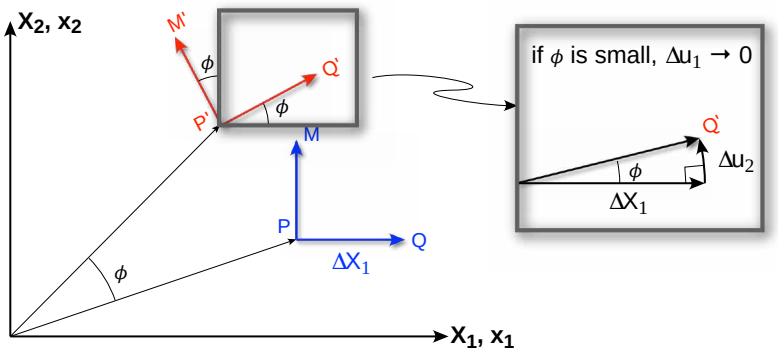


**Figure 7.6 — The pure rotation of two perpendicular vectors parallel to the axes of the coordinate system.**

parallel. Note that the $E_{21} + E_{12}$ *combined* equal the change in angle, or shear strain, of two lines initially at 90° to each other. They are ***tensor shear strain*** components and each is equal to one-half of the engineering shear strain of Equation (7.7).

There is one more thing to learn about the displacement gradient tensor and, by extension, the deformation gradient tensor as well. Again, we'll examine a special case (Fig. 7.6). As in Figure 7.5, there are two vectors in the initial, undeformed configuration that are parallel to the coordinate axes. This time, however, we introduce a pure rotation by a small angle, $\phi$, with no deformation; that is, the vectors P′Q′ and P′M′ are still perpendicular after the rotation. You can see that:

$$E_{11} = \frac{\Delta u_1}{\Delta X_1} = 0 \quad \text{and} \quad E_{21} = \frac{\Delta u_2}{\Delta X_1} = \tan\phi \approx \phi \tag{7.17}$$

Likewise, $E_{22} = 0$ but $E_{12} = -\phi$ because it is also a counterclockwise rotation even though positive $E_{12}$ should be a clockwise rotation. Thus our two dimensional displacement gradient tensor for the case of pure rotation is:

$$E_{ij} = \begin{bmatrix} 0 & -\phi \\ \phi & 0 \end{bmatrix} \tag{7.18}$$

We've just learned two really important things: First, ***the displacement gradient tensor is an asymmetric tensor*** (because $-\phi \neq \phi$), and second, ***the tensor includes both strain and rotation***.

Any asymmetric matrix can be additively decomposed into a symmetric matrix and an antisymmetric matrix. An antisymmetric matrix has zeros along the

principal diagonal and the values below the principal diagonal must be the negative of those above the principal diagonal. For the displacement gradient tensor, we can write:

$$E_{ij} = \varepsilon_{ij} + \omega_{ij} \tag{7.19}$$

where

$$\varepsilon_{ij} = \frac{1}{2}\left(E_{ij} + E_{ji}\right) \quad \text{and} \quad \omega_{ij} = \frac{1}{2}\left(E_{ij} - E_{ji}\right) \tag{7.20}$$

$\varepsilon_{ij}$ is the symmetric ***infinitesimal strain tensor*** and $\omega_{ij}$ is the antisymmetric ***rotation tensor*** or ***axial vector***. $\omega_{ij}$ can be turned into a rotation vector, $r_i$, as follows:

$$r_1 = \frac{-\left(\omega_{23} - \omega_{32}\right)}{2}, \quad r_2 = \frac{-\left(-\omega_{13} + \omega_{31}\right)}{2}, \quad \text{and} \quad r_3 = \frac{-\left(\omega_{12} - \omega_{21}\right)}{2} \tag{7.21}$$

the magnitude of $\mathbf{r}$ gives the amount of rotation (in radians) and the unit vector, $\hat{\mathbf{r}}$, gives the orientation of the rotation axis. Equation (7.19) basically says that deformation is equal to a strain plus a rotation, thought that is strictly true only for small strains.

Like any symmetric tensor, the infinitesimal strain tensor has principal axes, found by solving the eigenvalue problem, and invariants. The first invariant of the infinitesimal strain tensor:

$$I_\varepsilon = \varepsilon_{11} + \varepsilon_{22} + \varepsilon_{33} = \varepsilon_1 + \varepsilon_2 + \varepsilon_3 \tag{7.22}$$

is the infinitesimal ***volume strain*** or the ***dilatation***. The infinitesimal strain ellipsoid is defined by the equation:

$$\frac{x_1^2}{\left(1+\varepsilon_1\right)^2} + \frac{x_2^2}{\left(1+\varepsilon_2\right)^2} + \frac{x_3^2}{\left(1+\varepsilon_3\right)^2} = \frac{x_1^2}{S_1^2} + \frac{x_2^2}{S_2^2} + \frac{x_3^2}{S_3^2} = \frac{x_1^2}{\lambda_1} + \frac{x_2^2}{\lambda_2} + \frac{x_3^2}{\lambda_3} = 1 \tag{7.23}$$

where $S_1$, $S_2$, and $S_3$ are the stretches along the principal axes and $\lambda_1$, $\lambda_2$, and $\lambda_3$ are the quadratic elongations. If the intermediate principal stretch is 1, the deformation is two dimensional and we refer to it as ***plane strain***.

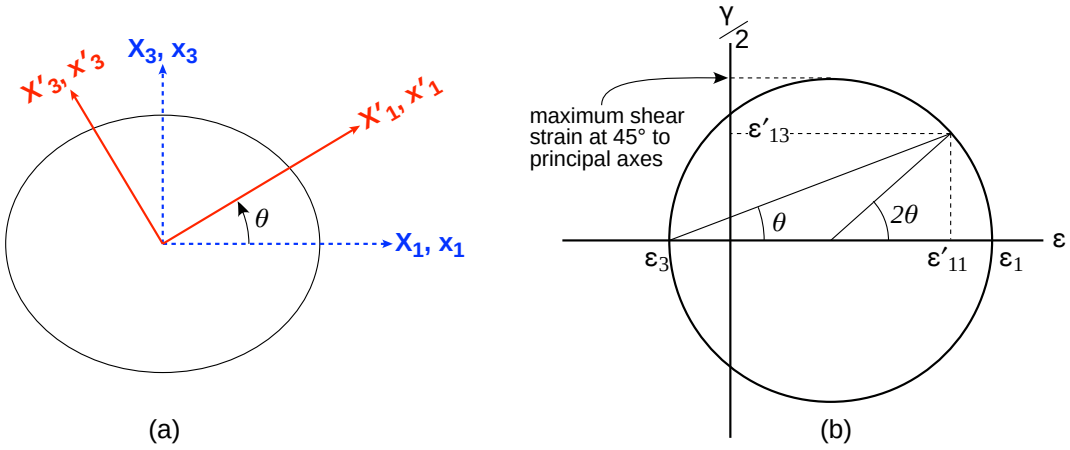


**Figure 7.7 — The construction of the Mohr's Circle for infinitesimal strain. (a) The infinitesimal strain ellipsoid with the old coordinate system in blue and the new, primed coordinate system in red, rotated about the intermediate principal axis by an angle θ. (b) the Mohr's Circle for infinitesimal strain. Elongations are plotted on the horizontal axis and the shear strain on the vertical axis.**

Just like any symmetric tensor, the infinitesimal strain tensor can be represented by a Mohr's Circle construction (Fig. 7.7). We start with the axes of the infinitesimal strain ellipse parallel to the axes of the coordinate system:

$$\varepsilon_{ij} = \begin{bmatrix} \varepsilon_1 & 0 & 0 \\ 0 & \varepsilon_2 & 0 \\ 0 & 0 & \varepsilon_3 \end{bmatrix} \tag{7.24}$$

And transform the tensor by a rotation of $\theta$ about the intermediate principal axis (Fig. 7.7a). The transformation matrix is:

$$a_{ij} = \begin{pmatrix} \cos\theta & 0 & \sin\theta \\ 0 & 1 & 0 \\ -\sin\theta & 0 & \cos\theta \end{pmatrix} \tag{7.25}$$

The tensor transformation equation is:

$$\varepsilon_{ij}' = a_{ik} a_{jl} \varepsilon_{kl} \tag{7.26}$$

So, the infinitesimal strain tensor in the new coordinate system is:

$$\varepsilon_{ij}{}' = \begin{bmatrix} \varepsilon_{11}{}' & 0 & \varepsilon_{13}{}' \\ 0 & \varepsilon_2 & 0 \\ \varepsilon_{31}{}' & 0 & \varepsilon_{33}{}' \end{bmatrix} = \begin{bmatrix} \left(\varepsilon_1 \cos^2\theta + \varepsilon_3 \sin^2\theta\right) & 0 & \left(\left(\varepsilon_3 - \varepsilon_1\right)\cos\theta \sin\theta\right) \\ 0 & \varepsilon_2 & 0 \\ \left(\left(\varepsilon_1 - \varepsilon_3\right)\cos\theta \sin\theta\right) & 0 & \left(\varepsilon_1 \sin^2\theta + \varepsilon_3 \cos^2\theta\right) \end{bmatrix} \quad (7.27)$$

And the equations for Mohr's Circle for infinitesimal strain (Fig. 7.7b) are:

$$\begin{aligned} \varepsilon_{11}{}' &= \frac{\left(\varepsilon_1 + \varepsilon_3\right)}{2} + \frac{\left(\varepsilon_1 - \varepsilon_3\right)}{2}\cos 2\theta \\ \varepsilon_{13}{}' &= \frac{\gamma}{2} = \frac{\left(\varepsilon_1 - \varepsilon_3\right)}{2}\sin 2\theta \end{aligned} \quad (7.28)$$

One of the most important features of infinitesimal strain, which is made especially clear by the Mohr's Circle construction, is that ***the maximum infinitesimal shear strain is oriented at 45° to the principal axes of strain***. This has profound implications for our practical study of common structures, from brittle to ductile shear zones (Fig. 7.8).

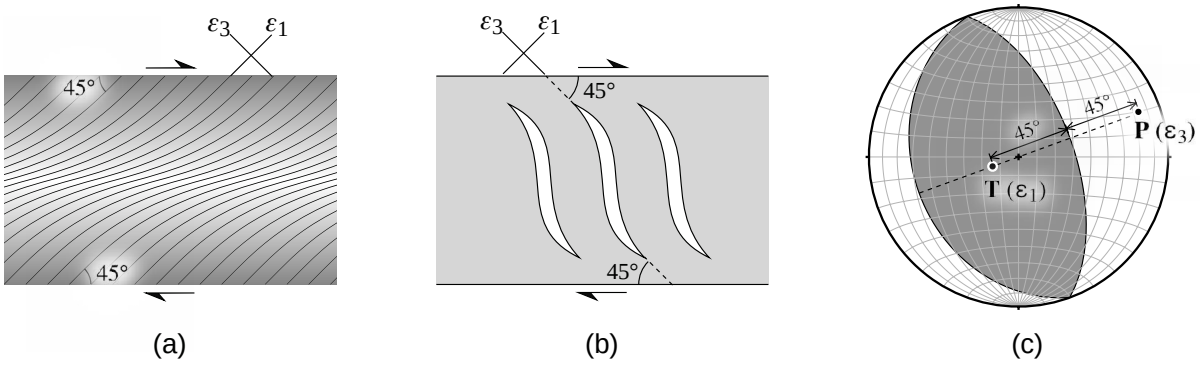


**Figure 7.8 — Three geological/geophysical examples demonstrating the importance of the fact that the principal axes of infinitesimal strain are at 45° to the planes of maximum shear strain. (a) a heterogeneous ductile shear zone in granitoid rocks, (b) sigmoidal extension fractures in a brittle shear zone, (c) P & T axes for an earthquake or fault slip analysis. Despite their names, P and T axes are infinitesimal principal strain axes.**

# Some Geological Applications

Many structural geology problems we face break the assumptions of infinitesimal strain and thus require a more complicated analysis. However, the fields of active tectonics and brittle fault analyses are of significant importance for modern structural geology and are amenable to an infinitesimal strain approach. That is because the deformation accrues over a short, commonly geologically instantaneous, period of time and thus is very small in magnitude.

## *Strain from GPS*

The Global Positioning System (GPS) has revolutionized earth sciences in the last 25 years by providing geologists and geophysicists with real time monitoring of active deformation. Modern continuous geodetic GPS provides sub-centimeter resolution of the displacement of monuments or stations relative to a stable reference frame. Because the changes in displacements measured are on the order of centimeters between stations separated by tens of kilometers, the deformation measured by GPS certainly qualifies as infinitesimal. GPS data present a common circumstance: we know displacements and want to calculate the strain rather than knowing the strain tensor and calculating displacements at different points.

We start with a simpler task: calculating the one-dimensional extension given a transect of GPS stations. Recall that, from Equation (7.7), the one dimensional extension is just:

$$E = \frac{\Delta u}{\Delta X}$$

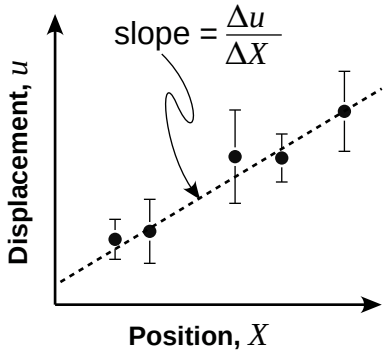


**Figure 7.9 — Plotting displacement against position in a GPS transect in order to determine the 1D extension. Because the slope is positive, the data represent an elongation; a negative slope would indicate shortening in the direction of the transect.**

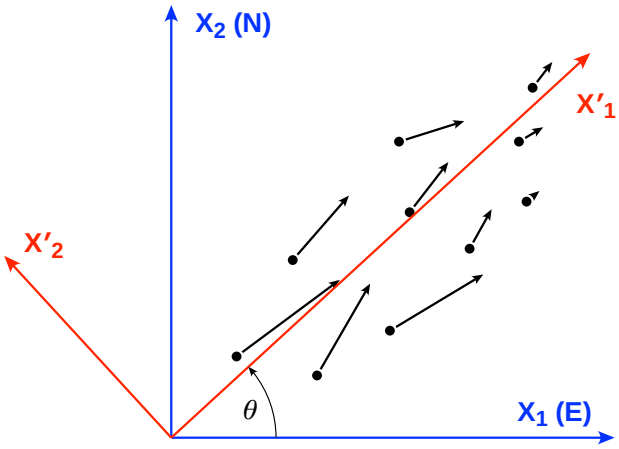


**Figure 7.10 — Map view of GPS vectors and a coordinate transformation so that the new coordinate system is parallel to the GPS mean displacement vector.**

Therefore, one can plot the displacement at a station on the Y-axis against the position of the station on the X-axis and fit a straight line (for homogeneous strain) or a curve (for heterogeneous strain) to the data points as in Figure 7.9. The equation for a straight line on the graph is:

$$u = t + EX \tag{7.29}$$

where $t$ is the intercept on the vertical axis. Note how similar this equation is to Equation (7.11).

To get to the point of making a graph like that shown in Figure 7.9, you will probably have to do several intermediate steps, which we have the background to do. It is unlikely that the GPS displacement (or velocity) vectors, or the transect, will be parallel to North or East. While you could eyeball the best orientation of the transect and then calculate the distances between each station, there is a more elegant way. First, calculate the orientation of the mean GPS vector just like we did in Chapter 2. Then rotate the coordinate system so it is parallel to the mean vector and transform both the station positions and the displacement vectors into this new coordinate system (Fig. 7.10). The two dimensional transformation matrix for this operation will be:

$$a_{ij} = \begin{pmatrix} \cos\theta & \cos(90-\theta) \\ \cos(90+\theta) & \cos\theta \end{pmatrix} = \begin{pmatrix} \cos\theta & \sin\theta \\ -\sin\theta & \cos\theta \end{pmatrix} \tag{7.30}$$

And the vector and station transformations will be, respectively:

$$u_i' = a_{ij}u_j \quad \text{and} \quad X_i' = a_{ij}X_j \tag{7.31}$$

Now, you can plot the component of the displacement parallel to X′1, $u'_1$, against the station's $X'_1$ coordinate (ignoring the X′2 components completely), as in Figure 7.9. Thus, expanding Equation (7.31) for those components only, we get:

$$u_1' = a_{11}u_1 + a_{12}u_2 \quad \text{and} \quad X_1' = a_{11}X_1 + a_{12}X_2 \tag{7.32}$$

To get the two (or three) dimensional strain from displacement vectors requires more involved methods. Recall that the multidimensional equivalent of Equation (7.29) is equation (7.11) which is repeated here:

$$u_i = t_i + E_{ij}X_j$$

We know the displacement vectors, **u**, and the positions of the stations, **X**. We don't know $E_{ij}$ or $t_i$; in two dimensions (ignoring the vertical component of the GPS data), there are thus six unknowns: $E_{11}$, $E_{12}$, $E_{21}$, $E_{22}$, $t_1$, and $t_2$. Each station and displacement vector pair provides two equations (one for $u_1$ and one for $u_2$), so in two dimensions, we need three non-collinear stations and displacements to solve for our six unknowns. You can visualize the three stations defining a triangle with a circle inscribed in it; when the points are displaced, the triangle becomes distorted and the inscribed circle becomes a strain ellipse (Fig. 7.11).

To calculate the unknowns, we need to gather them into a single matrix:

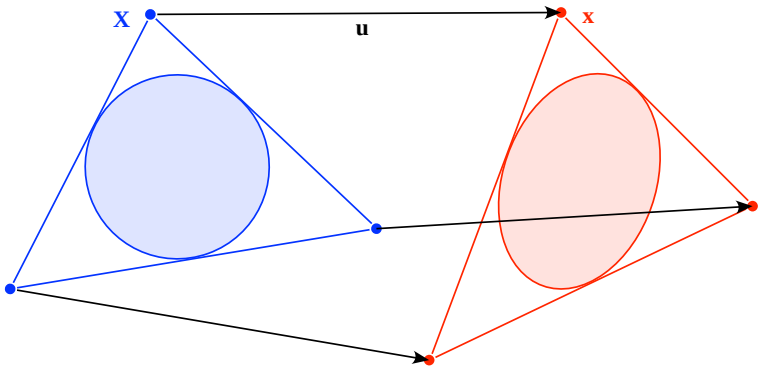


**Figure 7.11 — In 2D, three stations and displacement vectors are necessary to define the strain produced by the displacements. The strain here is finite (i.e., large), but the same principle holds for infinitesimal deformations like that measured by GPS.**

$$\begin{bmatrix} {}^1u_1 \\ {}^1u_2 \\ {}^2u_1 \\ {}^2u_2 \\ \cdots \\ \cdots \\ {}^nu_1 \\ {}^nu_2 \end{bmatrix} = \begin{bmatrix} 1 & 0 & {}^1X_1 & {}^1X_2 & 0 & 0 \\ 0 & 1 & 0 & 0 & {}^1X_1 & {}^1X_2 \\ 1 & 0 & {}^2X_1 & {}^2X_2 & 0 & 0 \\ 0 & 1 & 0 & 0 & {}^2X_1 & {}^2X_2 \\ \cdots & \cdots & \cdots & \cdots & \cdots & \cdots \\ \cdots & \cdots & \cdots & \cdots & \cdots & \cdots \\ 1 & 0 & {}^nX_1 & {}^nX_2 & 0 & 0 \\ 0 & 1 & 0 & 0 & {}^nX_1 & {}^nX_2 \end{bmatrix} \begin{bmatrix} t_1 \\ t_2 \\ E_{11} \\ E_{12} \\ E_{21} \\ E_{22} \end{bmatrix} \tag{7.33}$$

This equation is written, not for three stations but for *n* stations and vectors — more information than we actually need. That's okay, though, because with data redundancy, we can calculate the uncertainties using a least squares approach. Solving Equation (7.33) is non-trivial because it requires calculating the ***inverse*** of the large matrix full of zeros, ones, and X's. The techniques required to do this — generally referred to as ***inverse methods*** — are extremely powerful and form the basis of many very important calculations in earth sciences and other fields but are beyond the scope of this book. If you want to be a modern earth scientist, you will probably eventually want to learn these methods.

## *Analyzing Brittle Faults*

The upper crust of the earth is full of faults — discontinuous deformation features. If we assume that the faults are small relative to the volume of earth that contains them, we can analyze them using infinitesimal strain assumptions. The simplest approach is to leverage the fact that the plane of maximum shear strain is at 45° to the principal axes of infinitesimal strain. In fault slip (and earthquake) analysis, the principal infinitesimal shortening axis is referred to by the letter "P" and the principal elongation axis with the letter "T" (Fig. 7.8c)[3]. Faults are particularly easy to analyze because there is no movement perpendicular to the slip vector and thus each individual fault represents deformation in plane strain. The basic geometry is shown in Figure 7.12.

[3] Because these letters are short for "Pressure" and "Tension", legions of geologists have thought that these represent principal stress axes. They do not. They are infinitesimal strain axes which may, or may not, be parallel to the principal stresses! See McKenzie (1969) for proof.

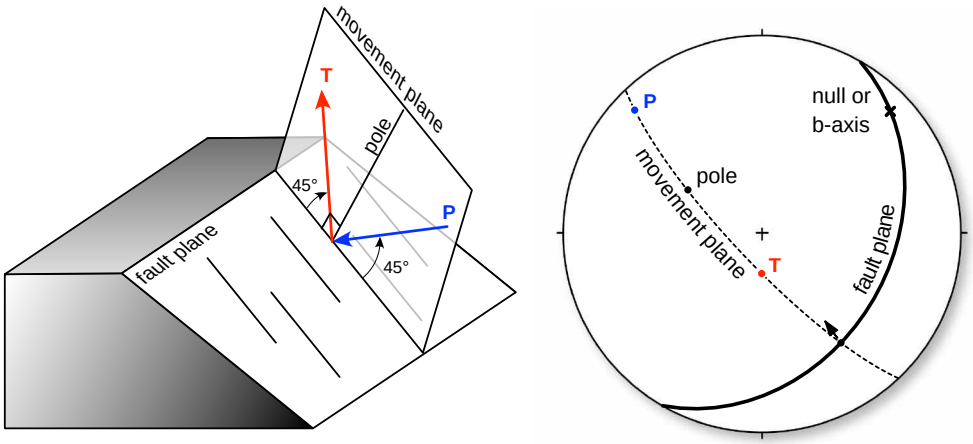


**Figure 7.12 — Anatomy of a fault plane. Right side: 3D perspective view showing the movement plane which contains the pole to the fault and the slickenside (or other movement indicator on the fault). Left side: lower hemisphere view of the same geometry. Arrow at the intersection of the fault and movement planes shows the movement of the hanging wall.**

If one is only interested in calculating the orientations of the individual P and T axes, the calculation is quite straightforward, involving nothing more than vector addition and subtraction. Figure 7.13 is a view perpendicular to the movement plane so that one sees the fault plane edge on and it appears as a line. The unit pole vector, $\hat{\mathbf{n}}$, points down into the footwall and the unit slip vector, $\hat{\mathbf{s}}$, also points down into the lower hemisphere (i.e., we are using a NED coordinate system). We need some way to specify the sense of slip, which we will do with a scalar value, *k*: for faults with a normal component of slip the hanging wall moves down

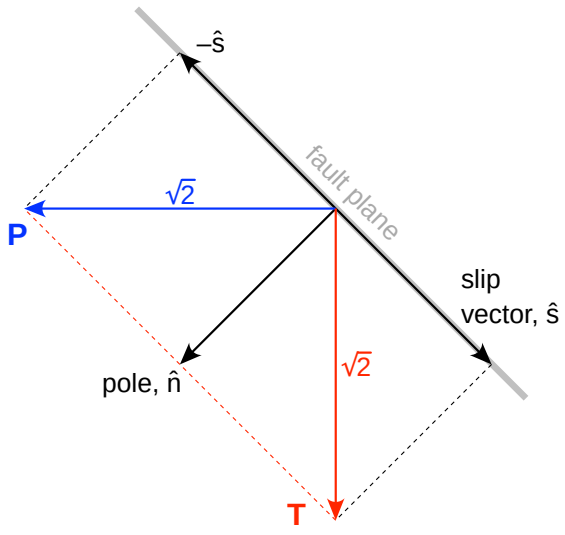


**Figure 7.13 — Edge-on view of the fault plane looking perpendicular to the movement plane. P and T can be calculated from a simple vector addition because a single fault is a plane strain deformation. Note that the vector addition yields vectors which have a magnitude of square root of two because they are 45°-45°-90° right triangle.**

and $k = 1$; for those with a reverse component, $k = -1$, because the hanging wall moves up whereas down in positive. Thus, we can write:

$$P_i = \frac{n_i + k s_i}{\sqrt{2}} \quad \text{and} \quad T_i = \frac{n_i - k s_i}{\sqrt{2}} \tag{7.34}$$

The square root of two in the denominator is necessary to ensure that **P** and **T** are unit vectors.

The preceding analysis is fine if we are concerned about calculating P and T axes of single faults, but what if we want to calculate the strain produced by a group of faults? For this case, we introduce a new concept from earthquake seismology, the scalar ***seismic moment***, $M_o$, and its sibling, the ***geometric moment***, $M_g$:

$$M_o = A \bar{s} \mu \quad \text{and} \quad M_g = A \bar{s} \tag{7.35}$$

where $A$ is the surface area that slipped, $\bar{s}$ is the average displacement, and $\mu$ is the shear modulus. The moment tensor is the sum of the scalar moment times the dyad product of the unit slip and normal vectors:

$$M_{ij} = \sum_{k=1}^{n\_faults} M_g u_i n_j \tag{7.36}$$

where $u_i$ is the unit slip vector and $n_j$ the unit normal (or pole) vector. This equation is for the geometric moment tensor. If you calculated $u_i n_j$ for a single fault and calculated the eigenvalues and eigenvectors, it would give us the P and T axes, just like Equation (7.34). It turns out that our old friend, the displacement gradient tensor, is equal to (Molnar, 1983):

$$E_{ij} = \frac{\sum M_g u_i n_i}{V} = \frac{M_{ij}}{V} \tag{7.37}$$

The summation of moment tensors of all of the faults in the data set is a simplification afforded us by the infinitesimal strain assumption. When the faults are large enough to cause finite strain, you can no longer add the tensors together. Instead, matrix multiplication is involved as we will see in a subsequent chapter.

$E_{ij}$ of Equation (7.37) is, of course, an asymmetric tensor and in infinitesimal strain can be additively decomposed into a symmetric strain and antisymmetric rotation tensors:

$$E_{ij} = \varepsilon_{ij} + \omega_{ij} = \frac{\sum M_g \left( u_i n_j + u_j n_i \right)}{2V} + \frac{\sum M_g \left( u_i n_j - u_j n_i \right)}{2V} \tag{7.38}$$

The symmetric part of (7.38), before being divided by $2V$ is Kostrov's (1974) symmetric seismic moment tensor. When you see a moment tensor reported in an earthquake catalog, it is Kostrov's symmetric tensor and the infinitesimal strain, $\varepsilon_{ij}$ in that case is:

$$\varepsilon_{ij} = \frac{\sum M_o \left( u_i n_j + u_j n_i \right)}{2V\mu} \tag{7.39}$$

If you don't have any scaling information — that is, you don't know $M_o$, $M_g$, $V$, or $\mu$ — you can still add up the moment tensors and get the principal axes of the group of faults assuming that each fault contributes equally to the overall strain in the region. If, however, some faults (or earthquakes) are markedly larger than others, that is a poor assumption; the moment tensor sum is always dominated by the largest features.

# Exercises—Chapter 7

All of the following exercises should be done either in a spreadsheet or Matlab. You will need the EigenCalc program that you downloaded last week for some of the exercises. All of the exercises have datasets that can be downloaded from the course web page.

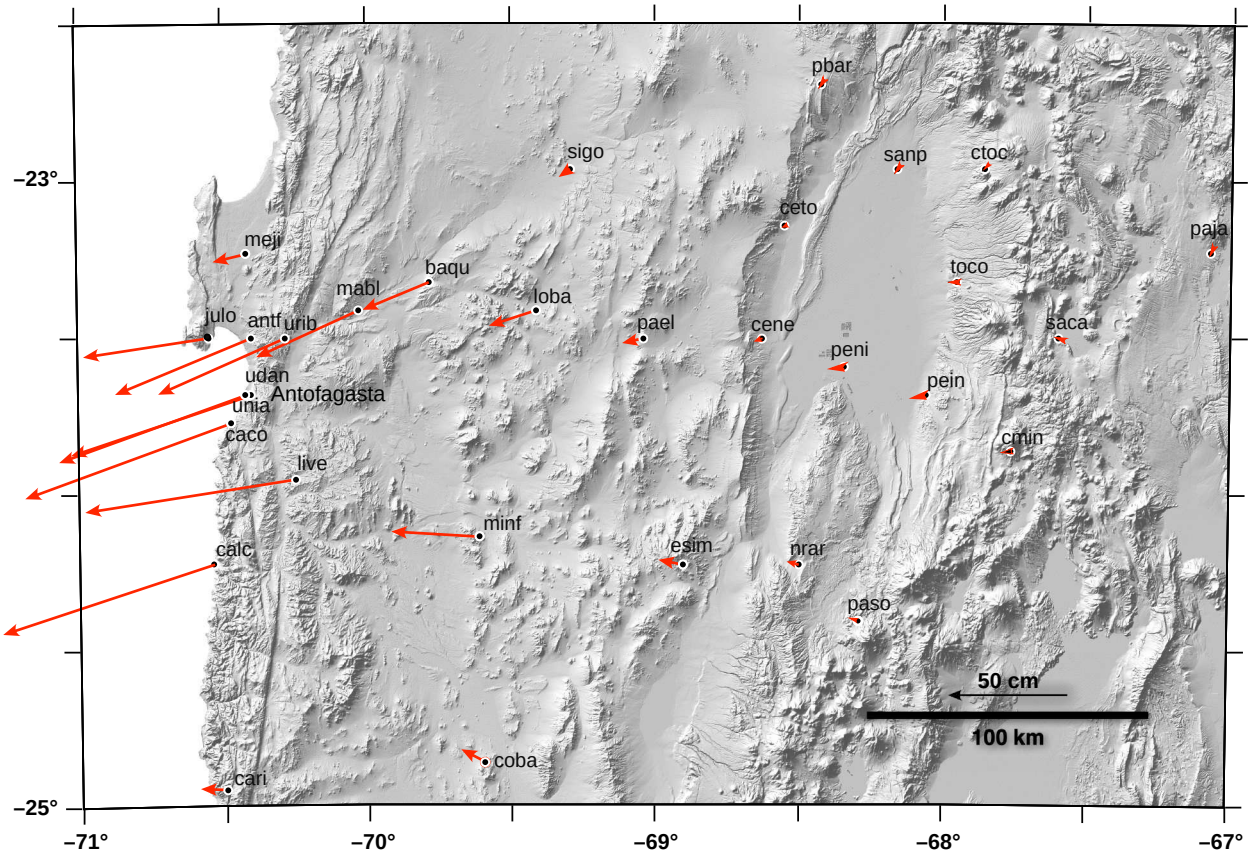


1. Calculate the 1D coseismic strain for the 1995 Antofagasta earthquake (figure, above), using the GPS data from Klotz et al. (1999). The data will be provided to you in a spreadsheet. Carry out the following tasks:

   (a) Determine the average or mean vector that characterizes, as best possible, the overall orientation of the vectors.

   (b) Determine the two-dimensional transformation matrix, $a_{ij}$, needed for a new coordinate system where the X′$_1$ axis is parallel to the mean vector direction.

   (c) Transform the East and North coordinates of the GPS stations, vectors, and errors into the new coordinate system.

(d) Plot the $u'_1$ component of each displacement vector, and its error, against the $X'_1$ component of the station position.

(e) Fit a straight line to approximately linear segments of the resulting curve using the relations or built in functions from the previous sections.

2. Fifteen measurements of faults and their slickensides are given in the table below. Calculate the **P** and **T** axes of the individual faults and then calculate an unweighted moment tensor summation. Use EigenCalc to determine the principal axes of infinitesimal strain. In the downloadable spreadsheet, the sense of slip (SOS) has been specified using $k$=+1 for normal faults and $k$= −1 for reverse faults as described in the text (Eqn. 7.34).

| Fault Plane | | | Slickensides | | Sense |
|---|---|---|---|---|---|
| **Strike** | **Dip** | **Direction** | **Trend** | **Plunge** | **of slip** |
| 149.5 | 47.2 | W | 164.4 | 15.4 | Normal |
| 127.6 | 60 | S | 134.6 | 11.9 | Normal |
| 189.4 | 34.6 | W | 349.6 | 13.1 | Thrust |
| 328 | 42.5 | E | 335.3 | 6.6 | Normal |
| 22.9 | 50.2 | E | 182 | 23.2 | Thrust |
| 108.8 | 31.1 | S | 169.2 | 27.7 | Normal |
| 184.6 | 39.8 | W | 317.1 | 31.6 | Thrust |
| 93.7 | 65 | S | 269.6 | 8.8 | Normal |
| 297.6 | 64.1 | N | 300.2 | 5.4 | Thrust |
| 272.5 | 34.5 | N | 284.4 | 8 | Thrust |
| 151.6 | 58.1 | W | 154.9 | 5.3 | Normal |
| 302.7 | 47 | N | 105.3 | 17.7 | Normal |
| 349.4 | 33.7 | E | 145.2 | 15.3 | Thrust |
| 90.9 | 71.1 | S | 96 | 14.6 | Thrust |
| 189.7 | 36.6 | W | 247.9 | 32.3 | Thrust |

3. You'll be given a spreadsheet containing 57 foreshocks of the Mw 8.2 Pisagua earthquake (northern Chile March-April 2014) which have nodal planes and scalar moments.

(a) Calculate the moment tensor sum from Eqn. 7.39 (ignoring $V$ and $\mu$) for the foreshocks and use EigenCalc to determine the orientation of the principal axes.

(b) Plot the P and T axes of the individual events in Stereonet and compare them to the moment tensor sum that you did in part (a).

# Chapter 8

## *Large Strains*

### Introduction

Most geological deformation, whether distorted fossils or fold and thrust belt shortening, accrues over a long period of time and can no longer be analyzed with the assumptions of infinitesimal strain. Fortunately, these large, or ***finite strains*** have the same starting point that infinitesimal strain does: the deformation and displacement gradient tensors. However, we must clearly distinguish between gradi-

ents in position or displacement with respect to the initial (material) or to the final (spatial) state and several assumptions from the last Chapter — small angles, addition of successive phases or steps in the deformation — no longer hold. Finite strain can get complicated very quickly with many different tensors to worry about. Most of our emphasis here will be on the practical measurement of finite strain rather than the details of the theory but we do have to review a few basic concepts first, so that we can appreciate the differences between finite and infinitesimal strain. Some of these differences have a profound impact on how we analyze deformation.

# Comparison to Infinitesimal Strain

## *A Plethora of Finite Strain Tensors*

There are lots of finite strain tensors and they come in pairs: one referenced to the initial state and the other referenced to the final state. The derivation of these tensors is usually based on Figure 7.3 and is tedious but straightforward; we will skip the derivation here but you can see it in Allmendinger et al. (2012) or any good continuum mechanics text. The first tensor is the ***Lagrangian strain tensor***:

$$L_{ij} = \frac{1}{2}\left[\frac{\partial u_i}{\partial X_j} + \frac{\partial u_j}{\partial X_i} + \frac{\partial u_k}{\partial X_i}\frac{\partial u_k}{\partial X_j}\right] = \frac{1}{2}\left[E_{ij} + E_{ji} + E_{ki}E_{kj}\right] \tag{8.1}$$

where $E_{ij}$ is the displacement gradient tensor from the last Chapter. Recall that the infinitesimal strain tensor, ε, is (from Eqn. 7.20):

$$\varepsilon_{ij} = \frac{1}{2}\left(E_{ij} + E_{ji}\right) \tag{8.2}$$

This highlights the first distinction between infinitesimal and finite strain: the former ignores the higher order term, $E_{ki}E_{kj}$. Expansion of the different terms in Equation (8.1) follows the usual summation convention rules. For example, to expand for $L_{11}$, we write:

$$L_{11} = \frac{1}{2}\left(E_{11} + E_{11} + E_{11}E_{11} + E_{21}E_{21} + E_{31}E_{31}\right) = E_{11} + \frac{1}{2}\left(E_{11}^2 + E_{21}^2 + E_{31}^2\right) \tag{8.3}$$

In contrast,
$$\varepsilon_{11} = \frac{1}{2}\left(E_{11} + E_{11}\right) = E_{11}$$

Just for practice, let's also expand for $L_{13}$:

$$L_{13} = \frac{1}{2}\left(E_{13} + E_{31} + E_{11}E_{13} + E_{21}E_{23} + E_{31}E_{33}\right) \tag{8.4}$$

As before, the higher order non-linear term on the right hand side of the equation is ignored in infinitesimal strain. The ***Eulerian finite strain tensor***, $\overline{L}_{ij}$, is the same as the Lagrangian strain tensor but referenced to the final state:

$$\overline{L}_{ij} = \frac{1}{2}\left[\frac{\partial u_i}{\partial x_j} + \frac{\partial u_j}{\partial x_i} + \frac{\partial u_k}{\partial x_i}\frac{\partial u_k}{\partial x_j}\right] = \frac{1}{2}\left[e_{ij} + e_{ji} + e_{ki}e_{kj}\right] \tag{8.5}$$

where $e_{ij}$ is the displacement gradient tensor referenced to the final state.

Alternatively, we can start with the deformation gradient tensor, $D_{ij}$ (Eqns. 7.8 and 7.13) and derive the ***Green deformation tensor***:

$$C_{ij} = \frac{\partial x_k}{\partial X_i}\frac{\partial x_k}{\partial X_j} = D_{ki}D_{kj} \tag{8.6}$$

referenced to the initial or material state. The equation (8.6) expansion for $C_{11}$ and $C_{13}$ (as before) is:

$$C_{11} = D_{11}D_{11} + D_{21}D_{21} + D_{31}D_{31} = D_{11}^2 + D_{21}^2 + D_{31}^2 \tag{8.7a}$$

$$C_{13} = D_{11}D_{13} + D_{21}D_{23} + D_{31}D_{33} \tag{8.7b}$$

And, finally, the ***Cauchy deformation tensor***, $\overline{C}_{ij}$, is similar to Equation (8.6), but referenced to the final or spatial state:

$$\overline{C}_{ij} = \frac{\partial X_k}{\partial x_i}\frac{\partial X_k}{\partial x_j} = d_{ki}d_{kj} \tag{8.8}$$

where $d_{ij}$ is the deformation gradient tensor referenced to the final state. For a vector parallel to the $\mathbf{X_1}$ axis, the quadratic elongation, λ, is equal to the square of the stretch, S, is equal to $C_{11}$.

$$\lambda_{(1)} = S_{(1)}^2 = C_{11} = 1 + 2L_{11} \tag{8.9}$$

And, a line parallel to the $\mathbf{x_1}$ axis in the final state:

$$\frac{1}{\lambda_{(1)}} = \frac{1}{S_{(1)}^2} = \overline{C}_{11} = 1 + 2\overline{L}_{11}$$

 

These tensors are not all independent of each other. The relations between them are:

$$L_{ij} = \frac{1}{2}\left(C_{ij} - \delta_{ij}\right) \tag{8.9}$$

and

$$\overline{L}_{ij} = \frac{1}{2}\left(\delta_{ij} - \overline{C}_{ij}\right) \tag{8.10}$$

Where $\delta_{ij}$ is the Kronecker delta that represents the components of the identity matrix. All of these tensors are symmetric. Thus $L_{ij}$ and $C_{ij}$ have the same principal axes, Likewise, $\overline{L}_{ij}$ and $\overline{C}_{ij}$ also have the same principal axes, which are different from those for $L_{ij}$ and $C_{ij}$. The difference in orientation between the principal axes of $L_{ij}$ and $\overline{L}_{ij}$ is the amount of rotation during the deformation.

### *Multiple Deformations*

In infinitesimal strain, the displacement gradient tensors are simply added together to sum the total deformation as we saw in the case of the moment tensor for earthquakes or faults in the previous chapter (Eqn. 7.37):

$$^{total}\mathbf{E} = \sum {}^{n}\mathbf{E} = {}^{1}\mathbf{E} + {}^{2}\mathbf{E} + \cdots + {}^{n}\mathbf{E} \tag{8.11}$$

Let's see how the finite strain version compares. Using the deformation gradient tensor for the first deformation, we get:

$${}^{1}\mathrm{d}\mathbf{x} = {}^{1}\mathbf{D}\mathrm{d}\mathbf{X} \tag{8.12}$$

The final state of the first deformation is the initial state of the second deformation — that is, ${}^{2}\mathrm{d}\mathbf{X} = {}^{1}\mathrm{d}\mathbf{x}$ — so for the second deformation, we can write:

$${}^{2}\mathrm{d}\mathbf{x} = {}^{2}\mathbf{D}{}^{2}\mathrm{d}\mathbf{X} = {}^{2}\mathbf{D}\left({}^{1}\mathbf{D}\mathrm{d}\mathbf{X}\right) = {}^{2}\mathbf{D}{}^{1}\mathbf{D}\mathrm{d}\mathbf{X} \tag{8.13}$$

We know that $\mathbf{E} = \mathbf{D} - \mathbf{I}$, so the expansion of the ${}^{2}\mathbf{D}{}^{1}\mathbf{D}$ term in Equation (8.13) is:

$${}^{2}\mathbf{D}{}^{1}\mathbf{D} = \left({}^{2}\mathbf{E} + \mathbf{I}\right)\left({}^{1}\mathbf{E} + \mathbf{I}\right) = {}^{1}\mathbf{E} + {}^{2}\mathbf{E} + \left({}^{2}\mathbf{E}{}^{1}\mathbf{E}\right) + \mathbf{I} \tag{8.14}$$

 

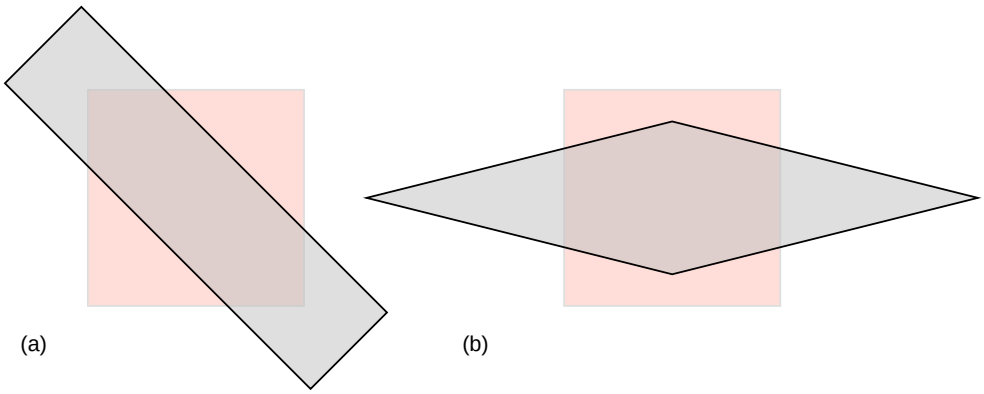


**Figure 8.1 — The order in which strains and rotations occur make a difference! (a) A horizontal stretch of 2 followed by a rotation of 45°. (b) a rotation of 45° followed by a horizontal stretch of 2. In both cases, the initial square is shown in pink.**

So, superposing deformations really has a higher order term, $\left({}^{2}\mathbf{E}{}^{1}\mathbf{E}\right)$, that is ignored in the infinitesimal strain summing of displacement gradient tensors. This term is a matrix multiplication which is non-commutative and thus, because ${}^{2}\mathbf{E}{}^{1}\mathbf{E} \neq {}^{1}\mathbf{E}{}^{2}\mathbf{E}$, ***the order in which the strain and/or rotation occurs makes a difference in the final result***. Figure 8.1 illustrates this important principle for a stretch and a rotation.

### *Mohr's Circle for Finite Strain in the Deformed State*

The Mohr Circle construction for the Cauchy deformation tensor (Eqn. 8.8) is particularly useful in practical strain analysis. This construction is derived, just like all Mohr's Circles, by rotating the coordinate system about a principal axis and you can see the derivation in Allmendinger et al. (2012). The equations are given by:

$$\overline{C}_{11}{}' = \frac{\left(\overline{C}_1 + \overline{C}_3\right)}{2} + \frac{\left(\overline{C}_1 - \overline{C}_3\right)}{2}\cos 2\theta \quad \text{and} \quad \overline{C}_{13}{}' = \frac{\left(\overline{C}_1 - \overline{C}_3\right)}{2}\sin 2\theta \qquad (8.15)$$

You will more commonly see these written as:

$$\lambda' = \frac{\left(\lambda_1{}' + \lambda_3{}'\right)}{2} + \frac{\left(\lambda_1{}' - \lambda_3{}'\right)}{2}\cos 2\theta \quad \text{and} \quad \gamma' = \frac{\gamma}{\lambda'} = \frac{\left(\lambda_1{}' - \lambda_3{}'\right)}{2}\sin 2\theta \quad (8.16)$$

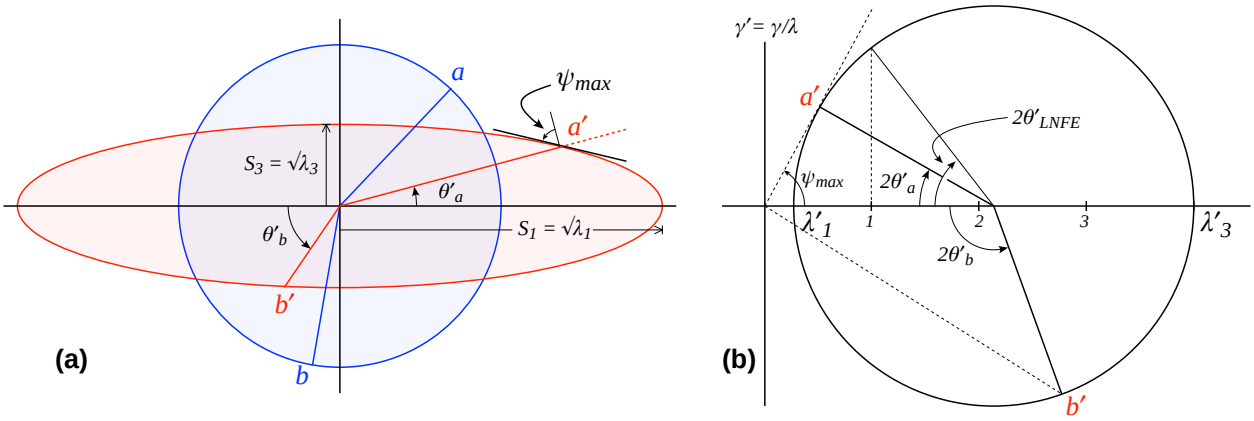


**Figure 8.2 — (a) the finite strain ellipse (red) and the initial circle with radius of one (blue). Two lines are shown in the undeformed (*a* and *b*) and deformed (*a*′ and *b*′) state. Because the initial length is 1, the major and minor axes of the ellipse are $S_1$ and $S_3$, respectively. Line *a*′ is drawn in the orientation of the line that experiences the maximum shear strain in the body. (b) The Mohr's Circle for finite strain in the deformed state. Lines *a*′ and *b*′ are plotted in their correct positions. Note that the angular shear is measured by drawing a line for the origin of the plot to the point on the circle, with the maximum angular shear determined by the line from the origin that is tangent to the circle (line *a*′). The orientation of a line of no finite elongation (LNFE), which has a $\lambda' = 1$, is also shown.**

where $$\lambda' = \frac{1}{\lambda} = \frac{1}{S^2}$$

Figure 8.2 shows a finite strain ellipse on the left and the corresponding Mohr's Circle construction on the right. This Mohr's Circle construction is very useful, particularly where the deformation is in plane strain.

## *Progressive Strain*

In Figure 8.2a, you see the finite strain ellipse (in light red) superimposed on the initial circle (in light blue). The points of intersection between the ellipse and circle define lines that are currently at the same length as they were when they started out; we call these ***lines of no finite elongation*** (LNFE) and they are symmetric with respect to the principal axes of strain. You can imagine making the same sort of diagram for the infinitesimal strain ellipse, which would be only very slightly different from the initial circle. In that case, there would be two ***lines of no infinitesimal elongation*** (LNIE) and they would be at 90° to each other. These concepts allow us to understand how strain progresses with time (Fig. 8.3).

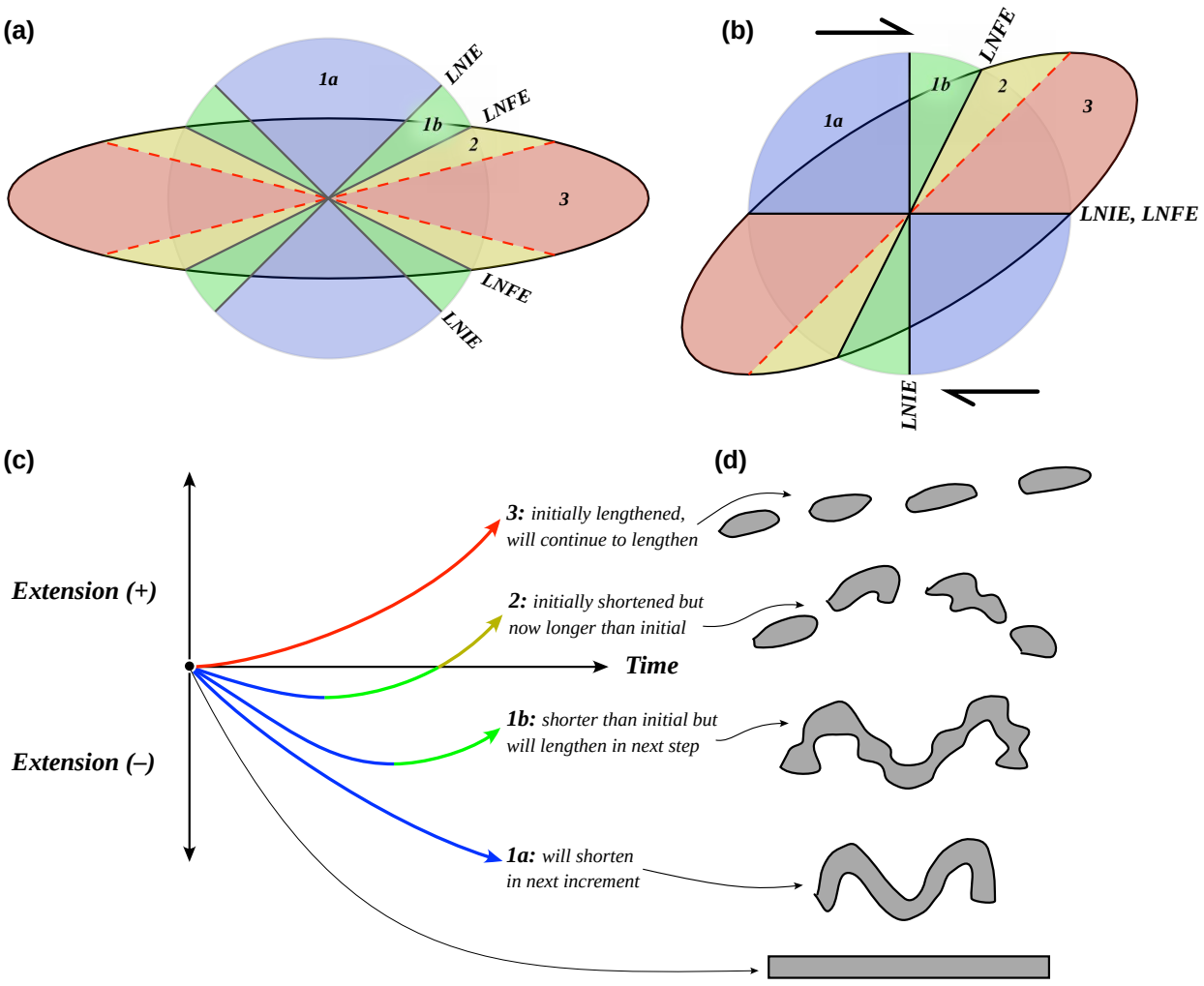


**Figure 8.3 — Illustration of progressive strain. (a) A pure shear strain path where the principal axes of finite strain and incremental infinitesimal strain remain parallel throughout the deformation. (b) A simple shear strain path where infinitesimal and finite principal axes are non-coaxial. (c) The meaning of fields 1-3 showing the history of shortening and lengthening of lines at time *t* in those fields. (d) Cartoon illustration of what a layer of rock might look like in each of the four fields.**

In the simplest of strain paths, there are two end-member cases: in ***pure shear***, the infinitesimal strain axes in each incremental step of the deformation are parallel to each other and to the finite strain axes representing the entire deformation (Fig. 8.3a). In ***simple shear***, the infinitesimal strain axes are not parallel to each other in each increment, nor are they parallel to the finite strain axes. A key aspect of simple shear is that one of the two LNFE is parallel to one of the two LNIE and these are parallel to the zone of simple shear (Fig. 8.3b). To understand how this works, imagine a deck of cards: You inscribe a circle onto the deck and

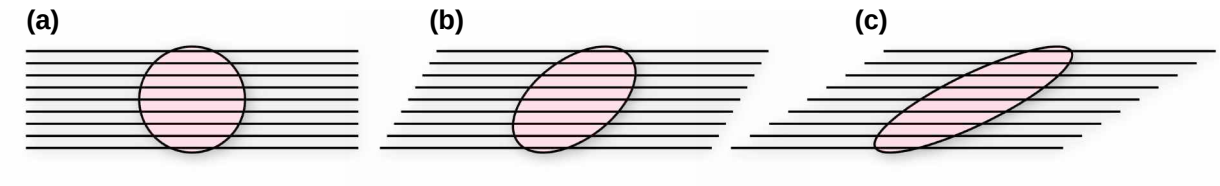


**Figure 8.4 — Illustration of at the classic card deck experiment to demonstrate simple shear. The cards are viewed edge-on and thus appear as parallel lines. (a) initial stack of cards with a circle inscribed on it. (b) and (c) progressive steps of shearing parallel to the cards, deforming the circle into an ellipse.**

then you progressively shear the deck by sliding the cards over each other (Fig. 8.4). The cards themselves do not change length; they are parallel to the LNIE and LNFE, but the circle deforms into an ellipse and the principal axes of the ellipse have different orientations in each step. Simple shear is particularly important in shear zones (Chapter 9) as well as in parallel folding (Chapter 10). The inherent asymmetry of the simple shear case (Fig. 8.3b) is what we look for to determine the sense of shear in fault zones.

As the strain progresses, material lines will experience different histories of shortening and/or lengthening, depending on their initial orientations (Fig. 8.3c). Some experience only shortening, others only lengthening, and still others are first shortened and then lengthened. As you will see in the exercises, this can have a profound effect on different lines, or layers, that start out with different orientations in

**Figure 8.5 — More competent layers in a deformed and metamorphosed limestone have been stretched, a process known as boudinage. We can frequently put the boudined pieces back together to give us a linear extension.**

the rock (Fig. 8.3d). Note that ***it is impossible to distinguish between pure and simple shear based on the finite strain alone***!

## Strain from Geological Objects

In geology, there are a variety of different objects that can be used for the calculation of strain. The problem, however, is two fold: first, they are generally in random orientations and second they provide different types of information. A layer that has been pulled apart in ***boudinage*** (Fig. 8.5) may provide evidence of linear extension but nothing quantitative about shear strain. A deformed fossil, on the other hand, may furnish information about shear strain but none about the original dimensions of the fossil and thus none about extensions. Mathematically, determining strain from such measurements is, like our GPS example (e.g., Eqn 7.33), another case where inverse methods are needed. In the absence of computing resources and knowledge of inverse methods, a large number of clever graphical constructions and methods have cropped up. Presented here are just a few of those

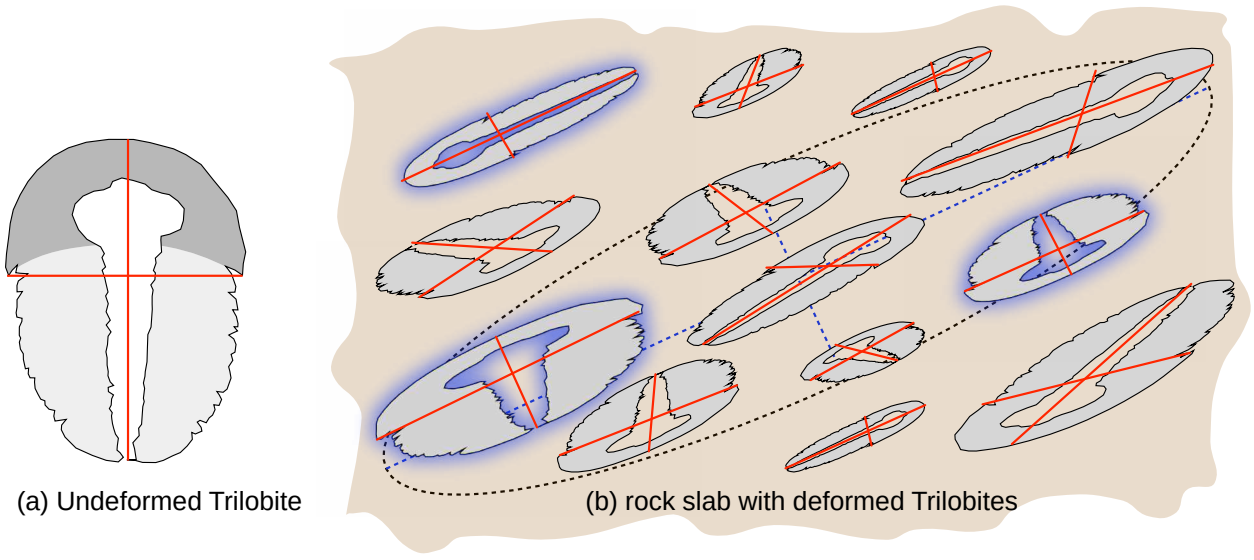


**Figure 8.6 — A trilobite fossil is just one of many types of fossils with bilateral symmetry. (a) In a tracing of the undeformed fossil, the medial line and line drawn at the base of the head (cephalon) are perpendicular (two lines in red). (b) On a tracing of a deformed rock slab which contains several trilobites, initially in different orientations, in most cases those lines will no longer be perpendicular because the fossils are in an orientation where they have experienced angular shear. However, in three of the trilobites (highlighted in blue), those two lines are still be perpendicular and therefore must be parallel to the principal axes of strain (dashed lines).**

methods; for a much more comprehensive treatment, see the works by Ramsay (1967) and Ramsay and Huber (1983).

## *Finding Principal Axes*

Sometimes, all we want to do is find the orientations of the principal axes of finite strain. If you examine Figure 8.2b, it is clear that there are just two sets of lines in a deformed body that have zero angular shear, $\psi$. Those sets of lines are parallel to the principal axes of finite strain. In other words, ***the principal axes of strain are the only lines that have no shear strain or angular shear***. Fortunately, there are many different types of features in geology that are initially perpendicular, for example: fossils with bilateral symmetry (Fig. 8.6a), worm burrows perpendicular to bedding, etc. Where such features are present in deformed rocks, they give us a rapid way of finding the orientations of the principal axes: just look for the features where perpendicular lines in the undeformed state are still perpendicular in the deformed state (Fig. 8.6b). Those lines must be parallel to the principal axes.

## *Deformed Spherical Objects*

If you are fortunate, your field area will contain deformed, originally approximately spherical objects like the deformed quartz pebble conglomerate shown at

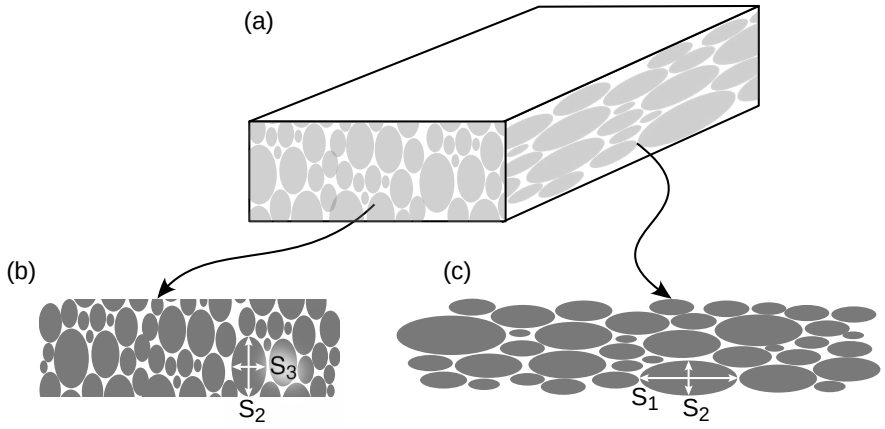


**Figure 8.7 — (a) A hypothetical rock sample bearing deformed spherical objects (light gray ellipses). By cutting the sample (b) perpendicular and (c) parallel to the long axis of the strain ellipse and measuring the aspect ratios, the full shape of the strain ellipsoid can be determined and plotted on a Flinn diagram (Fig. 8.8).**

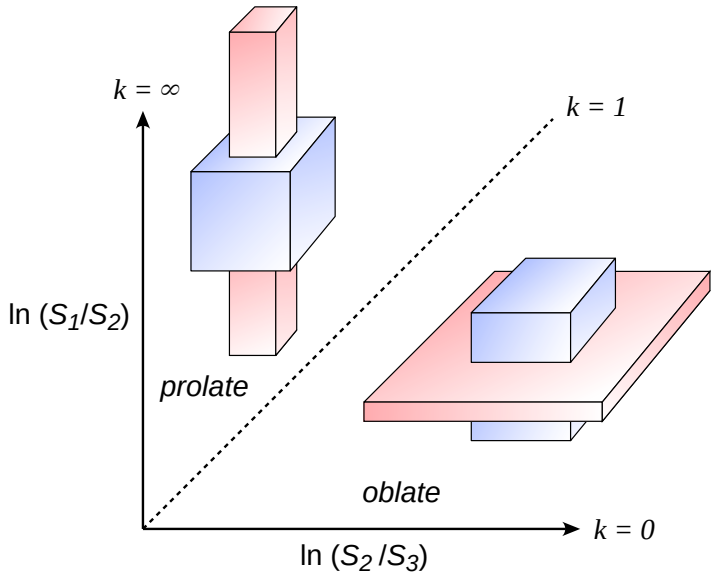


**Figure 8.8 — The Flinn Diagram depicting different types of strain. In the prolate field, the strain ellipsoids are cigar shaped whereas in the oblate field they are pancake shaped. The original cube is shown in blue and its deformation into the appropriate shape for the field of the Flinn diagram is shown in light red.**

the beginning of this chapter. Other examples include deformed oolites or pellets in carbonate rocks, reduction spots in slates, or even deformed vesicles in volcanic rocks. Each object is now distorted into it's own strain ellipsoid. In the simplest type of analysis, one would make two cuts of the sample, perpendicular to the long axis (Fig. 8.7b) and perpendicular to the short axis (Fig. 8.7c) of the ellipsoids. In many textbooks, the long, intermediate and short axes of the strain ellipsoid are referred to as the $X$, $Y$, and $Z$ axes, but we refer to them here as the $X_1$, $X_2$, and $X_3$ axes with magnitudes (i.e., principal stretches) $S_1$, $S_2$, and $S_3$. For each ellipse in each cut, we measure the long and short axis and calculate the ratio, $S_1/S_2$ or $S_2/S_3$ (i.e., $X/Y$ or $Y/Z$). If the strain is homogeneous, these ratios should ideally be the same for all of the ellipses, but measurement error and the variability inherent in naturally deformed particles means that you will want multiple measurements to get the best determination of the ratios.

Once you have the best fit ratio of $S_1/S_2$ and $S_2/S_3$, it is particularly convenient to visualize the result in a graphical plot known as a Flinn diagram (Fig. 8.8). This diagram can be further quantified by calculating a parameter, $k$, given by:

$$k = \frac{\left(\frac{S_1}{S_2}\right) - 1}{\left(\frac{S_2}{S_3}\right) - 1} \tag{8.17}$$

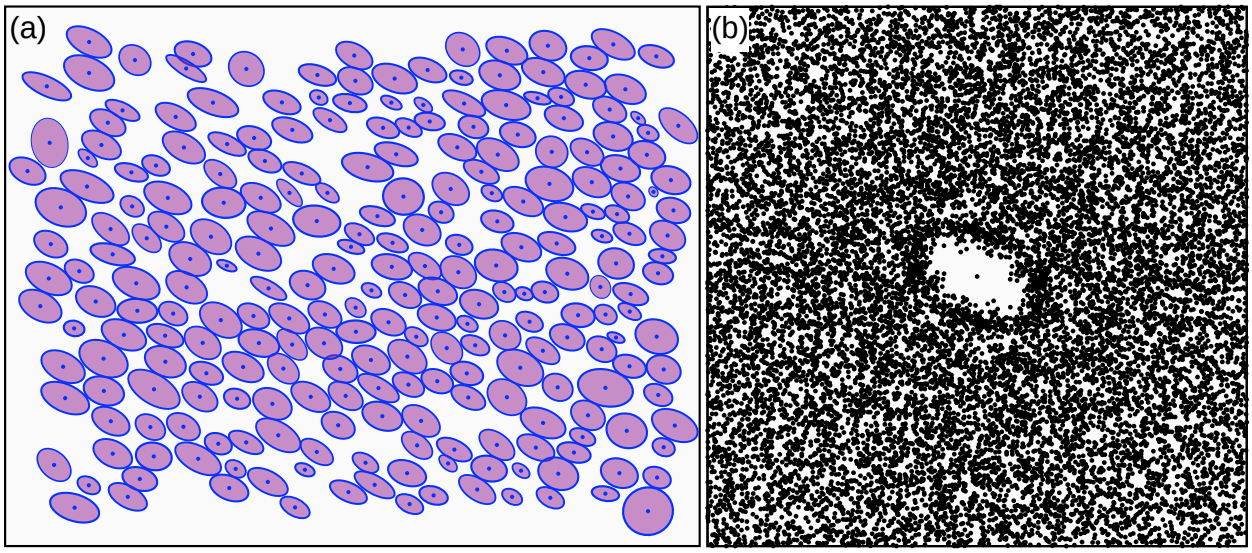


**Figure 8.9 — (a) tracing of deformed ooids from a photo in Ramsay and Huber (1983) and (b) a basic Fry plot of the same data. Both graphics were produced with Frederick Vollmer's (2015) excellent program, EllipseFit.**

Rocks in the prolate field with $k > 1$ are dominated by a linear fabric and are commonly referred to as ***L-tectonites***; those lying on the plane strain line ($k = 1$) are called ***LS-tectonites***, and those in the oblate field display a pronounced planar fabric and a called ***S-tectonites***.

In rocks where the spheroids have different mechanical properties than the matrix in which they lie, or their boundaries are poorly defined, measuring the aspect ratio of the ellipses in the two cuts may give a misleading answer. In that case, the method of choice for most structural geologists is the ***Fry plot*** (Fry, 1979). This method works by plotting the centers of the deformed spheroids rather than measuring their aspect ratios. The centers should be most closely spaced in the $S_3$ (or Z) direction of the strain ellipse. You can make this plot manually by placing a piece of tracing paper over a photograph of a section of the rock with the deformed spheroids in it. The center of the paper is marked and placed over an ellipse near the center of the image and all of the centers of the other ellipses are marked with points. Subsequently, the paper is shifted to a neighboring ellipse, taking care not to rotate the paper, and all of the centers of the other ellipses are again plotted on the paper. The process is repeated until all of the ellipses have formed the center of the plot. Although it is possible to construct a Fry plot by hand, there are many fine

computer programs available that will make the plot automatically once the ellipse centers have all been marked (Fig. 8.9).

### *Three Deformed Lines Graphically*

Three lines in different orientations, for which you can determine both the initial and the final length, can be used in combination with the Mohr's Circle for finite strain (Fig. 8.2) to determine the magnitude and orientation of the strain ellipse in two dimensions (i.e., assuming plane strain). The graphical procedure is depicted in Figure 8.10. To calculate the strain proceed as follows:

1. Find three lines in the sample for which you can determine the initial and final lengths. In Figure 8.10, they are the heavy black lines in the upper left corner, labeled **a**, **b**, **c**.
2. Measure the final linear and initial sinuous (or discontinuous) lengths of the three lines (red lines superimposed on the black) and calculate the stretch for each line (table in upper right corner of the figure).
3. Select the shortest final line to use as a reference line (we have used **c** in Figure 8.10), and use it as one side of the deformed state triangle (lower left). Draw the other two sides of the deformed triangle with the lines overlapping (e.g., lines **a** and **b**).
4. Our restoration to the undeformed state will not use the full lengths of **a** and **b**; instead we will restore the triangle shaded in yellow (**A** and **B**). Measure the lengths of just those parts of **a** and **b** that constitute the side of the deformed triangle.
5. Construct the undeformed triangle by first restoring side **C** to its undeformed length, keeping it parallel to **c** in the deformed triangle. Using a compass, swing arcs from the two ends of **C** with lengths appropriate to the restored lengths of **A** and **B**. You calculate the restored lengths using the ***inverse*** of the stretches in the table in the upper right of Figure 8.10.

6. Once you have the undeformed triangle, draw a line from each apex, perpendicular to the opposite side. For each side of the triangle, measure the distance from the nearest apex to the perpendicular. Using the stretch for the appropriate line, calculate those lengths in the deformed state and measure the resulting distances from the appropriate apex on the deformed triangle.

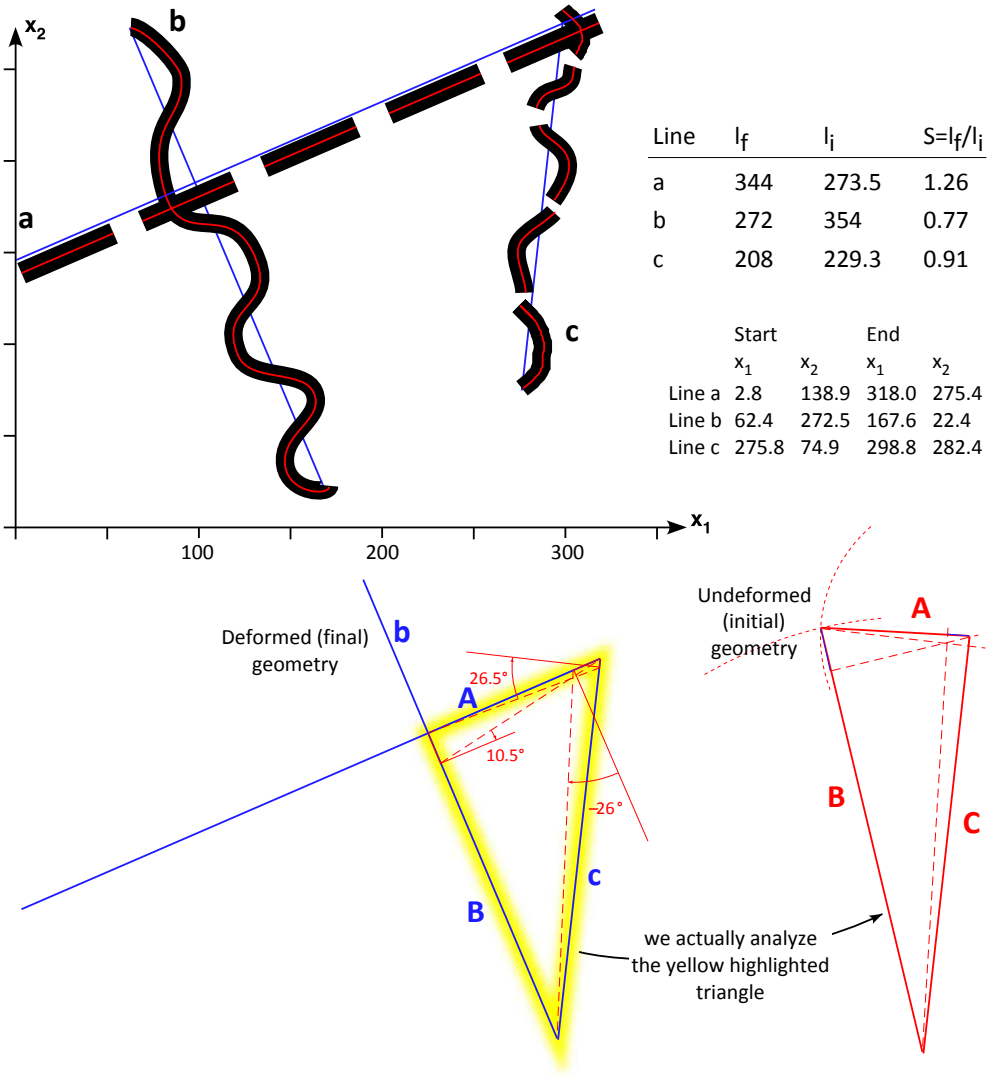


**Figure 8.10 — Graphical procedure for determining the strain ellipse from three deformed lines in different orientations (heavy black lines). Final lengths are shown in blue and initial lengths in red. In this construction, we have chosen C as the reference line so it has the same orientation in all three diagrams. The perpendiculars from the apices to the opposite side in the undeformed state are reconstructed in the deformed state triangle so that we can calculate the angular shears that each line has experienced.**

7. Construct lines from each vertex to the line segment that you calculated in step 6 on the deformed triangle (dashed red lines on the blue/gray triangle). In the initial state triangle these lines were perpendicular to the side, but they are not in the final state triangle. The difference in angle is the angular shear that each line experienced during the deformation.

8. You now have enough information to construct the Mohr's Circle for finite strain in the deformed state. From your measurements, calculate the inverse quadratic elongations, $\lambda'$, and $\gamma' = \gamma/\lambda$. Recall that the shear strain, $\gamma$, is the tangent of the angular shears that you calculated in step 7.

9. Plot the three points on your Mohr's Circle construction and fit a circle, centered on the axis, to the three points. You can now read the principal inverse quadratic elongations from the Mohr's Circle and you can calculate the orientation of the maximum principal axis of finite strain relative to line **c** by measuring the $2\theta'$ angle on the circle. The final plot for Figure 8.10 is shown in Figure 8.11.

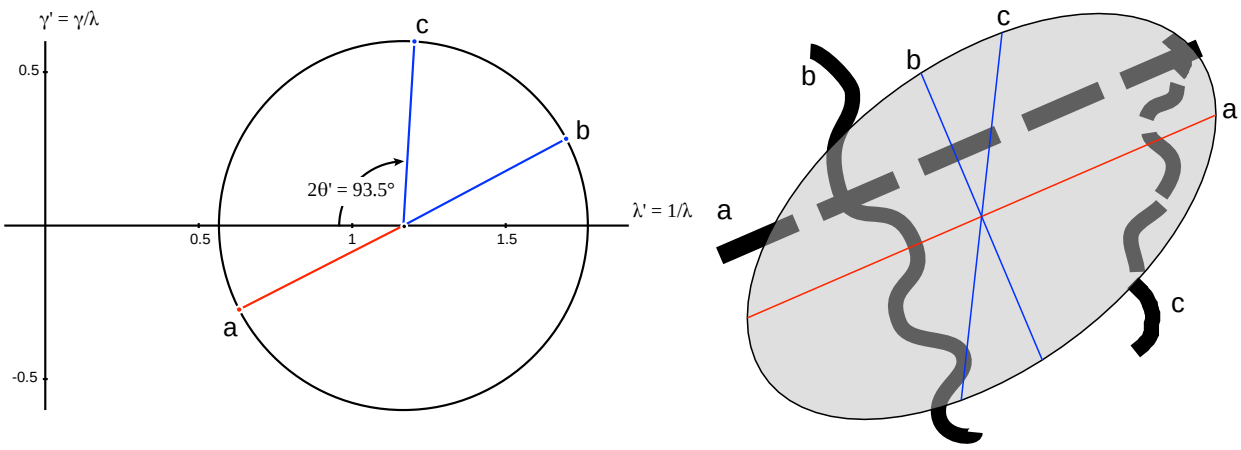


**Figure 8.11 — Mohr's Circle (left) for the deformation shown in Figure 8.10 and (right) the strain ellipse determined from the Mohr's Circle plotted on top of the original deformed lines from Figure 8.10. Blue lines are shorter than they started out and red lines are longer.**

### *Three Deformed Lines with Inverse Methods*

If this graphical construction method strikes you as particularly tedious and prone to small errors (and you would be right, it is), it should provide excellent motivation to learn inverse methods, first mentioned in the preceding Chapter. In this final section we outline just how to do that to demonstrate that it is not too scary! Malvern (1969) and Allmendinger et al. (2012) give the solution for the inverse quadratic elongation as a function of the Cauchy deformation tensor, $\overline{C}_{ij}$, as:

$$\frac{1}{S^2} = \frac{1}{\lambda} = \frac{\mathrm{d}x_i}{\mathrm{d}s}\overline{C}_{ij}\frac{\mathrm{d}x_j}{\mathrm{d}s} \tag{8.18}$$

where $ds$ is the scalar length of the deformed line, $\ell_f$, and $dx_i$ are as shown in Figure 8.12. This equation expands to:

$$\begin{aligned}\lambda' = \frac{1}{\lambda} = &\frac{\mathrm{d}x_1}{\mathrm{d}s}\bar{C}_{11}\frac{\mathrm{d}x_1}{\mathrm{d}s} + \frac{\mathrm{d}x_1}{\mathrm{d}s}\overline{C}_{12}\frac{\mathrm{d}x_2}{\mathrm{d}s} + \frac{\mathrm{d}x_1}{\mathrm{d}s}\overline{C}_{13}\frac{\mathrm{d}x_3}{\mathrm{d}s} \\ &+\frac{\mathrm{d}x_2}{\mathrm{d}s}\overline{C}_{21}\frac{\mathrm{d}x_1}{\mathrm{d}s} + \frac{\mathrm{d}x_2}{\mathrm{d}s}\overline{C}_{22}\frac{\mathrm{d}x_2}{\mathrm{d}s} + \frac{\mathrm{d}x_2}{\mathrm{d}s}\overline{C}_{23}\frac{\mathrm{d}x_3}{\mathrm{d}s} \\ &+\frac{\mathrm{d}x_3}{\mathrm{d}s}\overline{C}_{31}\frac{\mathrm{d}x_1}{\mathrm{d}s} + \frac{\mathrm{d}x_3}{\mathrm{d}s}\overline{C}_{32}\frac{\mathrm{d}x_2}{\mathrm{d}s} + \frac{\mathrm{d}x_3}{\mathrm{d}s}\overline{C}_{33}\frac{\mathrm{d}x_3}{\mathrm{d}s}\end{aligned} \tag{8.19}$$

The simple two-dimensional form of the equation, equivalent to the graphical analysis, above, is:

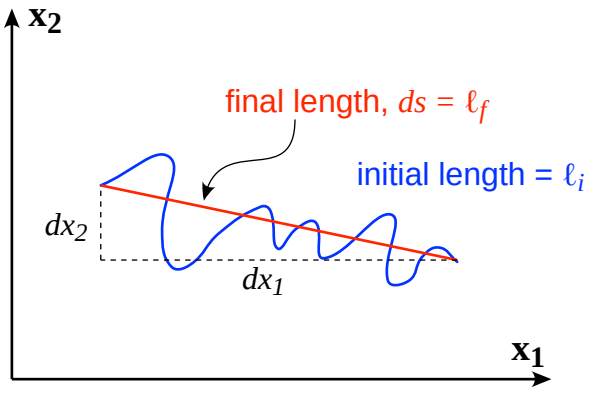


**Figure 8.12 — The meaning of *ds*, $dx_1$ and $dx_2$ in Equations 8.18-8.22.**

$$\lambda' = \frac{1}{\lambda} = \frac{\mathrm{d}x_1}{\mathrm{d}s}\overline{C}_{11}\frac{\mathrm{d}x_1}{\mathrm{d}s} + \frac{\mathrm{d}x_1}{\mathrm{d}s}\overline{C}_{12}\frac{\mathrm{d}x_2}{\mathrm{d}s} + \frac{\mathrm{d}x_2}{\mathrm{d}s}\overline{C}_{21}\frac{\mathrm{d}x_1}{\mathrm{d}s} + \frac{\mathrm{d}x_2}{\mathrm{d}s}\overline{C}_{22}\frac{\mathrm{d}x_2}{\mathrm{d}s} \tag{8.20}$$

Because $\overline{C}_{ij}$ is a symmetric matrix, $\overline{C}_{12} = \overline{C}_{21}$, we can simplify Equation (8.20) as:

$$\begin{aligned}\lambda' = \frac{1}{\lambda} &= \left(\frac{\mathrm{d}x_1}{\mathrm{d}s}\right)^2 \overline{C}_{11} + \left(\frac{\mathrm{d}x_1}{\mathrm{d}s}\frac{\mathrm{d}x_2}{\mathrm{d}s} + \frac{\mathrm{d}x_2}{\mathrm{d}s}\frac{\mathrm{d}x_1}{\mathrm{d}s}\right)\overline{C}_{12} + \left(\frac{\mathrm{d}x_2}{\mathrm{d}s}\right)^2 \overline{C}_{22} \\ &= \left(\frac{\mathrm{d}x_1}{\mathrm{d}s}\right)^2 \overline{C}_{11} + 2\left(\frac{\mathrm{d}x_1\mathrm{d}x_2}{\mathrm{d}s^2}\right)\overline{C}_{12} + \left(\frac{\mathrm{d}x_2}{\mathrm{d}s}\right)^2 \overline{C}_{22}\end{aligned} \tag{8.21}$$

There are three unknowns, so we need the quadratic elongations of three lines (a, b, and c) to solve for the two dimensional strain ellipse:

$$\begin{bmatrix} {}^a\lambda' \\ {}^b\lambda' \\ {}^c\lambda' \end{bmatrix} = \begin{bmatrix} a\left(\frac{dx_1}{\ell_f}\right)^2 & a\left(2\frac{dx_1dx_2}{\ell_f^2}\right) & a\left(\frac{dx_2}{\ell_f}\right)^2 \\ b\left(\frac{dx_1}{\ell_f}\right)^2 & b\left(2\frac{dx_1dx_2}{\ell_f^2}\right) & b\left(\frac{dx_2}{\ell_f}\right)^2 \\ c\left(\frac{dx_1}{\ell_f}\right)^2 & c\left(2\frac{dx_1dx_2}{\ell_f^2}\right) & c\left(\frac{dx_2}{\ell_f}\right)^2 \end{bmatrix} \begin{bmatrix} \overline{C}_{11} \\ \overline{C}_{12} \\ \overline{C}_{22} \end{bmatrix} \tag{8.22}$$

If we call the 3×3 matrix, M, then this equation has the general form of:

$$\lambda' = \mathbf{M}\overline{\mathbf{C}}$$

which can be solved by inverting matrix **M** (Fig. 8.13):

$$\overline{\mathbf{C}} = \mathbf{M}^{-1}\lambda' \tag{8.23}$$

With more than three lines, one can do a least squares best fit (Menke, 1984):

$$\overline{\mathbf{C}} = \left[\mathbf{M}^{\mathbf{T}}\mathbf{M}\right]^{-1}\mathbf{M}^{\mathbf{T}}\lambda' \tag{8.24}$$

In the three dimensional case, we would need the quadratic elongation of six lines on at least two different planes to solve for all six independent components of the Cauchy deformation tensor.

The $x_1$ and $x_2$ in Equation (8.22) are the endpoints of the lines in the deformed state. So, $dx_1$ would be the $x_1$ coordinate of the end of the line minus the $x_1$ coordinate of the start of the line as depicted in Figures 8.12 and 8.13.

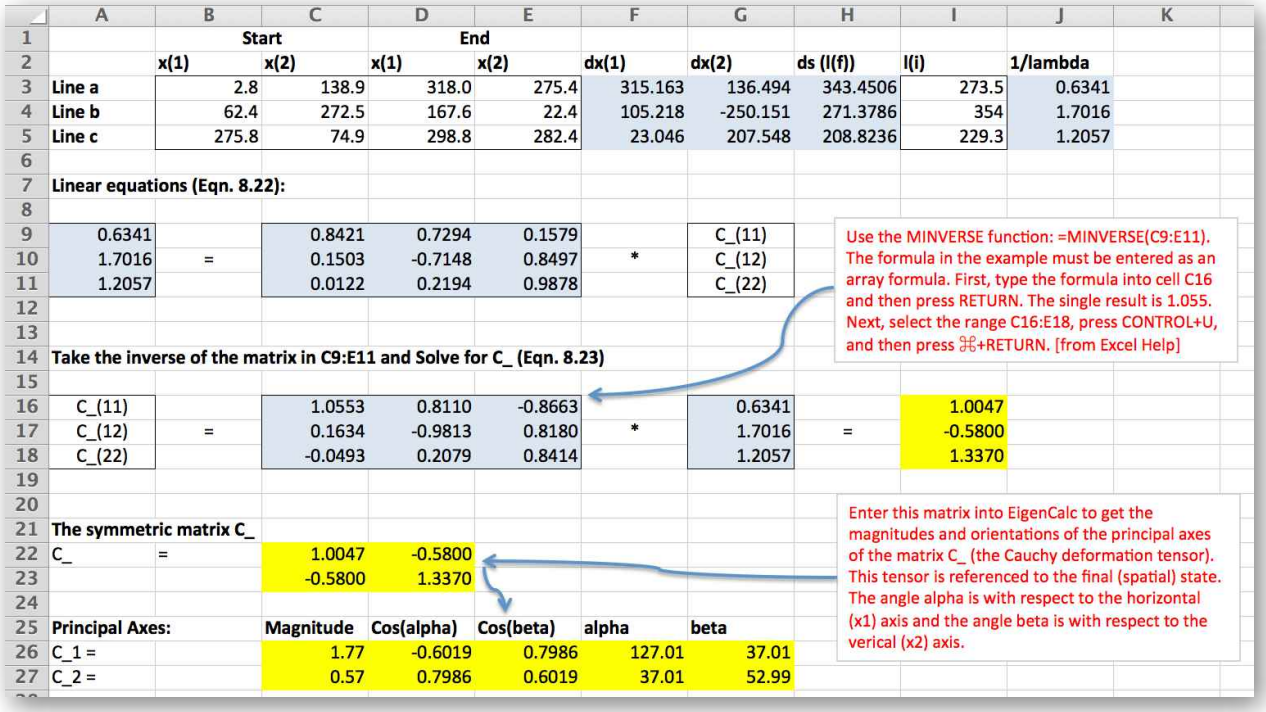

| | A | B | C | D | E | F | G | H | I | J | K |
|---|---|---|---|---|---|---|---|---|---|---|---|
| 1 | | Start | | End | | | | | | | |
| 2 | | x(1) | x(2) | x(1) | x(2) | dx(1) | dx(2) | ds (l(f)) | l(i) | 1/lambda | |
| 3 | Line a | 2.8 | 138.9 | 318.0 | 275.4 | 315.163 | 136.494 | 343.4506 | 273.5 | 0.6341 | |
| 4 | Line b | 62.4 | 272.5 | 167.6 | 22.4 | 105.218 | -250.151 | 271.3786 | 354 | 1.7016 | |
| 5 | Line c | 275.8 | 74.9 | 298.8 | 282.4 | 23.046 | 207.548 | 208.8236 | 229.3 | 1.2057 | |
| 6 | | | | | | | | | | | |
| 7 | Linear equations (Eqn. 8.22): | | | | | | | | | | |
| 8 | | | | | | | | | | | |
| 9 | 0.6341 | | 0.8421 | 0.7294 | 0.1579 | | C_(11) | | | | |
| 10 | 1.7016 | = | 0.1503 | -0.7148 | 0.8497 | * | C_(12) | | | | |
| 11 | 1.2057 | | 0.0122 | 0.2194 | 0.9878 | | C_(22) | | | | |
| 12 | | | | | | | | | | | |
| 13 | | | | | | | | | | | |
| 14 | Take the inverse of the matrix in C9:E11 and Solve for C_ (Eqn. 8.23) | | | | | | | | | | |
| 15 | | | | | | | | | | | |
| 16 | C_(11) | | 1.0553 | 0.8110 | -0.8663 | | 0.6341 | | 1.0047 | | |
| 17 | C_(12) | = | 0.1634 | -0.9813 | 0.8180 | * | 1.7016 | = | -0.5800 | | |
| 18 | C_(22) | | -0.0493 | 0.2079 | 0.8414 | | 1.2057 | | 1.3370 | | |
| 19 | | | | | | | | | | | |
| 20 | | | | | | | | | | | |
| 21 | The symmetric matrix C_ | | | | | | | | | | |
| 22 | C_ | = | 1.0047 | -0.5800 | | | | | | | |
| 23 | | | -0.5800 | 1.3370 | | | | | | | |
| 24 | | | | | | | | | | | |
| 25 | Principal Axes: | | Magnitude | Cos(alpha) | Cos(beta) | alpha | beta | | | | |
| 26 | C_1 = | | 1.77 | -0.6019 | 0.7986 | 127.01 | 37.01 | | | | |
| 27 | C_2 = | | 0.57 | 0.7986 | 0.6019 | 37.01 | 52.99 | | | | |



**Figure 8.13 — Spreadsheet solution to the same 3 lines problem solved graphically in Figures 8.10 and 8.11, using inverse methods (eqns. 8.22 and 8.23).**

# Exercises—Chapter 8

For some of these problems, you will need to download the StrainSim program from: http://www.geo.cornell.edu/geology/faculty/RWA/programs/strainsim-v-3.html

1. Using the StrainSim 3 program,
   (a) Draw a circle and triangle object and then choose animate from the model. Select simple shear and specify 100 steps of 2° each and click okay. You will see the objects progressively deformed. After the animation is finished, select the Info tab and copy the entire contents of the table on the right into a spreadsheet or graphing program. Do this for each of the three triangular bisectors, which you can select from the popup menu. In the spreadsheet or graphics program, plot the following:
      - The incremental extension for all three lines on a single plot
      - The finite extension for all three lines on a single plot
      - The angle for all three lines on a single plot

   (b) Now, start over and draw a circle with 4 lines at 90°, 75°, 45°, and 30° (but no triangle). Select Animation from the Model menu and specify pure shear with 100 steps of 0.014 horizontal extension. Again, plot the following:
      - The incremental extension for all three lines on a single plot
      - The finite extension for all three lines on a single plot
      - The angle for all three lines on a single plot

   Using your graphs as illustrations, discuss the similarities and differences between the progressive simple and pure shear deformation paths.

2. Use the strainSim 3 program to perform a simple shear deformation with an angular shear of 35°. Plot the result on a Mohr Circle for finite strain in the deformed state. Use the measurements from the Mohr Circle to figure out what to enter so that you get the exact same size and shape strain ellipse using a pure shear deformation.

3. The figure, below shows a tracing of a slab of deformed rock with a number of brachiopods and a crinoid stem that has been pulled apart, though the individual segments have not been deformed. Assuming plane strain and no volume change, plot the Mohr Circle for finite strain in the deformed state and deter-

mine the orientation of the principal axes of strain. What directions in the fossils have the same length as they had before the deformation?

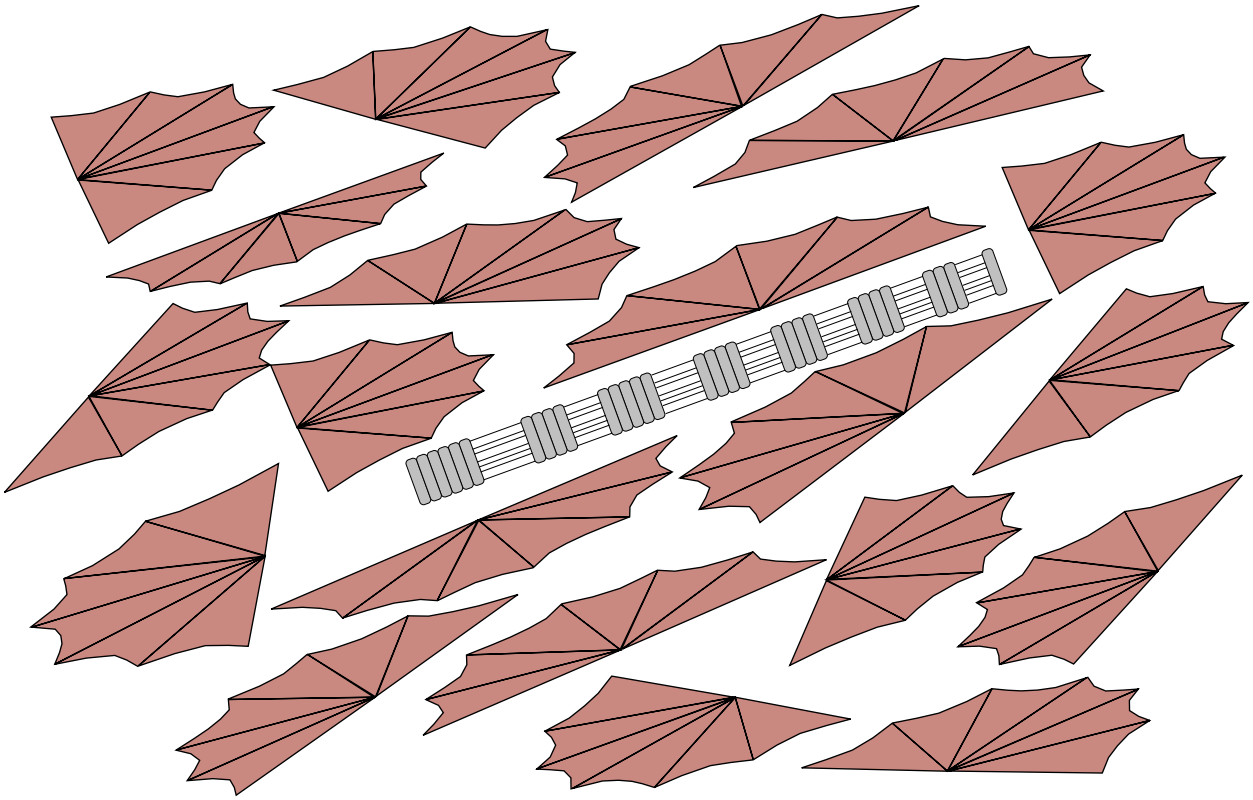

 

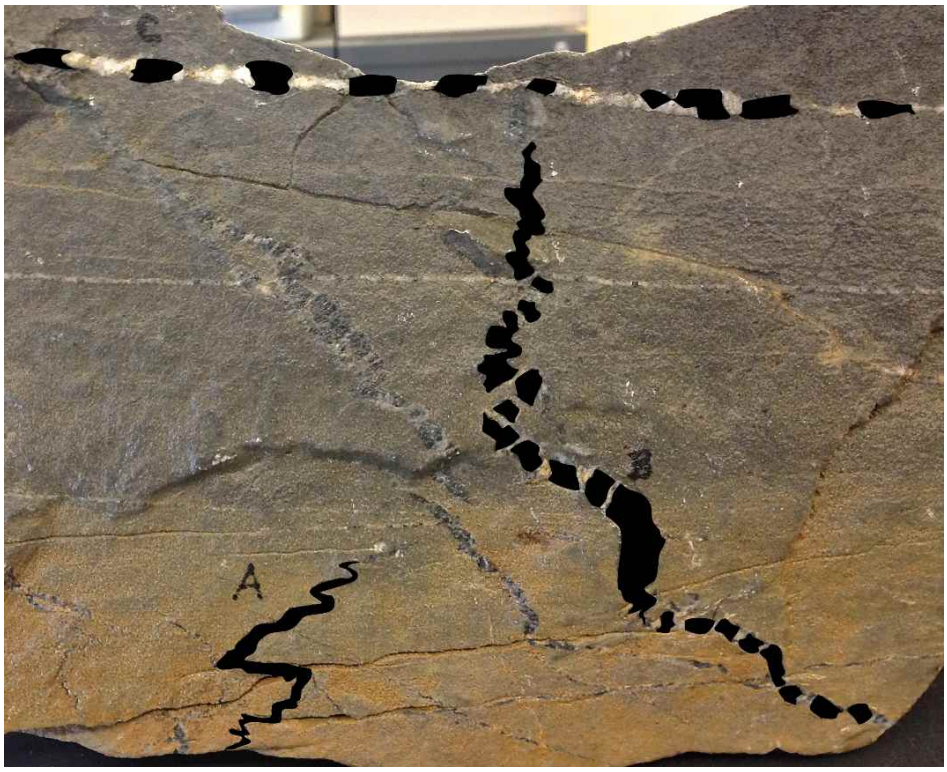


4. The photograph above is an annotated image of a Pennsylvanian limestone from the Blackpine Mountains in southern Idaho, part of the cover sequence of the Raft River metamorphic core complex. The folded layers and those stretched in boudinage have been highlighted in black to be easier to see. The actual initial and final measurements of A, B, and C are shown in expanded view on the next page.

   (a) Determine the magnitude and orientation of the finite strain ellipse following the steps outlined earlier in this chapter, either graphically or numerically. Be sure to show your Mohr's Circle for finite strain with the three lines plotted in correct orientation. Show the orientations of the principal axes of the strain ellipse on the diagram on the next page.

   (b) Can you tell whether the deformation was in plane strain? Explain.

   (c) Can you determine the orientation of the infinitesimal strain axes? Explain.

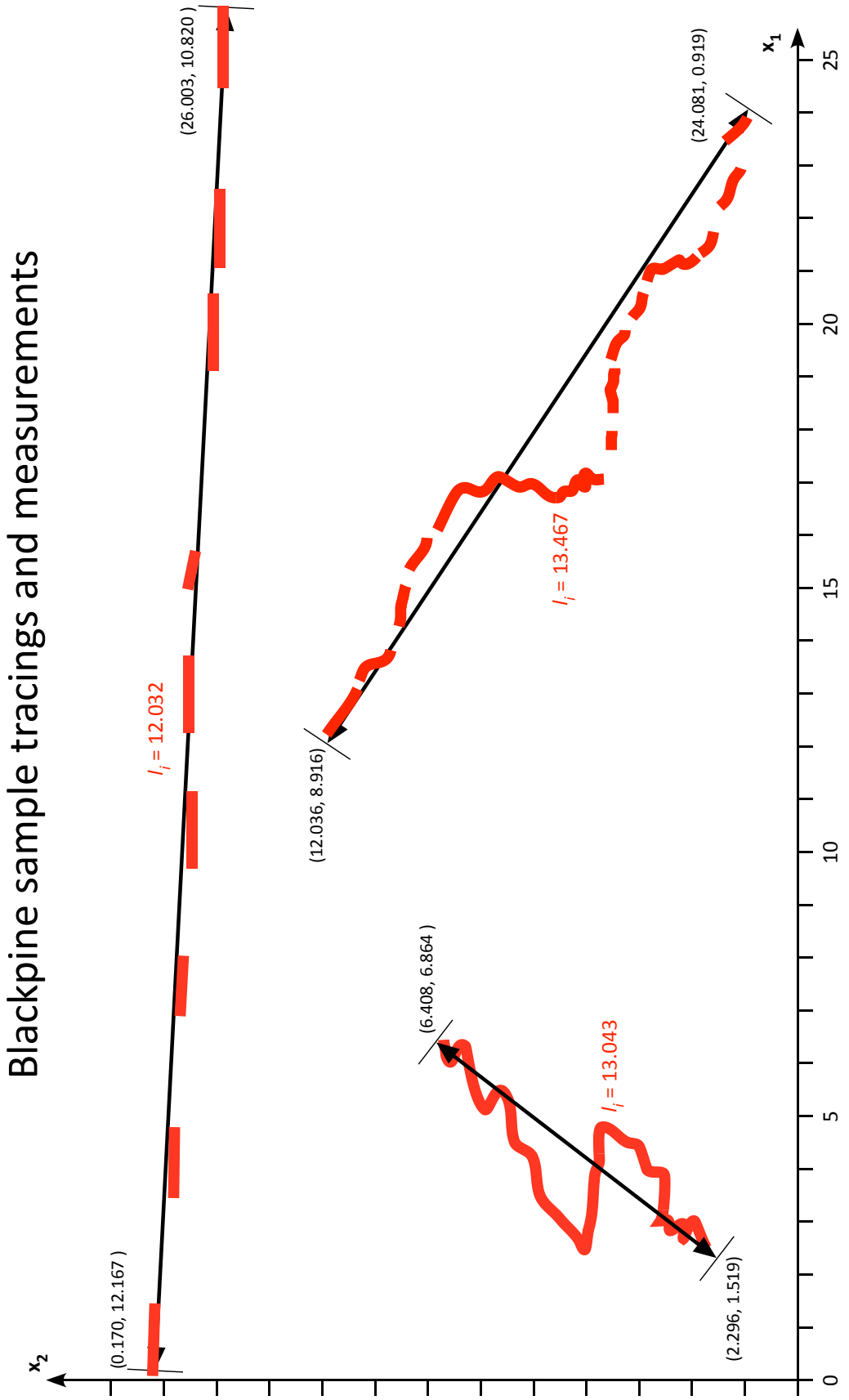
Blackpine sample tracings and measurements
x2
x1
0
5
10
15
20
25
(0.170, 12.167 )
(26.003, 10.820 )
$l_i$ = 12.032
(12.036, 8.916)
(24.081, 0.919)
$l_i$ = 13.467
(6.408, 6.864 )
(2.296, 1.519)
$l_i$ = 13.043

# Chapter 9

## *Rheology, Stress in the Crust, and Shear Zones*

### Introduction

Why is it that some rocks break whereas other rocks appear to flow seamlessly? Sometimes, one can observe these contrasting types of behavior in different minerals in the same rock? ***Rheology*** is the study of flow of rocks and to delve into this topic, and understand the question raised in the first sentence, requires us to understand the relations between stress and strain (or strain rate), the effects of

environmental factors on deformation, and how materials actually deform at the scale of the crystal lattice.

### Relationship Between Stress and Strain

At its simplest, deformation can be either ***non-permanent*** or ***permanent***. In the former case, the deformation exists only while the stress is applied and the material returns to its undeformed state upon removal of the stress. Permanent deformation, on the other hand, is forever. These topics are treated more formally in Chapter 12.

## *Elasticity*

Elastic deformation is, by definition, non-permanent and instantaneous. The material suffers distortion only while stress is applied and quickly returns to normal when he stress is removed. Many processes in geophysics and geology are mostly or completely elastic: the propagation of seismic waves, the earthquake cycle, or flexure of the lithosphere beneath a load such as a mountain belt or a sedimentary basin. The GPS data that you analyzed in Chapter 7 is largely non-permanent deformation that occurs when the earth on one side of a fault "snaps back" during an earthquake, something known as the elastic rebound theory. What distinguishes all of these deformations is that they are very small even though the stresses are larger.

From your physics courses and experiments with springs, you probably remember Hooke's Law, in which there is a linear relationship between force and displacement. However, you also know that both stress and infinitesimal strain are second order tensors and, therefore, the relationship between them should be a fourth order tensor:

$$\sigma_{ij} = - C_{ijkl}\varepsilon_{kl} \tag{9.1}$$

where, $C_{ijkl}$ is the ***stiffness tensor***. Although Equation (9.1) looks nasty with 81 terms, they re not all independent. In fact because of symmetry, there are at most 36 independent parameters and for all practical purposes, we only refer to a few ***elastic moduli***. They are:

- ***Young's modulus***, $E$, for axial strain (elongations or shortenings), where $\sigma = E\varepsilon$. A material with a high Young's modulus is very rigid.
- The ***shear modulus*** or ***modulus of rigidity***, $G$, is appropriate for simple shear deformations.
- The ***bulk modulus***, or ***incompressibility***, $K$, is likewise the one to use for simple contractions or dilations (i.e., volume strains).

These moduli can be related to one another if we know and independent parameter, known as Poisson's Ratio, $\nu$, which describes to what extent a shortening in one direction is balanced out by a lengthening in an orthogonal direction. Poisson's ratio is the ratio of the transverse to the longitudinal extension:

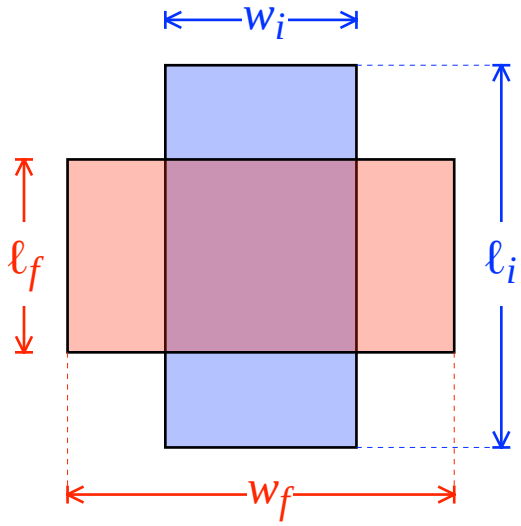


**Figure 9.1 — The blue rectangle is elastically deformed into the red rectangle (strains are highly exaggerated). Poissons ratio is defined as the ratio of the transverse extensions to the longitudinal extensions, calculated from the $w$'s and $\ell$'s, respectively as shown in equation (9.2).**

$$\nu = -\frac{e_t}{e_\ell} = -\frac{\left(\frac{w_f - w_i}{w_i}\right)}{\left(\frac{l_f - l_i}{l_i}\right)} \tag{9.2}$$

For volume constant deformation, $\nu = 0.5$ but for most rocks, $0.1 \leq \nu \leq 0.33$. All of these parameters are related by the following equation:

$$G = \frac{E}{2\,(1+\nu)} = \frac{3K\,(1-2\nu)}{2\,(1+\nu)} \tag{9.3}$$

Rocks only experience a very small amount of elastic strain before permanent deformation ensues. That permanent deformation can be in the form of a fracture or fault, something we saw in Chapter 6. When a fracture cuts across the material, there is a loss of cohesion and the sample falls apart. However, the material can also deform permanently without losing cohesion, a type of deformation we call…

## *Plasticity*

Plastic deformation results when a critical threshold stress, known as the yield stress ($\sigma_y$), is exceeded and the ratio of the change in differential stress to the change strain decreases drastically. Three different behaviors are possible (Fig. 9.2): (a) the slope of the stress strain curve decreases but remains positive, which is

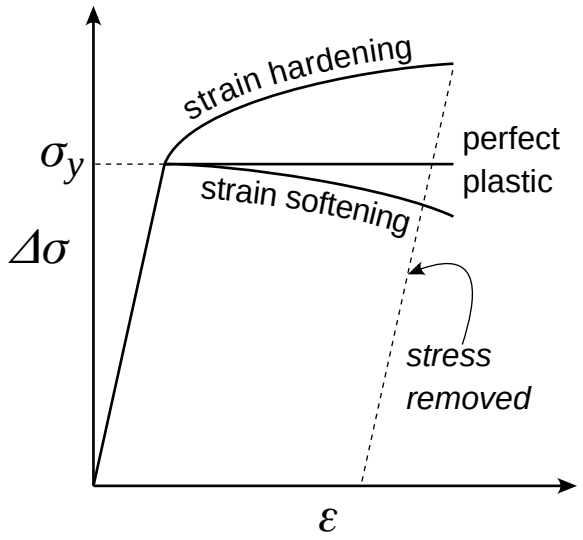


**Figure 9.2 — Idealized differential stress(Δσ)-strain(ε) curves exhibiting different types of plastic deformation once the yield stress, $\sigma_y$, is surpassed. Strain hardening occurs at lower temperatures where as strain softening at higher temperatures. If the stress is removed (dashed line), the initial elastic deformation is recouped but the deformation beyond the yield stress is not.**

known as strain hardening, (b) strain increases continually without any further increase in stress (perfect plastic behavior), or (c) the strain increases with decreasing differential stress, known as strain softening. Temperature largely controls which of these behaviors will occur.

### *Strain Rate and Viscosity*

So far, we haven't said anything about time except that elastic deformation is instantaneous. Consider the deformation shown in Figure 9.3a. The same material deforms continuously for a constantly applied differential stress, but the ***rate of deformation tensor***[4], $\dot{\varepsilon}$, increases with increasing stress. So, we can make a new curve (Fig. 9.3b) where the differential stress is plotted against strain rate; the ratio between stress and strain rate is known as the ***viscosity***, $\eta$, which is a measure of a fluid's resistance to flow. The material shown in Figure 9.3b exhibits a constant viscosity and thus is known as a ***Newtonian fluid***. Over a long period of time, even rocks within the earth can exhibit fluid-like behavior, but in contrast to Newtonian fluids, they tend to exhibit non-linear, power law viscosity as we shall see, below.

Viscous and elastic idealized models are combined in various ways. For example, ***viscoelastic*** deformation is non-permanent but develops over time and is

[4] The rate of deformation tensor is commonly confused with the time derivative of the strain tensor. For infinitesimal strain, the two are equivalent but in finite strain, the former is defined with respect to the spatial coordinates whereas the latter is defined with respect to the material coordinates (Malvern, 1969).

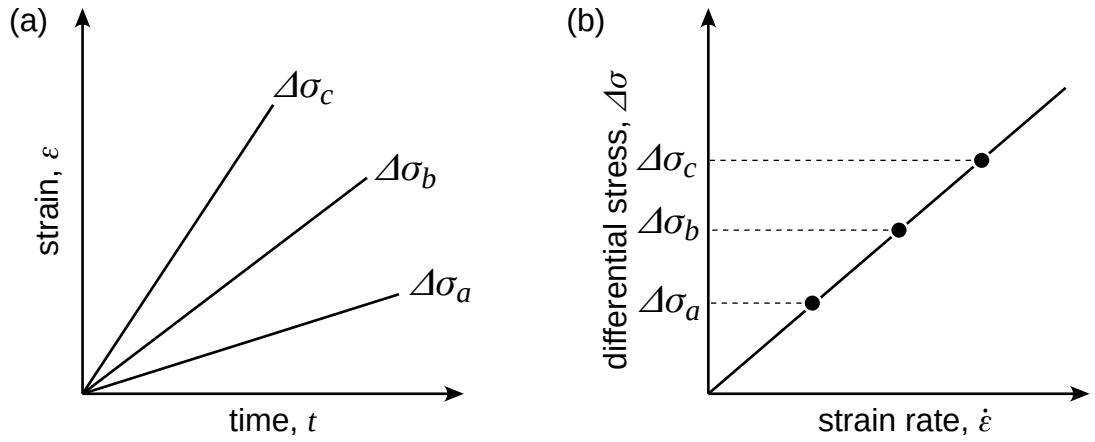


**Figure 9.3 — (a) A material that accrues strain over time at constant stress. $\Delta\sigma_a \leq \Delta\sigma_b \leq \Delta\sigma_c$ and thus the strain rate varies differential stress. (b) Same data plotted with differential stress against strain rate. The slope of the line is known as the viscosity and the simple material shown, with constant viscosity, is known as a Newtonian fluid.**

recovered over time as well. Likewise, there are ***viscoplastic*** models that combine elements of viscosity and plasticity. There are many additional hybrid mechanisms.

## Environmental Factors

The type of deformation that a rock experiences is due primarily to its composition and the environmental conditions under which the deformation occurred. You have undoubtedly reviewed the environmental factors in the lecture part of your course. The most important are:

- ***Confining Pressure*** — This is the uniform pressure surrounding the rock at the time of deformation. It commonly corresponds to the vertical stress or ***lithostatic load***, that is the weight of the overlying rocks. An increase in confining pressure makes rocks stronger (i.e., the yield stress increases), as reflected by the slope of the Coulomb part of the failure envelop. Because confining pressure increases with depth, rocks should get stronger deeper in the earth. The formula for lithostatic load is:

$$P_{lith} = \int_0^z \rho g \, \mathrm{d}z \approx \overline{\rho} g z \tag{9.4}$$

The right side of this equation is a common approximation for the case where the density, $\rho$, does not vary with depth, $z$, and the change in gravitational acceleration, $g$, is small with changes in depth corresponding to crustal conditions. The confining pressure effect is relatively insensitive to rock composition, except of course to the extent that composition determines density.

- ***Temperature*** — With increasing temperature, mechanisms of crystal plasticity described below, which depend on composition, begin to kick in and reduce the yield stress. The increase in conductive temperature with depth varies with tectonic setting, being about 15-20°C/km with depth (a ***heat flow*** of about 60 mW/m$^2$) in stable continental interiors, ~30°C/km in rift provinces (~90 mW/m$^2$), and >40°C/km in active volcanic provinces (~120 mW/m$^2$). Because temperature increases with depth, its effect is opposite to that of confining pressure. Thus these are the two great competing factors, but they are modified by other factors as well, including…
- ***Fluids*** — There are three distinct ways in which fluids act to weaken rocks: (a) increasing the ***pore fluid pressure*** counteracts confining pressure by reducing the effective normal stress; (b) ***pressure solution*** dissolves soluble minerals, especially at high stress grain-to-grain contacts, redepositing the material locally in low stress "pressure shadows" or flushing the dissolved material completely out of the rock; and (c) ***hydrolytic weakening*** where water in the crystal structure weakens the bonds of the crystal.
- ***Strain Rate*** — When the strain is high, rocks are more resistant to deformation and when they do deform, they are more likely to do brittlely. A slower strain rate allows the rocks to ***creep*** or flow under lower differential stress conditions, effectively lowering the yield stress.

## Deformation Mechanisms

Although the crust is complex, there are a relatively small number of deformation mechanisms which you have probably already reviewed in the lecture part of your class. Here is a commented list:

- Elastic deformation — Very low temperature, small strains
- Fracture — Very low temperature, high differential stress, pore fluid pressure important
- Frictional slip on preexisting fractures — Low temperature, high differential stress but less than that required for fracture, pore fluid pressure important
- Pressure Solution — Low temperature, fluids necessary
- Dislocation glide — Low temperature, high differential stress. Produces strain hardening behavior
- Dislocation glide and climb — Higher temperature, high differential stress. Requires increased lattice diffusion to permit dislocations to climb around obstacles.
- Grain boundary diffusion — Low temperature, low differential stress, slow strain rates
- Crystal lattice diffusion — Very high temperature ($T \approx 0.85 T_{melt}$), low differential stress. Probably only effective as a primary mechanism in the mantle of the earth.

## State of Stress in the Earth

The state of stress in the earth is important for a number of reasons ranging from where earthquakes nucleate to the thickness of the elastic lithosphere that flexes under loads. There is a fundamental principle underlying the determination of stress in the lithosphere: the dominant deformation mechanism is the one that requires the lowest differential stress to activate. If mechanism A requires 500 MPa at a particular set of environmental conditions, but mechanism B only require 200 MPa, not only will B dominate, but the differential stress will never significantly ex-

ceed 200 MPa. We tend to think of stress magnitude as something that is imposed externally and independently of the rocks but in fact, the strength of the rock controls the maximum differential stresses at any depth.

### *Frictional Slip on Preexisting Fractures*

Although we examined Coulomb failure in an earlier chapter, even a casual look at almost any outcrop will demonstrate that rocks are full of pre-existing fractures and in fact the brittle crust is much more likely to slip on this pre-existing fractures than by making new fractures. There is no such thing a pristine rock! Thus, the place to start is the failure envelope for preexisting fractures (following Sibson, 1974, 1985):

$$\tau = \sigma_n^* \mu \tag{9.5}$$

where the asterisk indicates effective normal stress. We expand this equation by substituting in the equations for Mohr's Circle for stress:

$$\left(\sigma_1^* - \sigma_3^*\right) \sin 2\theta = \mu \left[\left(\sigma_1^* + \sigma_3^*\right) - \left(\sigma_1^* - \sigma_3^*\right) \cos 2\theta\right] \tag{9.6}$$

and after some algebra, we get an equation for the ratio of principal stresses:

$$\Gamma = \frac{\sigma_1^*}{\sigma_3^*} = \frac{\left(1 + \mu \cot \theta\right)}{\left(1 - \mu \tan \theta\right)} \tag{9.7}$$

To find the minimum ratio of effective principal stresses that is necessary for reactivation, we set the derivative of Γ with respect to θ equal to zero:

$$\frac{\mathrm{d}\Gamma}{\mathrm{d}\theta} = 0 \quad \therefore \quad \Gamma_{min} = \left(\mu + \sqrt{\left(1 + \mu^2\right)}\right)^2 \tag{9.8}$$

We now have the basis for calculating the minimum differential stress at which reactivation will occur but first, however, what about $\mu$? Recall from Chapter 6 that Byerlee's Law shows that friction is relatively independent of rock type (Fig. 6.10). This result holds that at confining pressures of less than 200 MPa (a little over 8 km depth for a density of 2500 kg/m$^3$) $\mu = 0.85$ and at greater confining

pressures, $\mu = 0.6$. The only significant exceptions to this rule are the clays illite, montmorillonite, and vermiculite. Thus, to a first order, we can ignore composition in the upper crust, except for its obvious control on density.

Assuming that one of the principal stresses is vertical and equal to the lithostatic load minus the pore fluid pressure (here expressed as the pore fluid pressure ratio, λ):

$$\sigma_1^* - \sigma_3^* \geq \left(\Gamma_{min} - 1\right) \rho g z \left(1 - \lambda\right) \sigma_v^* = \rho g z \left(1 - \lambda\right) \tag{9.9}$$

we can derive expressions for the minimum differential stress that will activate slip on pre-existing weaknesses for the three basic conditions of Andersons Law (Table 9.1)

**Table 9.1: Frictional Strength of the Crust**

| Vertical Stress | Tectonic Environment | Minimum Differential Stress |
|---|---|---|
| $\sigma_3$ | thrust faulting | $\sigma_1^* - \sigma_3^* \geq \left(\Gamma_{min} - 1\right) \rho g z \left(1 - \lambda\right)$ |
| $\sigma_1$ | normal faulting | $\sigma_1^* - \sigma_3^* \geq \dfrac{\left(\Gamma_{min} - 1\right)}{\Gamma_{min}} \rho g z \left(1 - \lambda\right)$ |
| $\sigma_2$ | strike-slip faulting | $\sigma_1^* - \sigma_3^* \geq \dfrac{\left(\Gamma_{min} - 1\right)}{\Phi\left(\Gamma_{min} + 1\right) + 1} \rho g z \left(1 - \lambda\right)$ where $\Phi = \dfrac{\sigma_2 - \sigma_3}{\sigma_1 - \sigma_3}$ |

## *Power Law Creep*

We have seen that dislocation glide and climb is the dominant mechanism of crystal plasticity in the crust of the earth. Unlike frictional deformation, which is relatively independent of composition and strongly dependent on confining pressure, crystal plastic deformation depends strongly on composition and temperature but not on confining pressure. Through much experimental work, flow laws have

been developed to describe this type of deformation for many different rock types. The basic equation is:

$$\dot{e} = C_o \left(\sigma_1 - \sigma_3\right)^n \exp\left(\frac{-Q}{RT}\right) \tag{9.10}$$

Where

$\dot{e}$ = strain rate [$s^{-1}$]

Co = a constant [$GPa^{-n}s^{-1}$1; experimentally determined]

$\sigma_1 - \sigma_3$= the differential stress [GPa]

$n$ = a power [experimentally determined]

$Q$ = the activation energy [kJ/mol; experimentally determined]

$R$ = the universal gas constant = 8.3144 × 10-3 kJ/mol K

$T$ = temperature, K [K = °C + 273.16]

It is called ***power law creep*** because the strain rate is proportional to a power of the differential stress. Equation (9.10) describes a non-linear viscous rheology. Because temperature occurs in the exponential function, this sort of rheology is going to be extremely sensitive to temperature. To think of it another way, over a very small range of temperatures, rocks

**Table 9.2: Power Law Creep Parameters**

| Rock Type | Log(Co) $GPa^{-n}s^{-1}$ | n | Q (kJ/mol) |
|---|---|---|---|
| Albite Rock | 6.1 | 3.9 | 234 |
| Anorthosite | 6.1 | 3.2 | 238 |
| Aplite | 2.8 | 3.1 | 163 |
| Clinopyroxenite | 9 | 2.6 | 335 |
| " | 14.4 | 6.4 | 444 |
| Diabase | 6.5 | 3.4 | 260 |
| " | 11.72 | 3 | 356 |
| Dolomite | 14.4 | 9.1 | 349 |
| Olivine (dry) | 14.4-15.3 | 3.4-3.5 | 528-544 |
| Olivine (wet) | 14.2,16.1 | 3.4,4.5 | 444,498 |
| Granite (dry) 1 | -0.2 | 2.9 | 106 |
| Granite (dry) 2 | 1.6 | 3.4 | 139 |
| Granite (wet) | 2 | 1.9 | 137 |
| Limestone | 9.9 | 2.1 | 210 |
| Marble | 25.8 | 7.6 | 418 |
| " | 20.6 | 4.2 | 427 |
| Quartz Diorite | 4.3 | 2.4 | 219 |
| Quartzite (dry) | 1.2 | 1.9 | 149 |
| Quartzite (dry) | 3 | 2.9 | 184 |
| Quartzite (wet) | 3 | 1.8 | 134 |
| Quartzite (wet) | 3.7 | to 2.6 | to 167 |
| Salt (halite) | 16.7 | 5.3 | 102 |

change from being very strong to very weak. The exact temperature at which this occurs depends on the lithology. Also unlike the equations for frictional strength, there is no depth term in Equation (9.10). Instead, we must use temperature as a proxy for depth by assuming a geothermal gradient. Some of the experimentally determined parameters for different common rock types are shown in Table 9.2. There are many more that are available in the literature.

Generally, one will want to calculate the differential stress as a function of temperature. That requires rewriting Equation (9.10) as:

$$\sigma_1 - \sigma_3 = \left( \frac{\dot{e}}{C_o \exp\left(\frac{-Q}{RT}\right)} \right)^{\frac{1}{n}} \tag{9.11}$$

### *Stress Variation in the Lithosphere*

To plot the variation of stress in the crust one simply plots the appropriate equation in Table 9.1 and Equation (9.11) against depth (Fig. 9.4). The temperature in (9.11) will have to be converted to depth by assuming a geothermal gradient and here we have also assumed a continental strain rate of $10^{-15}s^{-1}$. You can see from Figure 9.5 that the transition from frictional to crystal plastic occurs where the two lines cross and depends on tectonic regime, pore fluid pressure, geothermal gradient, strain rate and composition.

Care should be taken **not** to interpret these curves too literally! In Figure 9.4, for example, we assume that the crust has a quartz diorite composition when, in fact, crustal composition is highly variable. Likewise the mantle here is assumed to be dry olivine but in some tectonic environments, wet olivine would be more appropriate. Furthermore, we have not even taken into account mechanisms like pressure solution which are known to be quite important in the crust.

What this analysis does demonstrate is that the middle crust can support the highest stresses, on the order of several hundred megapascals, whereas the lower crust is very weak, supporting < 20 Mpa of differential stress. In some areas where the crust is < ~40 km thick and/or heat flow is not very high, there will be a jump

| | A | B | C | D | E | F |
|---|---|---|---|---|---|---|
| 1 | Differential Stress (Mpa) | | | | Depth | Temperature |
| 2 | Frictional Thrust | Frictional Normal | Quartz Diorite | Olivine (dry) | (km) | °C |
| 3 | 0.00 | 0.00 | 1.65E+11 | 1.05E+22 | 0 | 20 |
| 4 | 48.56 | 12.14 | 1.51E+10 | 1.80E+20 | -1 | 40 |
| 5 | 97.12 | 24.28 | 1.84E+09 | 5.02E+18 | -2 | 60 |
| 6 | 145.68 | 36.42 | 2.85E+08 | 2.10E+17 | -3 | 80 |
| 7 | 194.24 | 48.56 | 5.39E+07 | 1.23E+16 | -4 | 100 |
| 8 | 242.80 | 60.70 | 1.21E+07 | 9.66E+14 | -5 | 120 |
| 9 | 291.36 | 72.84 | 3.12E+06 | 9.68E+13 | -6 | 140 |
| 10 | 339.92 | 84.98 | 9.16E+05 | 1.20E+13 | -7 | 160 |
| 11 | 388.48 | 97.12 | 2.99E+05 | 1.79E+12 | -8 | 180 |
| 12 | 437.04 | 109.26 | 1.08E+05 | 3.14E+11 | -9 | 200 |
| 13 | 485.60 | 121.40 | 4.20E+04 | 6.33E+10 | -10 | 220 |
| 14 | 534.15 | 133.54 | 1.76E+04 | 1.45E+10 | -11 | 240 |
| 15 | 582.71 | 145.68 | 7.91E+03 | 3.69E+09 | -12 | 260 |
| 16 | 631.27 | 157.82 | 3757.72 | 1.04E+09 | -13 | 280 |
| 17 | 679.83 | 169.96 | 1880.42 | 3.20E+08 | -14 | 300 |
| 18 | 728.39 | 182.10 | 985.96 | 1.07E+08 | -15 | 320 |
| 19 | 776.95 | 194.24 | 539.21 | 3.82E+07 | -16 | 340 |
| 20 | 825.51 | 206.38 | 306.35 | 1.46E+07 | -17 | 360 |
| 21 | 874.07 | 218.52 | 180.18 | 5.92E+06 | -18 | 380 |
| 22 | 922.63 | 230.66 | 109.37 | 2.53E+06 | -19 | 400 |
| 23 | 971.19 | 242.80 | 68.33 | 1.14E+06 | -20 | 420 |
| 24 | 1019.75 | 254.94 | 43.83 | 5.34E+05 | -21 | 440 |
| 25 | 1068.31 | 267.08 | 28.80 | 2.61E+05 | -22 | 460 |
| 26 | 1116.87 | 279.22 | 19.36 | 1.33E+05 | -23 | 480 |
| 27 | 1165.43 | 291.36 | 13.28 | 6.99E+04 | -24 | 500 |
| 28 | 1213.99 | 303.50 | 9.28 | 3.80E+04 | -25 | 520 |

| Frictional Slip | |
|---|---|
| Density | 2750 |
| Pore Fluid Pressure ratio | 0.4 |
| Coefficient of friction | 0.75 |

| Power Law Creep | | |
|---|---|---|
| Parameter | Quartz Diorite | Olivine (dry) |
| Strain rate | 1E-15 | 1.00E-15 |
| Co | 4.3 | 14.4 |
| n | 2.4 | 3.4 |
| Q | 219 | 528 |
| geotherm. Grad. | 20 | 20 |

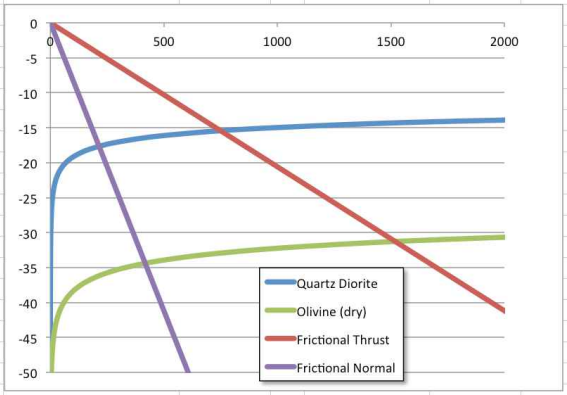


**Figure 9.4 — Spreadsheet illustrating the calculation of differential stress magnitude in the crust of the earth assuming that strength is controlled by frictional slip on pre-existing fractures and power law creep. Note that we have assumed a single average coefficient of friction rather than the two from Byerlee's Law. The power law creep parameters are for quartz diorite from Table 9.2. Note that Equation (9.11) gives differential stress in GPa whereas the equations in Table 9.1 yield stresses in Pa. Conversion factors have been added to the spreadsheet to cover all values to MPa.**

in strength of the uppermost mantle. In the case of oceanic lithosphere or continental rift provinces with low heat flow, the upper mantle may be strong enough to support upper mantle earthquakes. This notion of a strong middle crust and strong (-ish) upper mantle has given rise to the concept of the lithosphere as a so-called "jelly sandwich": two strong layers separated by a weak lower crust.

## Shear Zones

As faults cut down through the earth, they change from simple fracture planes, to zones of anastomosing fault planes to ductile shear zones that may be tens to thousands of meters in thickness. One of the great accomplishments of the last thirty years in structural geology is the understanding of genesis of shear zones, especially the minor structures which are key to understanding the ***sense of shear***.

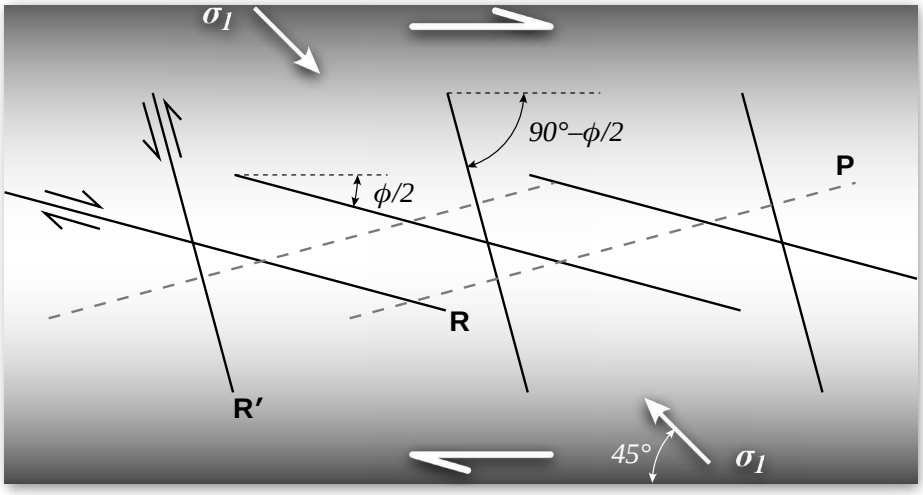


**Figure 9.5 — Cross-section showing Riedel shears in a right lateral shear zone. The gray dashed lines are P-shears that form after Riedel shears at the time of through-going rupture.**

## *Brittle Shear Zones*

Brittle shear zones that form in the upper ten kilometers or so of the Earth's crust develop a suite of structures that reflect their evolution from pre- to post-rupture. The pre-rupture structures remain preserved in the wall rocks long after the fault surface is fully developed. The most important of these structures are the ***Riedel shears***. These are conjugate Coulomb fractures that form in an en echelon manner within an overall shear zone that is, ideally, oriented at ~45° to the principal stresses (Fig. 9.5). Because they are Coulomb fractures, the two planes have opposite senses of shear: the R, or ***synthetic Riedel shears***, form at an angle of $\phi/2$ with respect to the shear zone and have the same sense of shear as the main shear zone, itself (clockwise in Fig. 9.5) whereas the R′or ***antithetic Riedel shears*** form at $90–\phi/2$ and have a sense of shear that is opposite to that of the main shear zone (counterclockwise in Fig. 9.5). The angle ϕ is the angle of internal friction (Chapter 6). ***P-shears*** may form at the time of rupture and have the same sense of shear as the main shear zone.

A number of publications emphasize the use of Riedel shears and P-shears to determine the sense of shear in fault zones (e.g., Petit, 1987). Some imply that any fracture at a low angle to the shear zone is an R-shear and any at a high-angle is an R′shear. These are dangerous assumptions because rocks are full of fractures that existed prior to, and have nothing to do with, the formation of the fault. To improve your chances of a correct interpretation, one should always determine that (a) there has been shear on the minor fractures (e.g., by observing slickensides, etc.)

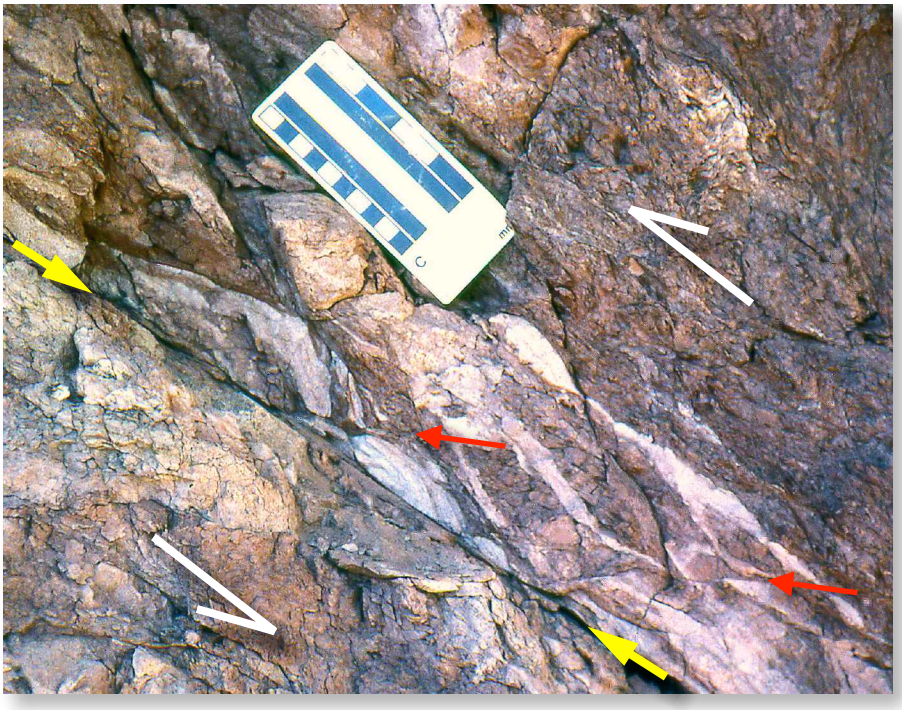

**Figure 9.6 — Synthetic Riedel shears (red arrows) showing correct sense of offset associated with a larger fault zone (yellow arrows). Sense of shear (white arrows) is opposite that shown in Figure 9.5.**

and (b) the shear on the minor fractures is consistent with that associated with Riedel shears (Fig. 9.6).

Where fluids flow and precipitate minerals — commonly quartz or calcite — in crevices and fractures associated with faulting, the resulting geometries can be very indicative of the sense of shear. Two types of structures are very useful. The first are ***sigmoidal veins***, which are sometimes referred to in older literature as "tension gashes" (Fig. 9.7). The asymmetry of the veins and their shape reflects the rotation of the older, central parts of the veins that occurs during large magnitude finite strain. The tips of the veins propagate parallel to the shortest principal axis of

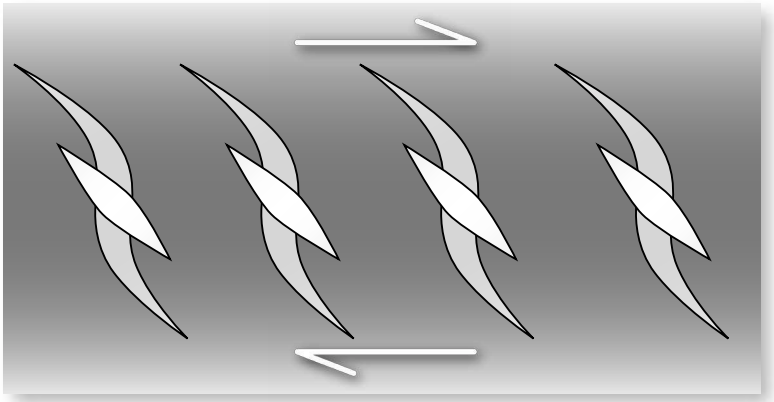

**Figure 9.7 — Sigmoidal veins in cross-section in a right lateral shear zone. Two generations are shown: an older inactive set in light gray and a younger smaller set at 45° to the shear zone boundary in white.**

infinitesimal strain which, we know from Chapter 7 is at 45° to the shear zone boundary. Eventually, the central part of the vein may rotate so much that it is no longer favorably oriented for opening. When that happens, new veins at 45° may form, crosscutting the older generation of veins (Fig. 9.7). Sigmoidal veins are highly reliable indicators of sense of shear.

The second case of minerals precipitating from fluids in shear zones is the situation where an undulatory fault surface opens up a void during fault motion (Fig. 9.8). These voids are ideal places in which to precipitate minerals such as calcite or quartz during fault movement. Under these conditions, the mineral fibers, sometimes called ***slickenfibers***, are oriented parallel to the direction of motion. On an exposed surface (Fig. 9.8b), one can identify the step from which the fibers grew, usually by the sharp contact between the step and the fibers which marks the "upstream" (with respect to the movement of the upper plate) side of the void. Like sigmoidal veins, slickenfibered steps are highly reliable indicators of fault motion (Fig. 9.9).

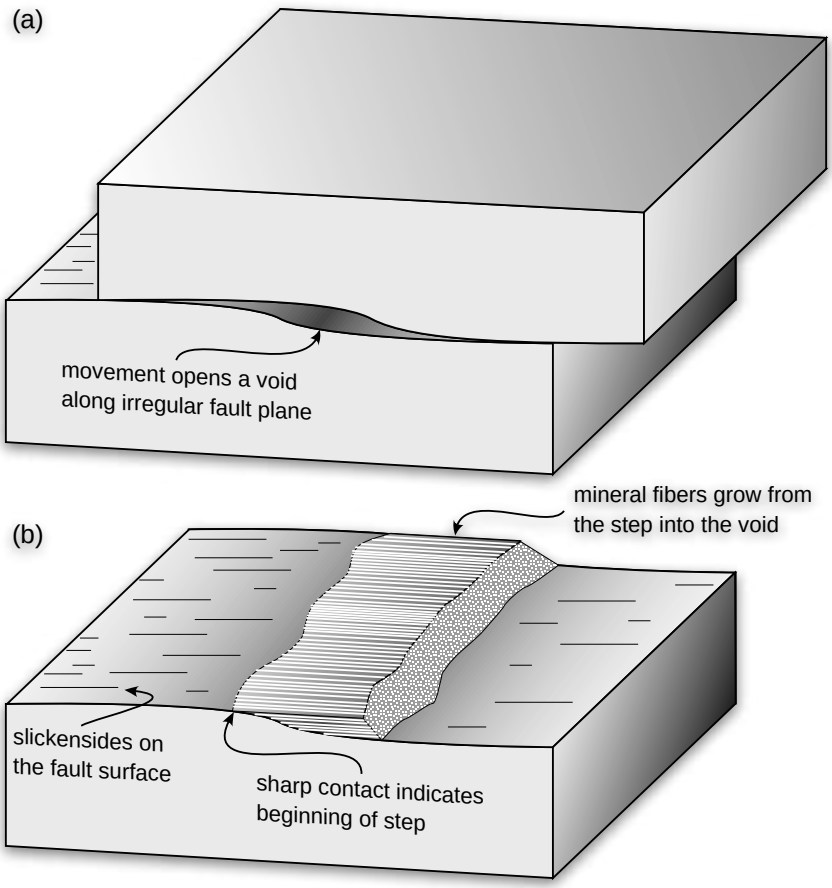


**Figure 9.8 — The formation of mineral fiber steps on an undulatory fault plane. (a) The void produced by the fault slip is an ideal place in which to precipitate fibrous minerals such as calcite or quartz. (b) The fibers grow in the direction of fault slip as the void grows in size. The key to correct interpretation of fault slip from the exposed geometry in (b) is to identify the sharp contact between the top of the step in the footwall and the fibers. A right-lateral or top to the right shear sense is indicated.**

**Figure 9.9 — Calcite slickenfibers on a fault surface in limestone. Large red arrows indicate the sense of shear in this oblique view with the upper (missing) block having moved down towards the lower left corner of the photo. Small yellow arrows indicate the sharp contact between the fibers and the fault surface which indicates the upstream side for the void.**

Finally, although we tend to think of foliations forming in metamorphic rocks, brittle fault zones can likewise have local foliation developed in the high strain zone that parallels the fault surface. Two morphologies of fault-related foliations are common (Fig. 9.10): (a) where there is a discrete zone of ***gouge*** — clay-like material produced by mechanical grind along the rock surface — the largest movements and thus highest shear strains occur between the gouge and the much less deformed wall rock. The foliation in the gouge reflects this heterogeneous simple shear strain and produces curving foliation planes (Fig. 9.10a). (b) Where the fault plane is in carbonate rocks, a localized pressure solution cleavage can form; in this case the highest shear strains are at next to the discrete fault surface and dies out upward into the country rock on either side (Fig. 9.10b). Both of these cases are examples of a type of brittle S-C fabric, a term we will define in the next section.

## *Ductile Shear Zones*

To appreciate how far structural geology has come consider that, in the middle of the last century, it was common place for structural geologists to interpret that every planar foliation in a rock represented a separate deformation, labeling them $S_0$ to $S_n$, where $S_0$ was the original stratification. We now understand that progressive deformation in shear zones can develop two more more planar folia-

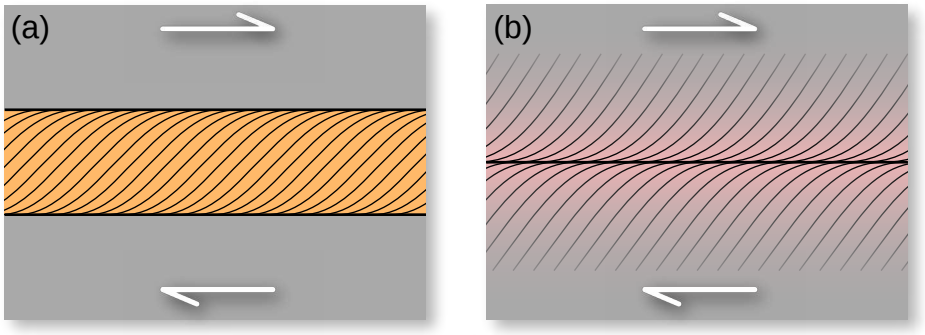


**Figure 9.10 — Cross-sections of fault related foliations in (a) fault gouge in siliciclastic rocks, and (b) zones of enhanced pressure solution next to faults in carbonates.**

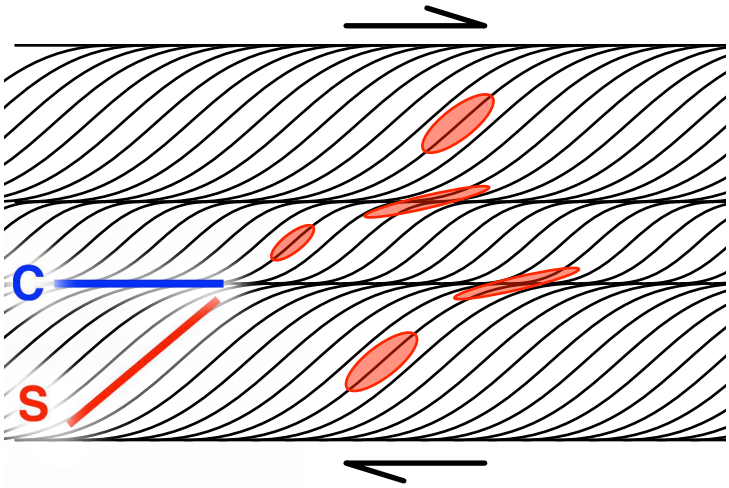


**Figure 9.11 — Idealized diagram showing the arrangement of S and C planes in an SC mylonite. Red ovals represent the strain schematically in different parts of the structure.**

tions. The basic shear zone foliations (Fig. 9.11) are known as ***S-C fabrics***; with the "C" standing for French word for shear, "cisaillement", and the "S" the French word for "schistosité" or foliation in English. As you can tell, French geologists were amongst the first to correctly describe S-C fabrics (Berthé et al., 1979)! The geometry of S and C planes develops by extremely heterogeneous simple shear. From your experiments with simple shear in the last chapter, you know that, the larger the shear strain, the closer and closer the long axis of the finite strain ellipse rotates towards the plane of shear, itself (though technically never being exactly parallel, because there is no shear strain on planes parallel to a principal strain axis). The C, or shear, planes are region of extremely high shear strain and thus the S or foliation planes become asymptotic to the C planes as they approach them (Fig. 9.11). Basement rocks in which one tends to find mylonites commonly lack easily identifi-

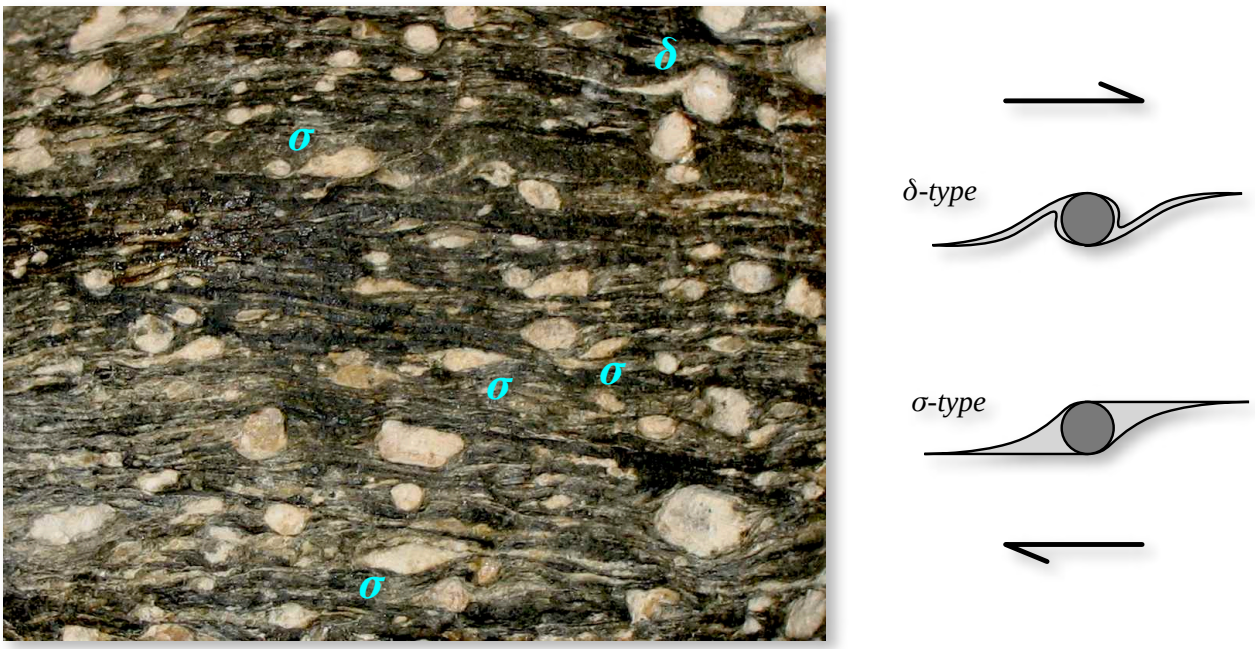


**Figure 9.12 — Asymmetric porphyroclasts in a mylonite from NW Argentina (left) and schematically on the right. Representative clasts are labeled on the photo. The top-to-the-right sense of shear is appropriate for both photo and sketch.**

able offset features, so the reliable sense of shear indicated by S-C fabrics is quite important.

Before moving on to other sense of shear indicators, a word of caution: shear zone shapes commonly exhibit curving, sigmoidal geometries (re. Figs. 9.7, 9.10 and 9.11). However, if you compare Figures 9.7 and 9.11, the sense of curvature is opposite to each other even though both diagrams have the same sense of shear. To interpret these fabrics and shapes correctly, it is essential that you understand the kinematics (i.e., the strain and how it was produced) rather than simply trying to do pattern recognition. The curved feature in Figure 9.7 is a vein and therefore the long principal axis of the strain ellipse is ***perpendicular*** to it. The curving features in Figures 9.10 and 9.11 are foliations and therefore the long axis should be approximately ***parallel*** to them.

There are a variety of other shear sense indicators in mylonitic rocks based on the geometry of individual grains and grain aggregates. These include σ- and δ-shaped asymmetric porphyroclasts (Fig. 9.12) and fractured and rotated mineral grains (commonly feldspars as in Fig. 9.13). Although beyond the scope of this manual, crystallographic c-axis fabrics and other microscopic preferred orienta-

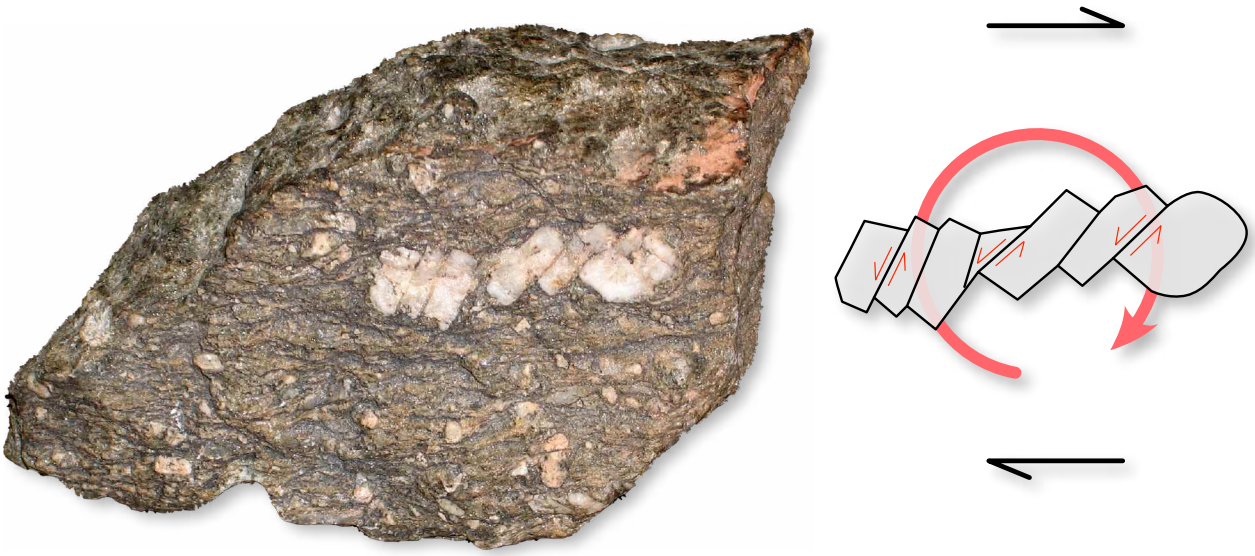

**Figure 9.13 — Fractured and rotated plagioclase crystal from a mylonite in the Sierra Chango Real of NW Argentina. Note the domino-style deformation of the feldspar: the overall rotation gives the sense of shear, even though the micro faults have the reverse sense of displacement**

tions are likewise commonly used to determine sense of shear in plastically deformed mineral grains.

### *Displacement in Heterogenous Shear Zones from Foliations*

So far, we have looked mostly at features that give us the sense, but not the magnitude, of displacement in a shear zone. Displacement is commonly not easy to determine due to lack of identifiable piercing points in basement rocks. If we make the assumption that only heterogeneous simple shear is responsible for displacement, there is quite a nice method published by Ramsay and Graham (1970). Consider a homogeneous simple shear zone (Fig. 9.14). In the field, we can't measure $\psi$ directly, but we can measure $\theta'$, which is just the angle between the foliation (assumed to be kinematically similar to S-planes) and the shear zone boundary. If the foliation is parallel to the XY plane of the strain ellipsoid then there is a simple relationship between $\theta'$ and $\gamma$:

$$\tan 2\theta' = \frac{2}{\gamma} \tag{9.12}$$

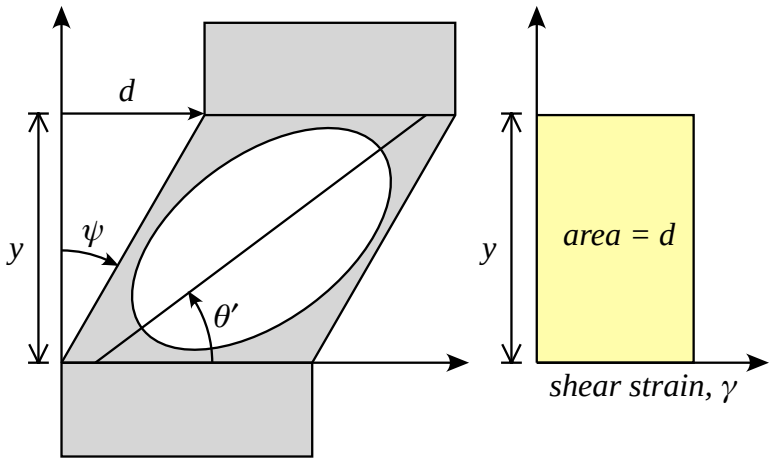


**Figure 9.14 — Hypothetical homogeneous simple shear zone demonstrating how the area under the shear strain-*y* curve is equal to the displacement, *d*.**

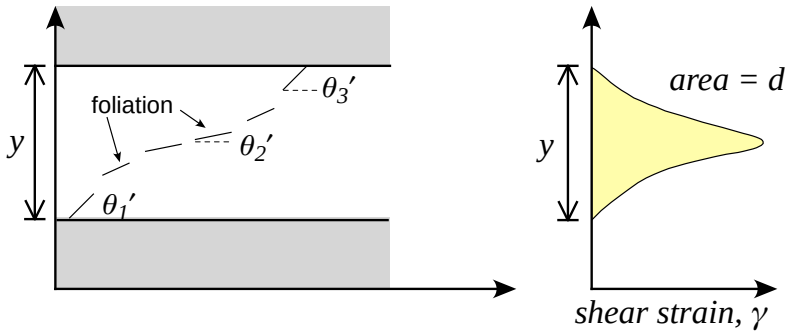


**Figure 9.15 — Variation in foliation across a heterogeneous simple shear zone (left) and the calculation of displacement by determining the are under the curve of shear strain versus distance across the shear zone.**

Although it is trivial in the case of a homogeneous shear zone, we could compute the displacement graphically by plotting γ as a function of the distance across the shear zone *y* and calculating the area under the curve (Fig. 9.14):

$$d = \int_0^y \gamma \, dy = \int_0^y \frac{2}{\tan 2\theta'} dy \qquad (9.13)$$

For a heterogeneous shear zone — the usual case in geology — the situation is more complex, but you can still come up with a graphical solution as above. The basic approach is to (1) measure the angle between the foliation and the shear zone boundary, $\theta'$, at a number of places, (2) convert those measurements to the shear strain, $\gamma$, (3) plot $\gamma$ as a function of perpendicular distance across the shear zone, and (4) calculate the displacement from the area under the resulting curve (Fig. 9.15).

## *General (2D) Shear*

Alas, most natural shear zones probably do not fit the simplified assumptions of Ramsay and Graham (1970). Instead, they probably have a combination of pure and simple shear (sometimes known as "sub-simple" shear), and may also have volume changes, both of which would negate the elegant analysis of Ramsay and Graham (1970). We will only briefly look at the theory here, following the work of Tikoff and Fossen (1993) and Fossen and Tikoff (1993). Because we have studied tensors and strain already, this part should be (relatively) easy to follow. We start with the deformation gradient tensor, which relates the positions in the initial state to those in the final state:

$$x_i = D_{ij} X_j \tag{9.14}$$

Neglecting the constant of integration, this is the same equation as (7.13). In a coordinate system parallel to the stretches and the simple shear is parallel to the $\mathbf{X_1}$ axis, the tensor D that captures simultaneous pure and simple shear can be written in two dimensions as:

$$D_{ij} = \begin{bmatrix} S_1 & \Gamma \\ 0 & S_3 \end{bmatrix} = \begin{bmatrix} S_1 & \frac{\gamma(S_1 - S_3)}{2 \ln (S_1)} \\ 0 & S_3 \end{bmatrix} \tag{9.15}$$

Γ is known as the effective shear strain. This equation is appropriate for a constant volume deformation where $S_1 = 1/S_3$. The deformation matrix for simultaneous simple shear, pure shear, and volume change is:

$$D_{ij} = \begin{bmatrix} S_1 & \frac{\gamma(S_1 - S_3)}{\ln \left( \frac{S_1}{S_3} \right)} \\ 0 & S_3 \end{bmatrix} \tag{9.16}$$

$D_{ij}$, of course, is an asymmetric tensor. If you multiply D by its transpose, you get the symmetric Green deformation tensor, **C** (referenced to the initial state):

$$\mathbf{D D^T} = D_{ki} D_{kj} = C_{ij} \tag{9.17}$$

From **C** you can determine the principal axes of strain, etc.

There are an infinite number of potential paths that lead to any finite strain state. The deformation in Figure 9.16, for example, could be produced by (a) pure shear with stretch, $S_1 = 1.75$, followed by a simple shear with $\gamma = 4.0$ (76°); (b) a simple shear with $\gamma = 1.31$ (52.6°), followed by a pure shear with $S_1 = 1.75$; or (c) a general shear with $S_1 = 1.75$ and $\gamma_{effective} = 2.29$ (66.4°). One would need to extract information on the path — perhaps from curved mineral fibers — to distinguish these three possibilities.

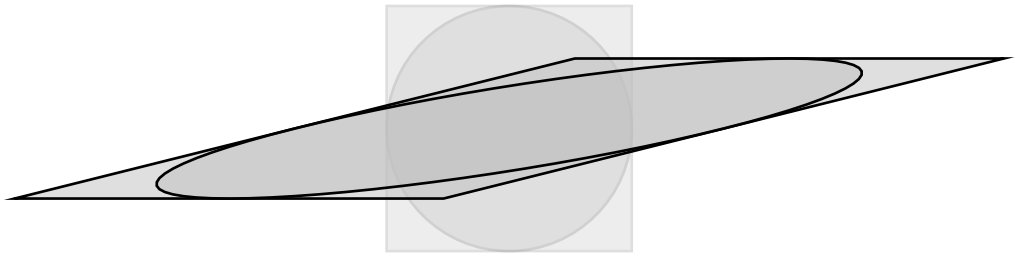

**Figure 9.16 — Any finite strain may arise from an infinite number of possible strain paths. The one shown here was produced by a general shear with horizontal stretch of 1.75 and an effective shear strain for 2.29, but many other paths will produce exactly the same final state from the given initial state.**

# Exercises—Chapter 9

1. Calculate the variation of differential stress with depth in the crust for Granite (dry) 2 (Table 9.2) assuming a strain rate of $10^{-15}s^{-1}$, geothermal gradient of 15°C/km, an average density of 2750 kg*$m^{-3}$, in an extensional environment with hydrostatic pore fluid pressure, and a coefficient of static friction of 0.70. You can to the calculations either in a spreadsheet or in Matlab.

2. The diagram, below, shows the case of simple shear of a square where the angular shear, $\psi$, is defined as the change in angle of two originally perpendicular lines (i.e., the sides of the box). A dashed line in the initial state makes an angle of $\theta$ with respect to the plane of shear. After the deformation, the same dashed line makes an angle of $\theta'$. Derive an equation which shows $\theta'$ as a function of $\theta$ and $\psi$.

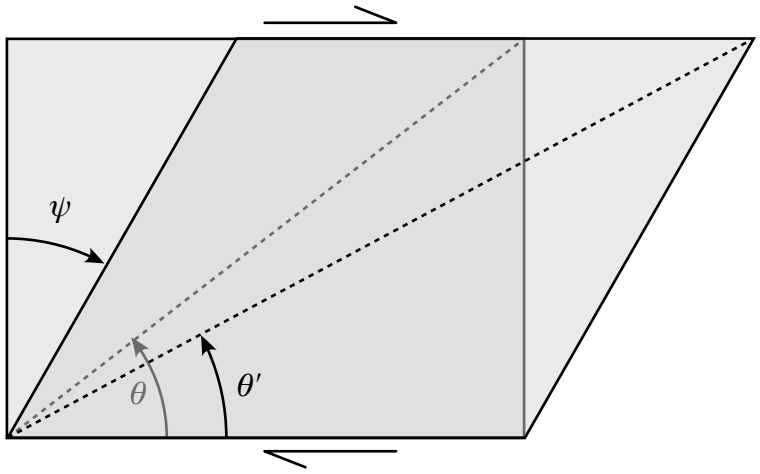


3. Once Riedel shears form, they become material lines (really, cross-sections of planes) that rotate in the shear zone. For the questions that follow, assume $\mu_{int}$ = 0.625, $\mu_s$ = 0.75, $\sigma_1$ = 120 MPa, $\sigma_3$ = 14.7 MPa, and the cohesion, $S_o$=20 MPa. Also assume simple shear, not general shear.

   (a) Calculate how much synthetic and antithetic Riedel shears will rotate before they become inactive. Show your calculations and include any plots that you used to come up with your answer.

   (b) What is the effect of changing the magnitude of the differential stress?

(c) Use your result from the previous problem to calculate the angular shear necessary to make the synthetic Riedel shears inactive.

(d) Given their different orientations within the shear zone, which shear, R or R′ do you anticipate would rotate faster and why?

4. The following questions relate to the sketch, below, of a ductile shear zone in in granitoid rocks. A grid has been laid over the sketch to help you make your measurements.

(a) Use the Ramsay and Graham (1970) relationship, described above, between orientation of foliation in a shear zone, $\theta'$, and shear strain, $\gamma$, to determine the displacement across the shear zone.

(b) What is the sense of shear in the shear zone?

(c) What assumptions does this calculation involve?

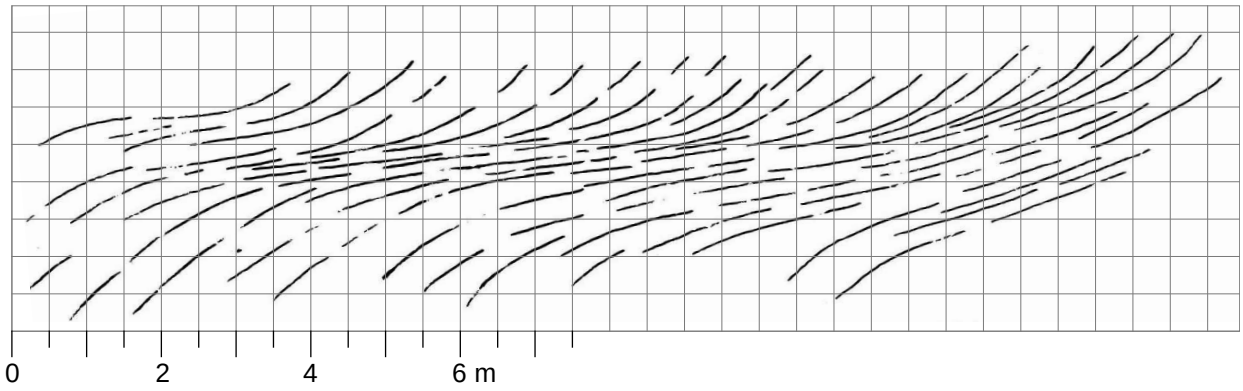


5. The photographs on the next pages are rock samples showing fault related deformation. For each one, interpret the sense of shear (relative to its orientation on the page) and make a quick sketch depicting the key features that helped you come to the conclusion that you did.

 

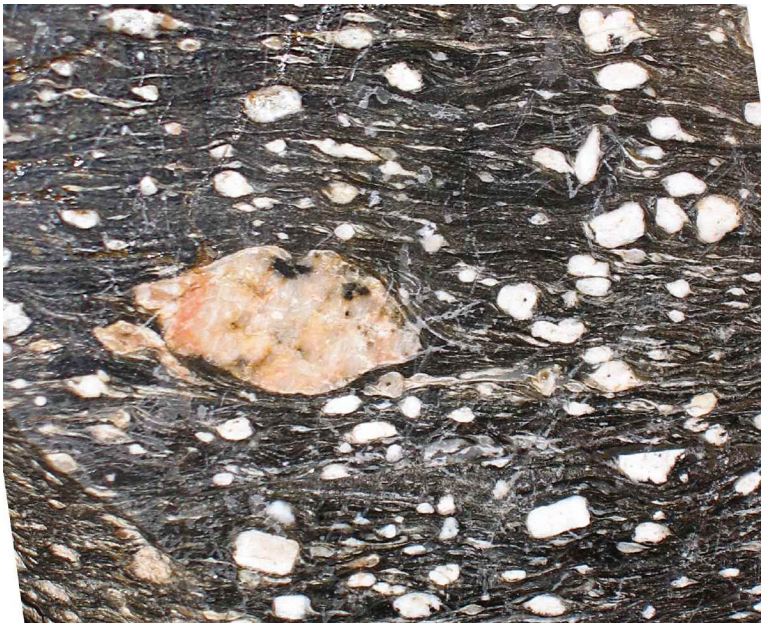

 

# Chapter 10

## *Fault-Related Folds and Cross Sections*

### Introduction

In this chapter, we change scale considerably from the previous few chapters, zooming out and looking at systems of structures. In the process, you will gain experience carrying out one of the most fundamental activities with which a structural geologist is commonly tasked: drawing cross sections. Cross sections are the primary way that we project the geometries of rock bodies into the subsurface and are

motivated by a variety of reasons both practical and intellectual. This task occurs at the intersection between data and interpretation. The difference between a good and a bad cross section can mean millions of dollars wasted or embarrassing gaffes in publications and public presentations. Cross sections can be informal freehand affairs when one is trying to understand different alternatives, but the final version can be significantly improved by application of "rules" and procedures based on our understanding of fold geometrics and their relations to faults. Regardless of the rigor with which one constructs a cross section, however, one should never forget that the cross section is only an under constrained model and not data. Uncertainty is where we will start.

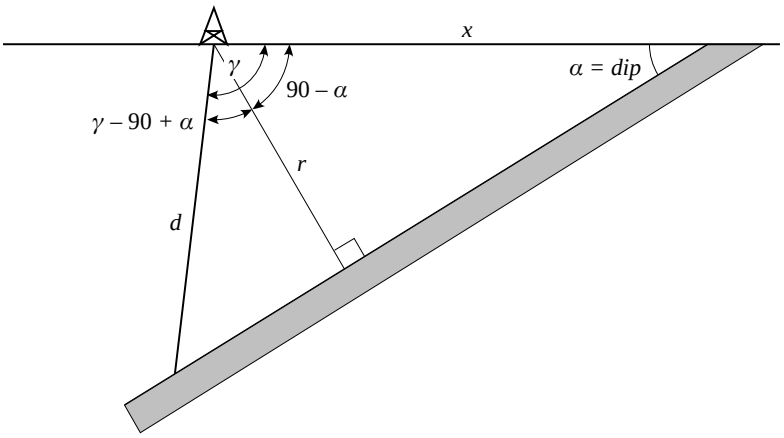


**Figure 10.1 — The calculation of the depth to a layer at a horizontal distance *x* from a surface outcrop with measured dip *a*. Quite on purpose, we do not assume that the borehole will be perfectly vertical.**

## Uncertainty in a Simple Depth Projection

Uncertainty is a topic that we visited briefly in the early chapters of this book but have not revisited since. You may recall that in Chapter 2, we saw the formula for the mean vector calculation (Eqn. 2.12). But now, let's say we know the mean vector of a series of poles to bedding and want to use that data in a calculation of the depth to that layer some distance away where the layer is in the subsurface (Fig. 10.1). This is the simplest sort of subsurface projection of geometry that one can imagine. Now, a question of great import for anyone who has ever paid for a drill hole to a particular layer: what is the uncertainty, or error, in our knowledge of the depth to the layer?

The first part of the problem, of course, is to calculate the depth, $d$, as a function of the horizontal distance, $x$, the dip, $\alpha$, and the angle that the borehole is drilled at, $\gamma$. Because the borehole is not necessarily vertical, we have to solve the two right triangles with sides $rx$ and $rd$, above. After some trigonometry, we get the expression for $d$:

$$d = \frac{x \sin \alpha}{\cos\left(\gamma - \frac{\pi}{2} + \alpha\right)} \tag{10.1}$$

Note that we are using $\pi/2$ which is 90° in radians, because most spreadsheets and programing languages require the use of radians rather than degrees. You can see that, for the special case of a vertical borehole, equation (10.1) would simplify to the much simpler:

$$d = x \tan \alpha \tag{10.2}$$

But we are going to use Equation (10.1) because that is more general and because it will allow us to incorporate uncertainties in the angle that the borehole is drilled.

Let's assume that $x$ is perfectly known but there are uncertainties in the dip, $\alpha$, of the layer were are interested in (the gray layer above) and in the angle of the borehole, $\gamma$. The standard error propagation equation for Gaussian errors (random and uncorrelated) for this case looks like (Taylor, 1997; Bevington and Robinson, 2003):

$$\delta d = \sqrt{\left(\frac{\partial d}{\partial \alpha}\delta\alpha\right)^2 + \left(\frac{\partial d}{\partial \gamma}\delta\gamma\right)^2} \tag{10.3}$$

Where $\delta d$ is the uncertainty in depth in the borehole, $\delta\alpha$ the uncertainty in dip, and $\delta\gamma$ the uncertainty in the angle of the borehole. So, we have to differentiate equation (10.1) with respect to $\alpha$ and $\gamma$. You probably don't remember how to do this off the top of your head but there is an online tool that can help: WolframAlpha (http://www.wolframalpha.com). To differentiate with respect to $\alpha$, enter this line into the search field: `d(x*sin(a)/cos(g-(pi/2)+a))/da`. And for $\gamma$, enter: `d(x*sin(a)/cos(g-(pi/2)+a))/dg`. Notice we are using the letters "`a`" and "`g`" in place of $\alpha$ and $\gamma$. This gives us the following equations:

$$\frac{\partial d}{\partial \alpha} = x \sin(\gamma) \csc^2(\alpha+\gamma) \quad \text{and} \quad \frac{\partial d}{\partial \gamma} = x \sin(\alpha)\left(-\cot(\alpha+\gamma)\right)\csc(\alpha+\gamma) \tag{10.4}$$

We can now simplify these and substitute into Equation (10.3) to get the propagated error in depth to the layer in the borehole:

$$\delta d = \sqrt{\left(\frac{x \sin(\gamma)}{\sin^2(\alpha+\gamma)}\delta\alpha\right)^2 + \left(\frac{-x \sin(\alpha)}{\tan(\alpha+\gamma)\sin(\alpha+\gamma)}\delta\gamma\right)^2} \tag{10.5}$$

Let's put this to work in a simple test example. Our input is:

| *Parameter* | *Magnitude* | *Uncertainty* |
|---|---|---|
| Horizontal distance , $x$ | 3000 m | 0 |
| Dip, $\alpha$ | 35° | 5° |
| Borehole angle, $\gamma$ | 90° (i.e., vertical) | 5° |

Using equations (10.1) and (10.5) above, we calculate that uncertainty in the depth at which the top of the layer is pierced in the borehole is 2101 ± 411 m! The 5° of uncertainty in the borehole and dip angles yields an uncertainty equivalent to 20% of the depth of the borehole.

But these methods are even more powerful than that because we can now ask the question, which factor has a bigger effect on the uncertainty, the dip or the borehole angle. In other words, you now have the tools in hand to answer the question: "Should I invest more time/money in reducing the error on the dip or controlling the angle that the borehole is drilled?" You may be tempted to answer: "5° is five degrees" but in fact the trig functions are non-linear, so let's try it. If we set the borehole uncertainty to zero, we can then calculate that the 5° uncertainty in dip yields a depth uncertainty of 390 m, close to the total error. In contrast, perfectly known dip and 5° error in the drill hole orientation will give us 128 m of uncertainty in the depth. So now we know where to devote our time and resources: determining the dip better. As a field geologist, I like that outcome!

This will not always be the case: for some geometries, the angle of the borehole could be more important. If one has programed in these relationships in a spreadsheet or more complicated code (say, by propagating the errors in Equations 6.4 to 6.6), it becomes trivially easy to play "what if" games. With this lesson — that even the simplest type of subsurface projection contains considerable error — firmly in mind, let us return to the initial objective, that of drawing cross sections.

## Drawing Cross Sections

Cross sections are the projection of surface geology, supplemented by commonly sparse subsurface data, onto a vertical plane. Although similar to, they differ

from the down-plunge projections that we studied earlier, in that the profile plane of a fold is only vertical if the fold axis is horizontal. The data that one has available varies, but commonly includes:

- Stratigraphic contacts
- Intrusive contacts and metamorphic aureoles
- Structural information such as faults and fold axes
- Orientation data such as strikes and dips of bedding, cleavage, etc
- Borehole and/or seismic reflection data (Chapter 11)

### *Preparation for drawing a cross section*

Prior to starting any task, it is always worth examining your motives; otherwise your time can be wasted. Types of questions to ask yourself before you start to draw your cross section include:

- What is my purpose in drawing a geologic section?
    - Is this for a scientific study of the tectonics of a region or a detailed process-oriented study of a single feature
    - Is the section to be a balanced section?
    - Is it for some applied use such as oil and gas or minerals exploration?
    - Do I need to show the distribution of surficial features or interpret the upper 10 km of the crust? And so on.
- What types of rocks and structures will the section depict (because there are rules for different types)?
    - Unmetamorphosed sedimentary rocks with excellent lateral continuity?
    - Metamorphic and igneous rocks with irregular contacts?
    - An area with lots of pre-existing structure with abrupt lateral changes?
- Where is the best place to draw the section?

- Usually, we draw sections so that they are oriented perpendicular to the structures and the strike of bedding.
- In general, we try to avoid drawing sections through very complicated areas and also avoid drawing them parallel to structure, although there are good reasons for doing both.
- We usually want to locate sections where we have a lot of orientation data and in areas where the outcrop allows us to place contacts with some certainty

## *Step-by-Step Section Construction*

1. Select the ***line of section*** perpendicular to structure and where there are plentiful high quality data, avoiding local complications.
2. Construct a ***topographic profile*** 1:1 (i.e., without vertical exaggeration) along the line of section (Fig. 10.2). Profile should be the same scale as the map. Ink in the topographic profile or, if you are constructing the section in a graphics program, lock the profile or put it in a separate layer along with the elevation scale.
3. Plot ***apparent dip tick marks*** on the topographic profile (remember that if the strike is not perpendicular to the line of section, then you have to calculate the apparent dip!). For dips that lie close to, but not on the line of section, remember that you project them parallel to

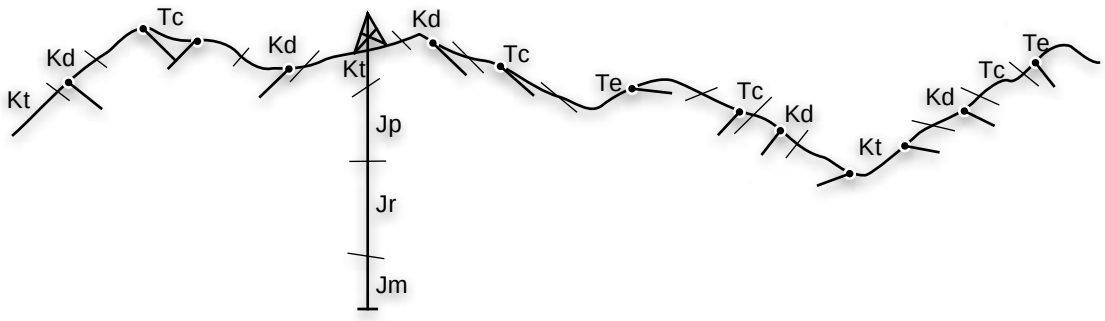


**Figure 10.2 — Plotting of data in preparation for drawing the cross section. We construct the topographic profile along the line of section and then project apparent dips, stratigraphic or structural contacts, and any subsurface information such as wells.**

the fold axis and not parallel to the strike. Do not project strikes and dips across faults onto the line of section. You can plot the apparent dip tick marks permanently. Some people prefer to use a "bar and ball" symbol, that is a small circle a that location of the projected orientation with a tick mark indicating the apparent dip in the plane of the section (Fig. 10.2).

4. Plot the geologic contacts on the topographic profile along the line of section. These should be marked lightly and in pen or pencil and labeled.

5. Plot any subsurface constraints you may have such as seismic reflection data or borehole data as shown in Figure 10.2.

6. If the region is folded, you need to decide on a ***folding model*** as well as the relationship between folds and faults. This will depend on your knowledge of the field area, field observations (e.g., slickensides on bedding planes, axial planar cleavage, etc.). In general, for unmetamorphosed sedimentary rocks, a parallel fold model is most appropriate whereas similar folds are more likely in cleaved rocks which have suffered some metamorphism. Trishear or parallel folds are most likely to be associated with tip lines of faults, etc. If you choose a parallel fold model, you must further decide whether the folds are kink (sharp hinges and planar limbs), concentric (limbs not planar, hinges broad), etc. Usually, the strikes and dips and field observations will guide you.

7. Once you decide on a fold model and the relationship between folding and faulting, you can begin to use the rules of the fold model (e.g., constant bedding thickness, dip isogons, kink axes, orientations of axial surfaces, etc.) to project your structures to depth.

8. For faults, be sure to show the ***sense of slip*** in cross section.

9. In general, do not draw your section deeper than the known stratigraphic section. Do not be afraid to use question marks where you don't know how a structure behaves.

A formal cross section is not a sketch! All features are plotted as precisely as possible following the rules that you have established for the region based on characteristics of the region that you have actually observed.

## Fold-Fault Models

Understanding the relations between coeval faults and folds is important for constructing the most plausible cross sections, especially in stratified rocks. We will start out with a simple two-dimensional assumption: that all of the folds are (approximately) cylindrical. As we saw in our π-diagram of the Big Elk anticline (Chapter 3, Exercise 3.2), with natural folds this is, at best, a crude approximation, but it does make our lives easier.

### *Fold Kinematics*

In this chapter, we deal exclusively with cylindrical folds for the simple reason that they represent plane (i.e., 2D) strain: a cross section perpendicular to the fold axis should capture, ideally, all of the strain. Within this general category, there

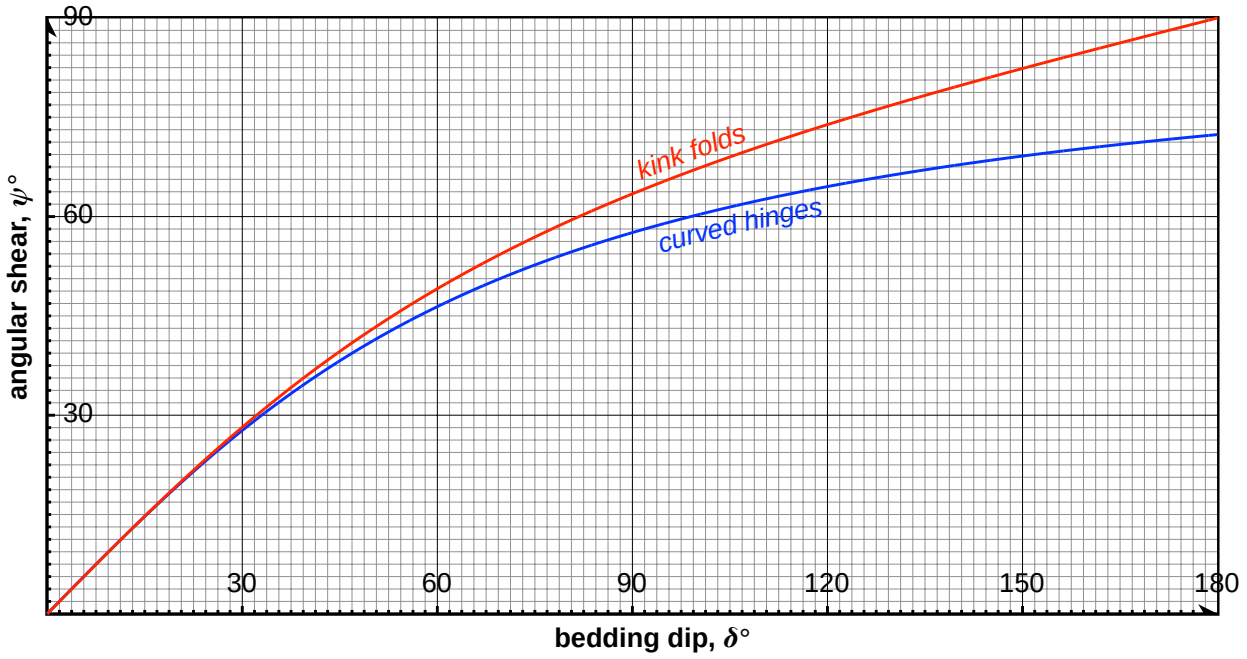


**Figure 10.3 — Graphs of Equations 10.6 showing angular shear as a function of bedding dip for curved and kink hinge parallel folds. Note that bedding dipping 180° is completely overturned.**

are three basic kinematic fold models and how we draw the cross section depends on which model we choose.

Parallel folds have Class 1 dip isogons and preserve bedding thickness throughout the fold. More importantly for section construction, the folds are flexural slip, meaning that shear occurs on the bedding surfaces between the beds. We can calculate the amount of angular shear, $\psi$, parallel to bedding as a function of the dip, $\delta$, of bedding (Fig. 10.3):

$$\text{kink folds: } \psi = \tan^{-1}\left(2\tan\left(\frac{\delta}{2}\right)\right); \quad \text{curved hinges: } \psi = \tan^{-1}\left(0.0175\delta\right) \quad (10.6)$$

*Because the shear is layer parallel, the bed surfaces themselves are lines of no finite elongation*. As we will see below, this is the critical assumption that enables us to do line length balancing. A surprisingly larger number of natural folds have relatively narrow hinges and straight, rather than curved limbs; these are known as ***kink folds***. In order to preserve bedding thickness, the axial planes of kink folds must bisect the interlimb angle; otherwise one limb will be thicker than the other. Kink folds are common where faults change dip over a very small distance and in stratified rock sequences with multiple thin layers with weak bedding planes. A second important category is the ***concentric fold*** (Fig. 10.4) where all of the bedding surfaces have

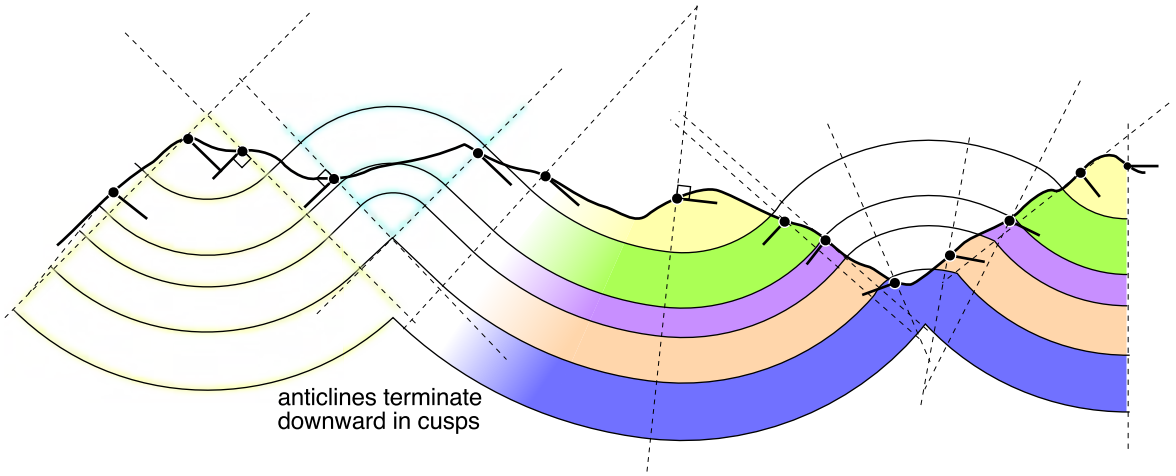


**Figure 10.4 — Illustration of the Busk method of cross section construction. Centers of curvature are determined from the intersection lines drawn perpendicular to adjacent dips. Two sets of concentric arcs are highlighted in yellow and light blue. In concentric folding, synclines become very broad down section whereas anticlines terminate in cusps.**

the same center of curvature but different radii of curvature. Concentric folding is the basis for the ***Busk method*** of cross section construction (Fig. 10.4).

***Similar folds*** have Class 2 dip isogons and kinematically can result from parallel shear planes oriented obliquely to bedding. Because of the oblique shear, these folds preserve neither bedding thickness nor bed length. They do, however, maintain area. In areas with curved fault planes, similar folding provides and easy and straightforward way of modeling how beds move over a bend or ramp in the fault plane. One should not mistake "easy" for "correct", however!

***Trishear folds*** constitute a third kinematic model of cylindrical folding. All shear planes emanate from a blind fault tip and spread out upward into a triangular zone of simple shear. We discuss these folds in some detail, below.

## *Fold Type and the Propagation/Slip Ratio*

The relationship between faulting and folding, and the type of fold that results, depends strongly on the ratio between the rate of propagation of the fault tip line and the slip rate of the fault, or ***propagation-to-slip ratio***, *P/S* (Williams and Chapman, 1983; Hardy and Allmendinger, 2011) For example, in the idealized ***fault-bend fold*** (Fig. 10.5a), the entire fault plane exists prior to any displacement on the fault, a $P/S = \infty$ (infinity) because the propagation is a finite number while the slip is zero. In ***fault-propagation folds*** (Fig. 10.5b), the rate of propagation is only somewhat greater than, or can even be slightly less than, the rate of slip. The loss of slip which is necessary near the tip line is diffused out into the folded rocks in a way that depends on the specific model assumed. ***Detachment*** or ***lift-off folds*** experience slip with essentially no propagation of the flat fault with which they are associated, which is known as a ***decollement*** (the French word for unsticking or ungluing). Think of pushing a carpet across a room: when the edge of the carpet runs into a wall the decollement between the carpet and the floor ceases to propagate and a bulge or ruck forms at the stationary tip. Tip-line folds, commonly referred to as ***"forced" folds***, associated with normal faults have negative propagation to slip ratios because the tip-line propagates towards the surface (as in thrust faults) whereas the slip of the hanging wall is downward relative to

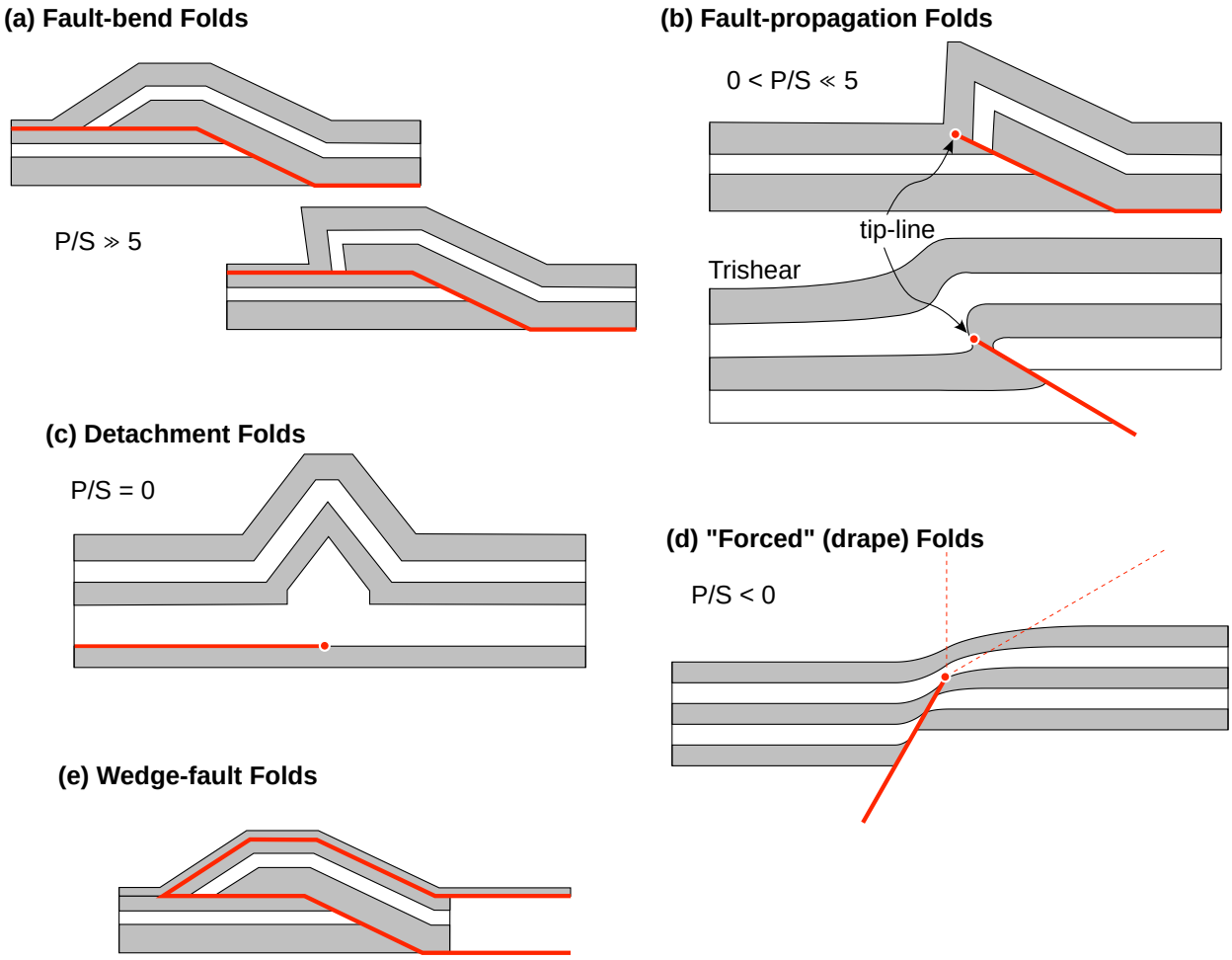


**Figure 10.5 — Spectrum of fault fold relationships, emphasizing the importance of the propagation to slip ratio, P/S. See text for discussion.**

the footwall. Finally, listric normal faults produce roll-over anticlines produced by similar folding during shear oblique to the upper plate

The kinematic models for many of these fold types fall into two general categories: ***instantaneous limb rotation*** and ***progressive limb rotation***. Faults with sharp bends produce kink folds where the limb changes from flat to its final dip without going through any intermediate stages. In contrast, the limbs of folds associated with curved faults tend to rotate progressively to its final dip. The differences between these two models are particularly striking when one sees the geometry of the **growth strata**, sediment that accumulate in the vicinity of the fold during its growth. We discuss each of these type of folds in the following sections.

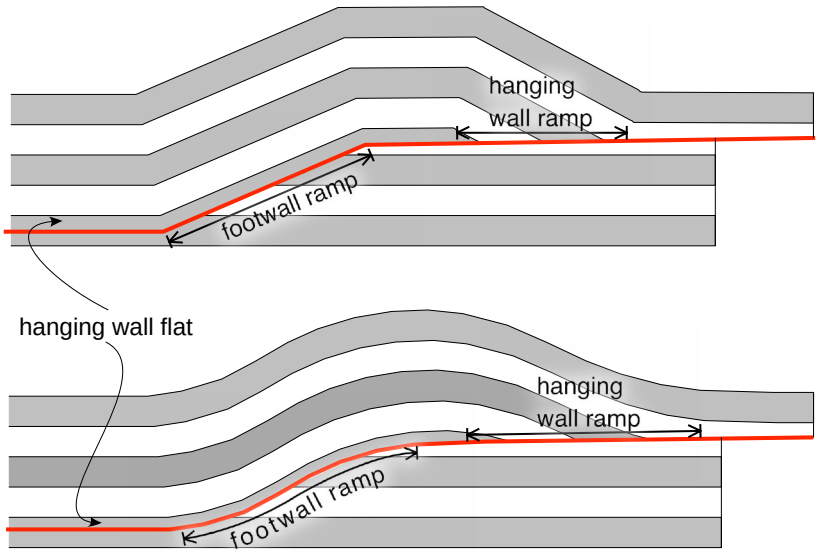


**Figure 10.6 — the ramp and flat geometry of fault-bend folds, illustrated with kink geometry (top) and curved fault geometry (bottom).**

## *Fault-bend Folds*

Fault-bend folds, or ramp or hanging-wall anticlines, are so named because the upper plate moves over pre-existing bend in the fault surface (Fig. 10.5a, 10.6). They were first described by J. L. Rich (1934) in his mapping of the Pine Mountain block in the southern Appalachians. Bends in faults occur because thrust faults in stratified rocks with differing mechanical properties tend to have a stair step trajectory producing a ***ramp and flat*** geometry. Ramps occur where the fault cuts across bedding whereas flats are where the fault is parallel to bedding. For every step in a fault, once motion has occurred there are two ramps: where the fault cuts across bedding in the hanging wall and where it cuts across bedding in the footwall (Fig. 10.6). The key to restoring these folds is matching up the ***hanging wall ramp*** with the ***footwall ramp***.

Many structural geologists prefer the kink fault-bend fold (Fig. 10.6, top) because its geometry can be reproduced very precisely using the equations of Suppe (1983). Suppe showed that:

$$\phi = \tan^{-1}\left\{\frac{-\sin(\gamma-\theta)\left[\sin(2\gamma-\theta)-\sin(\theta)\right]}{\cos(\gamma-\theta)\left[\sin(2\gamma-\theta)-\sin(\theta)\right]-\sin(\gamma)}\right\} \tag{10.7a}$$

$$\beta = \theta - \phi + (180 - 2\gamma) = \theta - \phi + \delta \tag{10.7b}$$

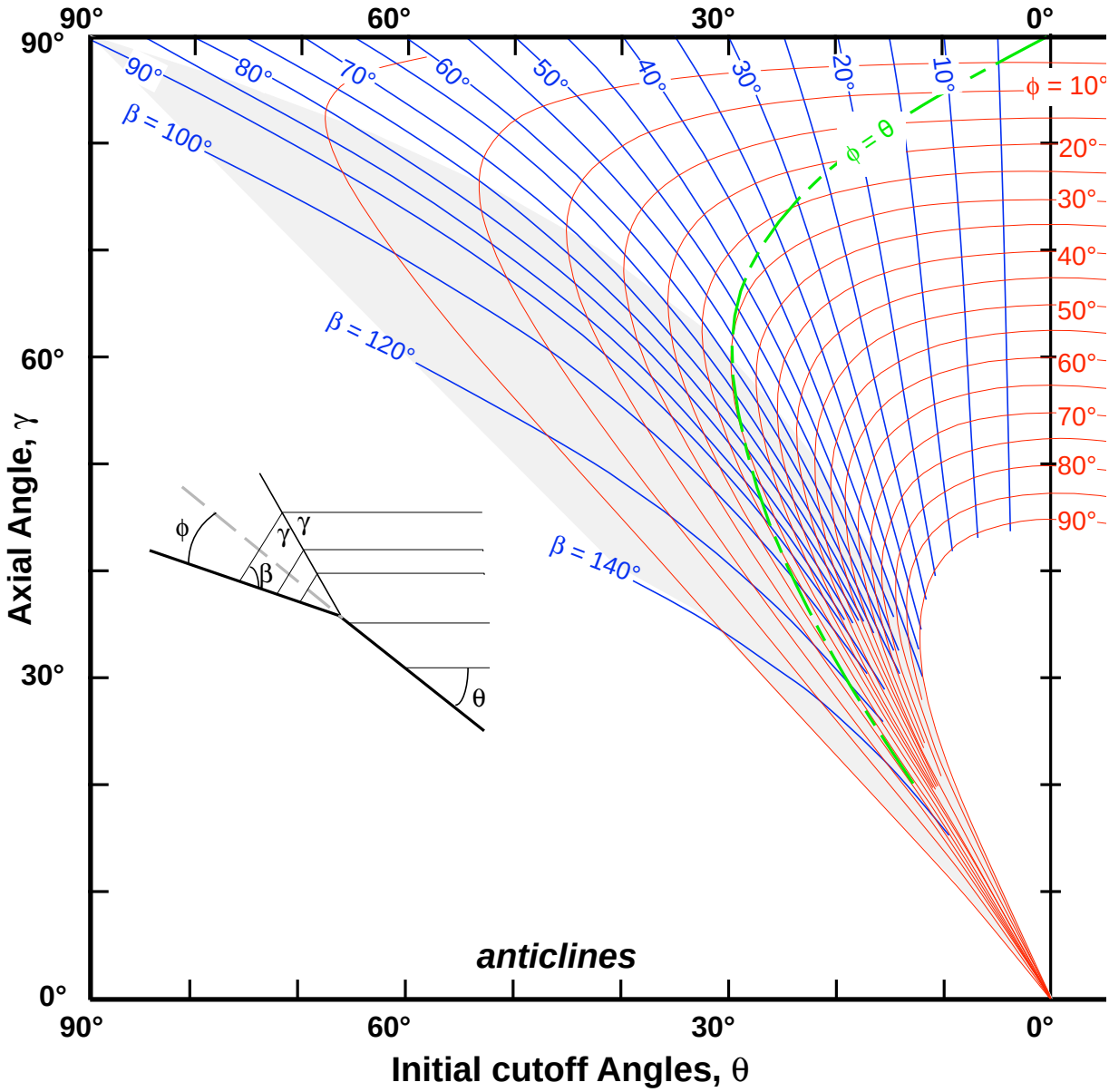


**Figure 10.7 — Graph of the solutions to Equation 10.6 for kink fault-bend folds modified from Suppe (1983). Knowing any two angles, the other two can be solved and a precise cross section constructed. The green curve shows the special case of $\theta = \phi$. For any ramp angle, $\theta$, there are generally two possible solutions, mode 1 with large axial angles, γ, and small hanging wall cutoffs, $\beta$, and mode 2 (gray shaded region) where the reverse is true.**

Where the angles are those shown in the inset diagram of Figure 10.7. Note that, as used here, $\gamma$ is the kink angle and not the shear strain! There are four unknown angles and two equations; Thus one need only determine any two of the four angle and the other two can be calculated. In practice, Equation (10.7) is usually solved

using Newton's method of successive approximations but a graph of solutions enables anyone to construct kink fault-bend folds (Fig. 10.7). Equation (10.7a) simplifies considerably when $\theta = \phi$, which represents a simple ramp up from a decollement. For that special case, the green line in Figure 10.7 shows a maximum at $\theta = 30°$. In other words, the steepest ramp up from a decollement that one can have and still preserve bedding thickness throughout the structure is 30°. One of the important consequences of the basic fault-bend fold theory is that, for parallel kink folding with no global shear in thrust plates (i.e., there is no layer parallel shear in horizontal beds), the hanging wall cutoff is larger than the footwall cutoff ($\beta > \theta$) and the ***fault slip must decrease across the hanging wall ramp***.

It is entirely possible to construct fault-bend folds using other approaches. For example, Figure 10.6 (bottom) was constructed using layer oblique shear and similar folding. We shall see the equations and approach for doing that when we talk about listric normal faults, below. Increasingly, structural geologists are applying full mechanical modeling to the problem, though that is beyond the scope of this book. In unmetamorphosed parts of thrust belts, however, the prevalence of slickenside bedding surfaces indicates that, to a first order, a flexural slip fold model is an adequate approximation.

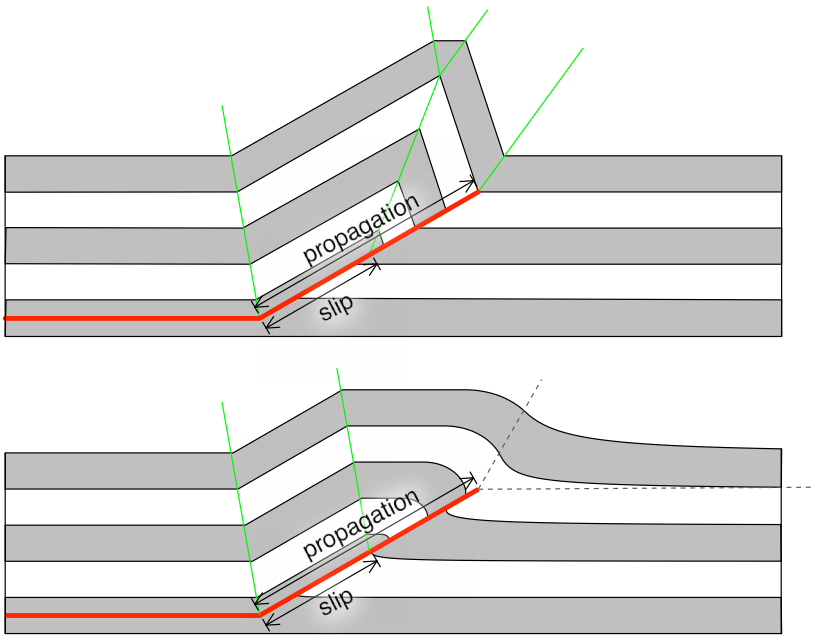


**Figure 10.8 — Two flavors of fault-propagation folding, both with a propagation to slip ratio of 2. Top, parallel kink fold model (Suppe and Medwedeff, 1990). Bottom, a trishear fault propagation fold. The dashed line is the triangular shear zone.**

## *Fault-propagation Folds*

Fault-propagation folds (Fig. 10.8) are produced by the propagation of the tip line at a rate that is somewhat faster than the slip rate of the fault. In drawing cross sections, the key question is: how is the loss of slip on the fault accommodated by folding? Two popular kinematic models exist in the literature: The first employs parallel kink folding where the loss of slip is compensated by enhanced growth of the crest of the fold (Fig. 10.8 top) and the second, trishear, results in deformation being resolved in a triangular zone of shear planes that radiate from the tip line of the fault (Fig. 10.8 bottom). The former model produces no deformation in the footwall of the fault whereas the latter yields a deformed footwall and bedding thickness changes for that part of the beds in the triangular zone.

### *Kink Fault-propagation Folds*

The kink fault-propagation fold model of Suppe and Medwedeff (1990) can be quantified much the same way as kink fault-bend folds can. The pertinent, messy looking equation (ignoring shear in horizontal layers) is (Fig. 10.9):

$$\sin\theta_2 = \left\{ \frac{\sin\left(\gamma^*\right)\sin\left(\gamma^* - \beta_1\right)}{\sin\left(\gamma_1 - \gamma^*\right) + \left[\frac{\sin\left(\gamma_1\right)\sin\left(\gamma^* - \beta_1\right)}{\sin\left(2\gamma^* - \beta_1\right)}\right]} \right\} \tag{10.8}$$

where $\gamma = 90^\circ + \gamma^* - \gamma_1$; $\beta_2 = 180^\circ - 2\gamma^* + \beta_1$; and $\delta_b = 2\left(\gamma - \gamma^*\right)$.

The parallel kink (constant thickness) fault-propagation fold theory yields several important results:

- The maximum ramp up from a decollement is 60° (unlike fault-bend folds where the maximum step up angle is 30°).
- The fold changes geometry at the stratigraphic level of the tip line: the fold in beds above that level has a flat crest but below that level the fold is a sharp kink.
- For ramps off of a decollement, the geometry fixes P/S = 2.

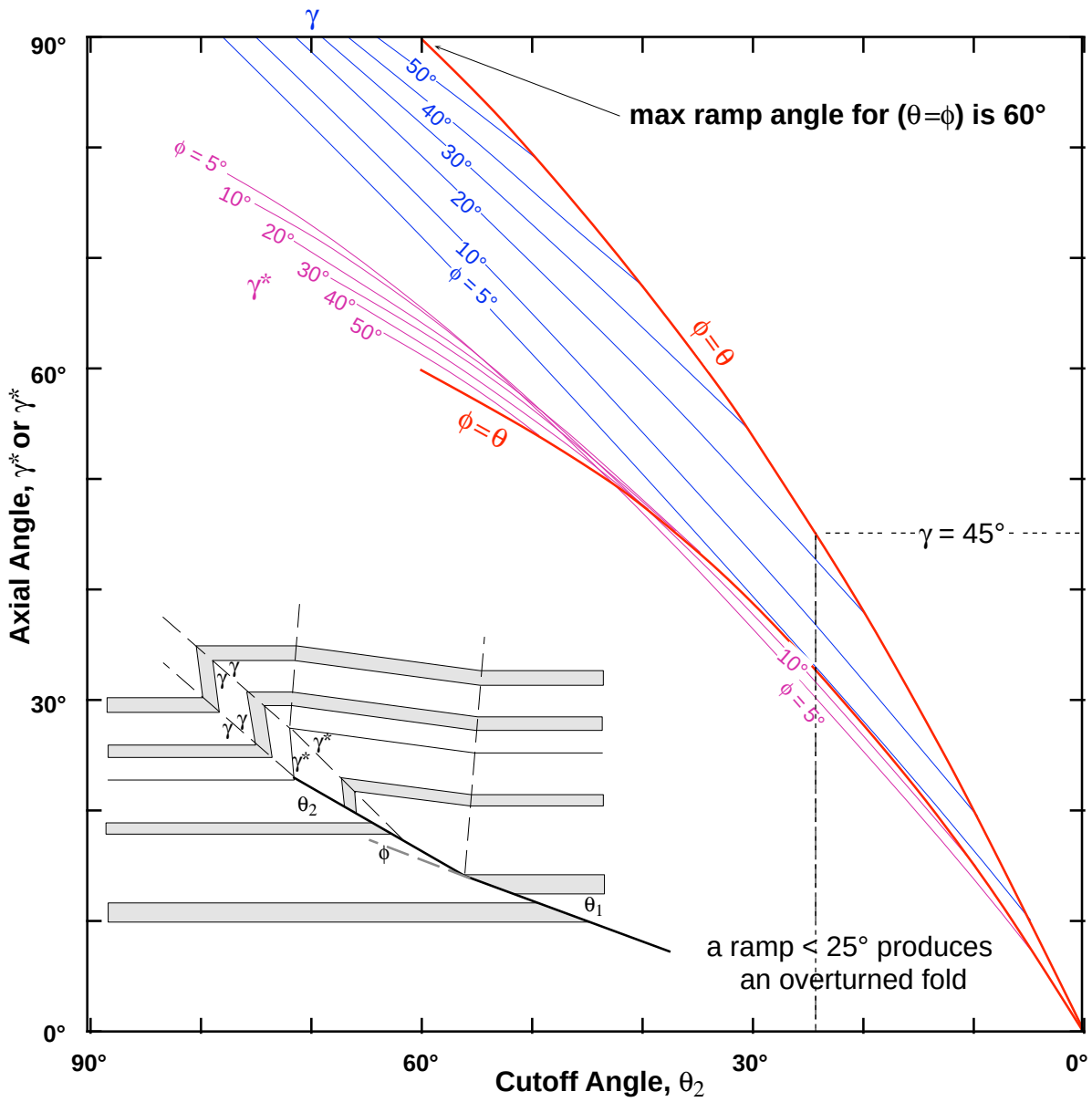


**Figure 10.9 — Graphs of fault-propagation fold geometry from equation 10.7, modified from Suppe and Medwedeff (1990).**

- The fore- and back-limb dips are quite diagnostic in fault propagation folds (Fig. 10.10). This is very useful because the dips are easy to determine from field data.

*Trishear*

Trishear fault propagation folds (Erslev, 1991) have more independent parameters (Fig. 10.11) and are thus not so amenable to geometric analysis. Several fine

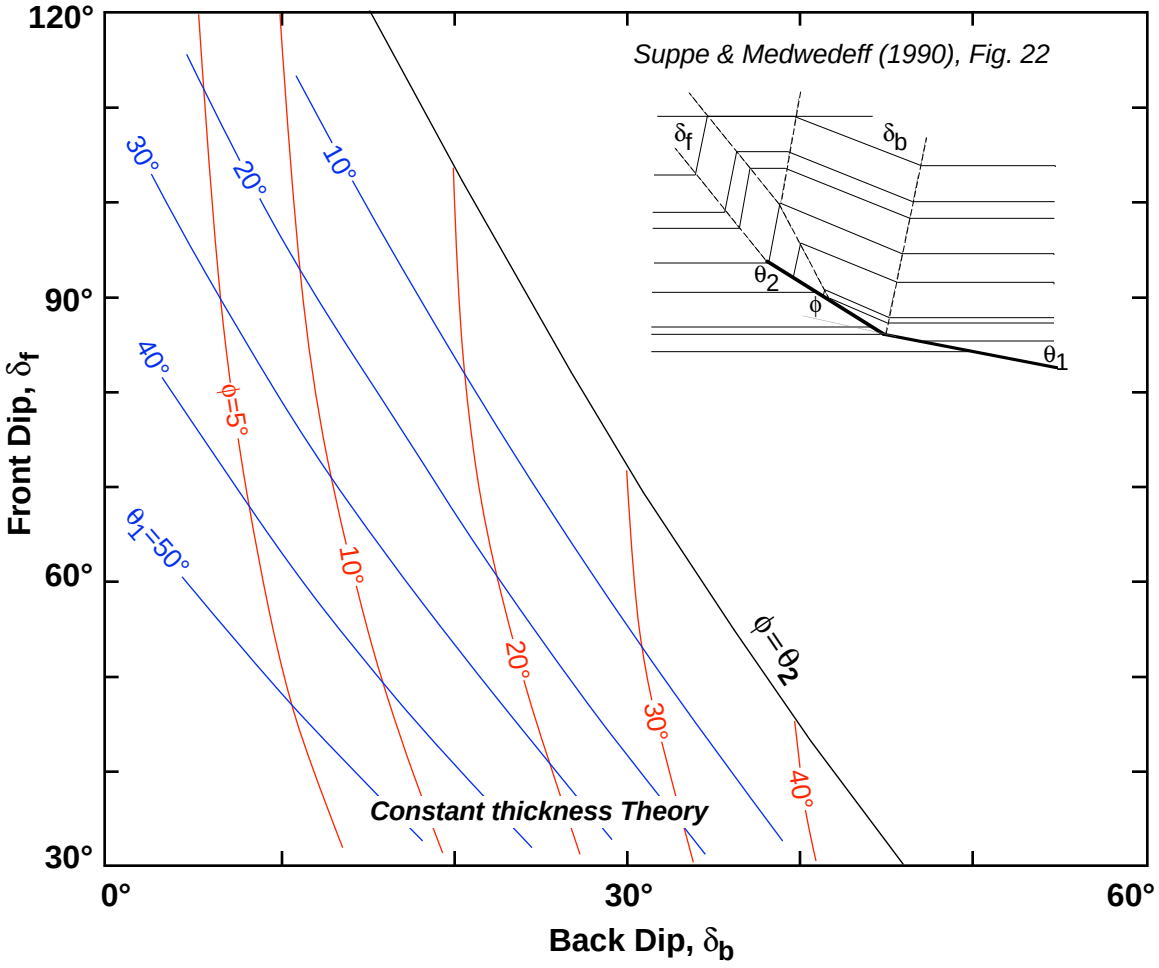


**Figure 10.10 — Fault-propagation fold geometry as a function of the forelimb and back limb dips (modified from Suppe and Medwedeff, 1990).**

computer programs are available to calculate forward models of these structures and because the models can be run backwards or forwards, there is even a grid search modeling strategy for application to real structures. The derivation of the most basic form of trishear following Zehnder and Allmendinger (2000) is instructive for its modern modeling approach.

We assume that the footwall is fixed and the hanging wall moves at a constant velocity, $v_o$. The only particles that experience deformation are located inside the triangular shear zone (delimited by the dashed lines in Fig. 10.11) and we need to determine a velocity field of a point inside the triangular zone. The velocity field will be written in vector form as

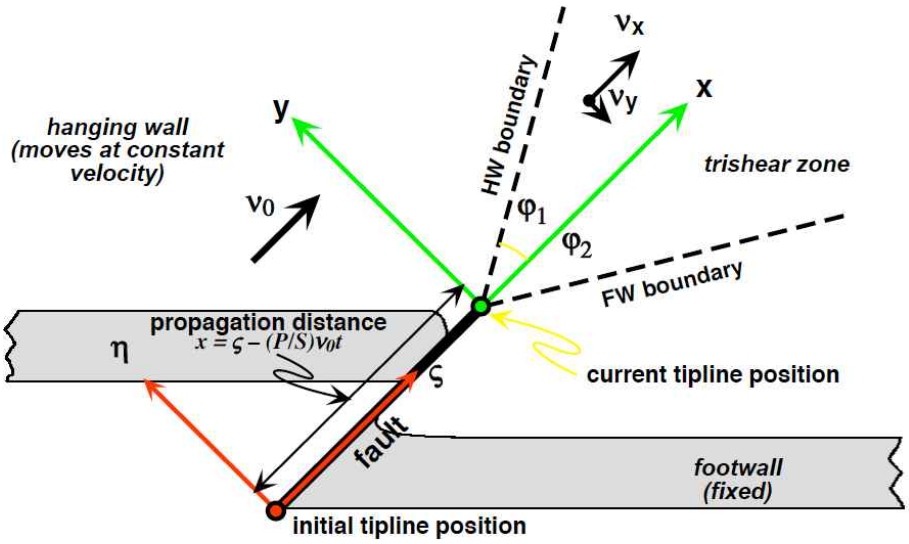


**Figure 10.11 — The key parameters of the trishear kinematic model, showing the velocities, angles, and coordinate systems. All of the relations below are given in the XY coordinate system, which moves with the tip line of the fault. After Zehnder and Allmendinger (2000).**

$$\vec{v}\,(x,y) = v_x\,(x,y)\,\hat{i} + v_y\,(x,y)\,\hat{j}$$

where the x and y axes are parallel and perpendicular to the fault line, and $\hat{i}, \hat{j}$ are the usual unit vectors in the x and y directions. The origin of the coordinates is attached to the fault tip (Fig. 10.11).

In the hanging wall sector, $\vec{v} = v_o\hat{i}$. In the footwall sector, $\vec{v} = 0$. We now seek to construct a velocity field in the trishear zone that conserves area, is continuous and matches the hanging wall and footwall sector velocities on the top and bottom boundaries of the zone. The boundary conditions are

$$\begin{aligned} v_x = v_0,\, v_y = 0 \quad &\text{on} \quad y = x\tan\phi_1 \\ v_x = 0,\, v_y = 0 \quad &\text{on} \quad y = -x\tan\phi_1 \end{aligned} \tag{10.9}$$

The condition that area is conserved, or that the flow is ***incompressible***, is that the ***divergence of the velocity field*** is zero,

$$\text{div}\,\vec{v} = \nabla v \equiv \frac{\partial v_x}{\partial x} + \frac{\partial v_y}{\partial y} \tag{10.10}$$

The approach will be to choose a $v_x$ field consistent with Eq (10.9), then determine the $v_y$ field from the above equations. Other than satisfying the boundary conditions and continuity, any reasonable field and any combination of trishear

angles can be chosen. Note that equation (10.10) can be stated in three dimensions for analyzing 3-D deformation.

The simplest of an infinite number of conditions we could assume, is that the velocity field is symmetric, so $\varphi_1 = \varphi_2 = \varphi$, and that $v_x$ varies linearly in $y$. To simplify writing the equations, let $m = \tan\varphi$. One choice for $v_x$ is

$$v_x = \frac{v_0}{2}\left(\operatorname{sgn}(y)\left(\frac{|y|}{xm}\right)+1\right), \quad x>0, \quad -xm \le y \le xm, \tag{10.11}$$

where sgn(y) denotes the sign of y. For s = 1, the velocity distribution is linear in $x$, producing a strain rate that is nearly uniform with respect to $y$. It can easily be seen that the above field satisfies the $v_x$ boundary conditions in Eqs. (10.9). To find $v_y$, we differentiate Eq. (10.11) with respect to $x$, invoke incompressibility (Eqn. 10.10),

$$\frac{\partial v_y}{\partial y} = -\frac{\partial v_x}{\partial x},$$

and integrate with respect to $y$ yielding

$$v_y = \frac{v_0 m}{2(1+s)}\left(\frac{|y|}{mx}\right)^2 + C$$

The constant of integration, C, is found by using the boundary conditions given in Eqs. (10.9). The resulting velocity field in the trishear zone is

$$\vec{v}(x,y) = \frac{v_0}{2}\left\{\left[\left(\frac{y}{mx}\right)+1\right]\hat{i} + \frac{m}{(1+s)}\left[\left(\frac{|y|}{mx}\right)^2 - 1\right]\hat{j}\right\} \tag{10.12}$$

Although Equation (10.12) represents just one of an infinite number of possible velocity fields that fits the boundary conditions, it does a surprisingly good job of producing realistic appearing geometries and strain distributions.

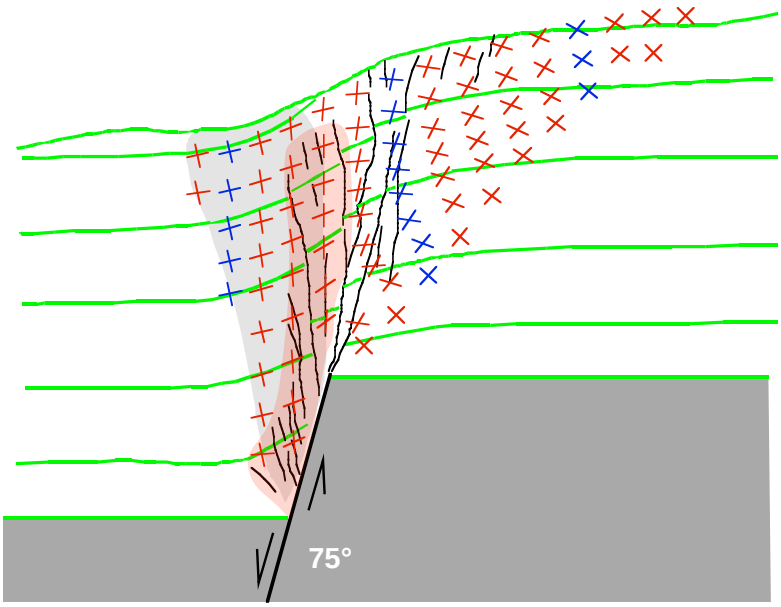


**Figure 10.12 — Green layer and black lines: tracing of a photograph of a clay slab deformed over a faulted rigid substrate. Blue and red "×'s" lines of no finite elongation as proxies for shear planes in trishear model of structure. Light gray and red shaded areas: region of reverse faulting in trishear model and analog clay experiment, respectively. From Allmendinger (1998).**

## *Extensional Drape Folds*

We commonly think of folding in connection with horizontal shortening though folds can also form in regions of horizontal extension. In the trishear model, where $P/S < 0$ normal faulting results. In these cases, the tip line propagates towards the surface while the hanging wall moves downward with respect to the footwall. The fold that forms in front of the advancing tip line has been called drape fold or a "forced" fold because, qualitatively, sediments are being draped over faulted rocks beneath (Fig. 10.5d). The exact same equation (10.12) can be used to model the extensional folds. It is important to realize that the deformation that accrues in the hanging wall and footwall when a particle was located within the triangular zone remains after tip line migrates past the particle. An interesting result of both numerical trishear forward models and analog experiments of extensional forced folds is, when the underlying fault is steep enough, some of the shear zones within the triangular zone will be oriented as high angle reverse faults (Fig. 10.12)!

## *Roll-over Anticlines and Listric Normal Faults*

In ***listric normal faults***, the hanging wall must deform to remain in contact with the footwall. Although it is possible to model such deformation using parallel folding, the standard approach is to assume shear oblique to the layers, which

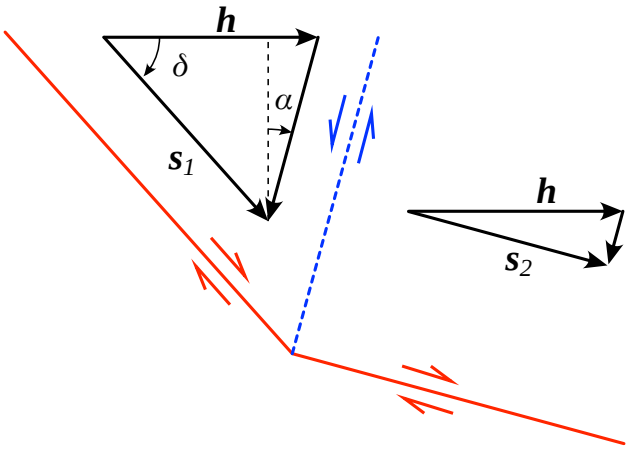


**Figure 10.13 — The constant heave method of shear oblique to layers for deformation above a normal fault with two different dip segments. The fault is shown in red and the upper plate antithetic shear plane in blue dashed line. The black triangles show the vector addition necessary to ensure that the slip vector is parallel to the fault segment.**

is borne out by the common observation of populations of normal faults deforming the hanging wall.

The ***constant heave*** method, which uses simple vector addition, is generally applied (Fig. 10.13). We assume that, points overlying each constant dip segment of the fault are displaced horizontally by the same amount, $h$. So that the actual slip vector, $s$, over that segment is parallel to the fault, the point must be sheared downwards by a vector that is parallel to the upper plate shear planes. Those planes are defined by their deviation from vertical, angle $\alpha$ in Figure 10.13. Thus, the slip vector and the amount of shear parallel to the upper shear planes changes over each fault segment. The upper plate shear can be antithetic, vertical, or synthetic with respect to the shear on the fault plane. Equation (10.13) shows how the slip magnitude varies with respect to the dip of the fault segment ($\delta$), the heave ($h$), and the upper plate shear angle ($\alpha$).

$$s_n = \frac{h}{\cos\left(\delta_n\right)\left(1 + \tan\left(\delta_n\right)\tan\left(\alpha\right)\right)} \tag{10.13}$$

where $n$ refers to the $n$-th fault segment. The equation works equally well for antithetic, synthetic, or vertical shear and in either extensional or shortening environments.

The same approach just describe can be used to reconstruct the trajectory of listric faults in the subsurface if the shape of the roll-over anticline is known (Fig. 10.14a). In this method, the heave, $h$, is set by projecting the hanging wall shear di-

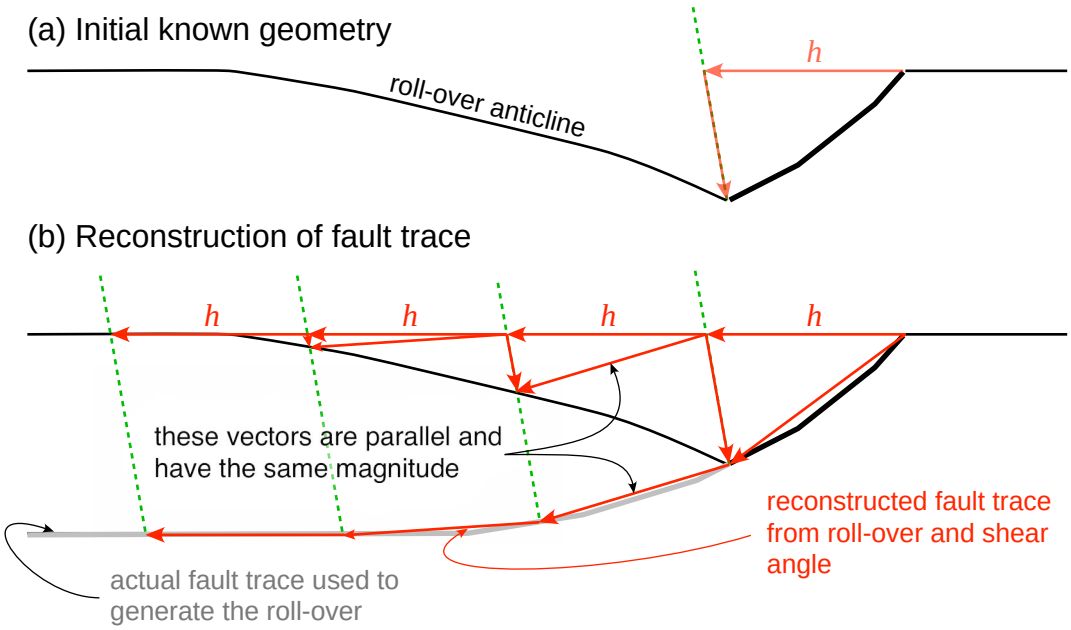


**Figure 10.14 — Graphical reconstruction of the fault trace knowing the shear angle and the shape of the roll-over anticline. (a) the initial, know geometry; (b) the reconstruction of subsequent segments of the fault. Green dashed lines show upper plate shear planes. In (b), the fault originally used to generate the roll-over is show as a light gray line.**

rection from the known intersection of the fault plane and the top of the roll-over (in pre-growth strata) to a level equal to the top of the fault (Fig. 10.14a). One then uses the shape of the roll-over, itself, to constrain the subsequent vector additions as shown in Figure 10.14b. The method depicted in Figure 10.14 can be used for synthetic or antithetic shear planes.

## Balanced Cross-sections

The fault-fold relations described in the last section allow us to construct rigorous cross-sections that "obey" geometric and kinematic rules. An ***admissible section*** is a geologic cross-section which represents the known structures of the region. A ***viable section*** is one that can be restored to an undeformed state without gaps or overlaps that cannot be explained by geologic observation. The "without gaps or overlaps" bit is an acknowledgment of ***strain compatibility***. A cross-section which is both admissible and viable is known as a ***balanced cross-section***.

*The Fundamental Bases for Balanced Cross-sections*

1. **Conservation of mass** — At the most basic level, matter is neither created nor destroyed and little if any is converted into energy. Thus, mass is conserved. In continuum mechanics, this condition is specified with the ***continuity equation***:

$$\frac{\mathrm{d}\rho}{\mathrm{d}t} + \rho \frac{\partial \left(v_i\right)}{\partial x_i} = 0 \tag{10.14}$$

This equation basically says that the change in density (ρ) with respect to time (t) of a volume, plus the flux of mass in and out of the volume (given by the second term of the equation, "v" = velocity), must be equal to zero. This equation can be expanded as:

$$\frac{\mathrm{d}\rho}{\mathrm{d}t} + \rho \nabla \mathbf{v} = 0 \tag{10.15}$$

where $$\nabla \mathbf{v} = \left[\frac{\partial v_1}{\partial x_1} + \frac{\partial v_2}{\partial x_2} + \frac{\partial v_3}{\partial x_3}\right] \tag{10.16}$$

"$\nabla \mathbf{v}$" is the ***divergence of the velocity field***.

2. **Conservation of Volume (no change in density)** — For subaerial thrust belts, compaction during deformation is not generally important so densities do not change during the deformation. Thus, volume is conserved. This means that:

$$\frac{\mathrm{d}\rho}{\mathrm{d}t} = 0$$

Because density itself is finite, this condition, known as ***incompressibility***, means that the divergence of the velocity field in equation must be equal to zero:

$$\nabla \mathbf{v} = \left[\frac{\partial v_1}{\partial x_1} + \frac{\partial v_2}{\partial x_2} + \frac{\partial v_3}{\partial x_3}\right] = 0 \tag{10.17}$$

 

3. **Conservation of Area (Plane Strain)** — Because the wavelength of individual structures in a thrust belt is short compared to their strike parallel dimension, we can assume plane strain. This means that there is no velocity parallel to strike (the $\mathbf{X}_3$ axis):

$$\frac{\partial v_3}{\partial x_3} = 0$$

Thus, cross-sectional area perpendicular to strike must be conserved and we can write the two dimensional form of the incompressibility criterion:

$$\nabla \mathbf{v} = \left[ \frac{\partial v_1}{\partial x_1} + \frac{\partial v_2}{\partial x_2} \right] = 0 \tag{10.18}$$

This is the necessary condition for area balancing.

4. **Conservation of Bedding thickness** — Finally, if bedding thickness is preserved, then we can assume parallel folding with shear parallel to bedding. Thus, line lengths parallel to bedding is preserved. Bedding marks the orientation of one of the two lines of no finite elongation.

In summary:

**Table 10.1**

| Type of Balance | Dimension | Assumptions | Folding Model |
|---|---|---|---|
| **Volume** | 3D | density of rocks constant during deformation, no compaction, pressure solution, or growth strata | non-cylindrical or cylindrical |
| **Area** | 2D | Plane strain with no strain perpendicular to the line of section, area preserved | Cylindrical folding (parallel, similar, trishear, etc.) |
| **Line Length** | 1D | Linear strain, no bedding thickness changes during deformation, shear parallel to layers so beds are lines of no finite elongation | Parallel folding (kink, concentric, etc.) |

To date, only area and line length balancing are really practical although there is a lot of noise about true 3-D balancing. The general sorts of geologic fea-

tures to watch out for which violate the assumptions of line length and area balancing are:

**Volume changes:**

- compaction during deformation (particularly important in accretionary prisms and foreland basin strata)
- Sediment accumulation during faulting
- Pressure solution (especially in carbonates but also in silicic rocks like shales and siltstones)
- intrusions, diapirs, etc.

**Non-plane strain:**

- strike-slip faults
- lateral ramps

## *Line Length Balancing*

Most of the cross sections in the literature, especially those drawn by hand and not with a computer program such as 2DMove, are one dimensional line length balanced sections. There are actually two cross sections that are constructed simultaneously: The present day, deformed section and the restored, or ***retrodeformed***, stratigraphic section. In the case of a thrust belt, the retrodeformed section will be much longer than the present day section and the difference in length will be the ***horizontal shortening*** that occurred due to thrusting. The basic procedure is to work from the external part of the deformed belt to the internal part.

The steps to constructing a line length balanced section are illustrated in Figure 10.15:

1. To begin, one constructs the stratigraphic sequence in the undeformed footwall of the most external thrust fault. This will become our ultimate frame of reference, which is signified in line length sections as the ***regional pin line***.

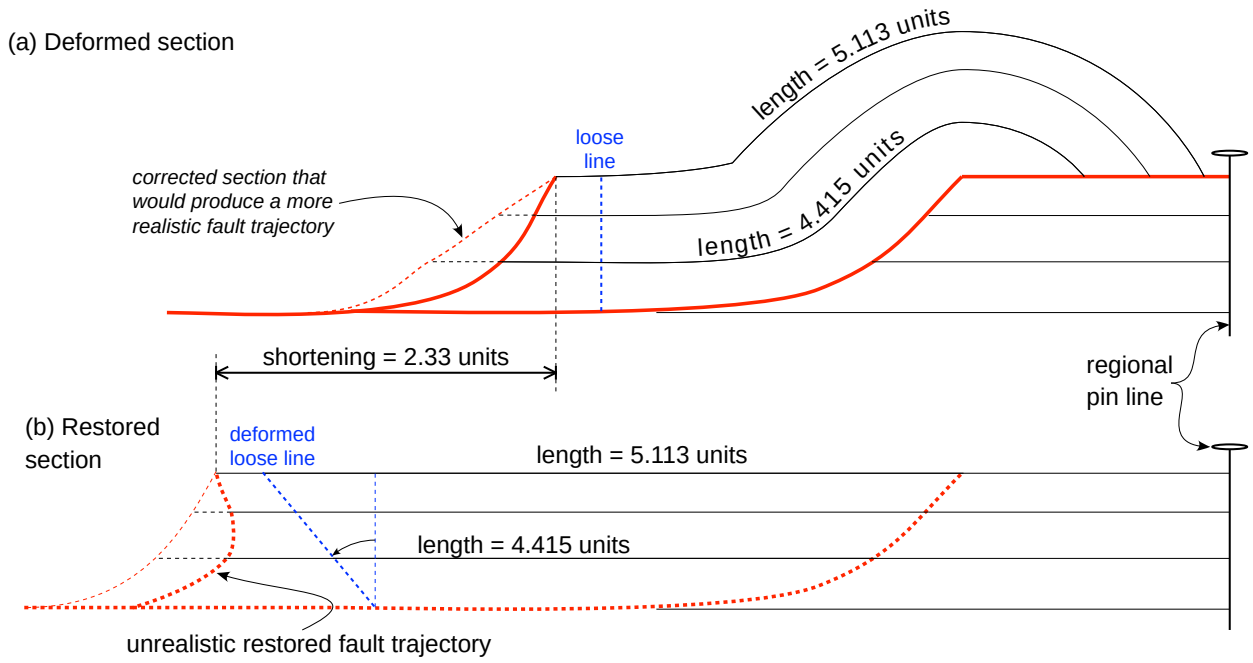


**Figure 10.15 — A simple line length balanced section, illustrating the restoration of the most external thrust plate, some problems with the initial restoration, and a modification (thin dashed lines) to the deformed section to correct the unrealistic restored fault (although more subtle problems remain).**

2. The deformed section of the first thrust plate, back to the next thrust at the trailing margin of the plate, is drawn using parallel folding constrained by the surface geology and any subsurface information available.

3. Next, measure the lengths of the deformed stratigraphic horizons and draw those as straight lines of the same length, measured from the right hand thrust in the restored footwall.

4. The left ends of the restored stratigraphic horizons (Fig. 10.15b) define the restored geometry of the trailing thrust fault (on the left side of the section). This restored geometry appears unrealistic because it bends back on itself. Some explanations for this result are:

   (a) The left-hand thrust fault is younger than the right hand thrust, a so-called out-of-sequence relationship as the "normal" progression of thrust in a thrust belt is from internal to external.

(b) The deformed section is in error, lacking bed length in either the footwall of the right thrust or the footwall of the left thrust. The suggested correction shown in Figure 10.15 adds additional bed length to the footwall of the second thrust.

(c) Although the correction shown improves the initial trajectory of the left thrust, it does not correct another problem which is identified by the "***loose line***" — a line drawn perpendicular to horizontal strata in the deformed state, which is retrodeformed with the stratigraphy in the restored state. The loose line shows that the fold style and hanging wall ramp geometry implies that there must have been very significant angular shear in horizontal beds. This might actually be the case, but can be tested by looking for slickensides on horizontal bedding surfaces in the field.

5. Correcting the bed length in the hanging wall of the right-hand thrust (effectively lowering the ramp angle of the fault) would reduce, but not eliminate the issues raised by the loose line. To remove completely the effect would require a reevaluation of the hanging wall ramp and the style of folding depicted in the section.

6. Note that we correct all of these issues **before** drawing the structure in the upper plate of the left thrust! Otherwise, all of these errors will propagate through the entire section.

The simple example in Figure 10.15 that we just went through is a special case where the hanging wall cutoffs at the hanging wall ramp are preserved. A much more common case is depicted in Figure 10.16a: the hanging wall cutoffs are eroded away. In these cases, we don't know exactly where the hanging wall was relative to the footwall, so we need a local reference frame that is specific to that individual thrust plate. That is the role of ***local pin lines***. The location of the local pin lines is a key issue (Fig. 10.16b, c). Ideally, it should be placed in horizontal strata. If horizontal strata are not available, you can calculate the amount of angular shear in the layers based on their dip from Equations 10.6 or Figure 10.3 and ad-

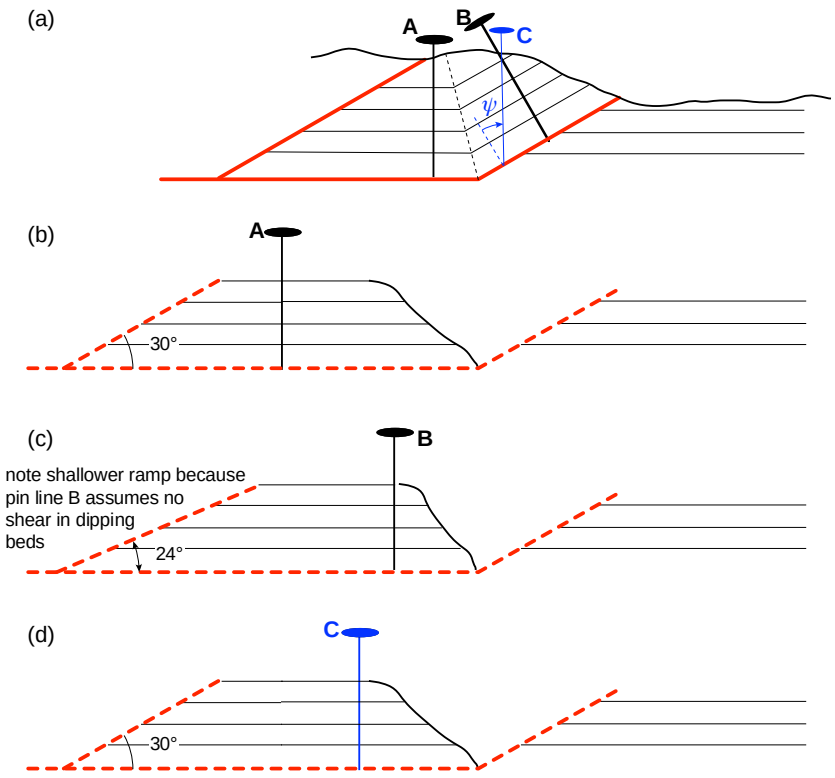


**Figure 10.16 — The use of local pin lines to reconstruct a thrust plate with eroded hanging wall cutoffs. (a) The deformed section. (b) restoration using a local pin line in horizontal rocks in section (a). (c) Restoration using pin line B, which introduces a layer-parallel shear in the undeformed state. In (d), we use a local pin line C that has been drawn to take into account the angular shear in dipping beds (Eqn. 10.6).**

just the local pin line accordingly so that, when restored to vertical, there is no shear in horizontal beds (Fig. 10.16d).

The restored thrust plate is placed as close to the footwall as possible without overlapping it (Fig. 10.16b, c); this is the reason that many structural geologists will claim that their balanced section is a minimum estimate (more on that, below). The initial shape of the thrust plate itself is reconstructed by measuring the lengths of the stratigraphic horizons in both directions from the local pin line.

## *Area Balancing*

Line length balancing is restricted to parallel folds and there are many cases where shear oblique to layering invalidates the preservation of line length assumption. In these cases, as long as the folds are cylindrical, horizontal shortening can still be estimated by carrying out an ***area balance***. In its most general form, area balancing assumes nothing more than that the deformed and initial areas must be equal (Fig. 10.17). The deformed area can be calculated by drawing a polygon

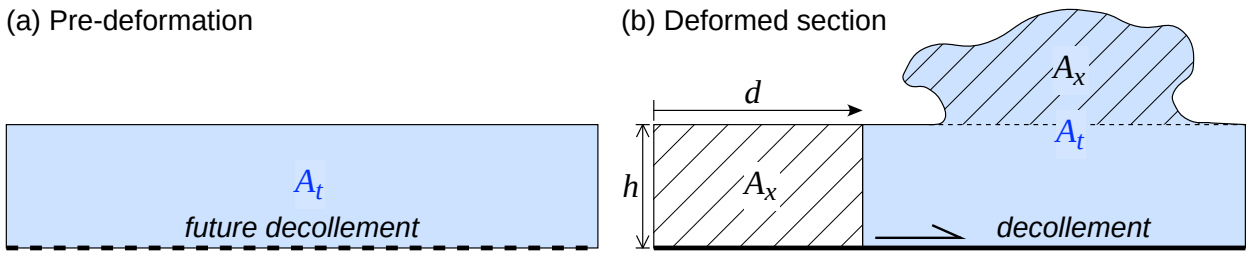


**Figure 10.17 — In a simple area balance, the total area ($A_t$) of the undeformed and deformed packages (shown in blue) must be equal. Eon. 10.18 can be used to calculate those areas. The excess area ($A_x$) above a regional datum of a surface can be used to calculate the displacement, $d$, or the depth to the decollement, $h$.**

around the region of interest. The area, $A$, of a polygon of $n$ vertices can be calculated as (Judge and Allmendinger, 2011):

$$A = \frac{1}{2}\sum_{i=0}^{n-1}\left(x_i y_{i+1} - x_{i+1} y_i\right) \tag{10.18}$$

where the first vertex ($x_0$, $y_0$) and the last vertex ($x_n$, $y_n$) are the same. Determination of the initial undeformed area requires knowledge of the initial unit thicknesses on either side of the deformed zone.

In cross sections where you can identify the local ***excess area*** ($A_x$ in Fig. 10.17b) above a regional datum of the unit, you can extract quite a lot more information. The concept has its origins with Chamberlin (1910, 1919) who used it, incorrectly as it turns out, to differentiate thin- (Appalachians) and thick-shelled (Colorado Rockies) mountain belts. Today, we know these terms as ***thin-*** and ***thick-skinned***. As you can see in Figure 10.17b,

$$A_x = dh \tag{10.19}$$

If you know the excess area, $A_x$, and the displacement, $d$, it is trivial to calculate the depth to the decollement, $h$ or vice versa. Using the approach of Epard and Groshong (1993), you can use the excess area of several beds to estimate both the displacement and the depth to the decollement. The method is illustrated in Figure 10.18:

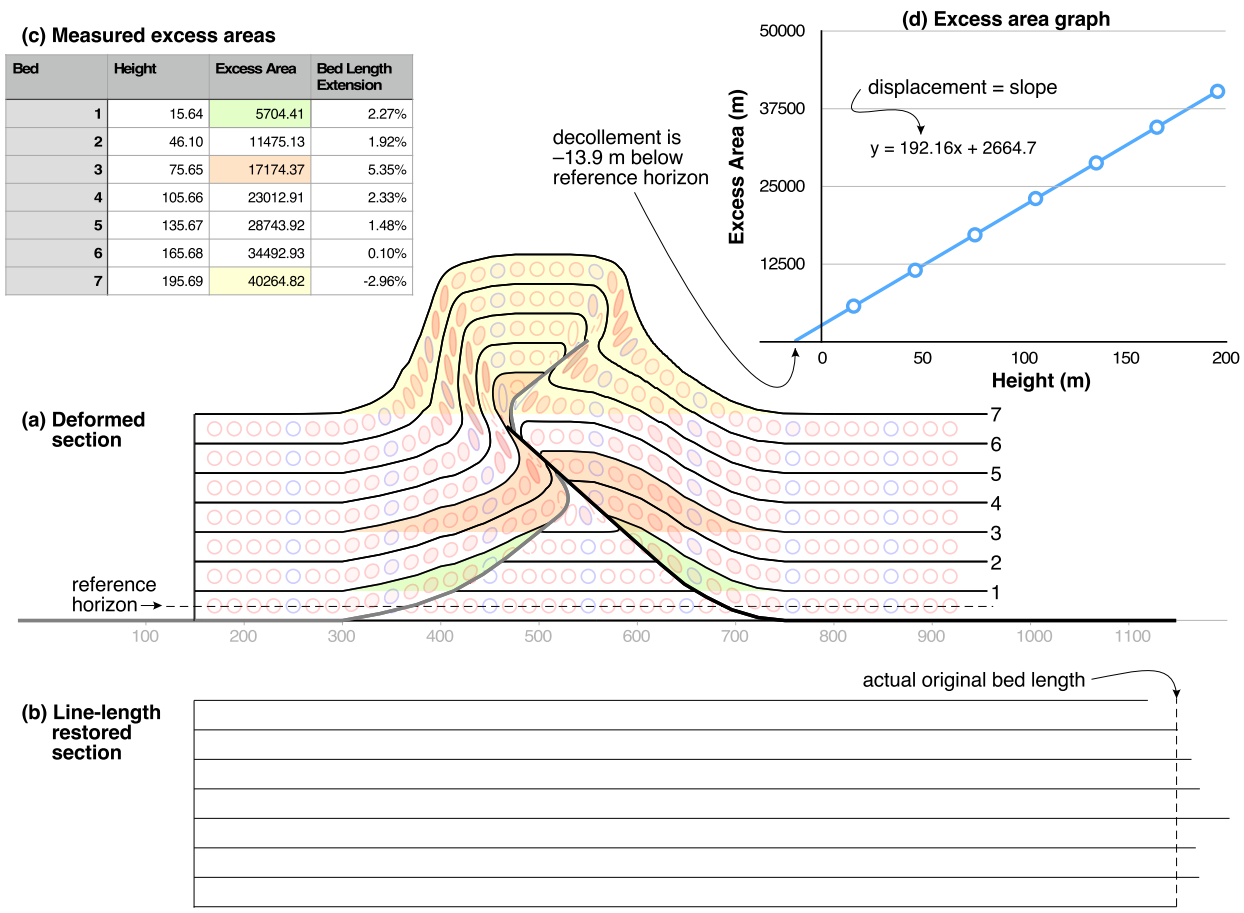


| Bed | Height | Excess Area | Bed Length Extension |
|---|---|---|---|
| 1 | 15.64 | 5704.41 | 2.27% |
| 2 | 46.10 | 11475.13 | 1.92% |
| 3 | 75.65 | 17174.37 | 5.35% |
| 4 | 105.66 | 23012.91 | 2.33% |
| 5 | 135.67 | 28743.92 | 1.48% |
| 6 | 165.68 | 34492.93 | 0.10% |
| 7 | 195.69 | 40264.82 | -2.96% |

**Figure 10.18 — The use of excess area of successive beds to determine displacement, depth to decollement, and average layer-parallel extension following Epard and Groshong's (1993) method. (a) The original model to be analyzed was generated in *Fault-FoldForward* as two propagating trishear structures with opposite vergence. The program calculates and colors the strain ellipses as shown. (b) A line-length restoration of each bed. Comparison of the restored length and actual original length yields the average bed length extensional strain. (c) Table of height, excess area, and bed length strain measurements that were used to generate the graphic in (d) where the horizontal displacement and depth to decollement are determined. The colored excess areas for three beds in (a) are show in cells of the same color in the table in (c).**

1. Determine the excess area of each resolvable bedding surface above its regional level. The excess area of three of the seven beds are highlighted in different colors in Figure 10.18a.
2. Measure the height of each surface above (or below) and arbitrary reference horizon or datum. the height is measured outside of the region of excess area. The reference horizon does not have to be the decollement level.

3. Plot the excess area against the height for each bedding surface (Fig. 10.18d). For simple structures, these data points should lie on a straight line. The slope of the line, $A_x/h$, is equal to the displacement, $d$.
4. The decollement is located where the excess area goes to zero. This can be found on the graph by projecting the best fit line until it incepts the height axis (Fig. 10.18d).
5. The displacement, $d$, can be compared to the restored bed lengths (Fig. 10.18b) to determine the average extension of each bed (Fig. 10.18c). Because this example was generated from a complex forward model, we already know the strain distribution. You can see that the actual strain is much more heterogeneous than implied by the average bedding parallel extension (Fig. 10.18a), but in the real world you are seldom lucky enough to have a whole bunch of strain ellipses at your disposal!

For the purposes of evaluating the horizontal shortening in a region, area balancing holds several advantages over line length balancing: it is independent of fold fault kinematic model and because it can be calculated analytically, one can formally propagate the errors associated with the calculation. It fails, however, when one is interested in predicting the structural geometry of a single structure, for reasons of resource extraction, seismic hazard evaluation, etc. In those cases, one should employ a variety of kinematic and mechanical models to evaluate the range of possibilities.

## *A Final Word About Balancing*

Thrust belts, with their imbricated stack of individual faults, are essentially sub-horizontal zones of simple shear. Thus, the horizontal shortening calculated from balanced cross sections is not a principal axis of shortening but instead is just a horizontal chord in a finite strain ellipse that is elongate and inclined towards the hinterland of the belt.

Although the minimum estimate referred to above is commonly cited in the literature, there are many other sources of error inherent in the construction and calculation of shortening in balanced sections. Some of those errors include:

- Appropriateness of structural model
- Quality of the geologic maps used
- Eroded hanging wall cutoffs
- Position of the decollement
- Location of other subsurface points
- Stratigraphic uncertainty (thickness & shape of the wedge)

It may come as a surprise that the uncertainty in the thickness and shape of the stratigraphic wedge is the single biggest source of error in section balancing (Allmendinger and Judge, 2013). Even the best constrained balanced sections have total uncertainty equivalent to ~20% of the calculated horizontal shortening value and this is for well-behaved thrust belts which deform a simple sedimentary package above basement. Although many people have attempted crustal scale balanced sections (including yours truly…), the uncertainties on those are unquantifiable to the extent that one might question whether whole crustal balancing is a worthwhile exercise!

# Exercises—Chapter 10

Cross sections are not sketches! They are precisely drafted documents. All angles should be measured and plotted with a protractor. There should be no vertical exaggeration, i.e., V:H = 1:1. Sloppy or incompletely labeled cross sections will have points taken off. Many of these exercises can be done in a vector graphics program as long as angles and line lengths can be measured accurately.

1. You'll be given a large sheet with a geologic map and space to draw a cross section. You have seen this geology before: The NE corner of the map is where calculated dips from three point problems and determined stratigraphic thicknesses of several units. The NW corner contains the Big Elk anticline for which you programmed a down plunge projection.

   Construct a cross section along line AA′ on the map in the space provided below the map. A topographic profile has been provided for you. The rocks are unmetamorphosed strata so you may assume a parallel fold model. Be sure to follow the basic guidelines in the "Drawing Cross Sections" part of this chapter. ***Be sure to work in pencil as you will undoubtedly be erasing a lot***.

2. Derive Equation (10.6) for kink folds using an area balance. The geometries and key angles are given for you in the following figure. The area, A, to the left of the kink axis in the undeformed (left) and deformed (right) sections must be the same. $\delta$ is the dip, $\psi$ is the angular shear, $\gamma$ the kink axial angle, and $h$ is the bed thickness.

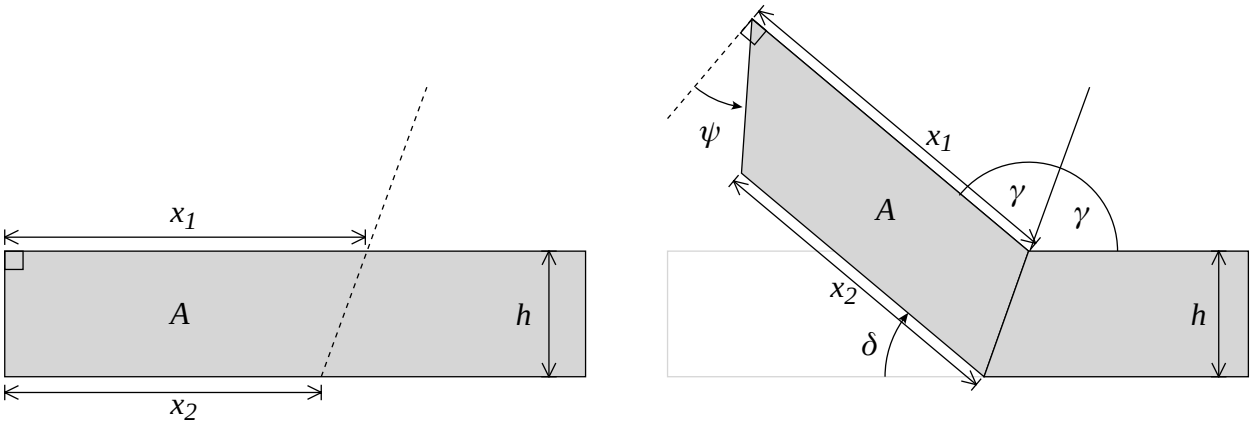

3. Given the fault bend fold templates on the following page, construct (a) a mode 1, and (b) a mode 2 fault bend fold, using the relations in Figure 10.5. In each case, determine how much slip changes from the left side of the structure to the right side.

4. Construct a fault-propagation fold from the given the stratigraphic template on page 234 and the angles from Figure 10.7.

5. The diagram on page 235 shows two identical rollover anticlines associated with a listric normal fault. From the shape of the rollover, construct the listric fault trajectory. As indicated, use antithetic simple shear in the first case and vertical simple shear in the second case

6. Derive Equation 10.13 in this chapter. Make sure to label and explain your calculations adequately.

## Exercise 3: Fault-bend fold exercise

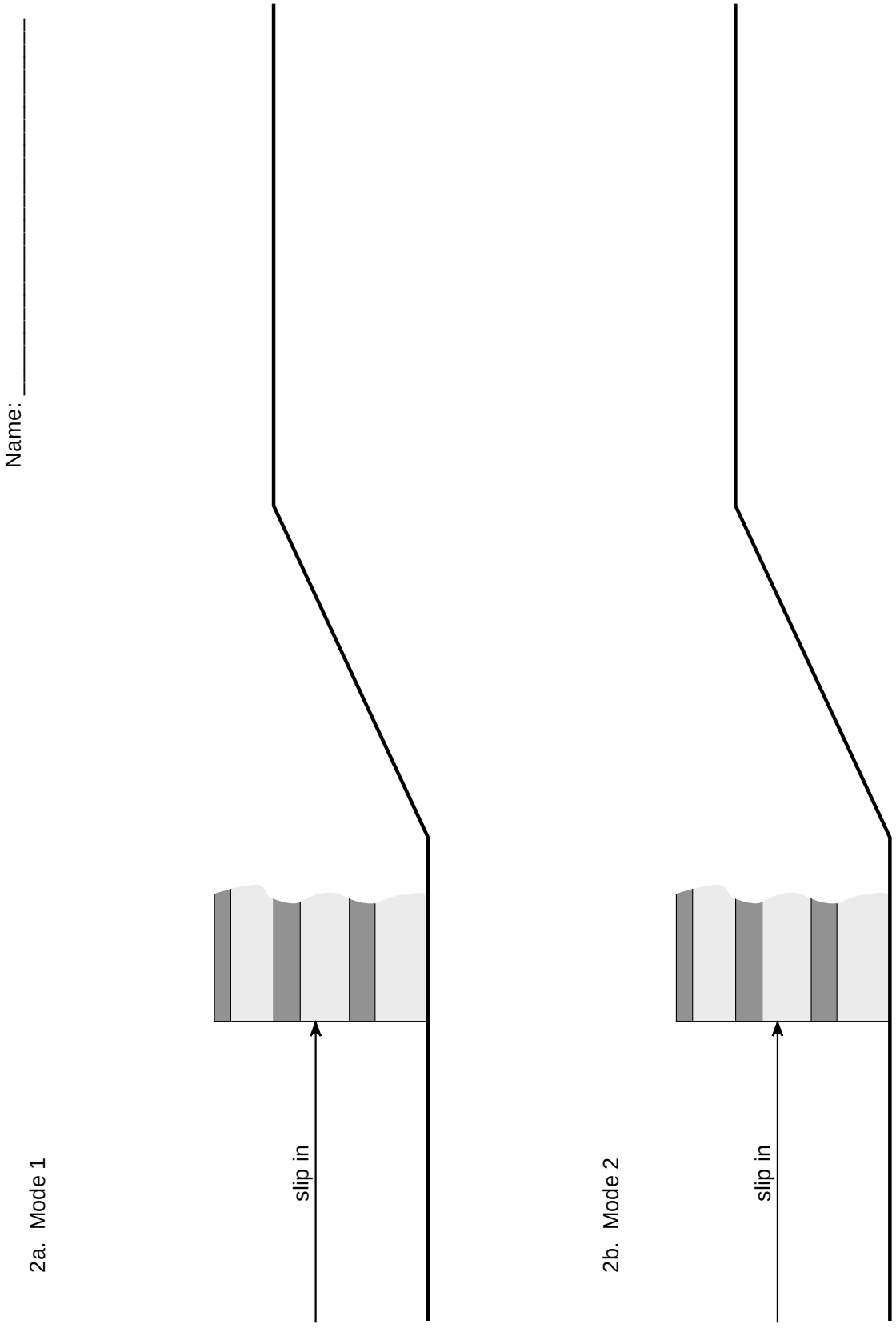


 

## Exercise 4: Fault-propagation fold exercise

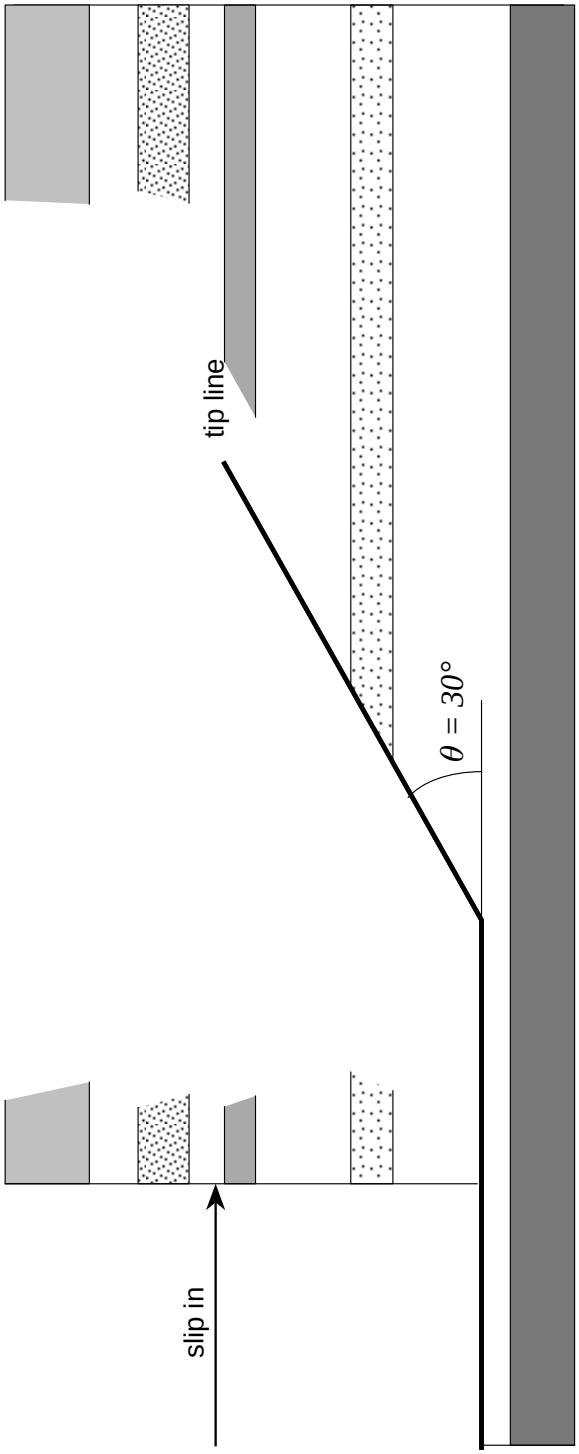

Exercise 5: Roll-over anticline exercise

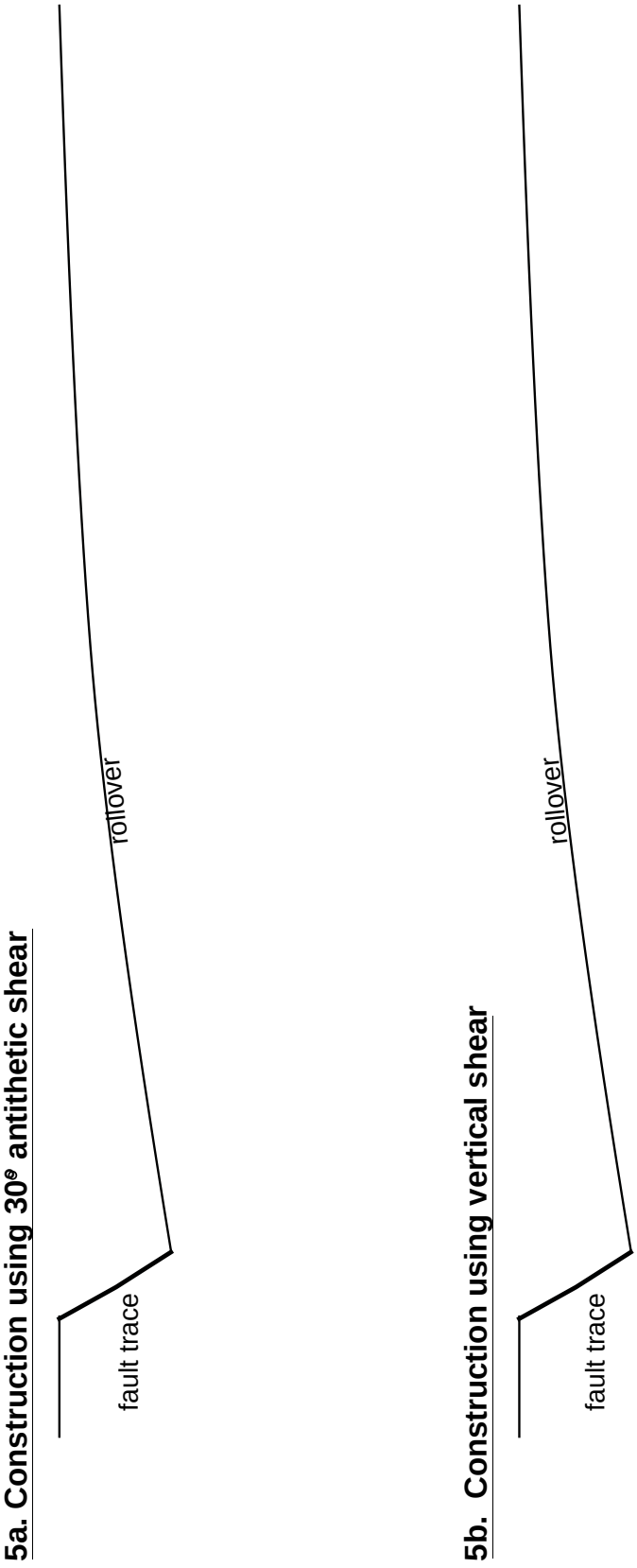


 

 

# Chapter 11

## *Structural Interpretation of Seismic Reflection Data*

### Introduction

Geology presents us with a basic problem. Because rocks are opaque, it is very difficult to see through them and thus it is difficult to know what is the three-dimensional geometry of structures. This issue is particularly obvious when constructing cross sections as in the previous chapters. It is too expensive to drill closely spaced holes in order to constrain the geometry of rocks in the subsurface and,

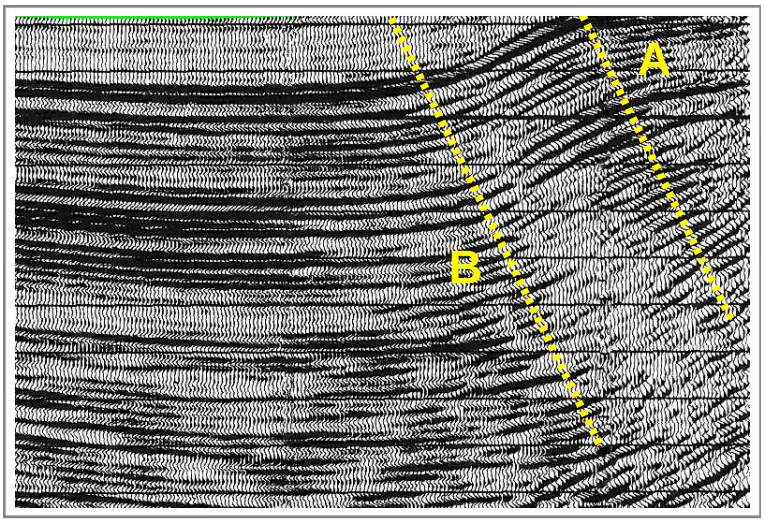


commonly, there are some structures that have no surface expression and thus cannot be projected to depth from surface outcrop.

To the rescue comes a geophysical technique for remotely sensing the subsurface using sound waves. ***Seismic reflection profiling*** has been standard practice in the oil and gas industry for more than 50 years and is the most commonly used technique for mapping the subsurface. Some of the most profound structural observations about our planet — thrust belts have decollements, low-angle normal faults exist — are best demonstrated with seismic reflection data. In this chapter, we will give you the bare-minimum background needed in order to begin using this uniquely useful type of data as structural geologists.

## Echo Sounding

Seismic reflection profiling is exactly analogous to echo sounding (Fig. 11.1). Lets examine the simple case of making an echo first to see what the important parameters are. Why do you get a reflection or an echo? You get an echo because the densities and sound velocities of air and rock are very different. If they had the same density and velocity, there would be no echo. More specifically, the P-wave velocity is:

$$velocity = \mathbf{V} = \sqrt{\frac{E}{\rho}} \tag{11.1}$$

where $E$ = Youngs Modulus and $\rho$ is the density. We tend to think of velocity increasing with density but you can see that in Equation (11.1) density is in the denominator. There are a few rock types that have high velocity but low density; the most common one is salt.

The acoustic impedance of a material is its density times the velocity of sound in the material, $\rho V$. The reflection coefficient is:

$$\text{reflection coefficient} = R = \frac{\text{amplitude of reflected wave}}{\text{amplitude of incident wave}} = \frac{\rho_2 V_2 - \rho_1 V_1}{\rho_2 V_2 + \rho_1 V_1} \tag{11.2}$$

This is what tells us how strong the reflection will be. If you were in Yosemite Valley making echo by shouting at the granite walls of the valley, the reflection coefficient, $R \approx 0.999944$. In other words, almost all of the sound is reflected back at you

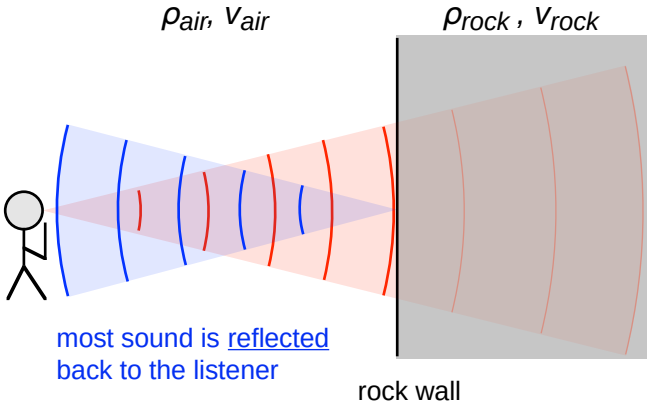


**Figure 11.1 — Anatomy of an echo. It is the density and velocity contrast across the air-rock interface that produces the echo.**

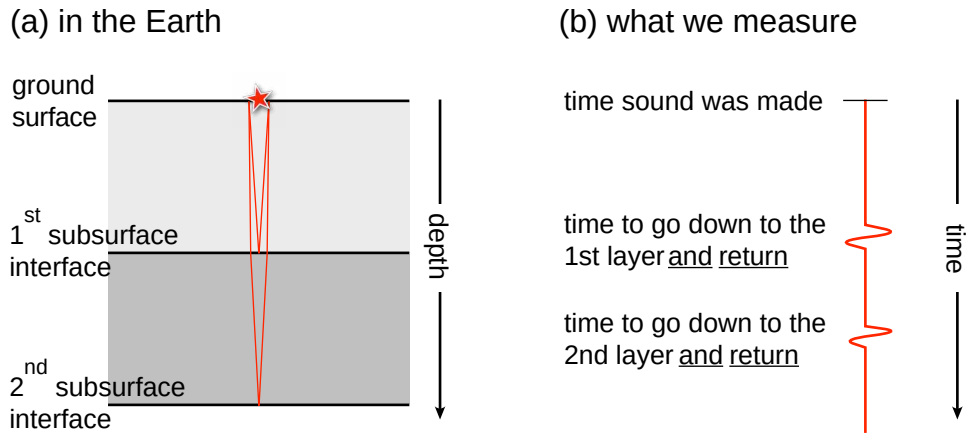


**Figure 11.2 —(a) We make a sound (red star) on the surface of the Earth, the sound then goes down to different interfaces within the earth and some of that sound is bounced back and recorded on the surface. (b) At the surface we can only measure the time that the sound was made and the time that it takes for the sound to go down to each interface and come back to the surface**

from the interface, but a very small proportion actually continues into the rock (Fig. 11.1).

In seismic reflection profiling, what do you actually measure? If you think about the Yosemite example again, we could measure the time that we made the sound and the time that we recorded the echo. The time difference is a function of the velocity of sound in the air and ***twice*** the distance between us and the wall because the sound has to go from us to the wall and come back again. When you make an echo, the ***source*** of the sound (your mouth) and the ***receiver*** of the sound (your ears) are essentially in the same place. As we will see below, in seismic reflection profiling, the source of the sound (an explosion, a vibrating truck, etc.) and receiver (the geophones) are offset from each other but we process them as if they were in the same place.

The above example highlights three important things about seismic reflection profiling (Fig. 11.2):

- Measure time, not depth,
- The time recorded is round trip or two-way time, and
- To get the depth, we must know the velocity of the rocks.

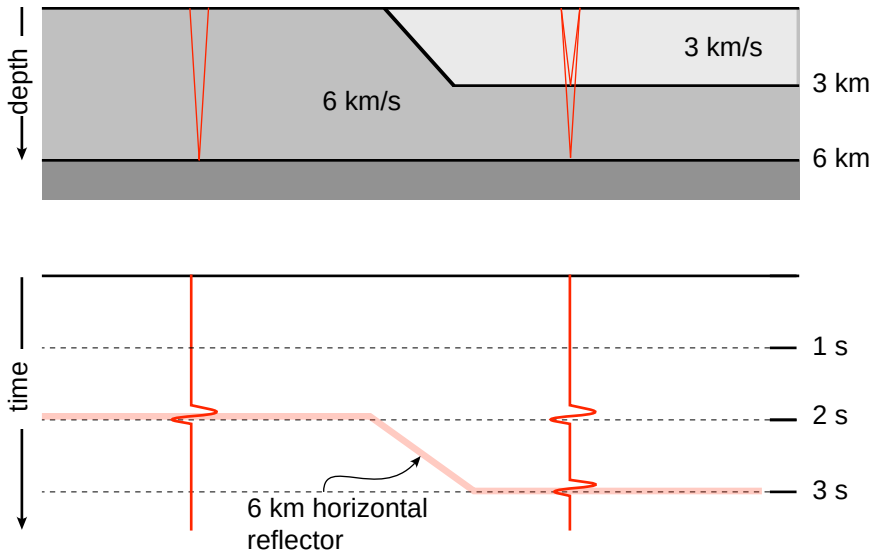


**Figure 11.3 — Top: geologic section showing a slow velocity sedimentary basin on the right hand side and continuous high velocity material on the left side. Bottom: a time section showing the distortion produced by the laterally varying velocity.**

Velocities of rocks in the crust range between about 2.5 km/s and 6.8 km/s. Most sedimentary rocks have velocities of less than 6 km/s. These are velocities of P-waves or compressional waves, not shear waves and most seismic reflection surveys measure P- not S-waves.

Because we measure time and not depth, although seismic reflection profiles resemble geologic cross-sections, they are not. They are a spatially distorted picture of the earth because rock velocities vary, both laterally and vertically. To illustrate impact of laterally varying velocities, consider the case depicted in Figure 11.3. This case is commonly encountered in rift provinces where sedimentary basins alternate with older, higher velocity rocks in mountain ranges. The horizontal interface at 6 km depth looks like it has a step in it on the time section at the bottom because the sound waves travel more slowly to the 6 km interface on the right hand side than they do on the left hand side. This is just one of many types of artifacts for which the structural geologist/seismic interpreter needs to be aware!

# Common Mid-Point (CMP) Method

In the real earth, the reflectivity at most interfaces is very small, $R \approx 0.01$, and the reflected energy is proportional to $R^2$. Thus, at most interfaces ~99.99% of the energy is transmitted and 0.01% is reflected. This means that your recording system has to be able to detect very faint signals coming back from the subsurface. An additional complication is that, because the source usually involves a lot of energy, it must be offset from the receivers.

## *Data Redundancy and Signal to Noise Ratio*

The standard strategy for dealing with very weak signals is to increase the ***signal-to-noise ratio***. If you measure something many times, the signal in which we are interested should add together constructively (because it is the same every time) whereas the random noise should add together destructively (because it is different every time).

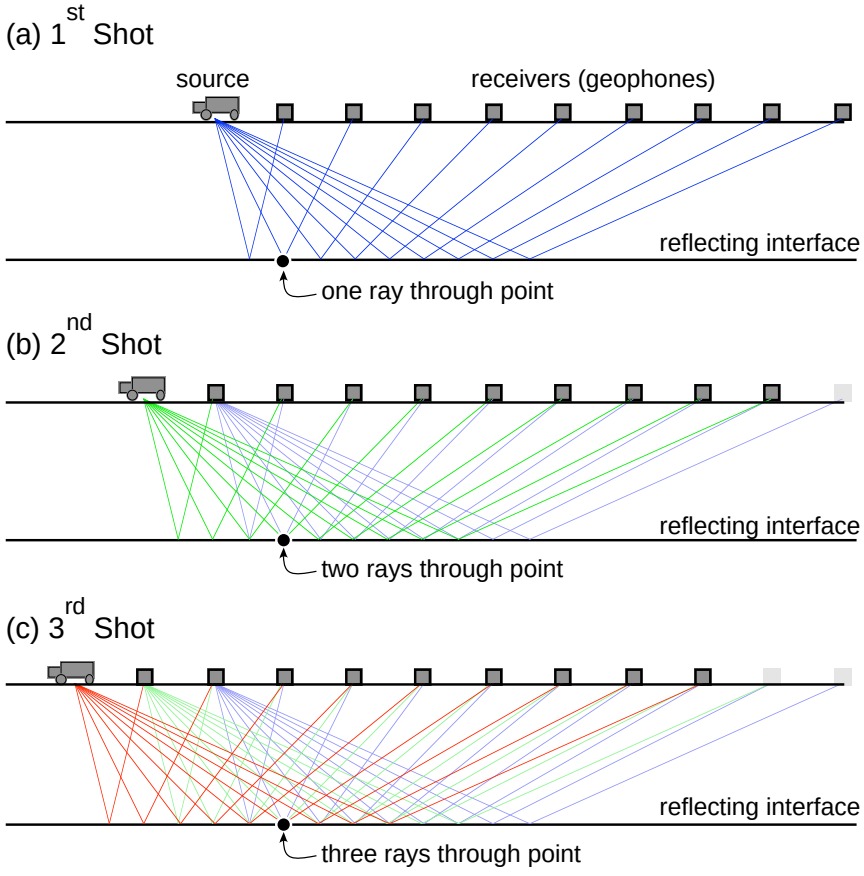


**Figure 11.4 — Cross sectional geometry of a standard common mid-point seismic reflection survey where the sound is emitted (a "shot", reflecting the fact that dynamite used to be the most common source) at three different stations.**

The geometry by which this is achieved is shown in Figure 11.4. Each of the three panels corresponds to one "shot" (i.e., one episode of making noise at a station on the surface). The black dot, and each point on the reflector with a ray going through it, is a ***common midpoint*** (CMP), sometimes referred to as a ***common depth point*** (CDP). Notice that there are twice as many CMPs as there are stations on the ground (where the geophones are). That is, there is a CMP directly underneath each station and a CMP half way between each station (hence the name "common midpoint"). As the source is advanced in the direction of the profile, each midpoint on the reflector of interest gets sampled multiple times.

In a complete survey, the number of traces through each midpoint will be equal to one half the total number of active stations at any one time (not including the ends of the lines where there are fewer traces and assuming that the source moves up only one station at a time). The number of channels in the recording system determines the number of active stations. Most modern seismic reflection surveys use at least 96 (and sometimes as many as 1024 channels or more), so that the number of traces through any one CMP will be at least 48.

This number is the ***data redundancy***, of the ***fold*** of the data. For example, 24 fold or 2400% means that each depth point was sampled 24 times. Sampling fold in a seismic line is the same thing as the "over-sampling" which you see advertised in compact disk players. In general, the higher the fold of the data, the better the profile.

### *Correction for Offset from the Source*

The first basic step in processing the data is to collect, or ***gather*** together all of the traces that go through each midpoint (Fig. 11.5). Even after that book-keeping step, although each CMP has been sampled multiple times (Fig. 11.4), we can't add them together because each ray through the midpoint is a different length and thus the travel time will also be different (Fig. 11.5). Thus, the processor has to determine a set of velocities, known as ***stacking*** or ***normal move out*** (NMO) velocities, which will correct for the fact that each ray through a CMP has a path of a different length. These velocities should line up all of the individual "blips" corre-

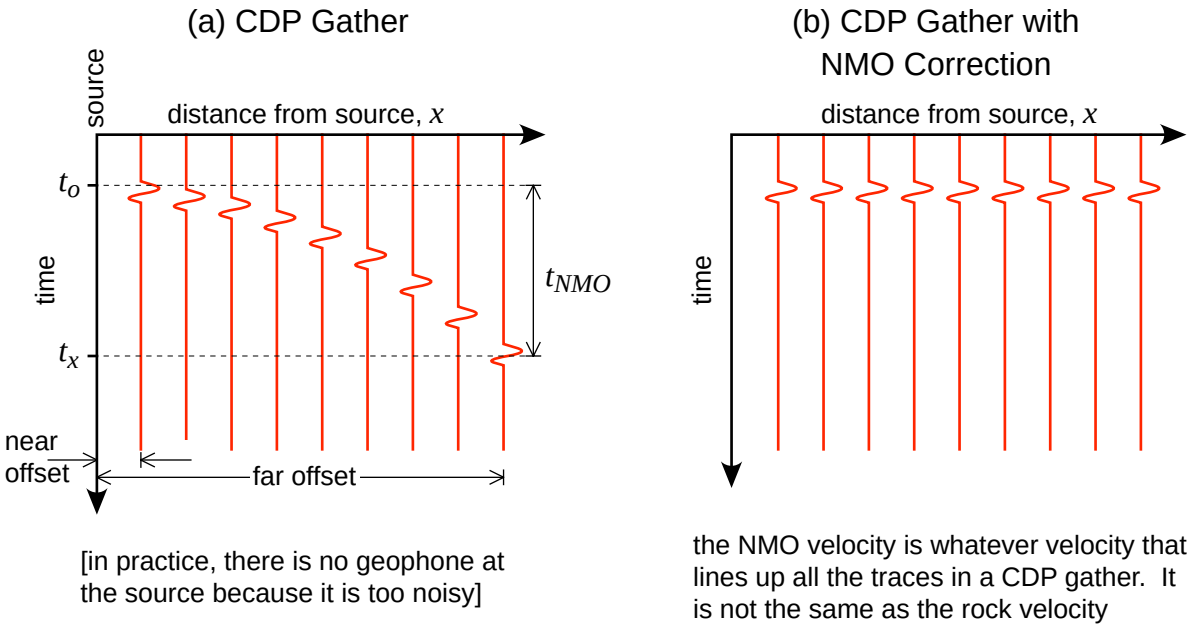


**Figure 11.5 — (a) Gathering together all of the traces that go through the same midpoint. There is a trace for each recording station. The time that the reflection is recorded at each station increases with offset from the source. (b) Before the traces can be added together, they must be lined up by applying a stacking velocity to correct for the moveout time.**

sponding to a single reflector on adjacent traces. The relation between the horizontal offset, $x$, and the time at which a reflector appears at that offset, $t_x$, is:

$$t_x^2 = t_o^2 + \frac{x^2}{V_{stacking}^2} \tag{11.3a}$$

Or

$$\Delta t_{NMO} = t_x - t_o = \sqrt{t_o^2 + \frac{x^2}{V_{stacking}^2}} - t_o \tag{11.3b}$$

If you have a very simple situation in which all of your reflections are flat and there are only vertical velocity variations (i.e. velocities do not change laterally), then you can calculate the rock interval velocities from the stacking velocities using the ***Dix Equation*** (11.4):

$$V_{i(1,2)} = \sqrt{\frac{V_{st2}^2 t_2 - V_{st1}^2 t_1}{t_2 - t_1}} \tag{11.4}$$

where $V_{i12}$ is the interval velocity of the layer between reflections 1 and 2, $V_{st1}$ is the stacking velocity of reflection 1, $t_1$ is the two way time of reflection 1, etc. The interval velocity is important because, to convert from two-way time to depth, we must know the interval, not the stacking, velocity. Once the correction for normal move out is made, we can add all of the traces together, or ***stack*** them. This is what produces the familiar seismic reflection profiles.

Processing seismic data like this is simple enough, but there are huge amounts of data involved. For example a typical academic deep seismic reflection profile is 20 s long, has a 4 ms digital sampling rate (the time interval between numbers recorded), and is 48 fold. In a hundred station long line, then, we have

$$\frac{(200 \text{ CDPs})(48 \text{ sums})(20 \text{ s})}{\left(\frac{0.004 \text{ s}}{\text{data sample}}\right)} = 48 \times 10^6 \text{ data samples}$$

If you are a field geologist by training or nature, which most structural geologists are, that seems like an intimidating amount of data! Even with modern digital recording systems like smart phone compass apps, it is pretty tough to collect even a couple of hundred measurements per day. But, don't let the numbers fool you: the vast majority of the numbers collected in a seismic reflection profile are worthless, they are noise rather than data. The geophones in a seismic reflection survey record everything — wind rustling the bushes, traffic, thunder, electrical noise — not just the reflections from subsurface interfaces in which we are interested. Much of the data processing, and we have ignored here most of the advanced processing, is meant to filter out or subdue the noise. Therein lies the difference between the field geologist and the geophysicist (Fig. 11.6)! Much of the process of learning field geology is learning how to filter information when you see it in the field and deciding small part of that data is worth writing down.

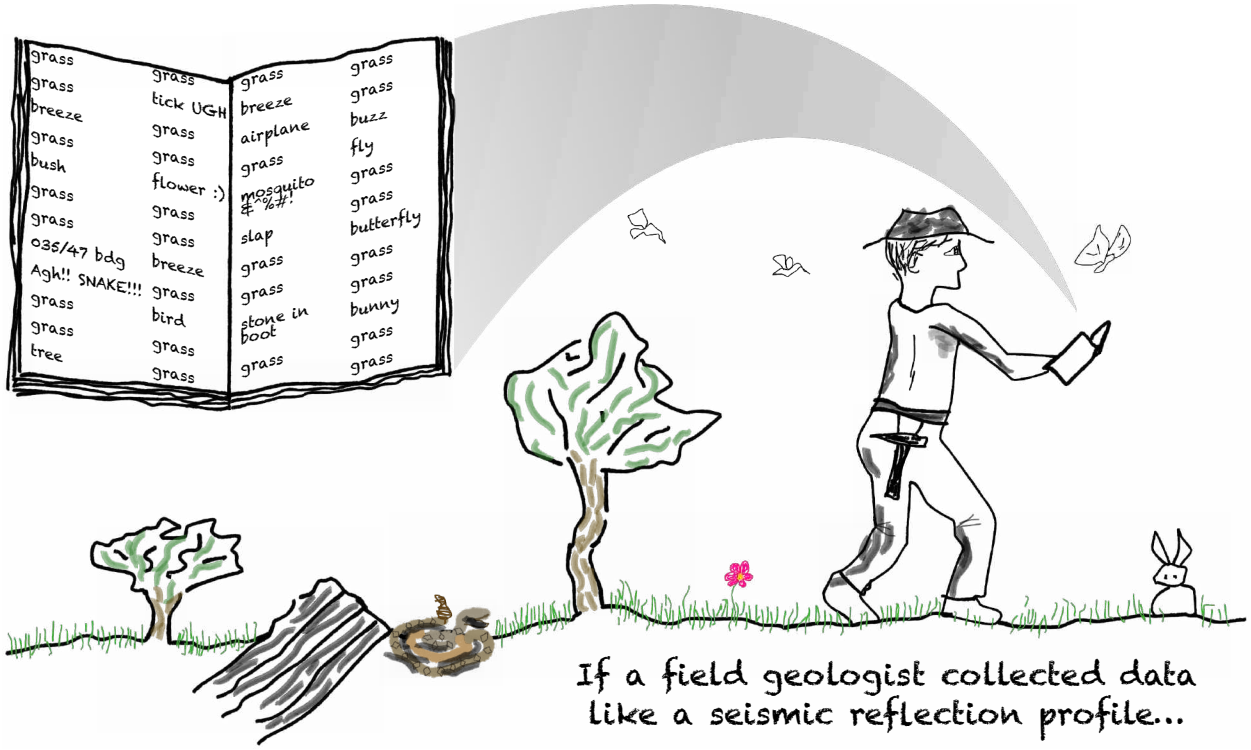


**Figure 11.6**

Geophysicists record all the data and then filter it in the computer whereas field geologists filter out what they consider to be noise before ever writing anything down!

## *Migration*

The effect of CMP processing is to make it look like the source and receiver coincide (e.g., having 48 vertical traces directly beneath the station). Thus, all common midpoints are plotted as if they were vertically beneath the surface. This assumption is fine for flat layers, but produces an additional distortion for dipping layers, because of course reflection from a dipping layer isn't beneath us (Fig. 11.7). The effect of this distortion is that all dipping reflections are displaced down-dip and have a shallower dip than the reflector that produced them. The magnitude of this distortion is a function of the dip of the reflector and the velocity of the rocks.

The process of ***migration*** corrects this distortion, but it depends on well-determined velocities and on the assumption that all reflections are in the plane of the section (see "sideswipe", below). A migrated section can commonly be identi-

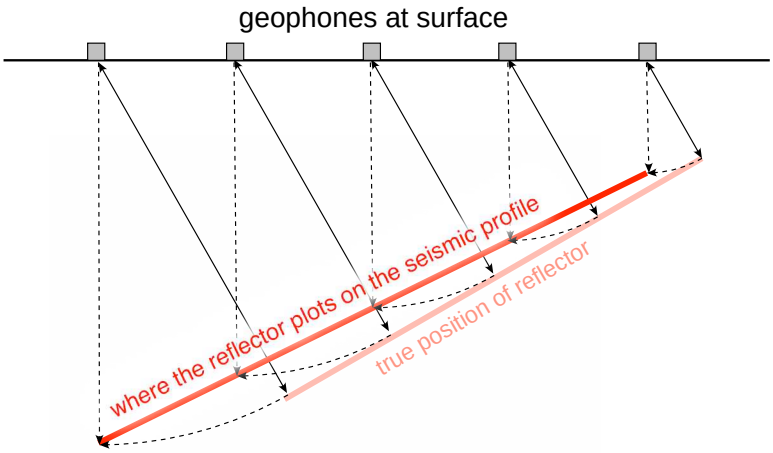


**Figure 11.7 — A dipping reflector in the subsurface will not appear in its proper position on a seismic reflection profile because all CMPs are assumed to be vertically beneath their corresponding station at the surface. Migration is a process that corrects this artifact.**

fied because it has broad "migration smiles" at the bottom and edges (Fig. 11.8). Smiles within the main body of the section probably mean that it has been "over-migrated." As we shall see, migration also removes diffractions.

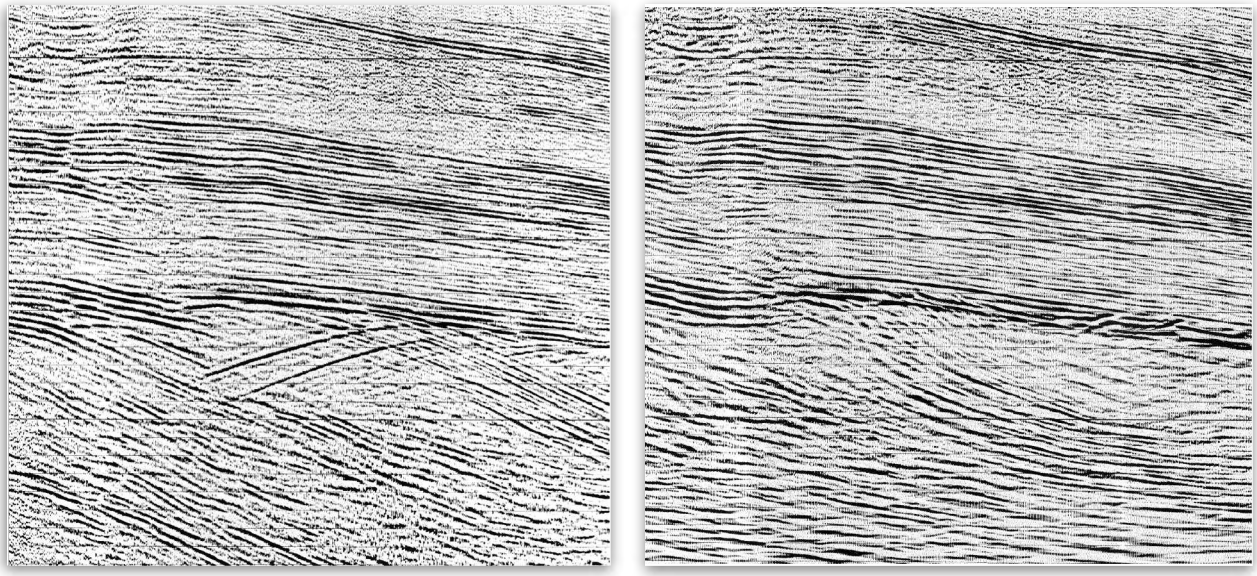

**Figure 11.8 — Same portion of a seismic section, shown both unmigrated (left) and migrated (right). In the bottom section, note the arcuate, sweeping features at the bottom of the section which are classic migration "smiles".**

## Resolution of Seismic Reflection Data

The ability of a seismic reflection survey to resolve features in both horizontal and vertical directions is a function of wavelength:

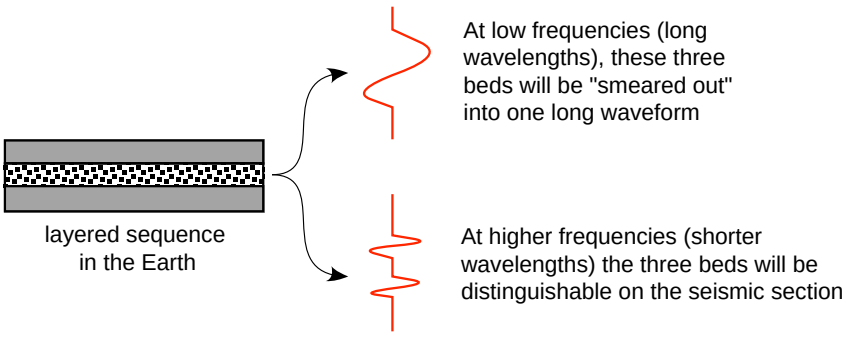


**Figure 11.9 — The dependence of vertical resolution on frequency.**

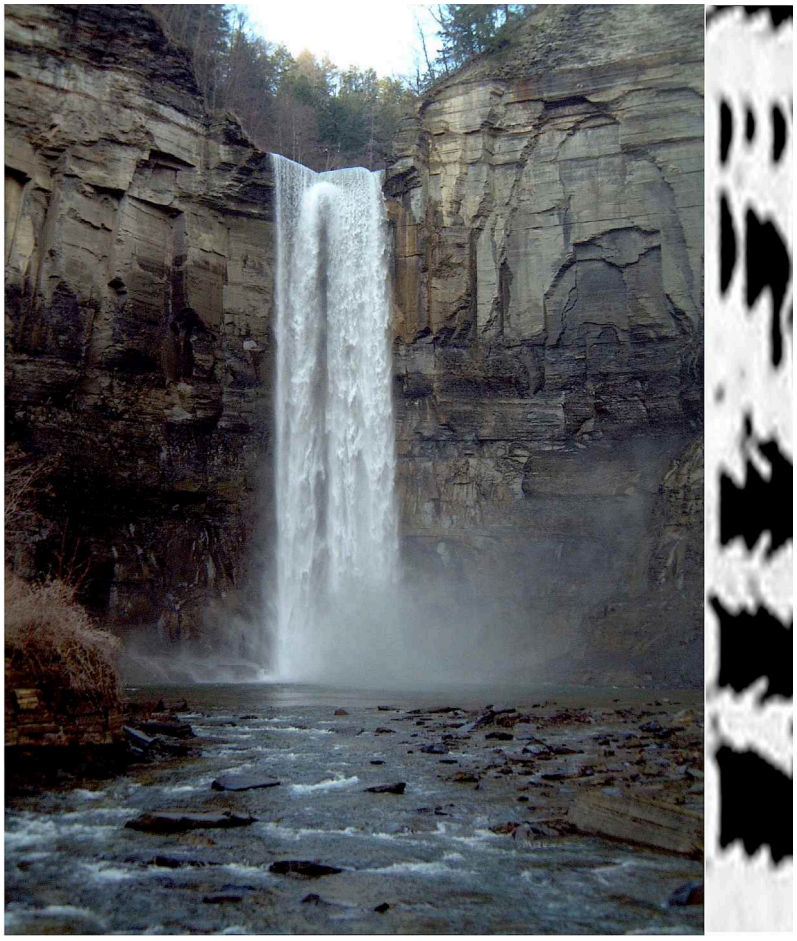

**Figure 11.10 — Taughannock Falls near Ithaca, New York is 65 m high. The snippet of seismic section on the right side is approximately scaled to the photograph for a frequency of 60 Hz and velocity of 4500 m/s.**

$$\lambda = \text{velocity} / \text{frequency}.$$

Wavelength increases with depth in the Earth because velocity increases and frequency decreases. Thus, seismic reflection surveys lose resolution with increasing depth in the Earth.

## *Vertical Resolution*

Generally, the smallest (thinnest) resolvable features are 1/4 to 1/8 the dominant wavelength. At a higher frequency, finer scale layering can be resolved but at a low frequency, detail is lost (Fig. 11.9). A shallow, high resolution seismic reflection survey may have dominant wave lengths in the range of 60 Hz. Assuming our sedimentary rock sequence has a velocity of 4500 m/s, we can calculate that one wavelength is about 18.75 m. Thus, you can see that even a high resolution seismic survey is imaging layering which is much coarser in scale (tens of meters) than the bedding or layering that the field geologist sees. This point is emphasized in Figure 11.10.

## *Horizontal Resolution*

The horizontal resolution of seismic reflection data depends on the ***Fresnel Zone***, a concept which should be familiar to those who have taken optics. The minimum resolvable horizontal dimensions are equal to the first Fresnel zone (Fig. 11.11). Because frequency decreases with depth in the crust, seismic reflection profiles will have greater horizontal resolution at shallower levels. At 1.5 km depth with typical frequencies, the first Fresnel Zone is ~300 m. At 30 km depth, it is about 3 km in width.

Consider a discontinuous sandstone body (Fig. 11.12). The segments which are longer than the first Fresnel Zone will appear as reflections, whereas those which are shorter will act like point sources. Point sources and breaks in the sandstone will generate ***diffractions***, which have parabolic curvature: Because fre-

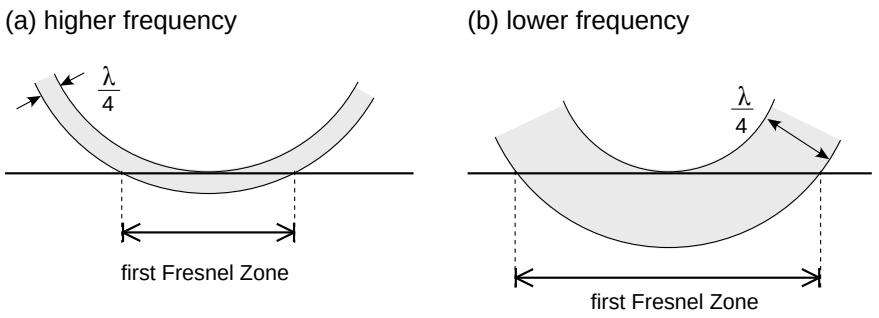


**Figure 11.11 — Illustration of the first Fresnel Zone dependence on wavelength, λ. Two wavefronts, a quarter wavelength apart, impinge on a horizontal surface.**

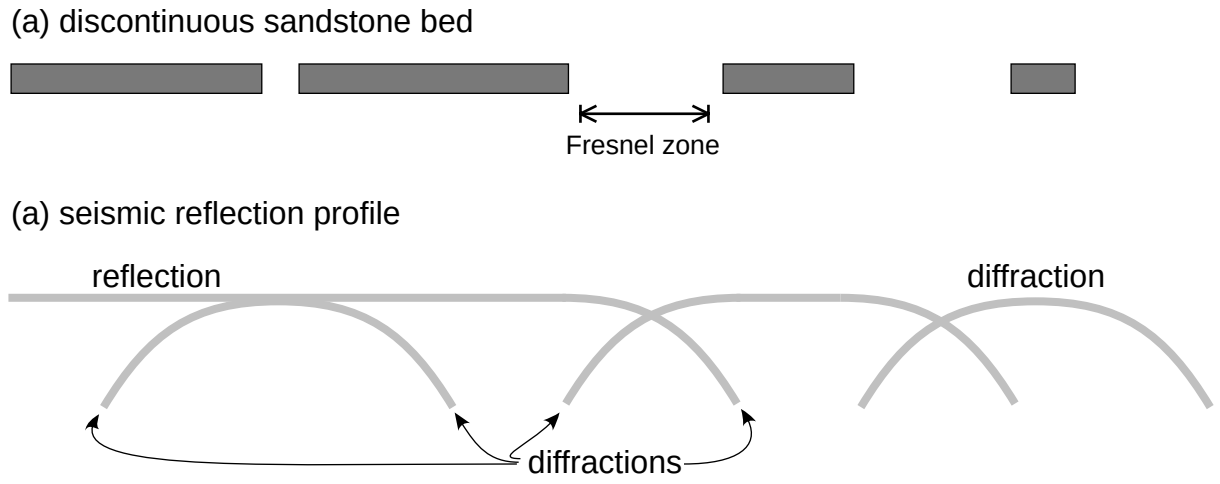


**Figure 11.12 — (a) cross section of a discontinuous sandstone bed. (b) holes in the bed, or segments of the bed that are smaller than the first Fresnel zone will generate diffractions rather than reflections.**

quency decreases with depth in the crust (and wavelength increases), seismic reflection profiles will have lower horizontal resolution at deeper levels.

## Diffractions

Diffractions may look superficially like an anticline but they are not. They can be extremely useful, especially because ***seismic reflection techniques are biased toward gently dipping layers and do not image directly steeply dipping or vertical features***. Diffractions help you to identify such features. For example, a vertical dike would not show up directly as a reflection but you could determine its presence by correctly identifying and interpreting the diffractions from it. High-angle faults are seldom imaged directly on seismic reflection profiles, but they, too, can be located by finding the diffractions from the truncated beds (Fig. 11.13). The shape and curvature of a diffraction is dependent on the velocity. At faster velocities, diffractions become broader and more open. Thus at great depths in the crust, diffractions may be very hard to distinguish from gently dipping reflections. Note that a well-done migration should remove all of the diffractions from the seismic reflection profile. For that reason, it is often advantageous to see both the unmigrated and migrated versions of a profile.

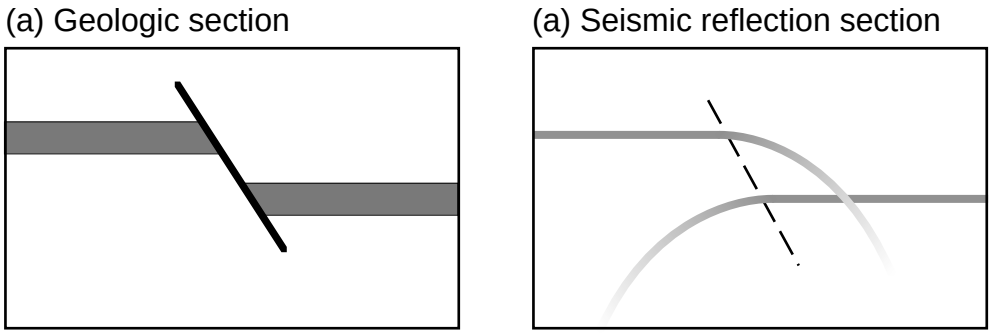


**Figure 11.13 — (a) geologic section of a high angle normal fault; (b) schematic seismic reflection profile. The fault plane would not be imaged seismically because it is too steep but the truncations of the offset bed would generate diffractions, allowing one to interpret at fault (dashed line).**

## Artifacts

The seismic reflection technique produces a number of artifacts — misleading features that are easily misinterpreted as real geology — which can fool a novice interpreter. A few of the more common "pitfalls" are briefly listed below.

### *Velocity Pullup/pulldown*

We have already talked about this artifact when we discussed the distortion due to the fact that seismic profiles are plotted with the vertical dimension in time, not depth (Fig. 11.3). When you have laterally varying velocities, deep horizontal reflectors will be pulled up where they are overlain locally by a high velocity body and will be pushed down by a low velocity body (as in the example in Figure 11.3). If unrecognized, this distortion could look like folding of the deeper layer.

### *Multiples*

Where there are very reflective interfaces, you can get multiple reflections, or ***multiples***, from those interfaces. When the acoustic energy bounces off of a reflector at depth and comes back to the surface, an additional bounce can be generated by the air-rock interface (Fig. 11.14). The effective reflectivity of multiples is the product of the reflectivity of each reflecting interface. For simple multiples (see below) then,

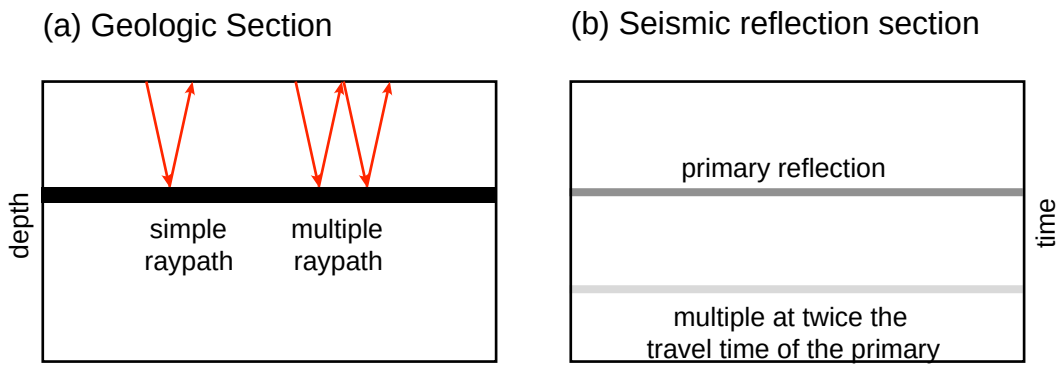


**Figure 11.14 — (a) Geologic section and (b) a simple multiple on a seismic section generated by the ray path bouncing off of the underside of the surface of the Earth.**

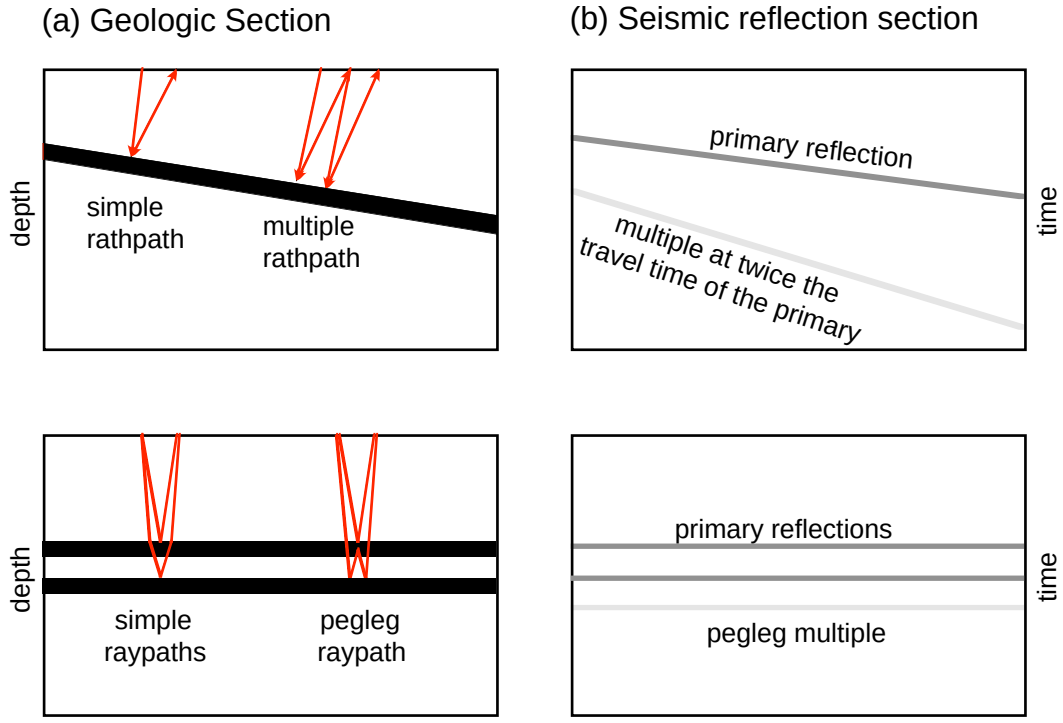


**Figure 11.15 — More complicated multiples can result from dipping horizons (top) and from reverberation between two layers (bottom).**

$$R_{\text{multiple}} = R^2_{\text{primary}}.$$

If the primary reflector has a reflection coefficient of 0.01 then the first multiple will have an effective reflection coefficient of 0.0001. In other words, multiples are

generally only a problem for highly reflective interfaces, such as the water bottom in the case of a marine survey or particularly prominent reflectors in sedimentary basins (e.g. the sediment-basement interface).

In addition to the simple multiple shown in Figure 11.14, more complicated reverberations can exist. For example, multiples from dipping layer have twice the dip of the primary reflector and you can have peg-leg multiples that result from the ray path bouncing around between two layers in the subsurface (Fig. 11.15)

## *Sideswipe*

In seismic reflection profiling, we assume that all the energy that returns to the geophones comes from within the vertical plane directly beneath the line of the profile. Geology is inherently three-dimensional so this need not be true. Even though geophones record only vertical motions, a strong reflecting interface which is out-of-the-plane can produce a reflection on a profile, as in the case illustrated in Figure 11.16. Reflections from out of the plane is called ***sideswipe***. Such reflections will cross other reflections and will not migrate out of the way. (Furthermore they will migrate incorrectly because in migration, we assume that there has been no sideswipe!) The main way of detecting sideswipe is by running a sufficient number of cross-lines and tying reflections from line to line. Sideswipe is particularly severe where seismic lines run parallel to the structural grain.

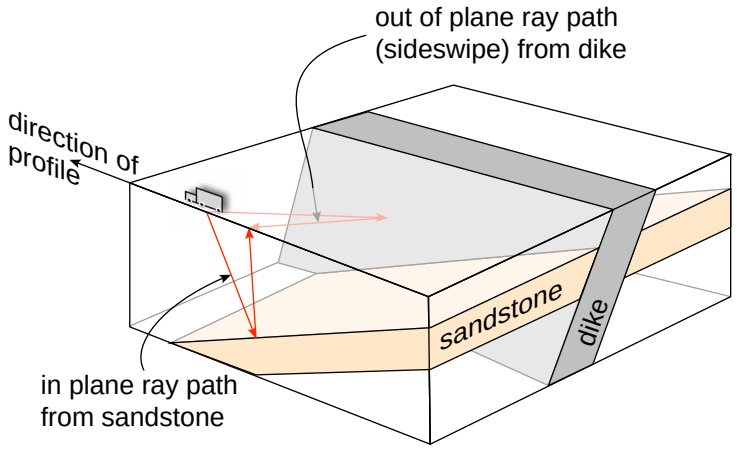


**Figure 11.16 — Illustration of a geometry where you could get out of plane reflections known as sideswipe.**

### *Buried Focus*

Tight synclines at depth can act like concave mirrors to produce an inverted image quite unlike the actual structure. Although the geological structure is a syncline, on the seismic profile it looks like an anticline. At the dawn of the seismic reflection age, many an unhappy petroleum geologist has drilled a buried focus hoping to find an anticlinal trap! The likelihood of observing a buried focus increases with depth because more and more open structures will produce the focus. A good migration will correct for buried focus.

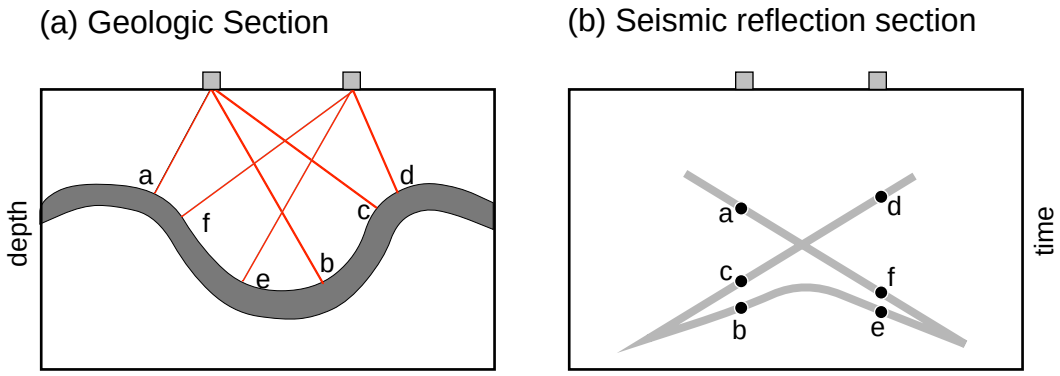


**Figure 11.17 — Tight synclines such as that depicted in (a) produce multiple CMPs on a single layer per station, an effect known as a buried focus. (b) When we use standard CMP processing, we plot all of those points from different parts of the structure directly beneath the station resulting in a bowtie pattern and what appears to be an anticline where there is really a syncline.**

## Structural Interpretation of Seismic Profiles

Modern seismic interpretation software packages are extremely powerful and provide excellent tools for interpretation of both two- and three-dimensional data. In fact, it is virtually impossible to interpret 3D data cubes without the benefit of such packages. Here, we have much more modest aims: how to extract useful structural data from traditional 2D data. Because every seismic profile is different, there is no cookbook approach to interpretation. Perhaps one of the most important things to remember is that ***seismic reflection data is biased towards horizontal reflectors and steeply dipping interfaces cannot be imaged di-***

***rectly at all***. In addition, there are some basic things that all interpreters look for: truncations, discontinuities, and kink axes.

## *Truncations and Discontinuities*

Truncations imply an abrupt geological boundary, though there are many potential explanations. Among the most common are: truncation at a fault, intrusive or diapiric contact, an angular unconformity, or various types of downlap or onlap. Which of these you choose will depend on your knowledge of the area.

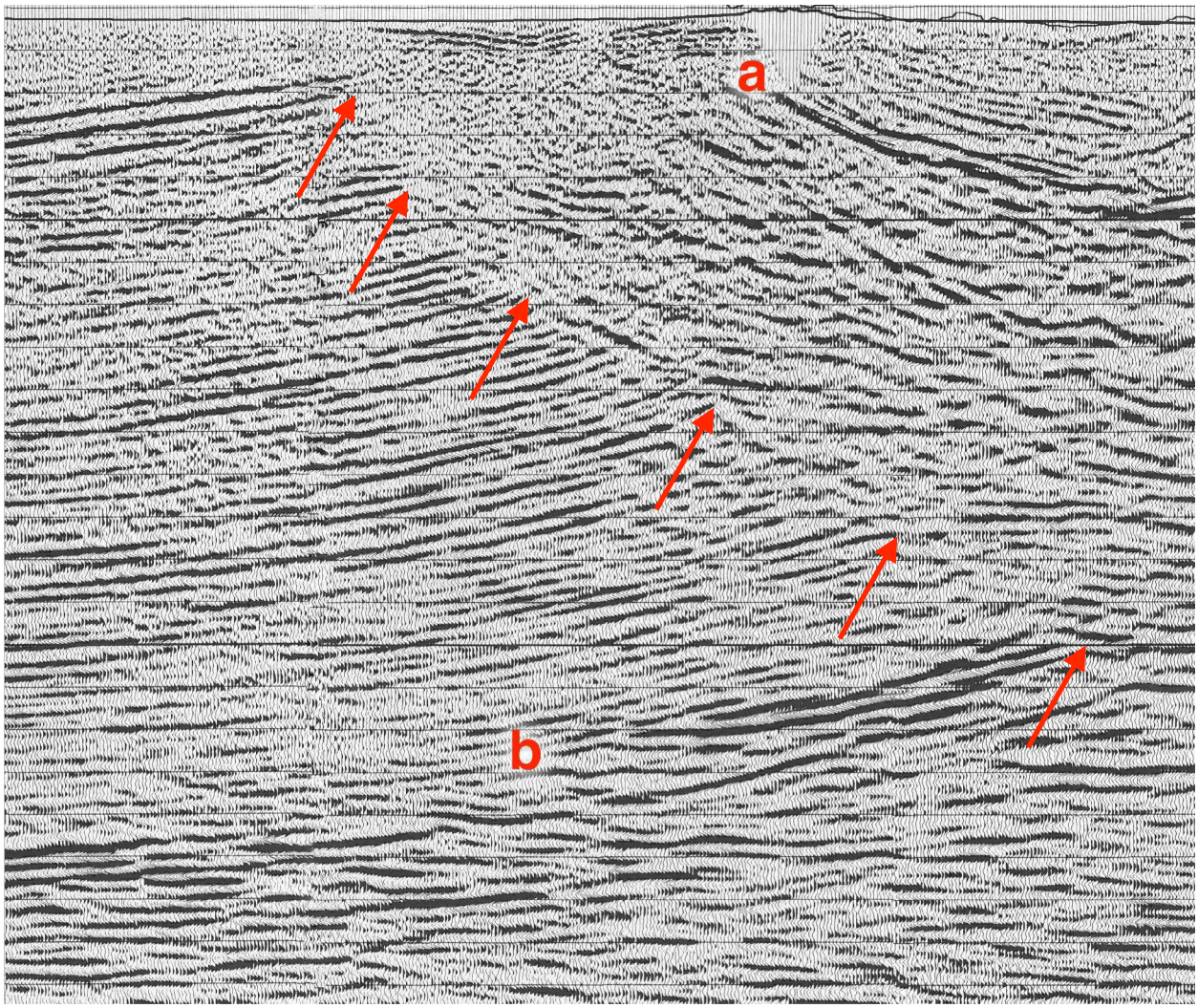


**Figure 11.18 — Migrated seismic reflection profile showing the truncations (red arrows) of well-defined reflections corresponding to a Cenozoic sedimentary basin sequence against a much less reflective zone. "a" and "b" show the base of the basin sequence in the hanging wall and footwall. Truncations are interpreted as a thrust fault, even though there are no fault plane reflections.**

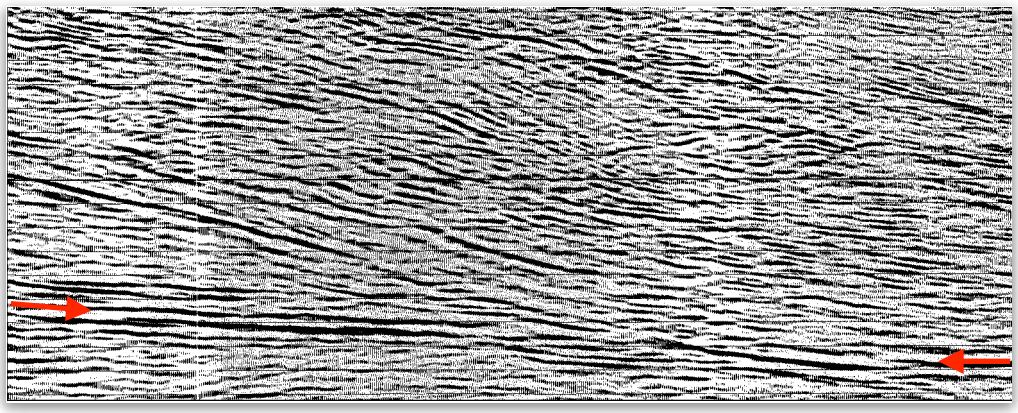

**Figure 11.19 — Migrated seismic reflection profile showing a discontinuity with dipping reflectors above the relatively flat lying reflector indicated by the red arrows.**

Truncations with layered reflections that represent strata on both sides are most likely either fault truncations, unconformities, or onlap or downlap. Truncations at a high angle with layered reflections on one side and a featureless area on the other could be fault, intrusive, or diapiric contacts.

Figure 11.18 shows numerous truncations, indicated by the red arrows. This section comes from an area of known thrust-faulting, so it is highly likely that the main set of truncations define a curved thrust fault inclined towards the right. The upper plate of this thrust has a zone of poorly resolved reflections that probably correspond to basement rocks or more highly folded and deformed Paleozoic strata. On top of this relatively transparent zone, above horizon "a", lies a perched Cenozoic sedimentary basin. The interpreted thrust fault parallels the base of the Cenozoic basin suggesting that the fault is in a position of a hanging wall flat over a footwall ramp. There are also more subtle truncations below horizon "b" at the base of the well-defined Cenozoic basin in the footwall. These could represent an angular unconformity but with the evidence available, one could not rule out the possibility of a sub-basin fault that parallels the Cenozoic basin fill.

Figure 11.19 shows an example of a discontinuity with dipping reflectors above a relatively flat reflection horizon indicated by the red arrows. This geometry is commonly indicative of a decollement or detachment in the crust above which the rocks have been either shortened or extended relative to the rocks below (you will get to decide which in the exercises!).

## *Kink Axes*

Even folds with curved hinges commonly have long, relatively straight limbs so it is possible to define kink axial surfaces on seismic reflection data. Recall that, in fault-related folds, kink axes are systematically related to the hanging wall and footwall ramps and thus, drawing kink axes on the seismic data can aid in the construction of the underlying fault geometry. In parallel folds, kink axes should bisect the angle between the two limbs, but on time sections, this will only be true if the section is displayed at a 1:1 scale for the rocks involved. Figure 11.20 depicts a small kink band imaged on a migrated seismic reflection profile. Despite the curved nature of the hinge regions, the axial surfaces A and B are relatively straightforward to position. They are parallel to each other and are reasonably close to being interlimb angle bisectors, suggesting that this part of the seismic section has little vertical exaggeration.

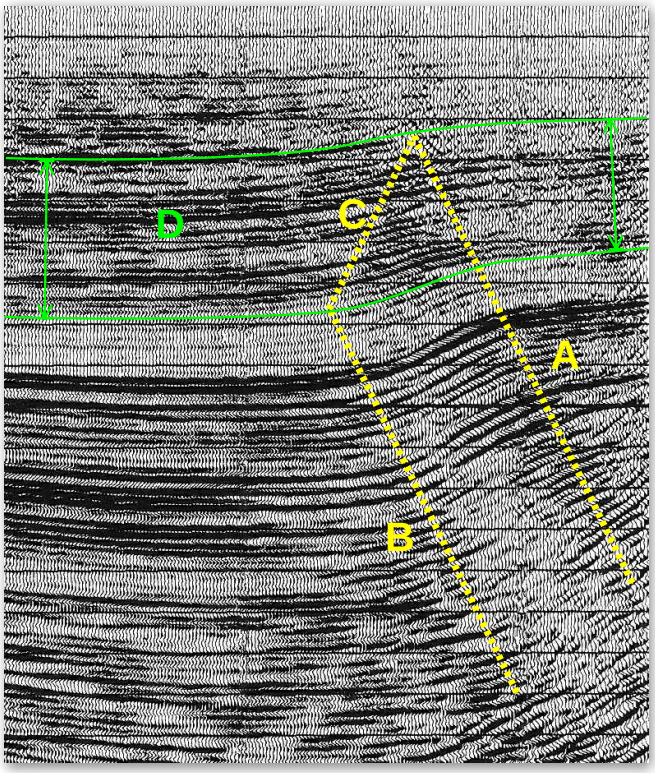


**Figure 11.20 —Kink band on a migrated seismic reflection profile. Sequence D changes thickness across the kink band producing the growth axial surface, C.**

## *Kink Axes and Growth Strata*

The axis C in figure 11.20 is poorly defined but is necessary because axis B disappears up-section before A does. The reason for this becomes clear upon careful inspection of stratigraphic section labeled D: this section is thicker to the left of B/C than it is to the right of A. Thus, we can interpret that the kink band began to grow at a time equivalent to the age of the strata at the change from B to C. The

end of growth would correspond to the age of the strata where C meets A; the exact position of this juncture is not well imaged on this section because of the lack of resolution higher in the profile. Axis C, which is known as a ***growth axial surface***, does not bisect the angle between the limbs because the thickness changes across this boundary. Sequence D is known as ***growth strata*** because they accumulate on and around a structure during its growth. In general, axes that produce folding of the entire section, such as A, are know as ***active axial surfaces*** and are commonly fixed to the footwall ramp of the underlying structure. B is known as a ***fixed axial surface*** and moves with the hanging wall ramp of the fault (Suppe et al., 1992). There is quite a bit more to interpreting growth strata geometries than what we have touched on here but, to review that, would make an already long chapter even longer!

A convenient plot for identifying growth strata is the ***vertical separation diagram***. Vertical separation is simply the vertical difference between the depth to a horizon in one vertical section (or drill hole) on top of the growing (or subsiding) structure and that in another vertical section lying outside of the structure. In pre-growth strata, the vertical separation is constant whereas in the growth strata, the vertical separation diminishes up-section towards zero at the depositional surface (Fig. 11.21). One great advantage of the vertical separation diagram is that it does

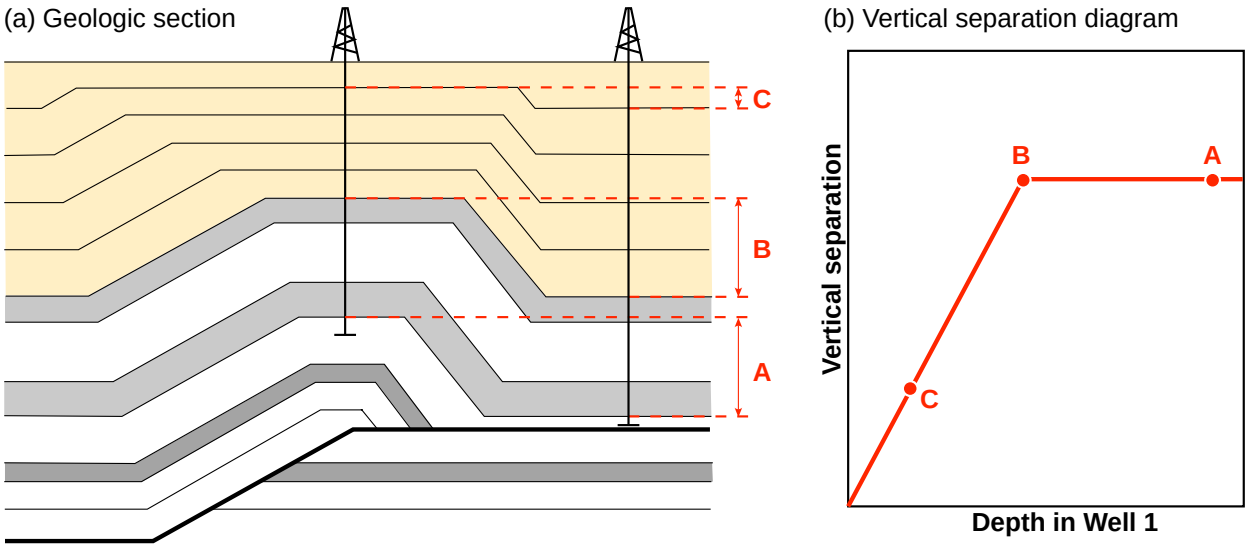


**Figure 11.21 — Construction of a vertical separation diagram over a growth fault-bend fold. This diagram has no dependence on fault-fold kinematic models**

not depend at all on the fault-fold kinematic model; one simply needs two vertical sections. It works equally as well for growth normal faulting on passive margins as it does for thrust faulting. The vertical separation diagram is also quite useful when studying fault reactivation (Mitra, 1993).

 

# Exercises — Chapter 11

1. The diagram below shows a very simple geological cross section where basement rock with a velocity of 6 km/s has been thrust over a sedimentary basin with a velocity of 3 km/s. Accurately construct what an unmigrated time section would look like, assuming both the base of the basin and the thrust fault plane are reflective.

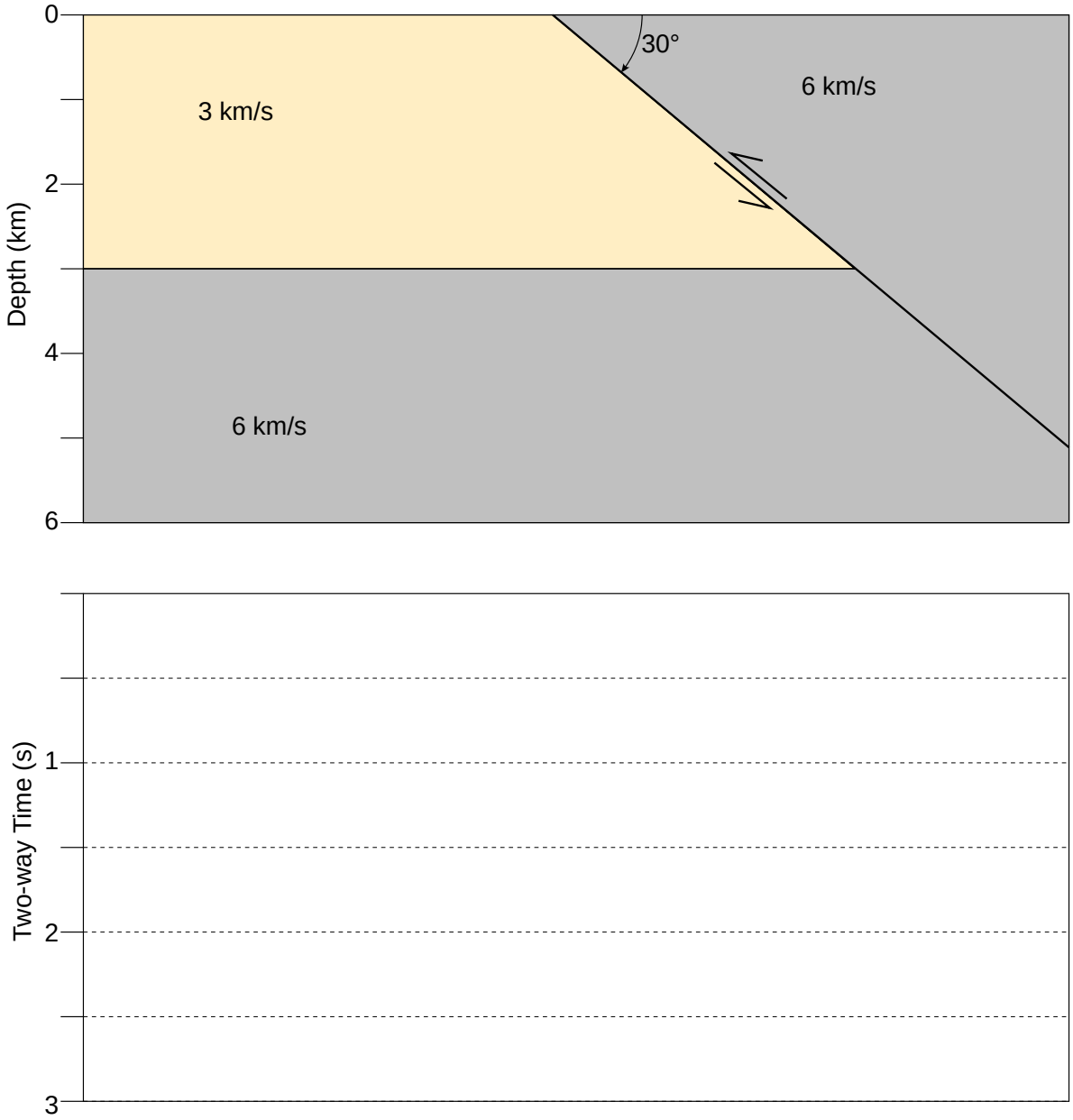


 

2. Interpret the migrated time section on the following page by plotting and interpreting kink axes. Finalize your interpretation by constructing a depth section in the box below the seismic section. Use the stacking velocities and times at points A, B, and C, given in the tables, below, to calculate the depths. Recall that the time is the two-way travel time.

Velocity at Point A

| Time (s) | Stacking Velocity (km/s) |
|---|---|
| 0.6 | 3.64 |
| 1 | 4.4 |
| 1.25 | 4.8 |
| 1.5 | 5.0 |
| 1.8 | 5.3 |
| 2.6 | 5.8 |
| 3.0 | 5.8 |

Velocity at Point B

| Time (s) | Stacking Velocity (km/s) |
|---|---|
| 0.6 | 4.27 |
| 0.88 | 4.8 |
| 1.54 | 5.52 |
| 1.9 | 5.6 |
| 2.7 | 5.8 |
| 3.0 | 5.9 |
| 4.0 | 6.3 |

Velocity at Point C

| Time (s) | Stacking Velocity (km/s) |
|---|---|
| 0.6 | 2.94 |
| 0.8 | 3.27 |
| 1.1 | 3.8 |
| 1.3 | 4.1 |
| 2.2 | 5.0 |
| 2.8 | 5.4 |
| 3.0 | 5.6 |

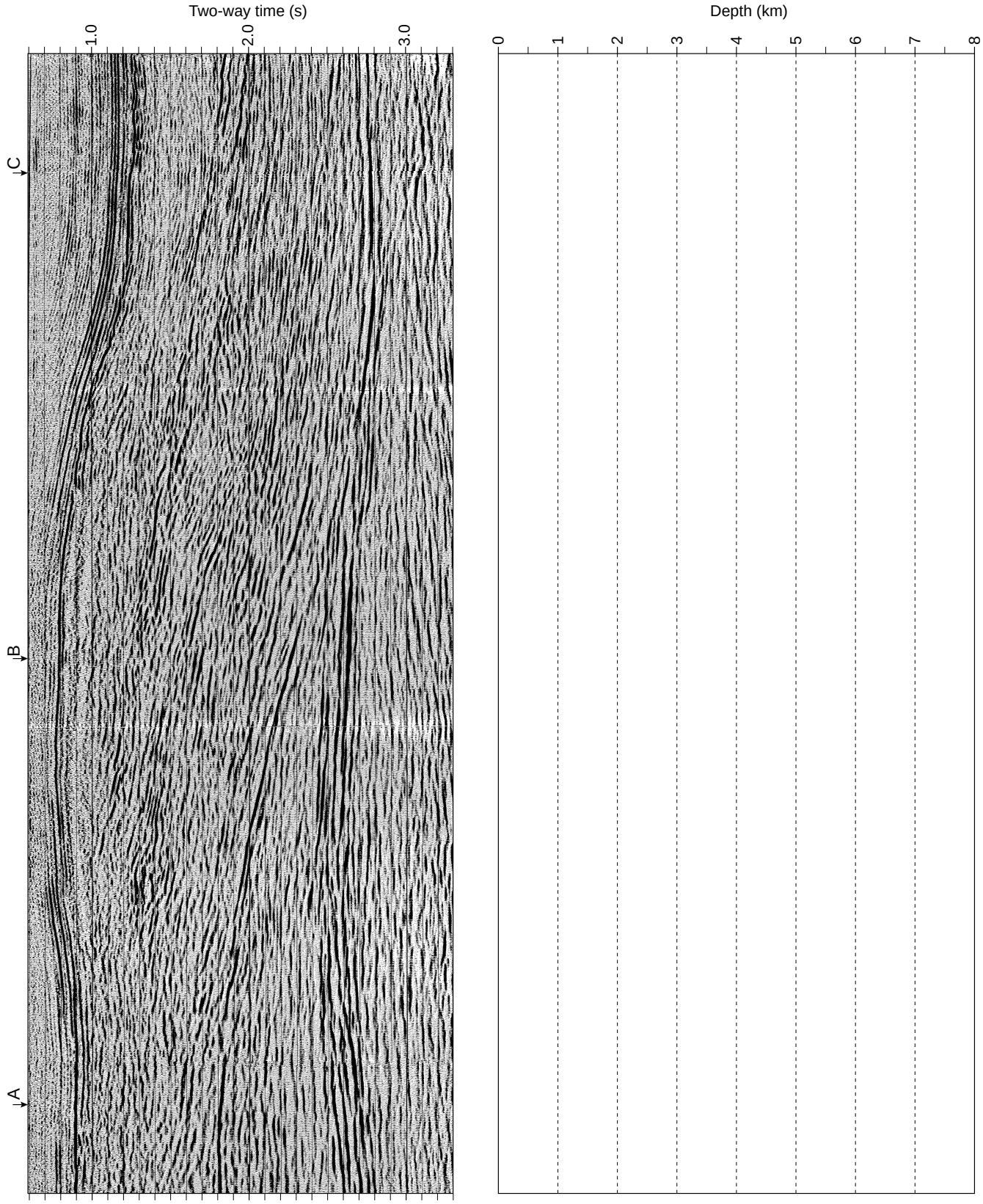
Two-way time (s)
1.0
2.0
3.0
A
B
C
Depth (km)
0
1
2
3
4
5
6
7
8

3. Interpret the section, below, using kink axial surfaces and, if you identify any growth strata, indicate at what level growth initiated. Is the structure still active?

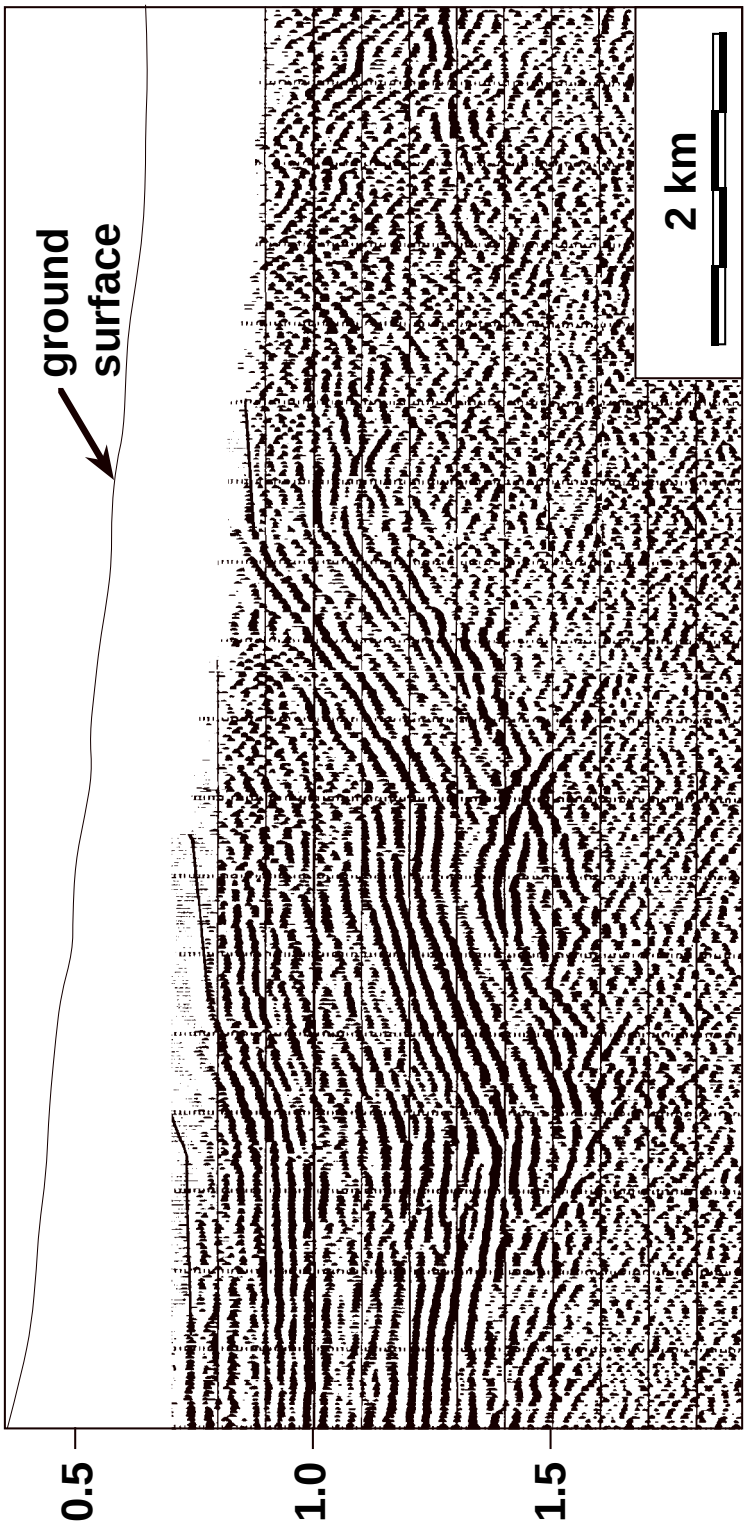

4. The table, below, shows the tops of dated formations in two well, A and B. Construct a vertical separation diagram and identify (a) which well is on the growing structure; (b) the time(s) of growth; (c) the rate of vertical displacement of the structure (assuming uniform compaction), and (d) the growth history of the region.

| Formation Age | Depth in Well A (m) | Depth in Well B (m) |
|---|---|---|
| Plio-Quaternary | 250 | 250 |
| Pliocene | 500 | 500 |
| 8 Ma | 800 | 738 |
| upper Miocene | 1355 | 1180 |
| 10 Ma | 1950 | 1650 |
| Miocene | 2280 | 1975 |
| middle Miocene | 2730 | 2435 |
| 14.3 Ma | 3198 | 2900 |
| lower Miocene | 3540 | 3160 |
| lower Miocene | 3875 | 3295 |
| lower Miocene | 4162 | 3405 |
| 27.5 Ma | 4480 | 3543 |
| Eocene | 4700 | 3678 |
| Paleocene | 5090 | 4065 |
| Upper Cretaceous | 5510 | 4485 |
| Upper Cretaceous | 5855 | 4830 |

# Chapter 12

## *Solid Mechanics and Structural Geology*

### Introduction

Up to this point, we have focused mostly on geometry and kinematics, borrowing a smattering of concepts from the much broader realm of solid mechanics. The concepts that we have developed so far — vectors, tensors, stress, strain, some basic material models, etc. — cover about the first 25-30% of a standard continuum mechanics textbook. This background provides a splendid point of departure

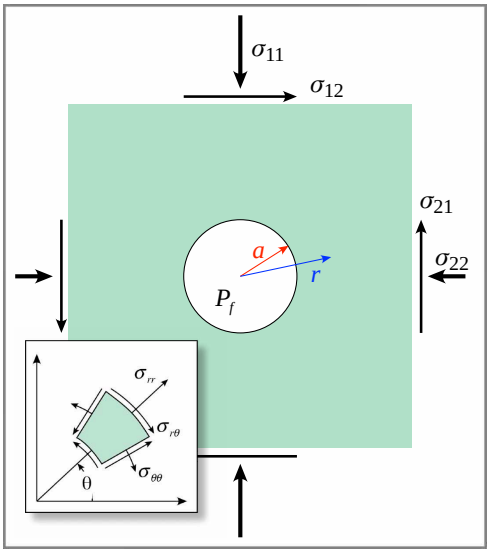


for beginning to explore the rich world of solid mechanics. One must become conversant with this world if you want to explore why structures form and behave as they do. Solid mechanics is a broad field and there are entire geology-oriented books devoted to this subject (Johnson, 1970; Turcotte and Schubert, 1982; Jaeger and Cook, 1976; Middleton and Wilcock, 1994; Pollard and Fletcher, 2005).

The purpose of this chapter is to give you a glimpse of the basic approach used in a more complete analysis provided by mechanics, as well as review some fundamental results that are particularly germane to structural geology. Bear in mind that this is only a taste, a teaser for the real thing. Hopefully, this will give you

the motivation to dive in deeper, either on your own or in subsequent classes, to explore this world.

## The Mechanical Approach

A mechanical approach involves a clear definition of the components necessary to solve the problem of interest. The starting point is commonly the simplifying assumption that the distribution of properties in a material is continuous; i.e., that the material is a ***continuum***. This is the origin of the term, continuum mechanics. Because properties vary smoothly in time or space, we describe them in terms of ***gradients***, which mathematically are derivatives. Because the Earth is a three dimensional place, the gradients in which we are interested vary in all directions and are specified along the three axes of our Cartesian coordinate system, so we will define how things vary in terms of ***partial differential equations***. We have already had a taste of this in Chapters 7 and 8 where the equations governing three dimensional strain are expressed as partial derivatives of displacement (or po-

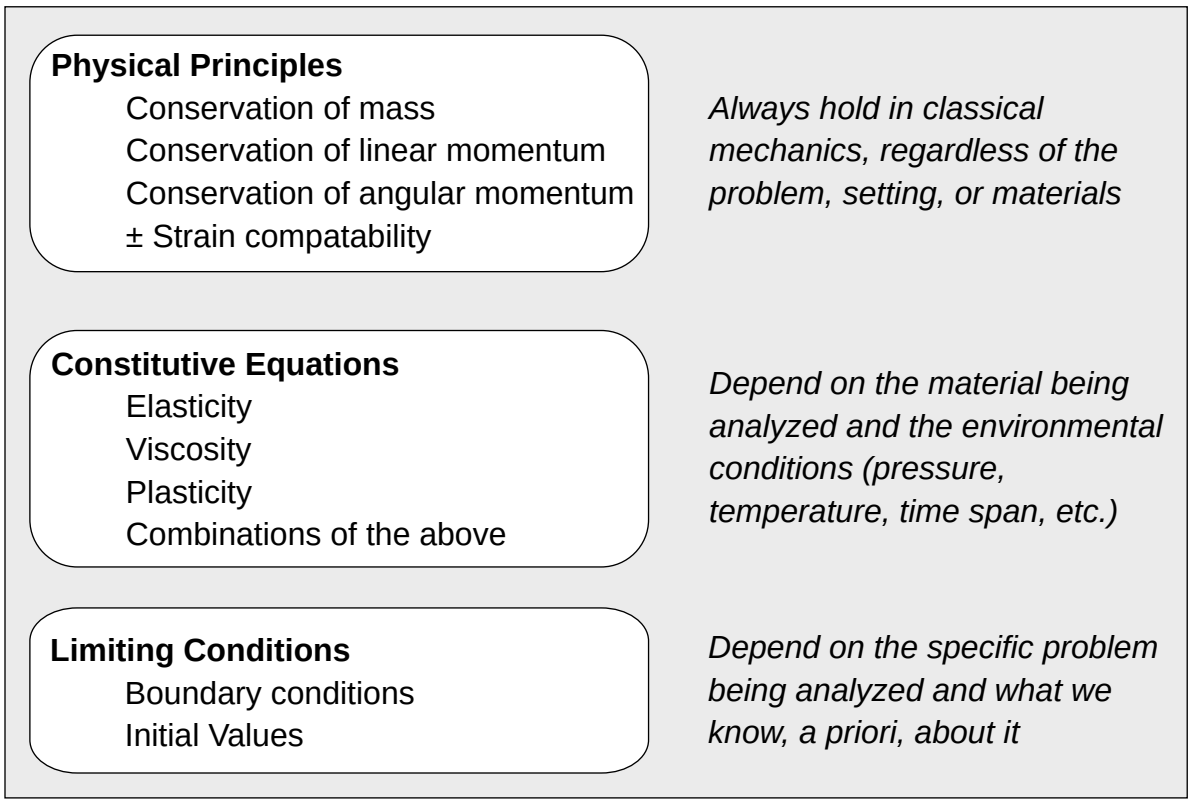


**Figure 12.1 — Hierarchy of components of a full mechanical analysis.**

sition) with respect to position. The basic approach relies on three levels of abstraction (Fig. 12.1; from most general to most specific): (1) ***physical principles***, (2) ***constitutive equations***, and (3) ***boundary conditions*** and ***initial values***.

## *Physical Principles*

Physical principles are those which apply to any body or substance. Any deformation of a continuous medium that we wish to analyze must conform to these principles which form the fundamental basis of classical mechanics. The first of these is ***conservation of mass***. As we have already seen in the introduction of balanced cross-sections and the trishear fault-fold model, the principle of conservation of mass is defined by the ***continuity equation***:

$$\frac{d\rho}{dt} + \rho \frac{\partial \left(v_i\right)}{\partial x_i} = 0 \tag{12.1}$$

where the first term is the material derivative of density with respect to time (sometimes written using capital "*D*"). This equation states that the change in density with time plus the flux of material in or out of the system must be equal to zero. It is from this general equation that we derive the specialized condition of incompressibility for volume constant deformation:

$$\text{div } \mathbf{v} = \left[ \frac{\partial v_1}{\partial x_1} + \frac{\partial v_2}{\partial x_2} + \frac{\partial v_3}{\partial x_3} \right] = 0 \tag{12.2}$$

The cornerstone of physical principles follows from Newton's Second Law, which deals with the ***conservation of momentum***. The momentum of a body is equal to its mass, $m$, times its velocity, $\mathbf{v}$. Newton stated that the rate of change of momentum is proportional to and in the direction of the "impressed" force, $\mathbf{F}$:

$$\mathbf{F} = \frac{d(m\mathbf{v})}{dt} \tag{12.3a}$$

The term, "impressed force" means the vector sum of all of the forces acting on a body. If the mass does not vary with time, then we can write Newton's second law in a more familiar format:

$$\mathbf{F} = m\frac{d\mathbf{v}}{dt} = m\mathbf{a} \tag{12.3b}$$

where **a** is the acceleration. When the force equals zero, momentum must be constant.

From the condition of Newton's second law, one can derive the ***equations of motion*** in various formats (see Malvern, 1969 or Pollard and Fletcher, 2005 for details of the derivation). Perhaps the most general and insightful is given by ***Cauchy's First Law of Motion***:

$$\rho\frac{dv_i}{dt} = \frac{\partial\sigma_{ij}}{\partial x_j} + \rho g_i \tag{12.4}$$

As with Equation (12.1), $d/dt$ is the material time derivative and $g_i$ is acceleration due to gravity. The terms in this equation have units of force per unit volume. This equation then says that the total force per unit volume is equal to the gradient of stress with distance [with units of N $m^{-2}$ $m^{-1}$ = (kg m $s^{-2}$) $m^{-2}$ $m^{-1}$ = (kg m $s^{-2}$) $m^{-3}$] or ***surface forces*** per volume plus the ***body forces*** per volume.

***Torque***, or ***moment***, is the force multiplied by the distance from a pivot point or fulcrum in a material. In a way exactly analogous to what we have just seen, the ***conservation of angular momentum*** says that the sum of all torques is equal to the rate of change of total angular momentum. ***Cauchy's Second Law of Motion*** is an expression of this and its result is a simple and elegant proof that the stress tensor must be symmetric.

$$\sigma_{ij} = \sigma_{ji} \quad \text{for} \quad i, j = 1 \text{ to } 3$$

For bodies in equilibrium, the change of linear and angular momentum with respect to time must equal zero. This condition yields two fundamental relationships: the balance of forces and the balance of moments (i.e., torques):

$$\sum \mathbf{F} = \sum \mathbf{F}_{surface} + \sum \mathbf{F}_{body} = 0 \tag{12.5}$$

$$\sum \mathbf{M} = 0 \tag{12.6}$$

These are the starting conditions for analyses involving mechanics of ***static equilibrium***. When you draw a free body diagram, it should depict all of the forces and torques on a body and, if it is a problem in static equilibrium as many problems in geology are, those should all sum to zero.

Finally, for some problems, we wish to ensure that the displacement field associated with a particular strain field is single valued and continuous. That is, the strains imposed produce no gaps or overlaps. This condition of ***strain compatibility*** which is specified by St.-Venant's equations:

$$\frac{\partial^2 \varepsilon_{ij}}{\partial X_k \partial X_l} + \frac{\partial^2 \varepsilon_{kl}}{\partial X_i \partial X_j} - \frac{\partial^2 \varepsilon_{ik}}{\partial X_j \partial X_l} - \frac{\partial^2 \varepsilon_{jl}}{\partial X_i \partial X_k} = 0 \tag{12.7}$$

where $\varepsilon_{ij}$ is the infinitesimal strain tensor (Chapter 7). Recall that for infinitesimal strain the material and spatial coordinates are the same. Equation (12.7) represents six equations that must be satisfied if the displacement field is to be smooth and continuous. This equation finds important applications in elasticity theory and is, for example, one of the underlying tenants of the construction of the world strain map (Holt et al., 2000). Nonetheless, in the pantheon of physical laws it is a lesser god and there are a number of perfectly physically plausible geological processes that do not comply.

## *Constitutive Equations*

So far in this chapter, we haven't said anything about materials, yet, and how they respond to applied forces (or body forces). Geological materials are extremely complex and different processes may be active at different scales and even in adjacent mineral grains. Nonetheless, there are a small number of models that successfully describe the macroscopic behavior of many natural materials under different conditions. We have already reviewed the three basic models in Chapter 9: ***elastic***, ***plastic***, and ***viscous***.

### *Elasticity*

Because rocks in the upper crust deform by fracturing at even modest strains, elasticity theory is intimately related to the concepts of infinitesimal strain (Chapter

7). We have already seen some of the basic equations of elasticity in Chapter 9. In elastic deformation, by ***Hooke's Law*** stress is linearly related to strain by a variety of elastic moduli depending on the type of deformation:

$\sigma_{11} = E\varepsilon_{11}$ where $E$ = Youngs Modulus (for axial deformations)

$\sigma_{11} = G\left(2\varepsilon_{11}\right)$ where $G$ = Shear Modulus (for i ≠ j ; i.e., simple shear deformations) (12.8)

$\left(\sigma_{11} + \sigma_{22} + \sigma_{33}\right)/3 = B\varepsilon_{ii}$ where $B$ = Bulk Modulus (for volume change deformations

An important additional parameter, ***Poisson's Ratio***, $\nu$, defines the relation of the axial to the transverse strain (Fig. 9.1):

$$\nu = -\frac{e_t}{e_\ell} = -\frac{\left(\frac{w_f - w_i}{w_i}\right)}{\left(\frac{\ell_f - \ell_i}{\ell_i}\right)} \tag{12.9}$$

For incompressible deformation, $\nu = 0.5$, but rocks have $0.10 \leq \nu \leq 0.33$. Poisson's ratio can be used to relate the elastic moduli of equation (12.8):

$$G = \frac{E}{2(1+\nu)} = \frac{3B(1-2\nu)}{2(1+\nu)} \tag{12.10}$$

Thus, for a linear isotropic material, only two elastic moduli are necessary to the elastic deformation. The constitutive equations for linear elasticity are usually written using ***Lamé's constants***:

$$\varepsilon_{ij} = \frac{(1+\nu)}{E}\sigma_{ij} - \frac{\nu}{E}\delta_{ij}\sigma_{kk} \tag{12.11a}$$

$$\sigma_{ij} = 2G\varepsilon_{ij} + \lambda\delta_{ij}I_\varepsilon \tag{12.11b}$$

Where $I_\varepsilon$ is the first invariant of the infinitesimal strain tensor and $\delta_{ij}$ is the Kronecker delta. The shear modulus, $G$, is sometimes written using the Greek letter, $\mu$. The Lamé constant, λ, is related to the other elastic moduli by:

$$\lambda = \frac{\nu E}{(1+\nu)(1-2\nu)} \quad \text{and} \quad \lambda = K - \frac{2}{3}G \tag{12.12}$$

*Viscosity*

Over long time spans, even seemingly solid materials creep viscously. In the simplest form of viscosity, a ***Newtonian fluid***, shear stress is linearly related to the deformation rate (Fig. 9.3) via the viscosity, $\eta$:

$$\tau = \eta \dot{\varepsilon} \tag{12.13}$$

In a manner similar to elasticity, the constitutive equation for linear viscosity can be written:

$$\sigma_{ij} = -p\delta_{ij} + \lambda \delta_{ij} \frac{\partial v_k}{\partial x_k} + \eta \left( \frac{\partial v_i}{\partial x_j} + \frac{\partial v_j}{\partial x_i} \right) \tag{12.14}$$

Where $p$ is the ***thermostatic pressure***, $\lambda$ is the ***second coefficient of viscosity*** and **v** is the velocity. You may recall that the mean pressure is equal to the first invariant of the stress tensor divided by three (Chapter 5):

$$\sigma_{mean} = \frac{\sigma_{11} + \sigma_{22} + \sigma_{33}}{3} \tag{12.15}$$

The thermostatic pressure can be related to the mean stress by:

$$\sigma_{mean} = -p + \left( \lambda + \frac{2\eta}{3} \right) \frac{\partial v_k}{\partial x_k} \tag{12.16}$$

*Plasticity*

Unlike the simple, linear forms of elasticity and viscosity theory, plasticity is inherently nonlinear and requires the use of hyperbolic partial differential equations. So, we will not pursue plasticity any more here except to point you towards the classic reference in the field: Hill (1950).

## *Boundary Conditions and Initial Values*

The general procedure for carrying out a mechanical analysis is to solve a set of differential equations that result from manipulation of the physical principles and appropriate constitutive equations by integration. This results in constants of

integration that must be evaluated. We have seen an example of this already (although not in the context of a full mechanical analysis): In Chapter 10, the velocity field for the trishear model was derived from the condition of incompressibility and an arbitrary choice for the $v_x$ component of the velocity field. Integrating to solve for the $v_y$ component resulted in a constant of integration, which we evaluated based on the boundary conditions on the two borders of the trishear zone (Eqn. 10.8).

In general, to solve the integrated differential equations, you must specify either the ***boundary conditions*** or the ***initial conditions***. Boundary conditions are limiting values or conditions on the dependent variables at the edges of your model. If you are analyzing the flow of material in a channel, a boundary condition might be that the velocity of the flow must go to zero at the edge of the channel, or in the case of the trishear model just discussed, that the velocity in the triangular shear zone must go to zero on the footwall boundary of the zone. In many problems, one might assume that an important boundary condition is that the surface of the Earth is a traction free surface and thus must be perpendicular to a principal stress. Initial conditions are the values of the time dependent variables at time zero of your analysis. In the case of the flow in the channel, you might specify the velocity of the fluid entering the channel.

Commonly, one specifies either the boundary conditions and solves for that dependent variable in the interior of the body or the initial conditions and solves for the values of that dependent variable at some later time. Imagine that you are studying the formation of a laccolith (Johnson, 1970; Pollard and Fletcher, 2005). You would specify where vertical displacements go to zero (boundary conditions) and, via elasticity theory, solve for the displacement of the bending layer. A problem where the boundary conditions are set is known as a ***boundary value problem*** whereas in analyses where the initial conditions are set it is known as an ***initial value problem***. Needless to say, which type of analysis you do is dependent on what you know already and what your objectives are in the analysis. Take the classic physics problem of a projectile (Middleton and Wilcock, 1994): if you know the mass, angle, and the velocity of the projectile, you know the initial conditions and can calculate how far the projectile should travel and where it will land. From a more practical standpoint, however, you know where the target is that you want to

hit (a boundary condition) and you want to calculate the initial velocity and angle that is necessary to hit the target.

## Some Simple Geological Examples

There is a rich geological literature of mechanical analysis of structures at various scales and complexity. In this section, however, we will limit ourselves to some simple, yet powerful results, first involving rigid bodies and then from linear elastic fracture mechanics. These results are germane to topics that we have already discussed: thrust belts, hydraulic fracturing and flexure.

### *Mechanics of Thrust Belts*

#### *Hubbert and Rubey's (1959) Force Balance for Thrust Plates*

One of the most famous papers in structural geology was entitled "Role of fluid pressure in mechanics of overthrust faulting" (Hubbert and Rubey, 1959). This paper build on earlier work by M. K. Hubbert (1951) and analyzed the case of a block of geological dimensions that was pushed over a pre-existing surface.

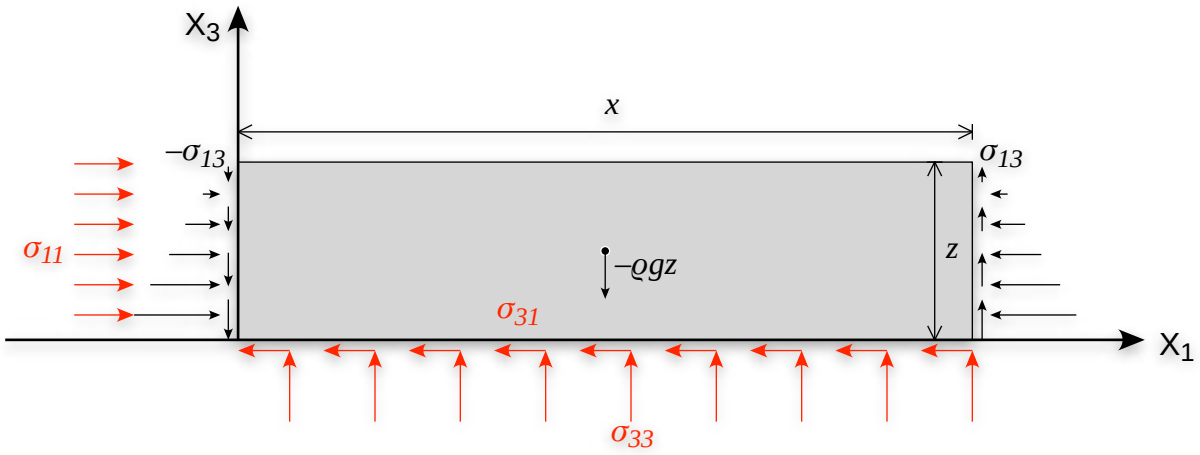


**Figure 12.2 — Free body diagram for pushing a block across a horizontal surface, the basic problem that Hubbert and Rubey (1959) set up to explore the importance of frictional resistance to sliding. The tractions in red are the ones that they explicitly analyzed. The black tractions would be necessary for a complete two-dimensional force balance. Fortunately, the lithostatic component of the normal tractions and the shear tractions on the ends of the block cancel each other out in the full analysis.**

Their analysis is a particularly nice example of static equilibrium balance of forces. In their paper, they only balance forces in the $X_1$ direction although Hubbert was clearly aware that this did not constitute a total force balance (Fig. 12.2). Consult Pollard and Fletcher (2005, p. 255-260) if you wish to see the entire three dimensional force balance. The free body diagram (Fig. 12.2) is posed in terms of tractions (stress vectors); we will have to covert these to forces by integrating the traction along the area of interest (i.e., the side or bottom of the block) in order to do the force balance. In the one-dimensional force balance, the normal force on the left side of the block should be equal to the frictional shear force on the base of the block:

$$\int_0^z \sigma_{11} dx_3 = \int_0^x \sigma_{31} dx_1 \tag{12.17}$$

Evaluating the right hand side of the equation, recall that the frictional resistance is a function of the normal stress, $\sigma_{33} = \rho g z$, times the coefficient of static friction (from Byerlee's law):

$$\int_0^x \sigma_{31} dx_1 = \int_0^x \mu_s \sigma_{33} dx_1 = \int_0^x \mu_s \rho g z dx_1 = \mu_s \rho g z x \tag{12.18}$$

Evaluating the left side of Equation (12.17) requires a slight explanation: There are two possible outcomes as the value of $\sigma_{11}$ is increased: (a) the push will exceed the frictional resistance to sliding that we have just calculated and the entire block will slide coherently, or (b) $\sigma_{11}$ will exceed the fracture strength of the material and the block will break up rather than slide as a rigid block. The problem we are going to solve is actually the latter. To do so, we need an expression for the Coulomb Failure criteria in terms of the principal stresses (Eqn. 6.8, repeated here):

$$\sigma_1 = C_o + K\sigma_3 \quad \text{where} \quad K = \frac{1 + \sin\phi}{1 - \sin\phi} \quad \text{and} \quad C_o = 2S_o\sqrt{K} \tag{12.19}$$

where $S_o$ is the cohesion and $\phi$ is the angle of internal friction. Under these conditions, $\sigma_{11} = \sigma_1$ and $\sigma_{33} = \sigma_3$. Now, we can expand the left side of Equation (12.17):

$$\int_0^z \sigma_{11} dx_3 = \int_0^z \left(C_o + K\sigma_3\right) dx_3 = \int_0^z \left(C_o + K\rho g z\right) dx_3 = C_o z + \frac{K\rho g z^2}{2} \quad (12.20)$$

With both sides of Equation (12.17) evaluated, we have:

$$C_o z + \frac{K\rho g z^2}{2} = \mu_s \rho g z x \quad (12.21)$$

Rearranging the result of Equation (12.21) we get an expression for the length of the block, $x$, in terms of its thickness, $z$, the friction along the base, etc.:

$$x_{max} = \frac{C_o}{\mu_s \rho g} + \frac{Kz}{2\mu_s} \quad (12.22)$$

For $z$ = 5 km, $\varrho$ = 2750 kg m$^{-3}$, $\phi$ = 30°, and $\mu_s$ = 0.85, we calculate the maximum length of the block is 11.8 km, which is much less than the dimension of large thrust sheets, such as the Lewis overthrust in Glacier National Park that can be tracked 80 km or more down dip and hundreds of kilometers along strike.

The basic problem is that, at these dimensions, rocks are fundamentally weak as Hubbert demonstrated in an earlier paper when he posed the thought experiment of whether a crane large enough could lift the entire state of Texas! This simple analysis captures the so-called paradox of low-angle thrust faults that structural geologists have been debating since the early 1900's. Hubbert and Rubey went on to propose that pore fluid pressures, combined with a thrust decollement that dipped gently towards the foreland, could explain large thrust plates. Their work on pore fluid pressures was pioneering but, alas, they were wrong about the dip of the decollement as well as the shape of the thrust block. Our modern understanding of the mechanics of thrust belts as critically tapered wedges is summarized by Dahlen (1990).

*Critically-Tapered Wedges (Dahlen, 1990)*

In a remarkable series of papers, beginning in 1983 (Davis et al., 1983) and culminating with Dahlen (1990), the Princeton group laid out the modern mechanical basis for understanding thrust belts. Their analysis built on earlier work by Elliot (1976) and Chapple (1978), both of whom recognized that thrust belts in cross

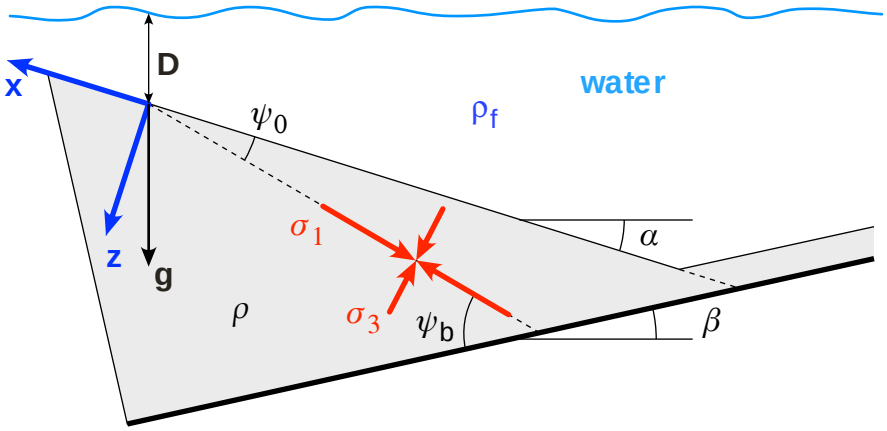


**Figure 12.3 — Diagram showing the coordinate system, key angles, and principal stresses for the general critically tapered wedge model, after Dahlen (1990).**

section had the form of a finely tapered wedge rather than an rectangular block. In this section, we summarize Dahlen's (1990) general two dimensional force balance in a non-cohesive wedge.

The equations of static equilibrium (force balances) in terms of partial differential equations take into account the z as well as the x direction (Fig. 12.3). Summing in the x direction first, we get:

$$\frac{\partial \sigma_{xx}}{\partial x} + \frac{\partial \sigma_{xz}}{\partial z} - \rho g z \sin \alpha = 0 \tag{12.23a}$$

and in the z direction:

$$\frac{\partial \sigma_{xz}}{\partial x} + \frac{\partial \sigma_{zz}}{\partial z} + \rho g z \cos \alpha = 0 \tag{12.23b}$$

At the upper surface of the wedge, the boundary conditions are: $z = 0$; $\sigma_{xz} = 0$ (i.e., no shear stress on the surface of the wedge); and $\sigma_{zz} = -\rho_f g D$ (the weight of the overlying water, or 0 in the case of subaerial wedges). The Hubbert and Rubey pore fluid pressure ratio in the interior of the wedge is given by:

$$\lambda = \frac{p_f - \rho_f g D}{-\sigma_{zz} - \rho_f g D} \tag{12.24a}$$

and along the base by

$$\lambda_b = \frac{p_{fbasal} - \rho_f g D}{-\sigma_{zz} - \rho_f g D} \tag{12.24b}$$

Assuming constant, $\lambda$, $\rho$, porosity, and coefficient of internal friction ($\mu$), the components of the stress tensor at any point within the wedge are:

$$\begin{aligned}
\sigma_{xz} &= \left(\rho - \rho_f\right) g z \sin\alpha \\
\sigma_{zz} &= -\rho_f g D - \rho g z \cos\alpha \\
\sigma_{xx} &= -\rho_f g D - \rho g z \cos\alpha \left[\frac{\csc\phi \sec 2\psi_o - 2\lambda + 1}{\csc\phi \sec 2\psi_o - 1}\right]
\end{aligned} \tag{12.25}$$

The angles that the principal stresses make with the upper and lower surfaces of the wedge are:

$$\begin{aligned}
\psi_o &= 0.5\left[\sin^{-1}\left(\frac{\sin\alpha'}{\sin\phi}\right) - \alpha'\right] \\
\psi_b &= 0.5\left[\sin^{-1}\left(\frac{\sin\phi_b'}{\sin\phi}\right) - \phi_b'\right]
\end{aligned} \tag{12.26a}$$

The primed $\alpha$ and $\phi$ are the surface slope and the basal friction angle, modified by the influence of pore fluid pressure:

$$\begin{aligned}
\alpha' &= \tan^{-1}\left[\left(\frac{1 - \rho_f/\rho}{1 - \lambda}\right)\tan\alpha\right] \\
\phi_b' &= \tan^{-1}\left[\mu_b\left(\frac{1 - \lambda_b}{1 - \lambda}\right)\right]
\end{aligned} \tag{12.26b}$$

Out of all this comes an exact and stunningly simple relationship for the critical taper of the wedge (Dahlen, 1990):

$$\alpha + \beta = \psi_b - \psi_o \tag{12.27}$$

The taper depends on no length parameters and is therefore self-similar. The angles of the principal stresses, and thus the taper, are dependent only on the material properties and the pore fluid pressure and thus do not vary throughout the wedge. Another assumption that we have made is that the entire wedge is on the verge of failure everywhere.

By making a number of small angle assumptions — that $\alpha$, $\beta$, $\psi_0$, and $\psi_b$ are all assumed to be much less than 1 — we can recover the initial result of Davis et al. (1983). For subaerial wedges, the approximate expression for the critical taper is:

$$\alpha + \beta \approx \frac{\beta + \mu_b \left(1 - \lambda_b\right)}{2\left(1 - \lambda\right)\left(\frac{\sin\phi}{1 - \sin\phi}\right)} \tag{12.28}$$

*Step-up Angle of Thrusts*

Now that we know the angles that the principal stresses make with the basal decollement, it is a simple matter to calculate the angle that faults within the wedge will make with respect to the decollement (Dahlen, 1990). From simple Mohr-Coulomb theory, the poles to newly formed faults should form at $(45 + \phi/2)°$ with respect to the $\sigma_1$ principal stress direction. Given the above calculations, there are two possible orientations faults (here given as the angle between the fault plane and the basal decollement):

$$\delta_b = \left(\frac{90 - \phi}{2}\right) - \psi_b \quad \text{and} \quad \delta_b' = \left(\frac{90 - \phi}{2}\right) + \psi_b \tag{12.28}$$

This gives rise to lower angle synthetic thrust faults (forward verging thrusts) and higher angle antithetic thrust faults, i.e., steep back-thrusts (Fig. 12.4). The failure stress on the thrusts within the wedge is:

$$|\tau| = \left(\rho - \rho_f\right) g z \sin\alpha \left(\frac{\cos\phi}{\sin 2\psi_o}\right) \tag{12.29}$$

and on the decollement

$$\tau_b = \left(\rho - \rho_f\right) g z \sin\alpha \left(\frac{\sin 2\psi_b}{\sin 2\psi_o}\right) \tag{12.30}$$

The ratio of these two stresses:

$$0 \le \frac{\tau_b}{|\tau|} = \frac{\sin 2\psi_b}{\cos\phi} \le 1 \tag{12.31}$$

In other words, the decollement must always be weaker than the wedge. This must obviously be the case or the thrust belt would not move but would break up internally. In fact, if you watch a pile of snow or sand in front of a plow blade, you can observe an alternation between failure of the wedge and sliding on the base.

## *Holes and Cracks: Some Important Results from Linear Elastic Fracture Mechanics*

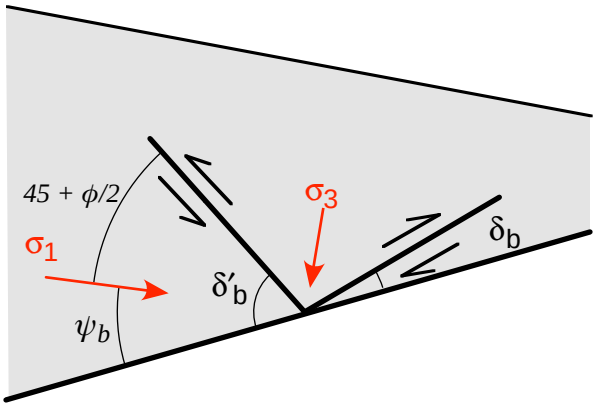


**Figure 12.4 — Step up angles of thrust faults within the wedge relative to the basal decollement. Faults within the wedge are assumed to be Coulomb shears.**

Linear elastic fracture mechanics has provided some deep insights into the deformation in the upper part of the Earth's crust. The derivations of some of the fundamental equations involve imaginary numbers, ***complex variable theory***, and the ***Cauchy-Riemann equations***. These are beyond the scope of this manual but the interested student may check out the development in Jaeger and Cook (1976) or McGinty (2015). As you will see, the results of this section are especially germane to subsurface exploration and drilling for hydrocarbons, geothermal, or fluid injection.

*Circular Holes*

The problem of the stresses around a circular hole in a material has been called the "most important single problem in rock mechanics" (Jaeger and Cook, 1976, p. 249). Given that we drill circular holes in rocks for a variety of reasons, it is not hard to see why this is the case! Kirsch (1898) gave the fundamental solution for the case of uniaxial loading but here we will go straight to the general two dimensional loading case.

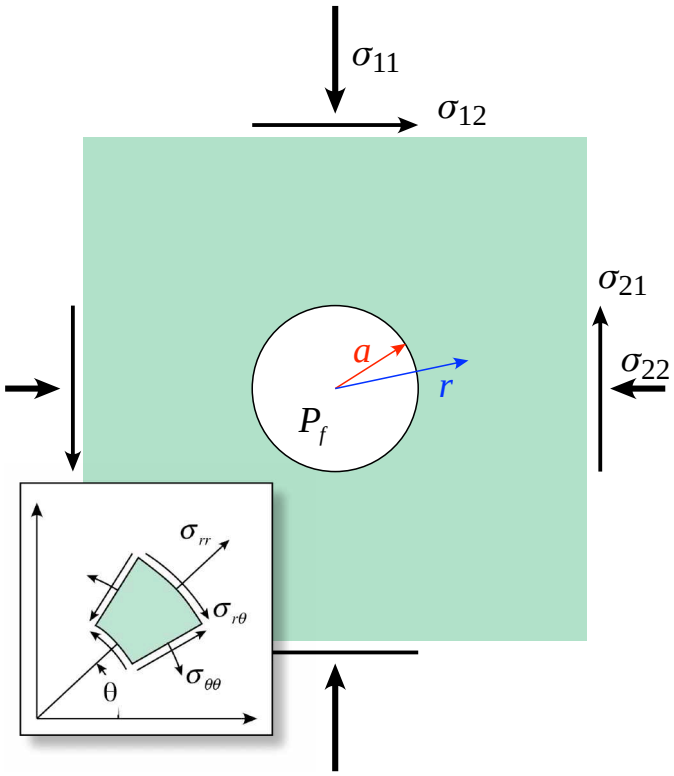


**Figure 12.5 — General two dimensional load on a plate with a circular hole. We use a Cartesian coordinate system with $X_3$ parallel to the axis of the hold and pointing into the page. Stresses around the hole are specified in polar coordinate system with the angle θ measured up from the horizontal (inset view). The hole has a diameter of *a* and the distance from the center of the hole is specified by *r*.**

We assume a far field coordinate system parallel and perpendicular to the axis of the hole and the far field stresses are defined in that coordinate system (Fig. 12.5). The stresses around the hole are defined in a polar coordinate system as shown in the inset diagram. The hole has a radius, *a*, and the stresses are calculated at a distance, *r*, from the center of the hole. The radial and tangential normal and shear stresses are:

$$\sigma_{rr} = \frac{(\sigma_{11}+\sigma_{22})}{2}\left[1-\left(\frac{a}{r}\right)^2\right] + \left[1-4\left(\frac{a}{r}\right)^2+3\left(\frac{a}{r}\right)^4\right]\left(\frac{(\sigma_{22}+\sigma_{11})}{2}\cos 2\theta + \sigma_{12}\sin 2\theta\right) \quad (12.32a)$$

$$\sigma_{\theta\theta} = \frac{(\sigma_{11}+\sigma_{22})}{2}\left[1+\left(\frac{a}{r}\right)^2\right] - \left[1+3\left(\frac{a}{r}\right)^4\right]\left(\frac{(\sigma_{22}+\sigma_{11})}{2}\cos 2\theta + \sigma_{12}\sin 2\theta\right) \quad (12.32b)$$

$$\sigma_{r\theta} = \left[1+2\left(\frac{a}{r}\right)^2 - 3\left(\frac{a}{r}\right)^4\right]\left(\frac{(\sigma_{22}+\sigma_{11})}{2}\sin 2\theta + \sigma_{12}\cos 2\theta\right) \quad (12.32c)$$

For the special case where $\sigma_{11} = \sigma_1$ and $\sigma_{22} = \sigma_2$ and there is fluid pressure, $P_f$, in the hole, the $\sigma_{12}$ term goes zero and the pertinent equations become:

$$\sigma_{rr} = \frac{(\sigma_1+\sigma_2)}{2}\left[1-\left(\frac{a}{r}\right)^2\right] + \frac{(\sigma_2-\sigma_1)}{2}\left[1-4\left(\frac{a}{r}\right)^2+3\left(\frac{a}{r}\right)^4\right]\cos 2\theta + P_f\left(\frac{a}{r}\right)^2 \quad (12.33a)$$

$$\sigma_{\theta\theta} = \frac{(\sigma_1+\sigma_2)}{2}\left[1+\left(\frac{a}{r}\right)^2\right] - \frac{(\sigma_2-\sigma_1)}{2}\left[1+3\left(\frac{a}{r}\right)^4\right]\cos 2\theta - P_f\left(\frac{a}{r}\right)^2 \quad (12.33b)$$

$\sigma_{\theta\theta}$ is commonly referred to as a ***hoop stress***.

Figure 12.6 shows how the stresses vary around the hole for the case of uniaxial loading with $\sigma_1$ = 50 MPa and $\sigma_2$ = 0 MPa. You can see that the tangential or hoop stress at 0° and 180° is three times greater than the far field $\sigma_1$ value! Furthermore, at 90° and 270° the stress is tensional. This value of 3 (in uniaxial load conditions) is known as the ***stress concentration factor***. Interestingly enough, this factor is independent of the size of the hole: a small hole produces just as much

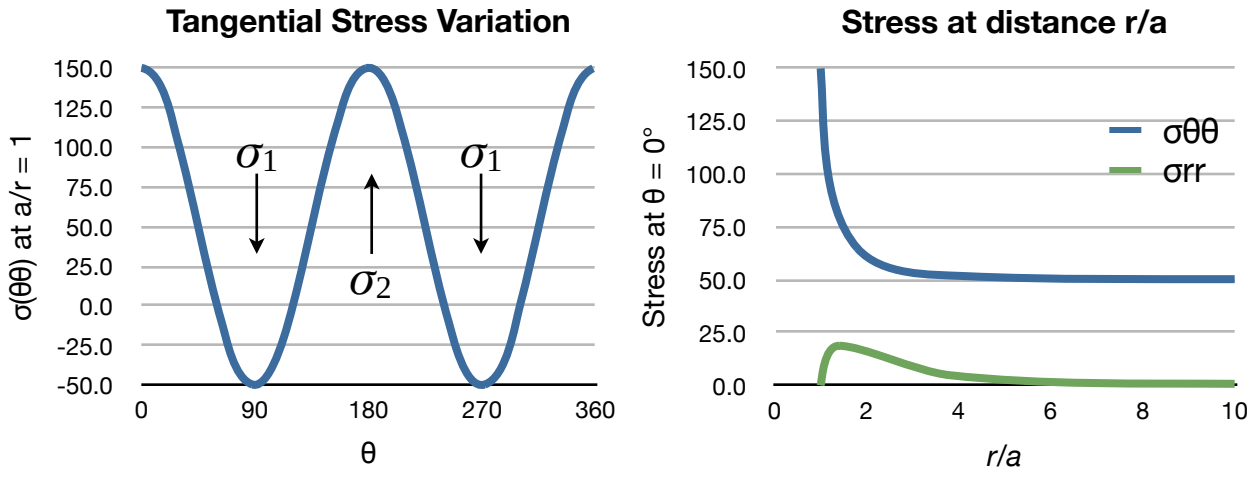


**Figure 12.6 — Left: Variation of the hoop stresses (σθθ) around the edge of a borehole for the case of uniaxial loading. Right: radial and tangential stress variation with distance from a borehole as a function of the radius of the borehole.**

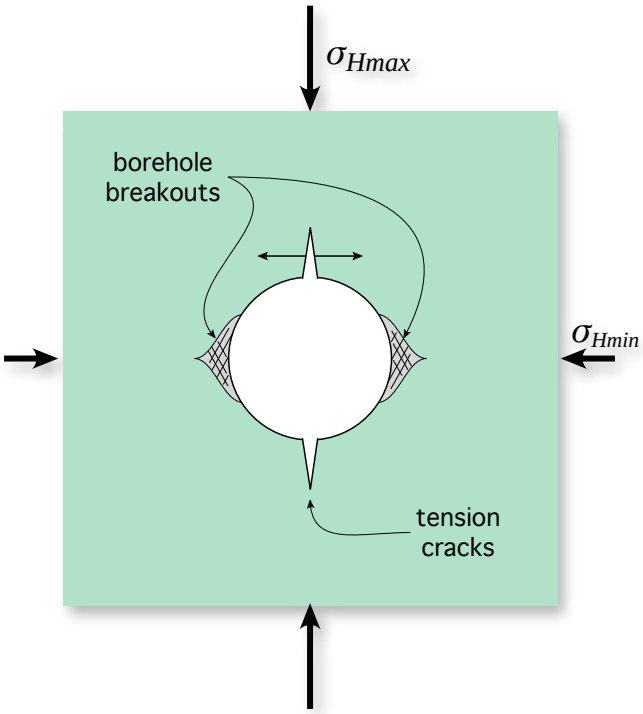


**Figure 12.7 — The location of breakouts and potential tension cracks around a vertical borehole. The breakouts should parallel the minimum principal horizontal stress direction.**

stress concentration as a large hole. You can see that the stress concentration is very localized near the hole (Fig. 12.6, right). Within a distance of five borehole radii, the hoop stress has dropped to within 2% of the regional value.

Now, let's say you are an oil company systematically drilling holes in a producing area. Every one of those boreholes will have these very large stress concentrations and in some cases the stresses will be high enough to cause the well bore to deform by spalling off of pieces in the areas of high stress concentration: these are known as borehole breakouts (Fig. 12.7). For traditional vertical boreholes, breakouts should form by compressive failure in the direction of the least principal horizontal stress and perpendicular to the maximum horizontal principal stress. This turns out to be one of the best ways to determine the orientations of the stress field in the plane perpendicular to the borehole. Figure 12.8 shows the orientations of $\sigma_1$ in the vicinity of the San Andreas fault in central California.

*Cracks*

After Kirsch's circular hole solution, the theory evolved to elliptical holes which in the extreme case become cracks. Cracks are important because, not only do they determine the ultimate strength of the material, but they also are the site

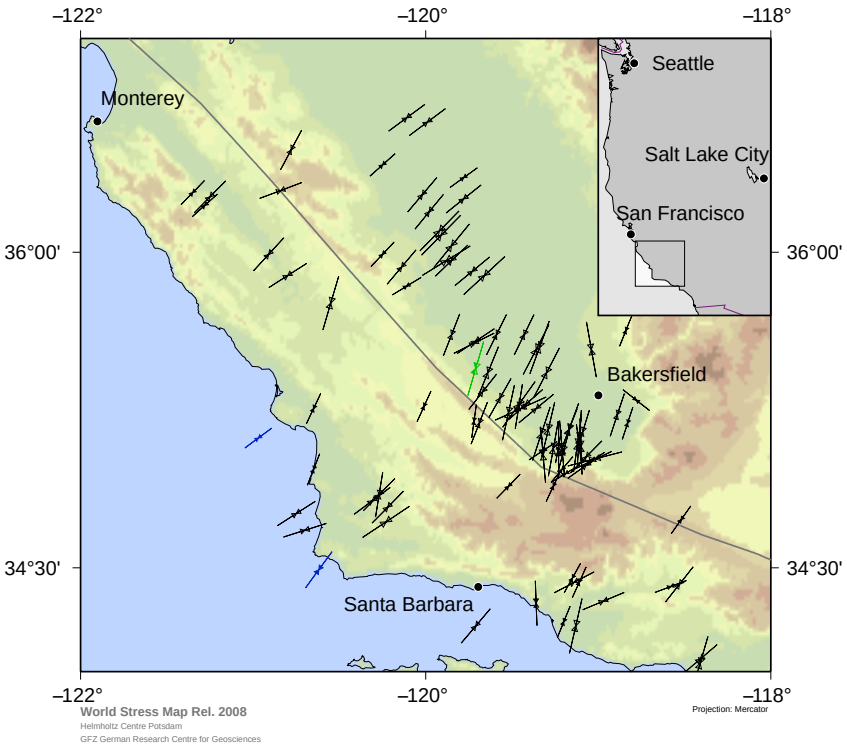


**Figure 12.8 — The orientation of $\sigma_1$ from borehole breakouts near the San Andreas fault (thin black line) in central California from the World Stress Map (Heidbach et al., 2008).**

where subsequent failure via fault tip migration occurs. Some complicated math ensued with each succeeding step forward, but the results are surprisingly simple and powerful. We skip here this important early development and go straight to Irwin's (1957) approximate solution for stresses near a crack tip, that is $r \leq a/10$ (Fig. 12.9). He calculated that the stresses are:

$$\sigma_{11} \approx \frac{\sigma_\infty \sqrt{\pi a}}{\sqrt{2\pi r}} \cos\left(\frac{\theta}{2}\right)\left(1 - \sin\left(\frac{\theta}{2}\right)\sin\left(\frac{3\theta}{2}\right)\right) \tag{12.34a}$$

$$\sigma_{22} \approx \frac{\sigma_\infty \sqrt{\pi a}}{\sqrt{2\pi r}} \cos\left(\frac{\theta}{2}\right)\left(1 + \sin\left(\frac{\theta}{2}\right)\sin\left(\frac{3\theta}{2}\right)\right) \tag{12.34b}$$

$$\sigma_{12} \approx \frac{\sigma_\infty \sqrt{\pi a}}{\sqrt{2\pi r}} \cos\left(\frac{\theta}{2}\right)\sin\left(\frac{\theta}{2}\right)\cos\left(\frac{3\theta}{2}\right) \tag{12.34c}$$

The quantity $\sigma_\infty \sqrt{\pi a}$ is know as the ***stress intensity factor***:

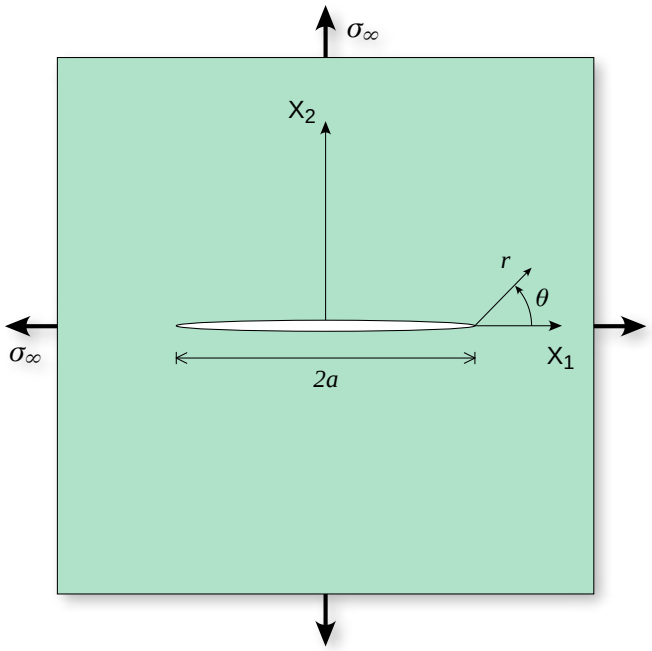


**Figure 12.9 — Stress around a crack tip for a crack with a half length of a. The coordinate system is for Irwin's (1957) approximate solution. $\sigma_\infty$ is the far field stress.**

$$K_I = \sigma_\infty \sqrt{\pi a} \tag{12.35}$$

The above analysis is appropriate for Mode I (opening) cracks (Fig. 6.1). For a Mode II (sliding) crack, the equations are (Pollard and Fletcher, 2005):

$$\sigma_{11} = \frac{K_{II}}{\sqrt{2\pi r}} \left[ -\sin\left(\frac{\theta}{2}\right) \left[ 2 + \cos\left(\frac{\theta}{2}\right) \cos\left(\frac{3\theta}{2}\right) \right] \right] \tag{12.36a}$$

$$\sigma_{22} = \frac{K_{II}}{\sqrt{2\pi r}} \sin\left(\frac{\theta}{2}\right) \cos\left(\frac{\theta}{2}\right) \cos\left(\frac{3\theta}{2}\right) \tag{12.36b}$$

$$\sigma_{12} = \frac{K_{II}}{\sqrt{2\pi r}} \cos\left(\frac{\theta}{2}\right) \left[ 1 - \sin\left(\frac{\theta}{2}\right) \sin\left(\frac{3\theta}{2}\right) \right] \tag{12.36c}$$

And, for a Mode III crack:

$$\sigma_{13} = \frac{K_{III}}{\sqrt{2\pi r}} \left[ -\sin\left(\frac{\theta}{2}\right) \right] \tag{12.37a}$$

$$\sigma_{23} = \frac{K_{III}}{\sqrt{2\pi r}} \left[ \cos\left(\frac{\theta}{2}\right) \right] \tag{12.37b}$$

In all of these cases, we find the square root of distance from the crack tip, *r*, in the

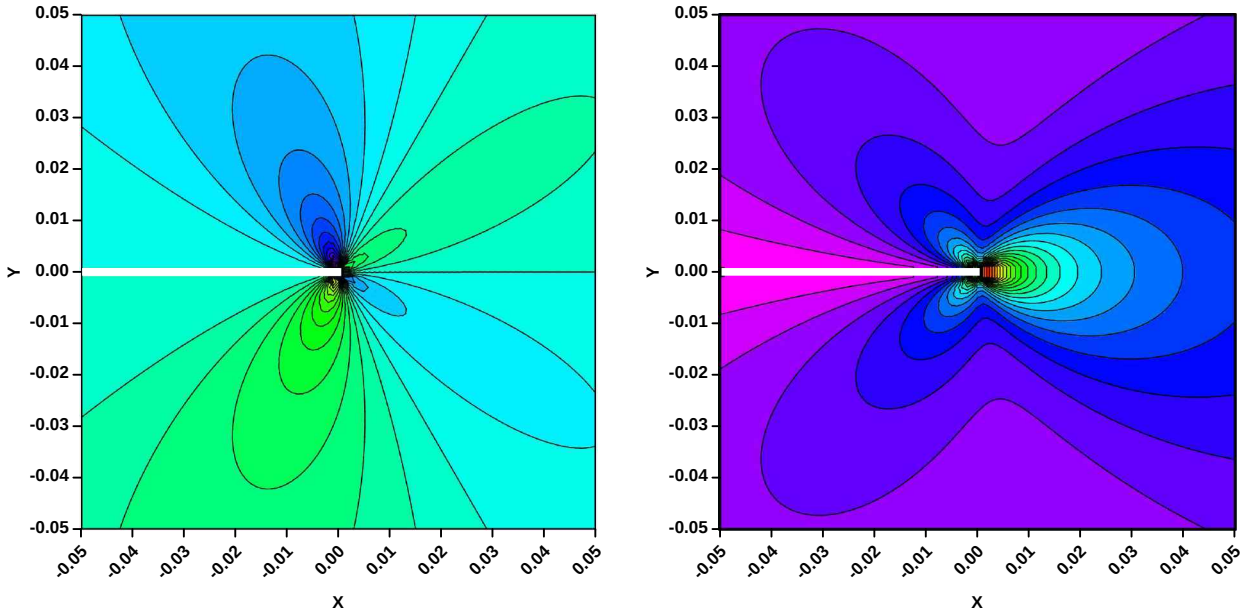


**Figure 12.10 — Two dimensional maps of the $\sigma_{12} = \sigma_{21}$ magnitude at the tip of a horizontal crack (white line), located at (0,0). Width of each diagram is ±0.05*a*. Color map is different in both but the contour interval is the same. In the Mode I case, blues and greens are opposite signs.**

denominator. Thus, at the crack tip itself, these equations all suggest infinite stress. Of course, there can't really be infinite stress there, it is just that linear elasticity doesn't apply near $r = 0$. Figure 12.10 shows plots of the magnitude of shear stress on planes perpendicular or parallel to the crack.

## Final Thoughts: Simulation vs. Illumination

There are many types of models constructed for different purposes. The fault-related folding models that we saw in Chapter 10, for example, have the goal of simulating the geometry, and occasionally the sequence, of deformation. This is a perfectly reasonable objective and there are many practical reasons why we want to project the geometry to depth using predominantly kinematic rules: to define the geometry of a structural trap in a hydrocarbon reservoir, calculate the amount and

distribution of shortening for a palinspastic restoration, evaluate the goodness of fit, or define the likely fault geometry to assess seismic hazard. The goal in simulation is to reproduce, as faithfully as possible, those parts of the structure that we cannot see and what they might look like. Some simulations (e.g., the trishear model) can be carried out extremely rapidly, allowing us to test many possible geometries and find a "best fit" to the data. The problem comes, however, when we assume that the kinematic model "explains" the structure, because we have not, in fact, tested whether the model conforms to the well known physical principles described in this chapter, nor whether the boundary or initial conditions are reasonable.

In this Chapter, we have gotten a glimpse of the suite of physical principles, constitutive equations, and boundary conditions that can be used to illuminate a structural problem of interest. Full mechanical models commonly do not have, as an objective, the simulation of an overall structural geometry. We are not trying to draw a more accurate cross section; instead we are trying to understand why something formed the way that it did. To answer that question, we don't need to reproduce all aspects of the geometry of a structure. What we try to do is distill the problem until all that remains are its most fundamental elements. By making a model simpler, we are more likely to be able to isolate, and illuminate, the key features. When we make models more complex, the number of free variables increases to a point that we can no longer say what is most likely or important. Powerful computer packages to carry out large scale numerical models — especially finite element and discrete element models — run the risk of being so complicated that one can no longer isolate, and get insight into, the key parameters.

So, both simulation and illumination have their place in structural geology. The student's goal is to learn the wisdom to decide what type of model is likely to answer the question of interest.

# Exercises — Chapter 12

1. A simple, well-known experiment in structural geology that relates directly to the Hubbert and Rubey analysis was proposed by the great French fluid mechanics expert, M. A. Biot, and was called the "beer can" experiment[5].

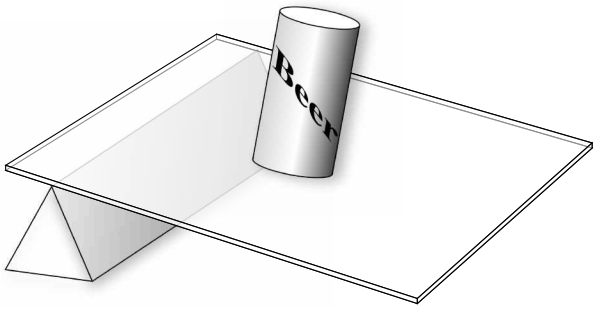


   (a) Experimental procedure

      (i) Take the glass plate provided and place the empty can on one end. Tilt the plate by raising the end on which the can rests. Record the angle of the plate at which the can begins to slide down the tilted glass.

      (ii) Cover the plate with a film of water (if the plate is dirty, you will have to clean it with mild detergent first). Repeat step one. Again, record the angle at which the can slides down the plate.

      (iii) Now chill the can by placing it in the cooler with dry ice [Safety note: Do not handle the dry ice with your bare hands or you run a serious risk of rapid frostbite. Use gloves to place or remove the can from the cooler. Dry ice — or frozen carbon dioxide — is much colder than ice made from water!].

      (iv) After two to three minutes, remove the can from the cooler and place the can on the wetted glass plate with the open end facing up. Tilt until the can slides and record the angle as before.

      (v) Finally, cool the can again, briefly, and place it on the wetted plate, open end down. Tilt until the can slides and record the angle

   (b) Draw a two dimensional free body diagram for the beer can experiment.

   (c) Use a force balance to calculate the coefficient of static friction between the can and the glass for steps (i) to (v) in part (a). How do you explain the result in step (v)? Derive the appropriate equations that demonstrate what is actually going on in step (v) relative to the other steps.

[5] Editorial note: Biot proposed this experiment back in the 1950's, when beer cans were sturdy affairs. Today's beer cans, while being ecologically much more acceptable (though much less welcome on college campuses), have wimpy thin sides that make them unusable for this experiment, so we are reduced to the ignominious fate of having to use a different type of can!

2. The following questions relate to Figure 12.6, which shows the orientations of $\sigma_1$ in central California.
   (a) Make a sketch showing the average orientation of breakouts in the boreholes that were used to calculate the map of stresses. Be sure to include geographic axes and the orientations of the principal stresses.
   (b) Hydraulic fracturing experiments at a depth of 1.3 km in the region show that $\sigma 1$ is 49 MPa with an azimuth of 036° and $\sigma 3$ = 25 MPa on an azimuth of 126°. Calculate the hoop and radial stresses around the borehole.
   (c) Assume that the breakouts formed by small Coulomb shear fractures that extend 1.2 borehole radii into the rock (measured from the center of the borehole). What are reasonable values of cohesion and internal friction for the rock mass that would explain the formation of the breakouts?
   (d) The breakouts reported are commonly from depths of around 3700 m. Assuming that the principal horizontal stresses remain the same and $\rho = 2600$ kg m$^{-3}$, calculate the values and orientations of $\sigma 1$, $\sigma 2$, and $\sigma 3$. How would these new values change your answer to part (c)?

3. Figure 12.8 shows the magnitudes of stresses $\sigma_{12}$ (i.e., $\sigma_{xy}$) with distance from the tip of a Mode I and Mode II crack. What exactly does this stress mean? Explain how you would go about calculating the maximum shear stress around the crack tip for the two cases.

4. The following questions apply to the critically tapered wedge theory described earlier in the Chapter.
   (a) Using Equations 12.26 and 12.27, describe what happens as either the static friction on the base of the wedge, $\mu_b \rightarrow 0$ or the pore fluid pressure ratio on the base, $\lambda_b \rightarrow 1$. The former applies where thrust belt decollements are located in salt horizons; the latter is commonly observed in submarine accretionary prisms.
   (b) The figure on the following page shows two cross sections and topographic profiles across the Subandean fold and thrust belt in Bolivia. The rainfall in the region of the northern profile is 1600 to 2400 mm/yr whereas along the southern profile it is 600-800 mm/yr. Discuss the contrasts between these two sections/profiles in the context of the critically tapered wedge theory and, where the possible explanations are non-unique, describe what type of

data you would like to collect to resolve any ambiguities (assume that money is no obstacle!). You may wish to read Dahlen (1990) first.

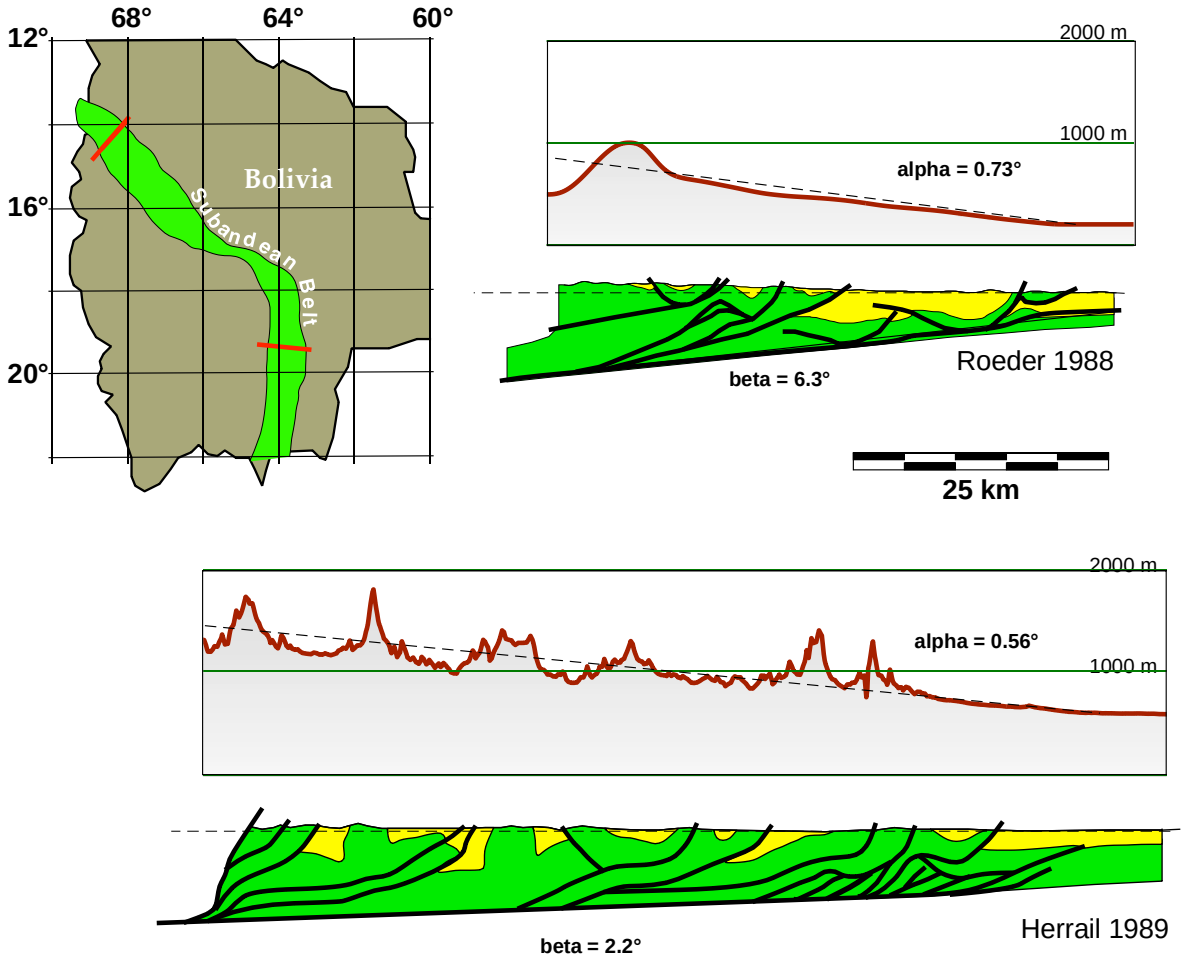

 

# Postface

## *What you've accomplished and where to go next*

If you have made it this far, to the end of this lab manual, congratulations! You have tackled material that takes serious work to learn. If you come from a typical undergraduate geology major background, this manual has introduced you to some tremendously important concepts and methods that are not typically, or adequately, taught to undergraduates in their first structure course. These concepts include powerful linear algebra methods such as transformations of coordinates, vectors, and tensors; the concepts of principal axes and invariants of tensors; the significant differences between stress, infinitesimal strain and finite strain. We have learned about material versus spatial coordinates and how important it is in the analysis of strain as well as in mechanics. We have seen that even the most basic structural geology calculation has significant uncertainty associated with it and gotten a glimpse of how to determine those uncertainties. Finally, you have seen that even the simple spreadsheet program is a powerful computing environment that enables you to solve problems that cannot be solved with traditional graphical methods. And now, a confession on my part: I hate spreadsheet programs! That is because I know how much more powerful, faster, and more capable traditional computer programming is. Hopefully this manual has given you the motivation to acquire those skills as well.

If you come from an engineering or physics background, you are probably wondering what all of the fuss is about! Most of the topics that we have touched on in this manual are treated in the first two years of a typical undergraduate curriculum in those disciplines. Structural geology is, fundamentally, solid mechanics applied to earth materials. Though the methods are the same, there are some significant differences in approach: an engineer might want to know the maximum load that a beam can bear and how much it will flex so that they can design a bridge to a particular specification. The structural geologist is more like a forensic scientist: they come upon the scene when the bridge has already collapsed and is lying in a heap on the valley floor. Our job is to extract from the chaos of a deformation that

has already happened — commonly many millions of years ago — what the key factors were and thereby what the Earth is capable of.

As forensic scientists, we have to go to the field which is the scene of the crime. There is a misconception that field geologists observe and map whereas quantitative or "theoretical" structural geologists stay at home and program their computers. The best structural geologists throughout history have done both: they go to the field (or lab) and make careful quantitative observations and they know how to analyze and probe their data quantitatively to extract meaningful conclusions. This is an iterative process. Initial observations may stimulate deeper mechanical analysis which provides a set of observables for testing with further observation, resulting in further refinements of the theory.

Let's say you come from that typical undergraduate geology major background. After reading this lab manual, I flatter myself to think that a few of you might now be inspired to join the ranks of the best structural geologists. Where should you turn next on this journey? In no particular order, I suggest the following studies:

- Take at least four semesters of college math, which will take you through ***linear algebra and partial differential equations***. The earth is a multivariate system with gradients of properties in all directions. Inverse methods, a branch of linear algebra, are extremely powerful. This is not just the minimum level of math required for structural geology but in fact the minimum level for anyone wanting to become a physical scientist or engineer in just about any field.
- ***Learn a real computing environment***, whether it be Matlab, Python, Fortran, Basic, C++, etc. If you cannot program, you have to wait until someone else writes the program for you and it is unlikely that, by the time that happens, the problem you wanted to solve will still be cutting edge. Like the previous bullet, computing is a skill that all scientists and engineers should have.
- Take ***geomechanics or engineering mechanics courses***. Because these courses require dedication and perseverance, they will be more approachable once you have some idea what the problems are that a

structural geologist wants to solve. This is a necessary step if, as mentioned in Chapter 12, you want to illuminate and not just simulate a structure of interest.

- Most of the problems that we wish to address in structural geology have a high degree of uncertainty due to incomplete data, subjective hypotheses and observation, and lack of knowledge about appropriate boundary conditions, initial values, and constitutive relations. Thus, you will need to ***learn some statistics***; fortunately much of the mathematical background needed for statistics is the same as that needed for structural geology itself. Once you have armed yourself with statistical methods, remember that statistics can only help you eliminate models or hypotheses; they cannot "prove" a hypothesis. The "best" model is simply one that has not yet been eliminated.

Structural geology provides the basis for a tremendously rewarding career: we study deformation features in some of the most beautiful and remote places on Earth. However, we also are expert on problems of extreme societal relevance and interest: earthquakes, induced seismicity, hydraulic fracturing, surface instabilities, and so on. The background that I have described above will enable you to pursue either or both of these branches of our science at the highest level. Good luck!

# References Cited

Albee, H. F., and Cullins, H. L., 1975, Geologic map of the Poker Peak Quadrangle, Bonneville County, Idaho: U.S. Geological Survey Geologic Quadrangle Map GQ 1260.

Allmendinger, R. W., 1998, Inverse and forward numerical modeling of trishear fault-propagation folds: Tectonics, v. 17, no. 4, p. 640-656.

Allmendinger, R. W., and Judge, P. A., 2013, Stratigraphic uncertainty and errors in shortening from balanced sections in the North American Cordillera: Geological Society of America Bulletin, v. 125, no. 9/10, p. 1569-1579, doi: 10.1130/B30871.1.

Allmendinger, R. W., Cardozo, N. C., and Fisher, D., 2012, Structural Geology Algorithms: Vectors & Tensors: Cambridge, England, Cambridge University Press, 289 pp.

Berthé, D., Choukroune, P., and Jégouzo, P., 1979, Orthogneiss, mylonite and non coaxial deformation of granites: the example of the South Armorican Shear Zone: Journal of Structural Geology, v. 1, no. 1, p. 31-42.

Bevington, P. R., and Robinson, D. K., 2003, Data reduction and error analysis for the physical sciences: New York, McGraw-Hill, 320 pp.

Byerlee, J., 1978, Friction of rocks: Pure and Applied Geophysics, v. 116, p. 615-626.

Cardozo, N., and Allmendinger, R. W., 2013, Spherical projections with OSXStereonet: Computers & Geosciences, v. 51, no. 0, p. 193 - 205, doi: 10.1016/j.cageo.2012.07.021.

Chamberlin, R.T., 1910, The Appalachian folds of central Pennsylvania.: Journal of Geology, v. 18, p. 228–251.

Chamberlin, R.T., 1919, The building of the Colorado Rockies: Journal of Geology, v. 27, p. 145–164.

Chapple, W. M., 1978, Mechanics of thin-skinned fold and thrust belts: Geological Society of America Bulletin, v. 89, p. 1189-1198.

Charlesworth, H. A. K., Langenberg, C. W., and Ramsden, J., 1976, Determining axes, axial planes, and sections of macroscopic folds using computer-based methods: Canadian Journal of Earth Science, v. 13, p. 54-65.

Dahlen, F. A., 1990, Critical taper model of fold-and-thrust belts and accretionary wedges: Annual Reviews of Earth and Planetary Science, v. 18, p. 55-99.

Davis, D., Suppe, J., and Dahlen, F. A., 1983, Mechanics of fold-and-thrust belts and accretionary wedges: Journal of Geophysical Research, v. 88, p. 1153-1172.

Elliott, D., 1976, The energy balance and deformation mechanisms of thrust sheets: Philosophical Transactions Royal Astronomical Society Philosophical Transactions Royal Astronomical Society, v. A-283, p. 289-312.

Epard, J.L., and Groshong, R.H., Jr, 1993, Excess area and depth to detachment: American Association of Petroleum Geologists Bulletin, v. 77, p. 1291–1302.

Erslev, E. A., 1991, Trishear fault-propagation folding: Geology, v. 19, no. 6, p. 617-620.

Fossen, H., and Tikoff, B., 1993, The deformation matrix for simultaneous simple shearing, pure shearing, and volume change, and its application to transpression-transtension tectonics: Journal of Structural Geology, v. 15, no. Nos. 3-5, p. 413-422.

Fry, N., 1979, Random point distributions and strain measurement in rocks: Tectonophysics, v. 60, no. 1, p. 89-105.

Hardy, S., and Allmendinger, R. W., 2011, Trishear: A review of kinematics, mechanics, and applications, in McClay, K. et al., eds., Thrust fault related folding: Tulsa, Oklahoma, American Association of Petroleum Geologists, Memoir 94, p. 95-119.

Heidbach, O., Tingay, M., Barth, A., Reinecker, J., Kurfeß, D. and Müller, B., 2008, The World Stress Map database release 2008 doi:10.1594/GFZ.WSM.Rel2008.

Hill, R., 1950, The mathematical theory of plasticity: London, Oxford University Press, 355 pp.

Holt, W. E., Shen-Tu, B., Haines, J., and Jackson, J., 2000, On the determination of self-consistent strain rate fields within zones of distribution continental deformation, in Richards, M. A. et al., eds., The history and dynamics of global plate motions: Washington, D.C., American Geophysical Union, Geophysical Monograph, p. 113-141.

Hubbert, M. K., 1951, Mechanical basis for certain familiar geologic structures: Geological Society of America Bulletin, v. 62, p. 355-372.

Hubbert, M. K., and Rubey, W. W., 1959, Role of fluid pressure in mechanics of overthrust faulting, I. Mechanics of fluid-filled porous solids and its applications to overthrust faulting: Geological Society of America Bulletin, v. 70, p. 115-166.

Irwin, G.R., 1957, Analysis of stresses and strains near the end of a crack traversing a plate: Journal of Applied Mechanics, v. 24, p. 361-364.

Jaeger, J. C., and Cook, N. G. W., 1976, Fundamentals of Rock Mechanics: London, Chapman and Hall, 593 pp.

Johnson, A. M., 1970, Physical processes in geology; a method for interpretation of natural phenomena; intrusions in igneous rocks, fractures, and folds, flow of debris and ice: San Francisco, Freeman, Cooper.

Judge, P. A., and Allmendinger, R. W., 2011, Assessing uncertainties in balanced cross sections: Journal of Structural Geology, v. 33, p. 458-467, doi: 10.1016/j.jsg.2011.01.006.

Kirsch, E.G.,1898, Die Theorie der Elastizität und die Bedürfnisse der Festigkeitslehre: Zeitschrift des Vereines deutscher Ingenieure, v. 42, p. 797-807.

Klotz, J., Angermann, D., Michel, G., Porth, R., Reigber, C., Reinking, J., Viramonte, J., Perdomo, R., Rios, V., Barrientos, S., Barriga, R., and Cifuentes, O., 1999, GPS-derived deformation of the Central Andes including the 1995 Antofagasta Mw = 8.0 Earthquake: Pure and Applied Geophysics, v. 154, p. 709-730.

Kostrov, V. V., 1974, Seismic moment and energy of earthquakes, and seismic flow of rock: Izv. Acad. Sci. USSR Phys. Solid Earth Izv. Acad. Sci. USSR Phys. Solid Earth, v. 1, p. 23-44.

Malvern, L. E., 1969, Introduction to the mechanics of a continuous medium: Englewood Cliffs, N.J., Prentice-Hall, Inc., 713 pp.

McGinty, B., 2015, Fracture mechanics: http://www.fracturemechanics.org/fm/index.html, (2015).

McKenzie, D.P., 1969, The relationship between fault plane solutions for earthquakes and the directions of the principal stresses: Bulletin Seismological Society America, v. 59, p. 591–601.

Menke, W., 1984, Geophysical Data Analysis: Discrete Inverse Theory: Orlando, Academic Press, 260 pp.

Middleton, G. V., and Wilcock, P. R., 1994, Mechanics in the earth and environmental sciences: Cambridge, UK, Cambridge University Press, 459 pp.

Mitra, S., 1993, Geometry and kinematic evolution of inversion structures: American Association of Petroleum Geologists Bulletin, v. 77, no. 7, p. 1159-1191.

Molnar, P., 1983, Average regional strain due to slip on numerous faults of different orientations: Journal of Geophysical Research, v. 88, p. 6430-6432.

Nye, J. F., 1985, Physical properties of crystals; their representation by tensors and matrices: Oxford, England, Oxford University Press, 329 pp.

Petit, J.-P., 1987, Criteria for the sense of movement on fault surfaces in brittle rocks: Journal of Structural Geology, v. 9, p. 597-608.

Pollard, D. D., and Fletcher, R. C., 2005, Fundamentals of Structural Geology: Cambridge, England, Cambridge University Press, 500 pp.

Ramsay, J. G., 1967, Folding and fracturing of rocks: New York, McGraw-Hill, 568 pp.

Ramsay, J. G., and Graham, R. H., 1970, Strain variation in shear belts: Canadian Journal of Earth Sciences, v. 7, p. 786-813.

Ramsay, J. G., and Huber, M. I., 1983, The techniques of modern structural geology, volume 1: Strain analysis: London, Academic Press, 307 pp.

Rich, J. L., 1934, Mechanics of low-angle overthrust faulting as illustrated by Cumberland thrust block, Virginia, Kentucky, and Tennessee: American Association of Petroleum Geologists Bulletin, v. 18, p. 1584-1596.

Sibson, R. H., 1974, Frictional constraints on thrust, wrench and normal faults: Nature, v. 249, p. 542-544.

Sibson, R. H., 1985, A note on fault reactivation: Journal of Structural Geology, v. 7, p. 751-754.

Suppe, J., 1983, Geometry and kinematics of fault-bend folding: American Journal of Science, v. 283, no. 7, p. 684-721.

Suppe, J., Chou, G. T., and Hook, S. C., 1992, Rates of folding and faulting determined from growth strata, in McClay, K. R., ed., Thrust tectonics: London, Chapman & Hall, p. 105-121.

Suppe, J., and Medwedeff, D., 1990, Geometry and kinematics of fault-propagation folding: Eclogae Geologicae Helvetiae, v. 83, no. 3, p. 409-454.

Taylor, J. R., 1997, An introduction to error analysis: The study of uncertainties in physical measurements: Sausalito, California, University Science Books, 327 pp.

Tikoff, B., and Fossen, H., 1993, Simultaneous pure and simple shear: the unifying deformation matrix: Tectonophysics, v. 217, no. 3, p. 267-283.

Turcotte, D. L., and Schubert, G., 1982, Geodynamics: Applications of Continuum Physics to Geological Problems: New York, John Wiley & Sons, 450 pp.

Vollmer, F., 2015, EllipseFit 3.2.0: http://www.frederickvollmer.com/ellipsefit/.

Williams, G., and Chapman, T., 1983, Strains developed in the hangingwalls of thrusts due to their slip/propagation rate; a dislocation model: Journal of Structural Geology, v. 5, no. 6, p. 563-571.

Zehnder, A. T., and Allmendinger, R. W., 2000, Velocity field for the trishear model: Journal of Structural Geology, v. 22, p. 1009-1014.

# Appendix A: Quick Reference

This section contains a listing of formulae that you are likely to use (a lot). They are listed in the order that they occur in the text with their original equation numbers. Click on the equation number to go to the discussion of the equation in the main text.

$$1 \text{ radian} = \frac{180^\circ}{\pi} = 57.2958^\circ$$

$$90^\circ = \frac{\pi}{2}; \quad 180^\circ = \pi; \quad 270^\circ = \frac{3\pi}{2}; \quad 360^\circ = 2\pi \tag{1.1}$$

Vector magnitude:

$$|\mathbf{v}| = \sqrt{v_1^2 + v_2^2 + v_3^2} \tag{2.2}$$

Unit vector and direction cosines:

$$\hat{\mathbf{v}} = \begin{bmatrix} \cos\alpha & \cos\beta & \cos\gamma \end{bmatrix} \tag{2.3}$$

Dot product:

$$\mathbf{u} \cdot \mathbf{v} = \mathbf{v} \cdot \mathbf{u} = |\mathbf{u}| \; |\mathbf{v}| \cos\theta = v_1 u_1 + v_2 u_2 + v_3 u_3 \tag{2.6}$$

$$\theta = \cos^{-1}\left(v_1 u_1 + v_2 u_2 + v_3 u_3\right) \tag{2.7}$$

Cross product:

$$\mathbf{v} \times \mathbf{u} = -\mathbf{u} \times \mathbf{v} = |\mathbf{v}| \; |\mathbf{u}| \sin\theta = \begin{bmatrix} (v_2 u_3 - v_3 u_2) & (v_3 u_1 - v_1 u_3) & (v_1 u_2 - v_2 u_1) \end{bmatrix} \tag{2.8}$$

Direction cosines of a line or pole from trend and plunge or strike and dip in a NED coordinate system:

**Table 2.1-1**

| Axis | Direction Cosine | Lines | Poles to Planes (strike & dip using RHR) |
|---|---|---|---|
| **North** | $\cos\alpha$ | $\cos(trend)\cos(plunge)$ | $\sin(strike)\sin(dip)$ |
| **East** | $\cos\beta$ | $\sin(trend)\cos(plunge)$ | $-\cos(strike)\sin(dip)$ |
| **Down** | $\cos\gamma$ | $\sin(plunge)$ | $\cos(dip)$ |

Trend and plunge from direction cosines:

$$plunge = \sin^{-1}\left(\cos\gamma\right)$$

$$trend = \tan^{-1}\left(\frac{\cos\beta}{\cos\alpha}\right) \text{ if } \cos\alpha > 0 \tag{2.11a}$$

$$trend = 180^\circ + \tan^{-1}\left(\frac{\cos\beta}{\cos\alpha}\right) \text{ if } \cos\alpha < 0 \tag{2.11b}$$

Special case of $\cos\alpha = 0$:

$$trend = 90^\circ \text{ if } (\cos\alpha = 0 \text{ and } \cos\beta \geq 0) \tag{2.11c}$$

$$trend = 270^\circ \text{ if } (\cos\alpha = 0 \text{ and } \cos\beta < 0) \tag{2.11c}$$

Mean vector standard deviation:

$$\cos\delta\alpha_p = 1 - \left(\frac{N-R}{R}\right)\left[\left(\frac{1}{1-p}\right)^{\frac{1}{N-1}} - 1\right] \tag{2.12}$$

Transformation matrix:

$$a_{ij} = \begin{pmatrix} a_{11} & a_{12} & a_{13} \\ a_{21} & a_{22} & a_{23} \\ a_{31} & a_{32} & a_{33} \end{pmatrix} = \begin{pmatrix} \cos\theta_{11} & \cos\theta_{12} & \cos\theta_{13} \\ \cos\theta_{21} & \cos\theta_{22} & \cos\theta_{23} \\ \cos\theta_{31} & \cos\theta_{32} & \cos\theta_{33} \end{pmatrix} \tag{4.2}$$

Vector transformation, new coordinates in terms of old:

$$\begin{aligned} v'_1 &= a_{11}v_1 + a_{12}v_2 + a_{13}v_3 \\ v'_2 &= a_{21}v_1 + a_{22}v_2 + a_{23}v_3 \\ v'_3 &= a_{31}v_1 + a_{32}v_2 + a_{33}v_3 \end{aligned} \tag{4.4}$$

Vector transformation, old coordinates in terms of new:

$$\begin{aligned} v_1 &= a_{11}v'_1 + a_{21}v'_2 + a_{31}v'_3 \\ v_2 &= a_{12}v'_1 + a_{22}v'_2 + a_{32}v'_3 \\ v_3 &= a_{13}v'_1 + a_{23}v'_2 + a_{33}v'_3 \end{aligned} \tag{4.5}$$

Stratigraphic thickness:

$$\begin{aligned} t''_3 - b''_3 = &\Big(\sin\big(strike\big)\sin\big(dip\big)\Big)\big(t_N - b_N\big) - \Big(\cos\big(strike\big)\sin\big(dip\big)\Big)\big(t_E - b_E\big) + \\ &\Big(\cos\big(dip\big)\Big)\big(b_U - t_U\big) \end{aligned} \tag{4.10}$$

Down plunge projection transformation matrix ($\mathbf{X}'_2$ is the fold axis):

$$b_{ij} = \begin{pmatrix} -\sin(TFA) & \cos(TFA) & 0 \\ \cos(TFA)\cos(PFA) & \sin(TFA)\cos(PFA) & \sin(PFA) \\ \cos(TFA)\sin(PFA) & \sin(TFA)\sin(PFA) & -\cos(PFA) \end{pmatrix} \tag{4.12}$$

Rotation transformation matrix:

$$\begin{aligned} a_{11} &= \cos\omega + \cos^2\alpha\,(1 - \cos\omega) \\ a_{12} &= -\cos\gamma\sin\omega + \cos\alpha\cos\beta\,(1 - \cos\omega) \\ a_{13} &= \cos\beta\sin\omega + \cos\alpha\cos\gamma\,(1 - \cos\omega) \\ a_{21} &= \cos\gamma\sin\omega + \cos\beta\cos\alpha\,(1 - \cos\omega) \\ a_{22} &= \cos\omega + \cos^2\beta\,(1 - \cos\omega) \\ a_{23} &= -\cos\alpha\sin\omega + \cos\beta\cos\gamma\,(1 - \cos\omega) \\ a_{31} &= -\cos\beta\sin\omega + \cos\gamma\cos\alpha\,(1 - \cos\omega) \\ a_{32} &= \cos\alpha\sin\omega + \cos\gamma\cos\beta\,(1 - \cos\omega) \\ a_{33} &= \cos\omega + \cos^2\gamma\,(1 - \cos\omega) \end{aligned} \tag{4.14}$$

Summation convention ($i$ is the free suffix and $j$ the dummy suffix):

$$v_i' = \sum_{j=1}^{3} a_{ij} v_j = a_{i1} v_1 + a_{i2} v_2 + a_{i3} v_3 \tag{5.5}$$

Tensor (dyad) product:

$$\mathbf{T} = \mathbf{u} \otimes \mathbf{v} = \mathbf{u}^{\mathbf{T}} \mathbf{v} \quad \text{or} \quad T_{ij} = u_i v_j \quad \text{where} \quad T_{ij} = \begin{bmatrix} u_1 v_1 & u_1 v_2 & u_1 v_3 \\ u_2 v_1 & u_2 v_2 & u_2 v_3 \\ u_3 v_1 & u_3 v_2 & u_3 v_3 \end{bmatrix} \tag{5.7}$$

Invariants of a tensor:

$$\lambda^3 - I\lambda^2 - II\lambda - III = 0 \tag{5.9}$$

$$\begin{aligned} I &= T_{11} + T_{22} + T_{33} + = T_1 + T_2 + T_3 \\ II &= \frac{\left(T_{ij} T_{ij} - I^2\right)}{2} = -\left(T_1 T_2 + T_2 T_3 + T_3 T_3\right) \\ III &= \det T = \left| T_{ij} \right| = T_1 T_2 T_3 \end{aligned} \tag{5.10}$$

Tensor transformation, new in terms of old:

$$T_{ij}{}' = a_{ik} a_{jl} T_{kl} \tag{5.11}$$

Orientation tensor:

$$\mathbf{T} = \begin{bmatrix} \sum \cos^2 \alpha_{[i]} & \sum \left(\cos \alpha_{[i]} \cos \beta_{[i]}\right) & \sum \left(\cos \alpha_{[i]} \cos \gamma_{[i]}\right) \\ \sum \left(\cos \beta_{[i]} \cos \alpha_{[i]}\right) & \sum \cos^2 \beta_{[i]} & \sum \left(\cos \beta_{[i]} \cos \gamma_{[i]}\right) \\ \sum \left(\cos \gamma_{[i]} \cos \alpha_{[i]}\right) & \sum \left(\cos \gamma_{[i]} \cos \beta_{[i]}\right) & \sum \cos^2 \gamma_{[i]} \end{bmatrix} \tag{5.22}$$

Cauchy's Law:

$$p_i = \sigma_{ij} \ell_j \tag{5.23a}$$

$$\begin{aligned} p_1 &= \sigma_{11} \ell_1 + \sigma_{12} \ell_2 + \sigma_{13} \ell_3 \\ p_2 &= \sigma_{21} \ell_1 + \sigma_{22} \ell_2 + \sigma_{23} \ell_3 \\ p_3 &= \sigma_{31} \ell_1 + \sigma_{32} \ell_2 + \sigma_{33} \ell_3 \end{aligned} \tag{5.23b}$$

Mohr's Circle for stress:

$$\sigma_n = \left(\frac{\sigma_1 + \sigma_3}{2}\right) + \left(\frac{\sigma_1 - \sigma_3}{2}\right)\cos 2\theta \tag{5.25a}$$

$$\tau = \sigma_s = \left(\frac{\sigma_1 - \sigma_3}{2}\right)\sin 2\theta \tag{5.25b}$$

Mean and deviatoric stress:

$$\sigma_m = \frac{I_\sigma}{3} = \frac{\sigma_{11} + \sigma_{22} + \sigma_{33}}{3} = \frac{\sigma_1 + \sigma_2 + \sigma_3}{3} \tag{5.26}$$

$$\sigma_{ij} = \begin{bmatrix} \sigma_m & 0 & 0 \\ 0 & \sigma_m & 0 \\ 0 & 0 & \sigma_m \end{bmatrix} + \begin{bmatrix} \sigma_{11} - \sigma_m & \sigma_{12} & \sigma_{13} \\ \sigma_{21} & \sigma_{22} - \sigma_m & \sigma_{23} \\ \sigma_{31} & \sigma_{32} & \sigma_{33} - \sigma_m \end{bmatrix} \tag{5.27}$$

Slip from piercing points, where **p1** is the position of the line, **v** is the direction cosines of the line, **p2** is a point on the plane, **n** the direction cosines of the pole to the plane:

$$u = \frac{\hat{\mathbf{n}} \cdot [\mathbf{p2} - \mathbf{p1}]}{\hat{\mathbf{n}} \cdot \hat{\mathbf{v}}} = \frac{n_1\left(p2_1 - p1_1\right) + n_2\left(p2_2 - p1_2\right) + n_3\left(p2_3 - p1_3\right)}{n_1 v_1 + n_2 v_2 + n_3 v_3} \tag{6.4}$$

$$p_1 = p1_1 + u v_1; \quad p_2 = p1_2 + u v_2; \quad p_3 = p1_3 + u v_3 \tag{6.5}$$

$$slip = \sqrt{\left(p\left(hw\right)_1 - p\left(fw\right)_1\right)^2 + \left(p\left(hw\right)_2 - p\left(fw\right)_2\right)^2 + \left(p\left(hw\right)_3 - p\left(fw\right)_3\right)^2} \tag{6.6}$$

Coulomb failure envelope:

$$\tau = \sigma_s = S_o + \sigma_n \mu \tag{6.7}$$

In terms of principal stresses:

$$\sigma_1 = C_o + K\sigma_3 \quad \text{where} \quad K = \frac{1 + \sin\phi}{1 - \sin\phi} \quad \text{and} \quad C_o = 2S_o\sqrt{K} \tag{6.8}$$

Failure envelope for frictional slip on pre-existing planes:

$$\tau = \mu_s \sigma_n \tag{6.9}$$

Coulomb failure with pore fluid pressure:

$$\tau = \sigma_s = S_o + \left(\sigma_n - P_f\right)\mu = S_o + \sigma_n^* \mu \tag{6.12}$$

Pore fluid pressure ratio:

$$\lambda = \frac{P_f}{P_{lithostatic}} \quad \text{where} \quad P_{lithostatic} = \bar{\rho}_{rock} g z \tag{6.13}$$

Principal stress ratio:

$$R = \frac{\sigma_2 - \sigma_1}{\sigma_3 - \sigma_1} = \left| \frac{c_{13} c_{23}}{c_{12} c_{22}} \right| \tag{6.22}$$

Stretch, $S$, and inverse stretch, $s$:

$$S = \frac{\ell_f}{\ell_i} = \frac{\Delta x}{\Delta X} \tag{7.2a}$$

$$s = \frac{\ell_i}{\ell_f} = \frac{\Delta X}{\Delta x} \tag{7.2b}$$

Extension, $E$ or $e$, can be defined as the change in length over the initial length (an initial state frame of reference) or the final length (a final state frame of reference):

$$E = \frac{\ell_f - \ell_i}{\ell_i} = \frac{\Delta \ell}{\ell_i} = \frac{\Delta u}{\Delta X} \tag{7.5a}$$

$$e = \frac{\ell_f - \ell_i}{\ell_f} = \frac{\Delta \ell}{\ell_f} = \frac{\Delta u}{\Delta x} \tag{7.5b}$$

Shear strain, $\gamma$, and the angular shear, $\psi$, as:

$$\gamma = \frac{\Delta u}{\Delta Y} \quad \text{and} \quad \psi = \tan^{-1}\left(\frac{\Delta u}{\Delta Y}\right) \tag{7.7}$$

Displacement gradient tensor (asymmetric):

$$\Delta u_i = \frac{\partial u_i}{\partial X_j}\Delta X_j = E_{ij}\Delta X_j \quad \text{or} \quad du_i = \frac{\partial u_i}{\partial X_j}dX_j = E_{ij}dX_j \tag{7.10}$$

$$\int du_i = \int E_{ij}dX_j \quad \Rightarrow \quad u_i = t_i + E_{ij}X_j \tag{7.11}$$

Deformation gradient tensor (asymmetric):

$$\Delta x_i = \frac{\partial x_i}{\partial X_j}\Delta X_j = D_{ij}\Delta X_j \tag{7.12}$$

$$\int dx_i = \int D_{ij}dX_j \quad \Rightarrow \quad x_i = c_i + D_{ij}X_j \tag{7.13}$$

Infinitesimal strain and rotation from the displacement gradient tensor:

$$E_{ij} = \varepsilon_{ij} + \omega_{ij} \tag{7.19}$$

$$\varepsilon_{ij} = \frac{1}{2}\left(E_{ij} + E_{ji}\right) \quad \text{and} \quad \omega_{ij} = \frac{1}{2}\left(E_{ij} - E_{ji}\right) \tag{7.20}$$

Rotation vector, $r_i$, as follows:

$$r_1 = \frac{-\left(\omega_{23} - \omega_{32}\right)}{2}, \quad r_2 = \frac{-\left(-\omega_{13} + \omega_{31}\right)}{2}, \quad \text{and} \quad r_3 = \frac{-\left(\omega_{12} - \omega_{21}\right)}{2} \tag{7.21}$$

Mohr's Circle for infinitesimal strain:

$$\begin{aligned} \varepsilon_{11}{}' &= \frac{\left(\varepsilon_1 + \varepsilon_3\right)}{2} + \frac{\left(\varepsilon_1 - \varepsilon_3\right)}{2}\cos 2\theta \\ \varepsilon_{13}{}' &= \frac{\gamma}{2} = \frac{\left(\varepsilon_1 - \varepsilon_3\right)}{2}\sin 2\theta \end{aligned} \tag{7.28}$$

P- and T-axes for faults and earthquakes, n is the pole, s the slip unit vectors. $k = 1$ for normal faults and $k = -1$ for reverse faults:

$$P_i = \frac{n_i + ks_i}{\sqrt{2}} \quad \text{and} \quad T_i = \frac{n_i - ks_i}{\sqrt{2}} \tag{7.34}$$

Seismic moment, $M_o$, and geometric moment, $M_g$:

$$M_o = A\bar{s}\mu \quad \text{and} \quad M_g = A\bar{s} \tag{7.35}$$

"Asymmetric moment tensor" as the dyad product of the slip and normal vectors:

$$M_{ij} = \sum_{k=1}^{n\_faults} M_g u_i n_j \tag{7.36}$$

Kostrov's symmetric moment tensor, $\varepsilon_{ij}$:

$$E_{ij} = \varepsilon_{ij} + \omega_{ij} = \frac{\sum M_g \left(u_i n_j + u_j n_i\right)}{2V} + \frac{\sum M_g \left(u_i n_j - u_j n_i\right)}{2V} \tag{7.38}$$

Lagrangian strain tensor (initial or material state):

$$L_{ij} = \frac{1}{2}\left[\frac{\partial u_i}{\partial X_j} + \frac{\partial u_j}{\partial X_i} + \frac{\partial u_k}{\partial X_i}\frac{\partial u_k}{\partial X_j}\right] = \frac{1}{2}\left[E_{ij} + E_{ji} + E_{ki}E_{kj}\right] \tag{8.1}$$

Eulerian finite strain tensor, $\overline{L}_{ij}$, is the same as the Lagrangian strain tensor but referenced to the final (spatial) state:

$$\overline{L}_{ij} = \frac{1}{2}\left[\frac{\partial u_i}{\partial x_j} + \frac{\partial u_j}{\partial x_i} + \frac{\partial u_k}{\partial x_i}\frac{\partial u_k}{\partial x_j}\right] = \frac{1}{2}\left[e_{ij} + e_{ji} + e_{ki}e_{kj}\right] \tag{8.5}$$

Green deformation tensor (initial or material state):

$$C_{ij} = \frac{\partial x_k}{\partial X_i}\frac{\partial x_k}{\partial X_j} = D_{ki}D_{kj} \tag{8.6}$$

Cauchy deformation tensor, $\overline{C}_{ij}$, is similar to Equation (8.6), but referenced to the final or spatial state:

$$\overline{C}_{ij} = \frac{\partial X_k}{\partial x_i}\frac{\partial X_k}{\partial x_j} = d_{ki}d_{kj} \tag{8.8}$$

Mohr circle for strain in the deformed (final or spatial) state:

$$\overline{C}_{11}{}' = \frac{\left(\overline{C}_1 + \overline{C}_3\right)}{2} + \frac{\left(\overline{C}_1 - \overline{C}_3\right)}{2}\cos 2\theta \quad \text{and} \quad \overline{C}_{13}{}' = \frac{\left(\overline{C}_1 - \overline{C}_3\right)}{2}\sin 2\theta \qquad (8.15)$$

$$\lambda' = \frac{\left(\lambda_1{}' + \lambda_3{}'\right)}{2} + \frac{\left(\lambda_1{}' - \lambda_3{}'\right)}{2}\cos 2\theta \quad \text{and} \quad \gamma' = \frac{\gamma}{\lambda'} = \frac{\left(\lambda_1{}' - \lambda_3{}'\right)}{2}\sin 2\theta \qquad (8.16)$$

Calculating the Cauchy deformation tensor from three deformed lines:

$$\begin{bmatrix} {}^a\lambda' \\ {}^b\lambda' \\ {}^c\lambda' \end{bmatrix} = \begin{bmatrix} a\left(\frac{dx_1}{\ell_f}\right)^2 & a\left(2\frac{dx_1 dx_2}{\ell_f^2}\right) & a\left(\frac{dx_2}{\ell_f}\right)^2 \\ b\left(\frac{dx_1}{\ell_f}\right)^2 & b\left(2\frac{dx_1 dx_2}{\ell_f^2}\right) & b\left(\frac{dx_2}{\ell_f}\right)^2 \\ c\left(\frac{dx_1}{\ell_f}\right)^2 & c\left(2\frac{dx_1 dx_2}{\ell_f^2}\right) & c\left(\frac{dx_2}{\ell_f}\right)^2 \end{bmatrix} \begin{bmatrix} \overline{C}_{11} \\ \overline{C}_{12} \\ \overline{C}_{22} \end{bmatrix} \qquad (8.22)$$

Poisson's ratio:

$$\nu = -\frac{e_t}{e_\ell} = -\frac{\left(\frac{w_f - w_i}{w_i}\right)}{\left(\frac{l_f - l_i}{l_i}\right)} \qquad (9.2)$$

Elastic moduli (G = shear modulus, E = Youngs modulus, K = bulk modulus):

$$G = \frac{E}{2\left(1+\nu\right)} = \frac{3K\left(1-2\nu\right)}{2\left(1+\nu\right)} \qquad (9.3)$$

Lithostatic load or pressure:

$$P_{lith} = \int_0^z \rho g dz \approx \overline{\rho} g z \qquad (9.4)$$

Minimum stress ratio for reactivation:

$$\Gamma_{min} = \left(\frac{\sigma_1^*}{\sigma_3^*}\right)_{min} = \left(\mu + \sqrt{\left(1+\mu^2\right)}\right)^2 \qquad (9.8)$$

**Table 9.1: Frictional Strength of the Crust-1**

| Vertical Stress | Tectonic Environment | Minimum Differential Stress |
|---|---|---|
| $\sigma_3$ | thrust faulting | $\sigma_1^* - \sigma_3^* \geq \left(\Gamma_{min} - 1\right) \rho g z \left(1 - \lambda\right)$ |
| $\sigma_1$ | normal faulting | $\sigma_1^* - \sigma_3^* \geq \dfrac{\left(\Gamma_{min} - 1\right)}{\Gamma_{min}} \rho g z \left(1 - \lambda\right)$ |
| $\sigma_2$ | strike-slip faulting | $\sigma_1^* - \sigma_3^* \geq \dfrac{\left(\Gamma_{min} - 1\right)}{\Phi\left(\Gamma_{min} + 1\right) + 1} \rho g z \left(1 - \lambda\right)$ where $\Phi = \dfrac{\sigma_2 - \sigma_3}{\sigma_1 - \sigma_3}$ |

Power law creep:

$$\dot{e} = C_o \left(\sigma_1 - \sigma_3\right)^n \exp\left(\frac{-Q}{RT}\right) \tag{9.10}$$

Shear zone displacement from foliation orientations ($\gamma$ = shear strain):

$$\tan 2\theta' = \frac{2}{\gamma} \tag{9.12}$$

$$d = \int_0^y \gamma \, \mathrm{d}y = \int_0^y \frac{2}{\tan 2\theta'} \mathrm{d}y \tag{9.13}$$

General 2D shear:

$$D_{ij} = \begin{bmatrix} S_1 & \dfrac{\gamma\left(S_1 - S_3\right)}{\ln\left(\frac{S_1}{S_3}\right)} \\ 0 & S_3 \end{bmatrix} \tag{9.16}$$

Amount of angular shear, $\psi$, parallel to bedding as a function of the dip, $\delta$, of bedding (Fig. 10.3):

$$\text{kink folds: } \psi = \tan^{-1}\left(2\tan\left(\frac{\delta}{2}\right)\right); \quad \text{curved hinges: } \psi = \tan^{-1}\left(0.0175\delta\right) \quad (10.6)$$

Fault-bend fold equations (Suppe, 1983):

$$\phi = \tan^{-1}\left\{\frac{-\sin\left(\gamma-\theta\right)\left[\sin\left(2\gamma-\theta\right)-\sin\left(\theta\right)\right]}{\cos\left(\gamma-\theta\right)\left[\sin\left(2\gamma-\theta\right)-\sin\left(\theta\right)\right]-\sin\left(\gamma\right)}\right\} \quad (10.7a)$$

$$\beta = \theta - \phi + \left(180-2\gamma\right) = \theta - \phi + \delta \quad (10.7b)$$

Fault-propagation fold equations:

$$\sin\theta_2 = \left\{\frac{\sin\left(\gamma^*\right)\sin\left(\gamma^*-\beta_1\right)}{\sin\left(\gamma_1-\gamma^*\right)+\left[\frac{\sin\left(\gamma_1\right)\sin\left(\gamma^*-\beta_1\right)}{\sin\left(2\gamma^*-\beta_1\right)}\right]}\right\} \quad (10.8)$$

$$\gamma = 90^\circ + \gamma^* - \gamma_1; \quad \beta_2 = 180^\circ - 2\gamma^* + \beta_1; \quad \text{and} \quad \delta_b = 2\left(\gamma-\gamma^*\right).$$

Trishear fault-propagation folding (linear velocity field):

$$\overrightarrow{v}\left(x,y\right) = \frac{v_0}{2}\left\{\left[\left(\frac{y}{mx}\right)+1\right]\hat{i} + \frac{m}{(1+s)}\left[\left(\frac{\left|y\right|}{mx}\right)^2-1\right]\hat{j}\right\} \quad (10.12)$$

Simple shear deformation of the hanging wall in similar folding:

$$s_n = \frac{h}{\cos\left(\delta_n\right)\left(1+\tan\left(\delta_n\right)\tan\left(\alpha\right)\right)} \quad (10.13)$$

Incompressibility:

$$\nabla\mathbf{v} = \left[\frac{\partial v_1}{\partial x_1}+\frac{\partial v_2}{\partial x_2}+\frac{\partial v_3}{\partial x_3}\right] = 0 \quad (10.17)$$

Area of a polygon with $n$ vertices:

$$A = \frac{1}{2}\sum_{i=0}^{n-1}\left(x_i y_{i+1} - x_{i+1} y_i\right) \tag{10.18}$$

P-wave velocity:

$$velocity = \mathbf{V} = \sqrt{\frac{E}{\rho}} \tag{11.1}$$

Stacking velocity and normal move out time:

$$\Delta t_{NMO} = t_x - t_o = \sqrt{t_o^2 + \frac{x^2}{V_{stacking}^2}} - t_o \tag{11.3b}$$

Dix Equation:

$$V_{i(1,2)} = \sqrt{\frac{V_{st2}^2 t_2 - V_{st1}^2 t_1}{t_2 - t_1}} \tag{11.4}$$

The continuity equation:

$$\frac{d\rho}{dt} + \rho\frac{\partial\left(v_i\right)}{\partial x_i} = 0 \tag{12.1}$$

Law of conservation of momentum ($m\mathbf{v}$):

$$\mathbf{F} = \frac{d(m\mathbf{v})}{dt} \tag{12.3a}$$

Cauchy's First Law of Motion:

$$\rho\frac{dv_i}{dt} = \frac{\partial\sigma_{ij}}{\partial x_j} + \rho g_i \tag{12.4}$$

Cauchy's Second Law of Motion:

$$\sigma_{ij} = \sigma_{ji} \quad \text{for} \quad i, j = 1 \text{ to } 3$$

Strain compatibility, specified by St.-Venant's equations:

$$\frac{\partial^2 \varepsilon_{ij}}{\partial X_k \partial X_l} + \frac{\partial^2 \varepsilon_{kl}}{\partial X_i \partial X_j} - \frac{\partial^2 \varepsilon_{ik}}{\partial X_j \partial X_l} - \frac{\partial^2 \varepsilon_{jl}}{\partial X_i \partial X_k} = 0 \tag{12.7}$$

Lamé's constants:

$$\varepsilon_{ij} = \frac{(1+\nu)}{E}\sigma_{ij} - \frac{\nu}{E}\delta_{ij}\sigma_{kk} \tag{12.11a}$$

$$\sigma_{ij} = 2G\varepsilon_{ij} + \lambda\delta_{ij}I_\varepsilon \tag{12.11b}$$

Where $I_\varepsilon$ is the first invariant of the infinitesimal strain tensor and $\delta_{ij}$ is the Kronecker delta. The Lamé constant, λ, is related to the other elastic moduli by:

$$\lambda = \frac{\nu E}{(1+\nu)(1-2\nu)} \quad \text{and} \quad \lambda = K - \frac{2}{3}G \tag{12.12}$$

Kirsch's (1898) solution for stresses around a circular hole:

$$\sigma_{rr} = \frac{(\sigma_{11}+\sigma_{22})}{2}\left[1-\left(\frac{a}{r}\right)^2\right] + \left[1-4\left(\frac{a}{r}\right)^2+3\left(\frac{a}{r}\right)^4\right]\left(\frac{(\sigma_{22}+\sigma_{11})}{2}\cos 2\theta + \sigma_{12}\sin 2\theta\right) \tag{12.32a}$$

$$\sigma_{\theta\theta} = \frac{(\sigma_{11}+\sigma_{22})}{2}\left[1+\left(\frac{a}{r}\right)^2\right] - \left[1+3\left(\frac{a}{r}\right)^4\right]\left(\frac{(\sigma_{22}+\sigma_{11})}{2}\cos 2\theta + \sigma_{12}\sin 2\theta\right) \tag{12.32b}$$

$$\sigma_{r\theta} = \left[1+2\left(\frac{a}{r}\right)^2-3\left(\frac{a}{r}\right)^4\right]\left(\frac{(\sigma_{22}+\sigma_{11})}{2}\sin 2\theta + \sigma_{12}\cos 2\theta\right) \tag{12.32c}$$

For the special case where $\sigma_{11} = \sigma_1$ and $\sigma_{22} = \sigma_2$ and there is fluid pressure, $P_f$, in the hole:

$$\sigma_{rr} = \frac{(\sigma_1+\sigma_2)}{2}\left[1-\left(\frac{a}{r}\right)^2\right] + \frac{(\sigma_2-\sigma_1)}{2}\left[1-4\left(\frac{a}{r}\right)^2+3\left(\frac{a}{r}\right)^4\right]\cos 2\theta + P_f\left(\frac{a}{r}\right)^2 \tag{12.33a}$$

$$\sigma_{\theta\theta} = \frac{(\sigma_1+\sigma_2)}{2}\left[1+\left(\frac{a}{r}\right)^2\right] - \frac{(\sigma_2-\sigma_1)}{2}\left[1+3\left(\frac{a}{r}\right)^4\right]\cos 2\theta - P_f\left(\frac{a}{r}\right)^2 \tag{12.33b}$$

Irwin's (1959) solutions for stresses near a crack tip:

$$\sigma_{11} \approx \frac{\sigma_\infty \sqrt{\pi a}}{\sqrt{2\pi r}} \cos\left(\frac{\theta}{2}\right)\left(1 - \sin\left(\frac{\theta}{2}\right)\sin\left(\frac{3\theta}{2}\right)\right) \tag{12.34a}$$

$$\sigma_{22} \approx \frac{\sigma_\infty \sqrt{\pi a}}{\sqrt{2\pi r}} \cos\left(\frac{\theta}{2}\right)\left(1 + \sin\left(\frac{\theta}{2}\right)\sin\left(\frac{3\theta}{2}\right)\right) \tag{12.34b}$$

$$\sigma_{12} \approx \frac{\sigma_\infty \sqrt{\pi a}}{\sqrt{2\pi r}} \cos\left(\frac{\theta}{2}\right)\sin\left(\frac{\theta}{2}\right)\cos\left(\frac{3\theta}{2}\right) \tag{12.34c}$$

Stress intensity factor:

$$K_I = \sigma_\infty \sqrt{\pi a} \tag{12.35}$$

For a Mode II (sliding) crack, the equations are (Pollard and Fletcher, 2005):

$$\sigma_{11} = \frac{K_{II}}{\sqrt{2\pi r}}\left[-\sin\left(\frac{\theta}{2}\right)\left[2 + \cos\left(\frac{\theta}{2}\right)\cos\left(\frac{3\theta}{2}\right)\right]\right] \tag{12.36a}$$

$$\sigma_{22} = \frac{K_{II}}{\sqrt{2\pi r}}\sin\left(\frac{\theta}{2}\right)\cos\left(\frac{\theta}{2}\right)\cos\left(\frac{3\theta}{2}\right) \tag{12.36b}$$

$$\sigma_{12} = \frac{K_{II}}{\sqrt{2\pi r}}\cos\left(\frac{\theta}{2}\right)\left[1 - \sin\left(\frac{\theta}{2}\right)\sin\left(\frac{3\theta}{2}\right)\right] \tag{12.36c}$$

And, for a Mode III crack:

$$\sigma_{13} = \frac{K_{III}}{\sqrt{2\pi r}}\left[-\sin\left(\frac{\theta}{2}\right)\right] \tag{12.37a}$$

$$\sigma_{23} = \frac{K_{III}}{\sqrt{2\pi r}}\left[\cos\left(\frac{\theta}{2}\right)\right] \tag{12.37b}$$

# Appendix B: SmartPhone Compass Apps

## Introduction

We are on the verge of a new era in structural geology data collection with the advent of smart phone compass apps that enable us to collect much more data than is possible with a traditional analog compass. Here, we review the state of the art in smart phone apps, understanding that this section could rapidly become outdated with technological advancements, changes in operating systems, and new or improved sensors. In particular, we describe how one such app actually does its calculations.

## Smart Phone Apps and Operating Systems

At the time of this writing (2017), work by Novakova and Pavlis (2017) suggests that Android devices are extremely variable and thus at least somewhat unreliable for structure data collection. In contrast, iPhone compass apps can be used with some simple precautions for all but the most demanding tasks (Lee et al., 2013; Cawood et al., 2017; Allmendinger et al., 2017). Thus, we focus here solely on iPhone apps.

There are a number of iPhone geological compass apps available, either for free or at very moderate cost, written by geologists. These include:

- *GeoID* (Lee et al., 2013)
- *Fieldmove Clino* (https://www.mve.com/digital-mapping)
- *Lambert* (http://www.nileus.de/lambert/)
- *ListerCompass* (http://geologycompass.com/listerCompass/)
- *Stereonet Mobile* (Allmendinger et al., 2017; http://www.geo.cornell.edu/geology/faculty/RWA/programs/stereonet-mobile.html)

Although no rigorous comparison of all the different apps yet exists, they all rely on the same sensors and thus are likely to have similar accuracy. This is certainly the

case with *Fieldmove Clino* and *Stereonet Mobile*, which we have tested against each other. Thus, choice of which app to use is one of personal preference. All of the apps have different interfaces and different degrees of functionality. *Stereonet Mobile*, for example, is the only one that has an augmented reality sighting mode using the device camera and has the greatest number of stereonet analysis functions and calculations (e.g., rotations, mean vector and cylindrical best fit calculations, etc.). *Fieldmove Clino* offers the greatest flexibility for tagging data with location and rock type information. *GeoID* is particularly well suited for slope stability measurements. Most have the ability to show your measurements on a map with differing degrees of specificity.

## Stereonet Mobile

Here we describe in some detail how one such program, *Stereonet Mobile* (selected because the author of this manual is also the author of the app), works. This section is taken from Allmendinger et al. (2017) with only minor changes.

### *Device Sensors*

Smart phones have a vast array of sensors to determine device orientation including GPS receivers, accelerometers, gyroscopes, magnetometers, and even barometers. From these sensors, it is possible to determine device orientation, position, velocity, and linear and rotational acceleration (e.g., Allan, 2011). The iOS operating system provides the programmer with this derived information through its CoreMotion routines which handle the translation of the raw sensor data into the orientations that we as geologists want. Foremost among these is magnetometer calibration which attempts to cancel out the effects of local magnetic fields, especially from other components within the device such as the power supply, etc., so that the orientation with respect to magnetic north can be determined. Dip measurements collected with smart phones are generally much more accurate than strikes because the magnetometer is much more sensitive to, and local perturbations more common in, the local magnetic field than in the local gravity field. The dip of the device can be determined from the three components of the acceleration due to gravity alone and does not have to depend on the magnetometer at all.

Sensors in the iPhone, sampled by the *Sensor Kinetics Pro* app at about 30 Hz, appear to be very stable (Allmendinger et al., 2017, Fig. 1) especially in comparison to the Android devices tested by Novakova and Pavlis (2017, their Figure 2). Nonetheless, the iPhone magnetometer is easily perturbed by passing even small metal objects within several centimeters of the device. This has considerable implications for best practices in the field when using phones as data collection devices.

## *Device Coordinate System and Determining Orientation*

The iOS device coordinate system and the rotations about the three axes are shown in Figure B1. One "reads" the face of the device like a right-handed map coordinate system: the first axis, X′1, is parallel to and in the short, or side-to-side, direction of the face with positive to the right. The second axis, X′2, is parallel to the face and the long axis of the device with positive toward the top of the phone, and X′3, the third axis, is perpendicular to the face and positive towards the user. The change in orientations of the device is determined by the rotation of this coordinate system with respect to a reference coordinate system. The iOS operating system provides the programmer with four different potential reference frames. *Stereonet Mobile* uses the "CMAttitudeReferenceFrameXTrueNorthZVertical" reference frame. That is, the rotation matrix is equal to the identity matrix when the phone face is horizontal with the short axis (X′1) aligned NS. To determine true north, the operating system must know the device position on the globe in order to calculate magnetic declination. Thus, reading an orientation must also turn on the device GPS receiver.

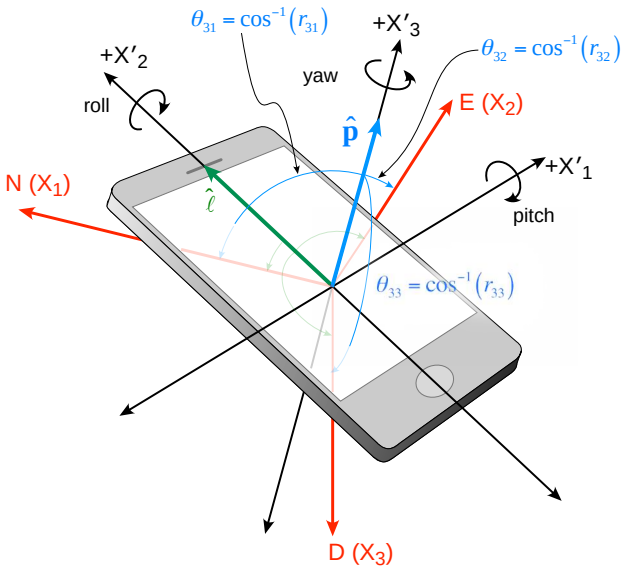


**Figure B1. The coordinate system of the iPhone and its relations to a North-East-Down coordinate system.**

The change in orientation is supplied to the programmer by iOS in several different ways. Perhaps most common is using the Euler angles (Fig. B1), the pitch,

roll, and yaw (sometimes known as the Tait-Bryan angles), which are familiar to anyone in aviation or boating. Determining device orientation using these angles, though, can be subject to an artifact known as gimbal lock where one degree of freedom is lost in certain orientations. Thus, iOS also provides orientation information via a rotation matrix or via quaternions. *Stereonet Mobile* uses the rotation matrix to calculate the orientation of the device relative to the reference frame. The rotation matrix, **r**, in terms of the pitch roll and yaw, for iOS is given as:

$$
\begin{aligned}
r_{11} &= \cos\left(roll\right)\cos\left(yaw\right) - \sin\left(roll\right)\sin\left(pitch\right)\sin\left(yaw\right)\\
r_{12} &= \cos\left(roll\right)\sin\left(yaw\right) + \sin\left(roll\right)\sin\left(pitch\right)\cos\left(yaw\right)\\
r_{13} &= -\sin\left(roll\right)\cos\left(pitch\right)\\
r_{21} &= -\sin\left(yaw\right)\cos\left(pitch\right)\\
r_{22} &= \cos\left(yaw\right)\cos\left(pitch\right)\\
r_{23} &= \sin\left(pitch\right)\\
r_{31} &= \sin\left(roll\right)\cos\left(yaw\right) + \cos\left(roll\right)\sin\left(pitch\right)\sin\left(yaw\right)\\
r_{32} &= \sin\left(roll\right)\sin\left(yaw\right) - \cos\left(roll\right)\sin\left(pitch\right)\cos\left(yaw\right)\\
r_{33} &= \cos\left(roll\right)\cos\left(pitch\right)
\end{aligned}
$$

The basic form of these equations will look familiar to anyone who has studied how rotations are accomplished in stereonet programs (e.g., Allmendinger et al., 2012) because they represent a single rotation accomplished by performing, in order, the three rotations about the three axes (i.e., three matrix multiplications).

The matrix, **r**, is an orthogonal transformation matrix between the device coordinate system and the North-East-Down (NED) coordinate system familiar to structural geologists (because dips and plunges are measured with positive downwards). To translate device orientation to geological orientation, we simply calculate the orientation of a unit vector parallel to $X'_3$ (i.e., the pole to the device) for planes and another unit vector parallel to $X'_2$, the long axis of the device, for lines (Fig. 2). In terms of direction cosines in a NED coordinate system, the pole to the phone and the geological surface against which it is held is given by:

$$pole.north = r_{31}$$
$$pole.east = -r_{32}$$
$$pole.down = -r_{33}$$

Likewise, a lineation's direction cosines are:

$$lineation.north = r_{21}$$
$$lineation.east = -r_{22}$$
$$lineation.down = -r_{23}$$

Because *Stereonet Mobile* uses the pole to the device, the user can place the back of the phone flush on the bedding surface in any orientation to measure the

(a) Stereonet view

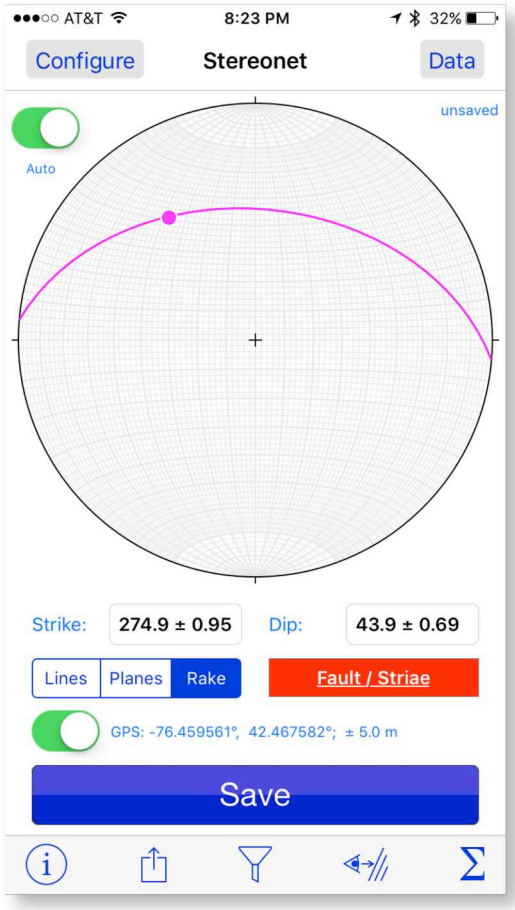


(b) Sighting view

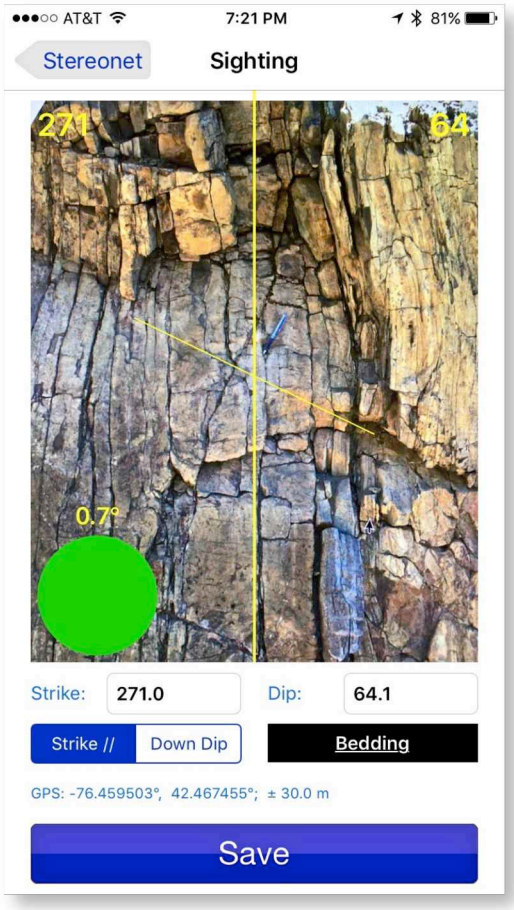


**Figure B2. (a) The stereonet view and (b) sighting view of *Stereonet Mobile*. In (b), the circle in the lower right corner is green because the user is holding the phone within 2° of a level sight.**

surface of interest. We have not noted any significant variation in accuracy when the phone is held in different positions, including upside-down. To measure a line, the long axis or edge of the phone must be parallel to the lineation on the rock but the back of the phone need not be flush against the rock. *Stereonet Mobile* can simultaneously measure the orientation of a plane and a line it contains by placing the back of the phone flush on the rock with the long axis parallel to the lineation in the plane (Fig. B2a).

In cases where one would not want, or cannot, place the phone on the surface to be measured, *Stereonet Mobile* is also capable of measuring a plane's orientation by sighting through the device camera (Fig. B2b). When making a sighting measurement with the plane viewed edge-on (Fig. B3), the pole to the device is assumed to be parallel to the strike direction and the long axis of the device parallel to the true dip direction. For sighting measurements made down-dip, the trend and

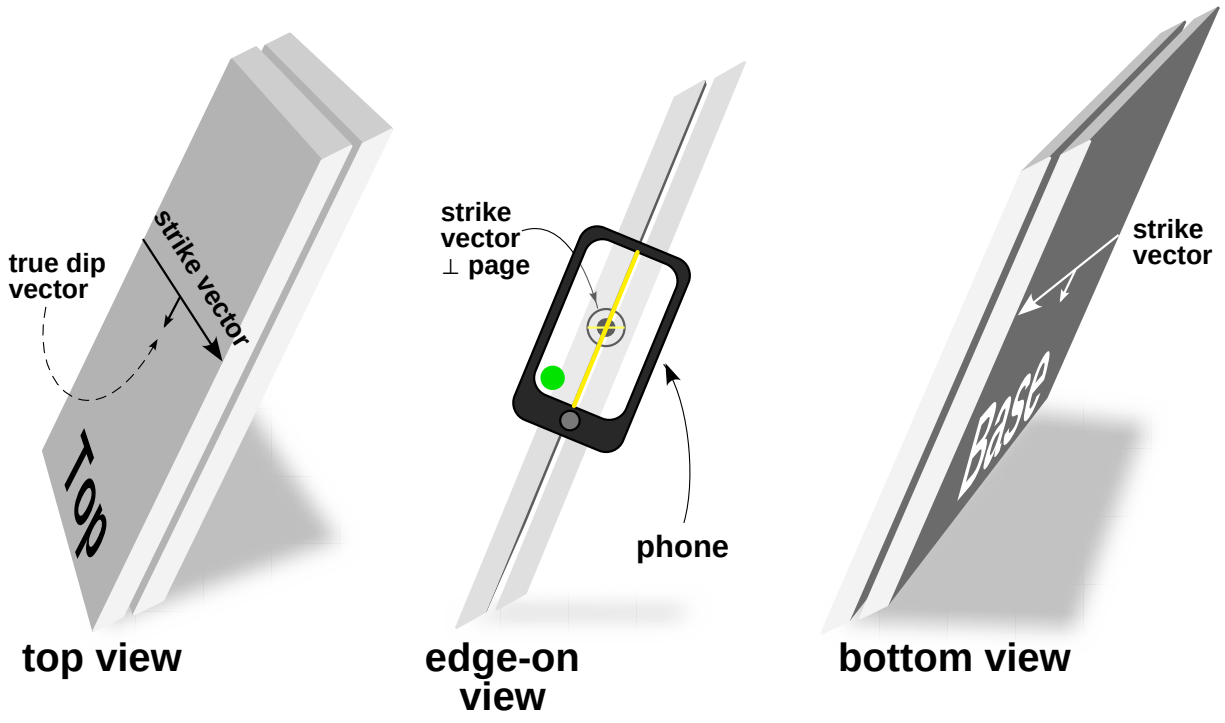


**Figure B3. Three views of the same plane illustrating the meaning of "edge-on" view. When you are aligned with the edge-on view, and the normal (pole) vector to the phone is horizontal (green dot in lower left corner of the screen), it is parallel to the strike of the plane and the long axis of the phone is parallel to the dip azimuth/dip vector of the plane. Strike and dip vectors are shown using right-hand rule convention.**

plunge of the pole to the phone is assumed to be equal to the dip azimuth and dip of the plane.

*Stereonet Mobile* offers the user three planes formats to display planes data: strike and dip (using right-hand rule), dip azimuth and dip, or as poles. Nonetheless, internally it keeps track of all planes measurements in the first of the three formats.

### *Redundant sampling*

Novakova and Pavlis (2017) demonstrated that, for Android devices, transients in the sensor data — brief marked excursions from the long term average value of the sensor — are a serious issue. While transients appear to be much less of an issue for iOS devices, *Stereonet Mobile* nonetheless uses oversampling to avoid any such problems. Before starting sampling, however, the device must be stable. *Stereonet Mobile* determines device stability using the acceleration and rotation rate data provided by the device. Absolute stability is not necessarily desirable as *Stereonet Mobile* permits the determination of orientation by sighting and, whenever the phone is not held against the rock, small motions are inevitable. Thus, stability in *Stereonet Mobile* is defined as user acceleration rates of $< 0.04$ m/s$^2$ and rotation rates of $< 0.09$ radians/s, values that were picked by trial and error. Stability constraints help to avoid inadvertent recording of data while the device is moving.

Once the user holds the device stably for 1 s, *Stereonet Mobile* determines the orientation every 100 ms and displays the mean and standard deviation of all measurements for as long as stability is maintained. For example, if the user holds the phone on a bedding surface for 5 seconds, the orientation and error displayed (Fig. 3) and recorded will reflect the average of 40 measurements ((5 s - 1 s wait time)×10 samples/s). If the error in strike or dip exceeds 3° or the device is moved above the stability threshold, the values are deleted and averaging begins anew. The same standards are used for lineation measurements and for measurements of planes by sighting with the device camera.

This sampling procedure is useful for eliminating random errors including sensor transients, but it does not eliminate systematic errors such as those that arise from the nearby environment. If the magnetic field is continuously perturbed by

the presence of a nearby metal object, data redundancy will not fix the problem. The standard way to attempt to reduce such problems is by magnetometer calibration. For iOS devices, this is achieved by waving the phone in a figure-8 pattern or tilting and rotating the phone. In iOS 10 and with recent Apple® devices, one almost never sees the calibration screen, reflecting the increasing sophistication of the CoreMotion routines and services provided to the programmer. Nonetheless, in our experience, moving the phone in a figure-8 before starting measurements at a new outcrop or after making several measurements still seems to give better results than just assuming the operating system is giving the best possible orientations.

## Best practices for smart phone data collection

1. **Consider device purchase carefully** — The four different iPhones tested by Allmendinger et al. (2017) appear to be demonstrably superior for data collection to the two Android devices tested by Novakova and Pavlis (2017). This suggests that anyone contemplating data collection with a smart phone should consider their device purchases very carefully, prioritizing quality and reliability over economy. However, on both platforms, phone components and operating systems change all the time and no one can guarantee absolutely that the most reliable phone today will be so two years from now. Unfortunately, most phone manufacturers have little incentive to make phones that are ideal for the structural geologist's purpose.
2. **Test individual devices for accuracy prior to field use** — Regardless of the device purchased, one should always do careful tests similar to those described here to determine the reliability of their individual instrument before heading out to the field. General reputation of a manufacturer does not guarantee that the individual device will be adequate to the task. If a particular device proves faulty, many apps, including those described here, can still be used as data recorders, providing the user with automatic time, date, and location tagging of all observations. Test should include:
    2.1. Monitor sensors for stability using an app designed for that purpose. Test the sensitivity of the magnetometer by passing metal objects nearby.

2.2. If using analog compass measurements as a baseline, be sure to compare average of multiple measurements of the Brunton to the average of multiple measurements of the phone app. Do not assume that a single Brunton measurement has absolute accuracy.

2.3. Compare the angular difference of the average poles to planes determined by each instrument. Strike measurement comparisons are only accurate when the dip of the device is 90° (see the supplemental material in Allmendinger et al., 2017, for an explanation of why this is true.).

2.4. If possible, compare phone measurements to the orientation of structures as viewed on high resolution satellite imagery or topographic data (e.g., LiDAR). This test is independent of devices that depend on measuring magnetic field orientation.

3. **Remove metallic and electronic objects from the vicinity when taking measurements** — When using a smart phone in the field, special care beyond that normally used with analog compasses should be taken around metal objects, magnets, and other electronic devices. There are many phone cases available with magnetic clips or closures that can thoroughly spoil your phone readings. Additionally, the user should be careful to remove from proximity seemingly innocent things like metal wristwatches, pens, hand lenses, pocket knives, tablets and laptops, etc.

4. **Calibrate the magnetometer in the device frequently** — Even though the magnetometer calibration screen seldom appears anymore in iOS 10, in our experience, it is a best practice to perform similar motions (figure-8s, tilting the phone in all orientations) before starting on any new outcrop. Additionally, similar calibrations should be undertaken periodically on a single outcrop, whenever a reading does not appear to make sense, or where digital and analog measurements differ significantly. Using a program that can display an orientation on a high-resolution satellite image so the user can verify that a measurement agrees with local geologic strike of the feature being measured can provided added confidence. Several field-based GIS systems, *Fieldmove Clino*, and the latest version of *Stereonet Mobile* can all do this.

5. **Take a traditional analog compass to the field with you** — You will want this to check your phone measurements periodically and whenever data from the phone doesn't seem right.
6. **Use a ruggedized water and dust proof case for the phone** — It goes without saying that any phone being used for data collection should be protected from dust, water, and other abuse in a ruggedized, non-magnetic case.
7. **Back up your data whenever you have a cell phone signal by emailing the data to yourself or uploading to the cloud** — In some ways, data collection with a well-protected phone may actually be more secure than in a paper notebook: whenever the user has a cell or wifi signal, s/he can simply email the current data file to themselves. This facilitates back up of critical field data at more frequent intervals than one would do if they had to wait until returning to town to find a photocopy shop to copy one's field notes!
8. **Take large capacity backup batteries to the field with you** — Standard field gear should include large capacity, rechargeable lithium ion batteries. Small, portable batteries with capacities exceeding 20,000 mAh cost less than $50 and can recharge a smart phone completely 5-7 times. When we were using our phones to make 300 or more measurements/day in Chile, the battery would become completely depleted at or even before the end of a ten hour field day. With 4 or 5 days between return trips into town, having such batteries available in one's camp and backpack is essential.

## Appendix B References

Allan, A., 2011, Basic sensors in iOS: Programming the Accelerometer, Gyroscope, and More: Sebastopol, California, O'Reilly Media 108 p.

Allmendinger, R.W., Siron, C.R., and Scott, C.P., 2017, Structural data collection with mobile devices: Accuracy, redundancy, and best practices: Journal of Structural Geology, v. 102, p. 98–112, doi:10.1016/j.jsg.2017.07.011.

Cawood, A.J., Bond, C.E., Howell, J.A., Butler, R.W.H., and Totake, Y., 2017, LiDAR, UAV or compass-clinometer? Accuracy, coverage and the effects on

structural models: Journal of Structural Geology, v. 98, p. 67–82, doi:10.1016/j.jsg.2017.04.004.

Lee, S., Suh, J., and Park, H.-d., 2013, Smart Compass-Clinometer: A smartphone application for easy and rapid geological site investigation: Computers & Geosciences, v. 61, p. 32–42, doi:10.1016/j.cageo.2013.07.014.

Novakova, L., and Pavlis, T.L., 2017, Assessment of the precision of smart phones and tablets for measurement of planar orientations: A case study: Journal of Structural Geology, v. 97, p. 93–103.